AFIT/DS/ENG/96-15

USING KRIGING TO INTERPOLATE
SPATIALLY DISTRIBUTED VOLUMETRIC
MEDICAL DATA

DISSERTATION

Stephen M. Matechik
Major, USAF

AFIT/DS/ENG/96-15

19970211 038

The views expressed in this dissertation are those of the author and do not reflect the official policy or position of the Department of Defense or the U.S. Government.

AFIT/DS/ENG/96-15

USING KRIGING TO INTERPOLATE
SPATIALLY DISTRIBUTED VOLUMETRIC MEDICAL DATA

DISSERTATION

Presented to the Faculty of the School of Engineering

of the Air Force Institute of Technology

Air University

In Partial Fulfillment of the

Requirements for the Degree of

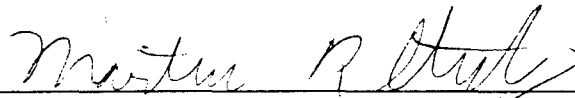Doctor of Philosophy

Stephen M. Matechik

Major, USAF

December 1996

USING KRIGING TO INTERPOLATE
SPATIALLY DISTRIBUTED VOLUMETRIC MEDICAL DATA

Stephen M. Matechik, B.S.E.E., M.S.E.E.
Major, USAF

Approved:

_____   5 Dec 96
Martin R. Stytz, Committee Chairperson

_____   5 Dec 1996
Gideon Frieder, Dean, George Washington University
         Committee Member
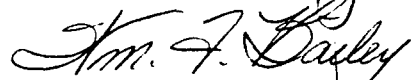
_____   5 Dec 1996
Steven K. Rogers, Committee Member

_____   5 Dec 1996
Mark E. Oxley, Committee Member

_____   5 Dec 1996
William F. Bailey, Dean's Representative
         Committee Member

Accepted:

_____
Robert A. Calico
Dean, School of Engineering

In Loving Memory of Michael

ACKNOWLEDGMENTS

First and foremost, I thank God for the opportunity, the strength and the perseverance to complete this endeavor. As He has done so many times before, He once again has seen me through a very difficult time.

My gratitude is also extended to LtCol Martin Stytz, my research advisor, and to my other committee members - Dean Gideon Frieder, Dr. Steve Rogers , Dr. Mark Oxley and Dr. William Bailey - for the time each of you contributed to this research. LtCol Stytz, your words of encouragement and positive outlook motivated me to press to the very end. Dr. Steve Rogers, I have learned lessons from you that one will never find in a course catalog.

Special mention is further due to Dr. John Haller, Washington University School of Medicine, Barbara McQuiston and LtCol Fred Berg. Dr. Haller, your prompt and generous reply to my request for MRI data says so much about the type of person that you are. I look forward to meeting you someday. Barb, you're a true professional and a cherished friend. Your critiques and insights were always well received and most appreciated. I wish you the best in your doctoral pursuit. LtCol Berg, had it not been for you, I might not have ever been able to find the time to "tie a bow" around one of the most important endeavors of my life. I thank you for your patience and understanding. Now it is my turn to fill in for you!

Mom and Dad, you'll never know just how much your thoughts and prayers assisted me along the way. Thank you. I am also indebted to my children - Stephen, Matthew, Thomas, Christopher, Gregory, Mark and Mary. Often times you may not have understood why I could not share those hours with you that fathers are expected

to share. I will always miss those hours. Nonetheless, I was always thinking of you. Always. I thank you for sacrificing time that belonged to you. I trust someday you will understand.

And finally, Susan, my wife and my inspiration. What can I say? God blessed me with the best when he blessed me with you. There is no one as understanding, as selfless, nor as lovely as you. *We made it!*

TABLE OF CONTENTS

Appendix

LIST OF FIGURES

IV. Designing The AFIT Kriging Algorithm To Interpolate MRI Volume Data

V. INTERPOLATION RESULTS USING THE AFIT KRIGING ALGORITHM

VI. CONCLUSIONS

LIST OF TABLES

VI. CONCLUSIONS

ABSTRACT

Routine cases in diagnostic radiology require the interpolation of volumetric data sets that are acquired using three-dimensional medical imaging modalities. Inaccurate renditions of the interpolated volumes can lead to the misdiagnosis of a patient's condition. It is therefore essential in medical applications that interpolated modality space estimates accurately portray patient space.

Kriging is a geostatistical estimation technique developed for the mining industry to minimize the estimation error of spatially distributed ore grade estimates. It is investigated in this research to interpolate medical imaging volumes. Kriging requires data to be spatially distributed. Therefore, magnetic resonance imaging (MRI) data is shown to exhibit spatially regionalized characteristics such that it can be modeled using regionalized variables and subsequently be interpolated using kriging. A comprehensive, automated, three-dimensional structural analysis of the MRI data is accomplished to derive a mathematical model of spatial variation about each interpolated point. This model identifies voxels that lie within a spatially dependent neighborhood about each point. Kriging uses these voxels to compute estimates of minimal estimation variance. Estimation accuracy of the kriged, interpolated MRI volume is compared and is demonstrated to exceed that achieved using trilinear interpolation if the derived model of spatial variation sufficiently represents the regionalized neighborhoods about each interpolated voxel. Models of spatial variation that assume an ellipsoid extent with orthogonal axes of continuity are demonstrated to insufficiently characterize modality space MRI data. Model accuracy is concluded to be critical to achieve estimation accuracies that exceed those of trilinear interpolation.

Chapter I

INTRODUCTION

Computed tomography (CT), magnetic resonance imaging (MRI), positron emission tomography (PET), and single photon emission computed tomography (SPECT) are examples of three-dimensional medical imaging modalities. Each of these modalities acquire series of voxel-based two-dimensional cross-sectional images of the human body. Each voxel-based two-dimensional image can be sequentially displayed, or a three-dimensional (3D) voxel array of the scanned patient space (PS) volume can be rendered in a single view using surface-based or volume-based rendering techniques. Regardless of the method of analysis, radiologists diagnose their patients based upon information contained in the rendered images. Accurate renditions facilitate correct diagnoses. Inaccurate representations of a patient space volume can contribute to misdiagnoses and subsequent mistreatment. Therefore, the minimization of errors in a modality space (MS) representation of a patient space volume is paramount.

Sources of errors are found in each of the two stages of the medical imaging process. The first stage encompasses the collection and modality space reconstruction of patient space data. Errors introduced during this stage of the medical imaging process are a result of physical constraints of the scanning device, and of the biological responses that stimuli evoke with a given imaging modality. The second stage of the process includes errors that are introduced when the modality space data is transformed to image space for viewing.

Medical imaging modalities sample and quantize a continuous patient space and thereby limit the modality space resolution in terms of voxel dimensions and amplitude

of evoked responses. A typical MRI scan of patient space may generate 128 cross-sectional images that are each 256x256 voxels. A radiologist may desire to display each slice so that it occupies 512x512 display pixels, or to zoom in and magnify a portion of the scanned volume and render it as a continuous three-dimensional view. In either case, the modality space data set must be interpolated to provide the "missing" data values that are necessary to effectively increase the displayed resolution of the acquired modality space volume.

Often times analysis of the modality space data requires estimating volume displacement or tissue type of an object of interest based upon contrast differences observed in the rendered image. Slight differences in intensities over a region of interest can result in different diagnoses. Thus, not only is the accuracy of interpolated values critical, but the confidence that can be placed upon the interpolated volume is also important.

Research Goal

The goal of this research is motivated by routine diagnostic cases in radiology that require the interpolation and display of three-dimensional modality space data sets. It is not sufficient that the estimated values of the interpolated volume merely *appear* to be correct in as much as their values are consistent with neighboring voxel values. Rather, it is essential in clinical applications that one is certain about the fidelity of the rendered image, or at least understands its limitations [Tied90]. Yet, many researchers including Udupa and Herman believe interpolation has received less attention than it deserves [Udup91]. Perhaps this has been attributable to the significant computational costs associated with nonconventional interpolation techniques. According to the 1989

Chapel Hill Volume Visualization Workshop, however, computing power will not be an issue in the years ahead [Hohn89]. In consideration of these factors, this research seeks to provide interpolated modality space estimates that are more accurate than estimates provided by trilinear interpolation, one of the most widely practiced methods of interpolation.

The tool designed to accomplish this goal shall run in an unsupervised manner requiring no user interaction aside from the entry of system initialization parameters. A three-dimensional implementation of the geostatistical estimation technique of kriging is used to obtain the modality space estimates and estimation errors. Kriging requires that the data to be interpolated can be represented using regionalized variables. Therefore, this research also demonstrates how to locate and model the existence of spatially regionalized volume data using a specific imaging modality.

The Geoscience and Clinical Analogy

Commonly employed interpolation techniques, such as trilinear interpolation, derives estimates based solely upon distance weighting contributions from adjacent voxel values. Spatial variation about a point to be estimated (PTBE) is not considered; voxel values are assumed to vary linearly as a function of distance. Kriging, on the other hand, is a geostatistical estimation technique that does not assume the variability of the data surrounding a PTBE. Kriging requires the spatial variation about each PTBE be modeled. Using the model, contributions of neighboring voxel values are weighted in accordance with the modeled local spatial variation to compute each estimate. A by product of the kriging process is an estimation error that can be

computed for each estimate. This error provides a measure of confidence for each estimate based upon the modeled spatial variation.

Kriging originated in the mining industry as a means to obtain improved ore estimates. Phenomena sampled beneath the earth's surface are observed to change gradually from point to point. Kriging utilizes fragmentary knowledge of these slowly changing structural traits to determine the bias that is placed upon one sampled voxel value over another in determining contributions of neighboring voxels. The mining engineer uses this technique to visualize structure beneath the earth's surface.

The quest to improve the estimation accuracy of interpolated modality space medical data sets while providing a measure of confidence for each estimate generates a similar analogy. Tissues of the human body possess unique structural characteristics that can be sampled using different imaging modalities and interpolated to permit radiologists and physicians to noninvasively visualize structure beneath the patient space surface. This analogy is the catalyst that prompts the investigation of the feasibility and potential benefits of using kriging to interpolate three-dimensional medical data.

Though geological and anatomical physical spaces both exhibit spatially regionalized characteristics, differences between employed sampling methods and subsequent interpolation requirements distort the parallelism between the geoscience and clinical analogy. The mining engineer has seemingly greater control over the ratio of feature size to sample size than does the radiologist. Features can extend hundreds or even thousands of feet while the drilling locations to obtain earth samples can literally be positioned only a few feet apart. MRI scanners, on the other hand, provide sampling resolutions on the order of millimeters and sample at regular intervals with

significantly greater density than the mining engineer obtains by drilling. Depending upon the size of the object of interest, these resolutions may or may not be sufficient to properly diagnose a patient's condition.

Another difference between the two sampling methods deals with the volumetric size of a sample relative to the sampling interval distance. In MRI, the evoked response associated with a given patient space position includes attenuated responses from neighboring regions. That is, the patient space extent over which a single MRI sample is obtained is significantly larger relative to the field of view (FOV) than is a single earth sample of a drilling campaign. For practical purposes, earth samples are considered mutually exclusive from one another. MRI samples, on the other hand, do not necessarily satisfy this condition. Ironically, the spatial uncertainty that results from this imaging phenomenon may increase the spatial correlation between neighboring MRI voxels for regions where multiple tissues coexist. Hence, this seemingly negative effect may be considered beneficial when applying an estimation technique that assumes neighboring regions are spatially dependent upon one another. Kriging is such a technique; it assumes the existence of spatially regionalized characteristics in the data that is interpolated.

Kriging is a computationally costly technique whose estimates require orders of magnitude as many arithmetic computations as do conventional linear estimation techniques. Its introduction and utility in clinical environments will undoubtedly require its optimized implementation be integrated with state-of-the-art computational resources. This introduction cannot be expected to occur unless kriging is demonstrated to show performance improvements that exceed present capabilities. The most

challenging interpolation scenarios exist in regions where the source data exhibits its greatest variability. This research emphasizes kriging's potential in these areas.

Another difference between the two sciences deals with the number of values required in a typical estimation scenario. The mining engineer, working with irregularly spaced samples, selects additional drilling locations on a case-by-case basis. Modeling the local spatial variation about each PTBE is likewise accomplished interactively on a case-by-case basis. The radiologist, on the other hand, working with regularly spaced data, finds it impractical to interactively model the local region about each PTBE. In a typical magnification operation, the number of estimates required to magnify an modality space volume is greater than six times the number of sampled values in the original volume. Considering the fact that the number of samples in a modality space volume can run into the tens or hundreds of thousands, the analysis and modeling tasks associated with kriging must be automated to be of utility to the medical imaging community.

Research Overview and Dissertation Organization

This research seeks to improve the accuracy of interpolated estimates of modality space volumes through the structural analysis of the spatial variation about each PTBE and the application of kriging as the employed estimation technique. Prerequisite to its application, the technique must be justified for a given data type and sampling modality. *Type* references medical imaging data of human anatomy. *Sampling modality* references the modality used to capture and generate the data and could be CT, MRI, PET or SPECT. Since each modality generates a representation of patient space somewhat differently using different principles and stimuli, one modality is

selected to narrow the scope of this research - magnetic resonance imaging. In this research, justification of applying kriging to modality space MRI data precedes and is accomplished independently from its application. This dissertation is likewise organized to facilitate the investigation of one objective independent of the other; that is, research that justifies using the technique is summarized independently of the research that develops, applies and analyzes the AFIT Kriging Algorithm. Figure 1-1 depicts this organization.
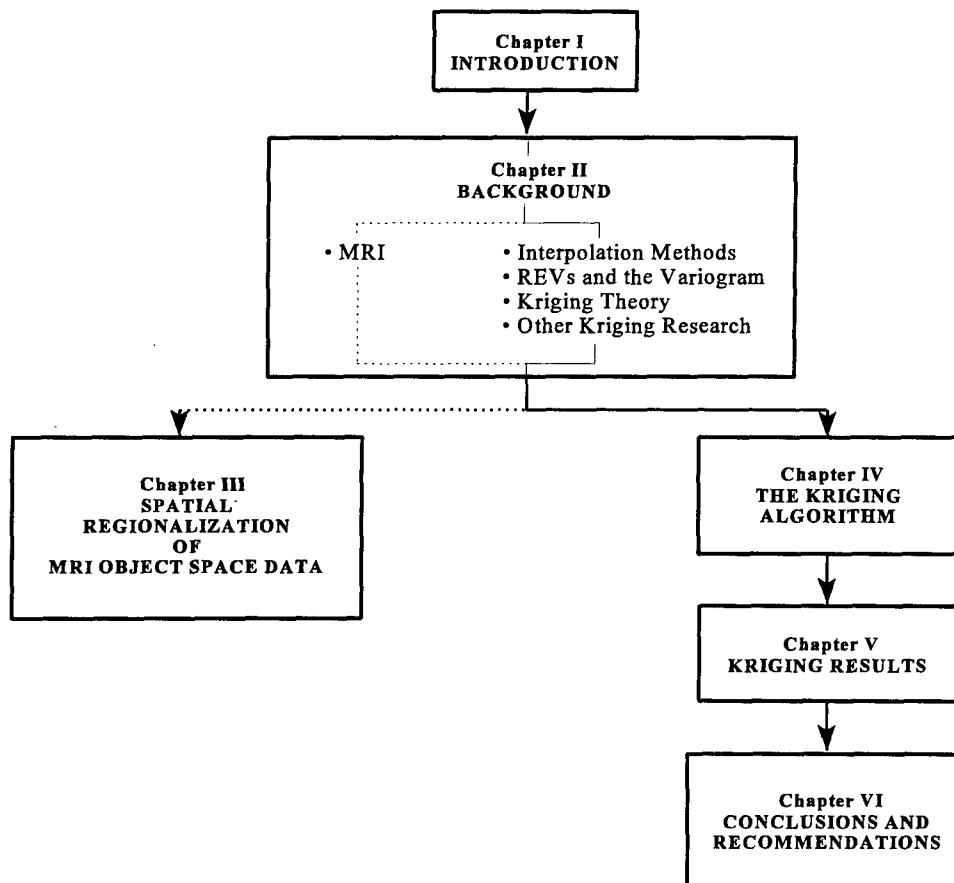
Figure 1-1. Dissertation Organization

Chapter I provides introductory material. It states the research goal as well as an analogy that prompted researching the use of kriging in the field of medical imaging. Chapter I also provides a chapter by chapter overview that briefly summarizes each research phase.

Chapter II provides supporting material for five areas. These areas describe the basic principles of MRI; conventional methods of interpolation; the structural analysis of regionalized variables (REVs) using the semivariogram; the kriging set of equations; and other medical imaging kriging research.

Kriging cannot be considered a valid method of interpolation for a given medical imaging modality unless the modality space data is shown to exhibit spatially regionalized characteristics. For this reason, the data acquisition and reconstruction processes of an MRI scanner are modeled in Chapter III as a means to determine if the distorted modality space representation of a spatially regionalized patient space volume is also spatially regionalized. Modality space representations of patient space phantom volumes are generated based upon simulated component magnetic and rf fields of an MRI scanner. The modality space volumes are spatially analyzed to determine the presence of spatial regionalization. Results of the simulations as well as conclusions drawn are also provided in Chapter III.

Readers who are interested exclusively in the principles and modeling of an MRI scanner and the regionalization of modality space volumes that have been simulated by the scanner model may choose to limit their reading to the Chapter II material and Chapter III as indicated by the path given by the dotted line in Figure 1-1. Readers who are interested in the structural analysis and kriging interpolation of volumetric medical data may skip over the previous material and limit their reading to the Chapter II

material indicated by the path given by the solid line in Figure 1-1 and Chapter IV through Chapter VI, which are introduced in the following paragraphs.

Chapter IV describes the AFIT Kriging Algorithm that is developed and applied to meet the objectives of this research. The AFIT Kriging Algorithm includes tasks to generate a validation data set that is necessary to compute the accuracy of each kriged estimate; identify border region voxels of the modality space volume that are suspected to correspond to locations where different tissue types meet; adaptively structurally analyze and model the spatial variation about each PTBE using both discrete and composite directional variograms; and obtain interpolated estimates and estimation errors based upon the modeled spatial variation. Consistent with the objectives of this research, the AFIT Kriging Algorithm is designed to run in a relatively unsupervised manner. Each algorithm task is described with the intent of providing level of detail sufficient to permit the reader to recreate any or all portions of the AFIT Kriging Algorithm. Reasons that led to the development and use of composite directional variograms as a structural analysis tool are also discussed in Chapter IV.

Several trials of the AFIT Kriging Algorithm are executed using actual modality space MRI data. Both discrete and composite directional variograms of varying angular tolerances are utilized to structurally analyze the local region about each PTBE. Results of each trial are published in Chapter V. Based upon these results, research conclusions and contributions are made regarding the use of kriging as a viable medical imaging interpolation method. These conclusions are summarized in Chapter VI, along with suggestions for future research.

A glossary of medical imaging, MRI and kriging terminology is provided in Appendix A for the reader's convenience. Point-by-point results for each of the

interpolation trials discussed in Chapter V are provided for reference in Appendix B

through Appendix F. Bibliographic references are provided in Appendix G.

Chapter II

BACKGROUND

This research seeks to improve the estimation accuracy of interpolated modality space estimates beyond accuracies obtained using conventional linear techniques. The geostatistical estimation technique known as kriging is used to compute each estimate. Because it uses a weighted linear sum of neighboring sampled values to derive each estimate, kriging is a linear estimator. Weights of neighboring samples are computed using a mathematical model to describe the spatial variation in three dimensions about each point to be estimated (PTBE). Kriging is said to be an unbiased estimator because it provides an estimation error that on the average is zero. The distinguishing characteristic of kriging is that it minimizes estimation error variance. In this respect, kriging is an optimal estimator.

Any of several medical imaging modalities can be utilized to sample a patient space volume and subsequently generate an interpolated modality space representation of that volume. However, kriging assumes that neighborhoods of spatial dependency exist about each PTBE. Therefore, it is necessary to show that spatial continuity, which is evident in patient space, is also present in modality space. For this reason, the scope of this research is limited to the analysis and interpolation of data acquired using a single modality - magnetic resonance imaging (MRI). Consistent with this scope, the purpose of this chapter is to provide a sufficient level of general knowledge in each of six areas related to this research. These areas include: an introduction to three-dimensional medical imaging, basic principles of MRI, conventional interpolation techniques, use of the semivariogram to structurally analyze regionalized variables, the kriging set of equations, and other medical imaging kriging research.

An Introduction to 3D Medical Imaging

As defined by Stytz and Frieder, three-dimensional medical imaging is the subspecialty of volume visualization and computer graphics that addresses issues associated with the rendering and display of medical image data [Styt92b]. Visualization is a discipline dealing with mechanisms that enable seeing structures in data and understanding the phenomenon [Udup92]. Physicians often times must be able to see inside a patient's body to diagnose and treat diseases. Three-dimensional medical imaging provides an alternative to exploratory surgery to allow a physician to complete his or her diagnosis.

The three-dimensional medical imaging process begins with the acquisition of the patient data which is captured from a subject in a patient space coordinate system. This coordinate system is typically attached to the patient such that the z-axis is parallel to the patient's head-to-toe axis, the y-axis is parallel to the patient's front-to-back axis, and the x-axis is parallel to the patient's side-to-side axis. The three-dimensional imaging modalities such as CT, MRI, PET, SPECT provide the data acquisition and processing capabilities necessary to reconstruct and render modality space representations of the patient space data. Different physical properties of the subject and modality are exploited depending upon the modality employed. For instance, ultrasound tomography takes advantage of acoustical impedance properties of body tissues using sound frequencies that are higher than our audible limit to form images. CT radiates collimated x-rays through the body to acquire its data. The x-rays are attenuated to different degrees as they pass through body tissues of different densities. MRI bases its acquisition of data upon the transfer of energy from a pulsed rf field to and from nuclear particles within the patient. PET and SPECT use radioisotopes to track fluid movement and metabolic activity within the body. The

reader is directed to [Styt90] for a more complete discussion of each of these medical imaging modalities.

Each modality samples and digitizes patient space into a three-dimensional modality object space that is referred to herein as modality space. Modality space is typically represented by a Cartesian coordinate system having three orthogonal axes as shown in Figure 2-1, though other coordinate systems may be employed. The medical imaging scanner generates a set of contiguous two-dimensional grids, or slices, of sampled points to construct the modality space volume. Slices that lie along the xz
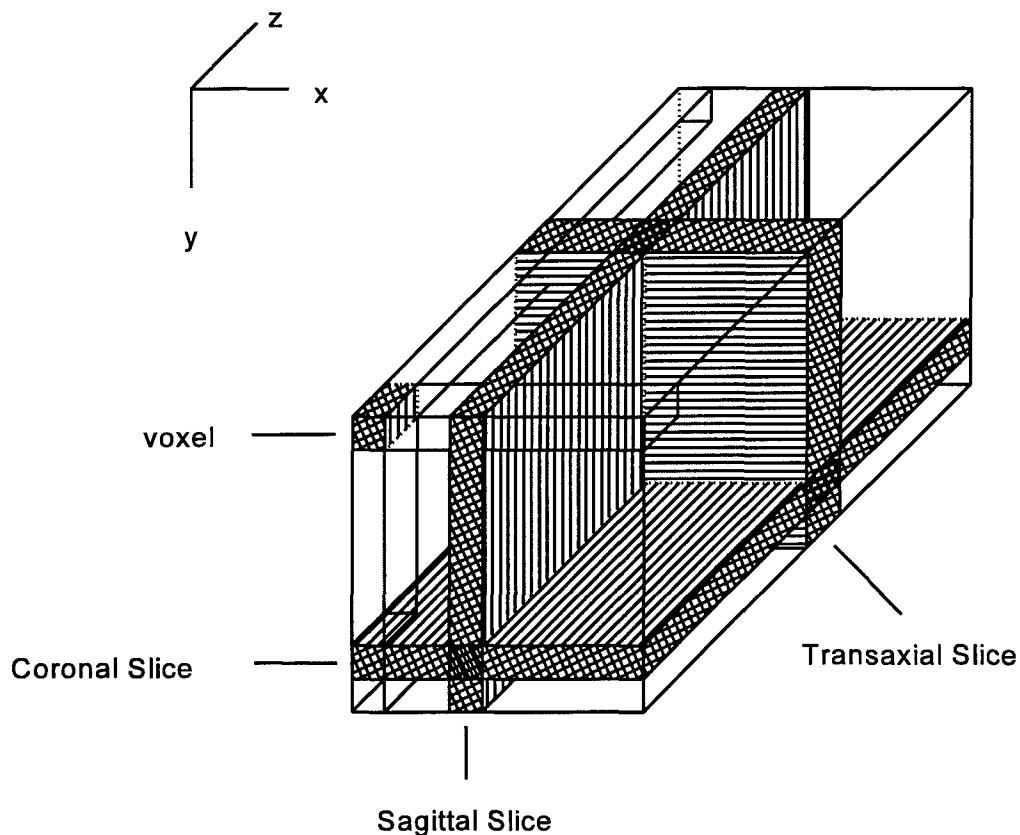
Figure 2-1. Orthogonal Data Slices

plane are referred to as *coronal* slices; slices along the *yz* plane are *sagittal* slices; and slices along the *xy* plane are *transaxial* slices. Visualization methods further partition the modality space volume into nonoverlapping voxels. A voxel is the smallest volume element in a three-dimensional domain. It is analogous to a pixel that is the smallest representation of area in a two-dimensional domain.

Depending upon the visualization approach that is employed, a voxel assumes one of two interpretations. It may be a rectangular volume element that is obtained when the modality space volume is partitioned by three sets of parallel planes, each set being orthogonal to the other two [Frie85], such that the eight vertices of the voxel are adjacent sampled points from two consecutive two-dimensional data slices. Voxels that assume this interpretation and are cubic, with sides of equal length are referred to as *cuberilles* [Herm79]. Alternatively, others consider the voxel as having no extent, but rather are only a point in space [Levo88, Levo89].

After the patient space volume is sampled, several image processing operations are often applied to the modality space volume to better portray or emphasize features that enable physicians to make accurate diagnoses. These image processing operations include but are not limited noise suppression, histogram equalization, interpolation, edge enhancement, classification and segmentation. For instance, voxels that are associated with the skull of a CT volume may be determined using a segmentation operator that discriminates between bone and soft tissue. See Stytz [Styt91] and Russ [Russ94] for detailed descriptions of these and other image processing operations.

This research focuses specifically on the operation of interpolation. Interpolation generates a new modality space volume with finer resolution than the volume from which it is generated. Assuming the field of view remains constant, interpolation increases the number of voxels in the new volume and decreases the dimensions of each

voxel when compared to those of the original volume. Voxels in the new volume that spatially map to voxels in the original volume assume the same value as in the original volume. Voxels of the new volume that do not map to the original volume assume estimated values. Each estimate may be linearly interpolated using a linear combination of values that map to a local region of voxels in the original volume.

Geometric viewing transformations may also be applied to the modality space volume to account for changes in the desired view reference point, rotation, translation, and scaling. Geometric viewing transformations are mentioned here for completeness. A complete discussion of these three-dimensional transformations is presented by Hearn and Baker [Hear86], and Foley and others [Fole90].

Principles of Magnetic Resonance Imaging

Kriging is the technique this research applies to obtain estimates of interpolated modality space data. It presumes the modality space representation of a patient space volume exhibits spatial characteristics that can be modeled and, in turn, used by the kriging system of equations to compute estimates that are consistent with the spatial variation of neighboring voxels. The scope of this research limits this analysis to a single three-dimensional imaging modality - magnetic resonance imaging.

MRI technology permits radiologists to view soft tissues, tumors, muscles, tendons and arteries with clarity [Soch88]. This imaging modality exploits the fact that the patient space volume consists of a composition of tissues. The water content of each tissue varies with its type. Hydrogen is the significant element in water molecules. Therefore, the density of hydrogen atoms also varies as a function of tissue type. In addition to the prominent magnetic properties of hydrogen, the fact that hydrogen density can be correlated to tissue type establishes the basis of MRI technology.

Atomic nuclei that have an odd number of protons possess a characteristic known as spin. Consider a hydrogen atom that consists of a single electron and a single proton in its nucleus. The atom's electron that is in orbit about the nucleus is effectively a small current loop that generates its own magnetic moment, μ. Before exposing hydrogen nuclei to an external magnetic field the magnetic moments of the hydrogen nuclei are randomly aligned [Youn84]. In an external, static magnetic field, however, a torque is experienced on the magnetic moments of the nuclei. The torque tends to align the magnetic moment produced by the orbiting electron with the external magnetic field [Hayt81]. Much like a spinning toy top that spins around its own axis, but wobbles about the earth's gravitational field, the magnetic moment μ that is established by the electron spinning around the proton will *precess* (wobble) around the alignment of the external, static magnetic field B_0 [Rinc93, Soly79, Youn84] as depicted in Figure 2-2.[1]

There are three component fields to consider when discussing the operating principles of an MRI scanner. The first of these is a static magnetic field B_0. Ideally, the static magnetic field should be homogeneous. Inhomogeneity of the static field can result in the incorrect placement of sampled patient space voxels in a reconstructed modality space image of the patient space anatomy. Hence, an inhomogeneous static magnetic field is one source of distortion in MRI. For imaging purposes, a magnetic field is considered sufficiently homogeneous if its inhomogeneity is about 1 part in 10^4 or 10^5 [Kean86]. This field typically has a strength between 1 kilogauss (kG) and 20 kG [Hill85]. By comparison, the strength of the earth's magnetic field is about 0.5G.

---

[1] Figure 2-2 is adapted from [Rinc93].
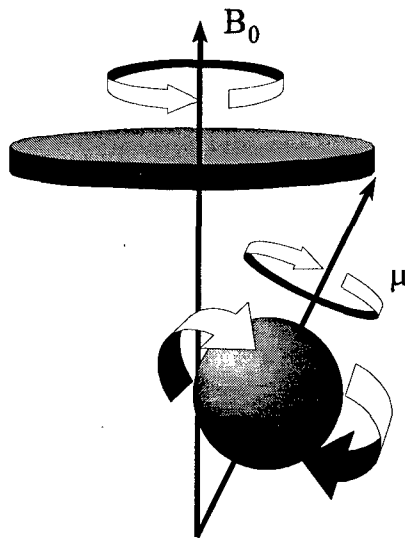
Figure 2-2. Nuclear Precession

[Hill85].   The static magnetic field surrounds the patient space volume and has the effect of orienting the nuclei of hydrogen atoms in the direction of the poles of the external field [Mack84, Soch88]. Even though each hydrogen nucleus aligns along the large magnetic field B_0, it precesses at a frequency that is given by the Larmor equation; that is

$$\omega = \eta \cdot B_o \qquad\qquad (2\text{-}1)$$

where ω is the angular frequency of precession, called the *Larmor frequency*; η is a constant (for each nuclear species) called the *gyromagnetic ratio*[2]; and B_0 is the magnetic field [Park90, Rinc93, Youn84]. From the Larmor equation it follows that since the gyromagnetic ratio η is constant, then the angular Larmor frequency ω is directly proportional to the magnetic field B_0. For protons in a 1000 G field, the Larmor

---

[2] The gyromagnetic ratio is usually represented as γ in the Larmor equation [Park90, Rinc93, Youn84]; however, so as not to be confused with the representation of the variogram γ, the gyromagnetic ratio is herein be represented by η.

frequency ω is observed to be 4.2578 million cycles per second; the gyromagnetic ratio η is said to be 4.26 MHZ/kG [Mack84].

A radio frequency (rf) field is the second of the three component fields that must be considered. The precessing protons are excited by a burst of energy from this rf field when it is tuned to the Larmor frequency [Park90, Scho88]. The Larmor frequency is the resonant frequency of the nuclei. The rf field is oriented perpendicular to the main magnetic field B_0 [Mack84]. The rf pulse has a typical peak power on the order of kilowatts, a duration of tens or hundreds of microseconds [Hill85] and though tuned to approximately 4 MHZ [Youn84], its frequency is ultimately dependent upon the strength of the imposed external magnetic field. When the rf pulse is tuned to the Larmor frequency, it has the effect of misaligning the hydrogen nuclei protons from the main magnetic field and exciting them to a higher energy state. The energy of the rf pulse is transferred to the resonating nucleus.

Within milliseconds of the deflection of the magnetic moment vectors of the hydrogen nuclei, phase coherence is lost and the nuclei return to their equilibrium state in longitudinal alignment with the external magnetic field. They regain their potential to radiate energy if they are excited by another rf pulse. Two characteristic relaxation times are of interest. They are the *longitudinal relaxation time* and the *transverse relaxation time*, represented by the symbols *T1* and *T2*, respectively. The longitudinal relaxation time is the time it takes for the longitudinal component of magnetization M_Z of the net tissue magnetic moment M_0 to return. The time is a result of the nucleus interacting with its neighboring lattice of nuclear magnetic fields; hence, in quantum mechanics it is referred to as the *spin-lattice time*. The *T1* time is given by

$$M_Z = M_0(1 - e^{\frac{-t}{T1}}) \qquad (2\text{-}2)$$

where M_z is the component of magnetization along the z axis (assuming an external magnetic field oriented along the z direction), and M_0 is the net equilibrium value of magnetization. Figure 2-3 depicts the exponential relationship between $T1$ time and time t. From the figure it can be observed that the equilibrium value of magnetization is beyond 99% recovered in about $5T1$.

Longitudinal Relaxation Time
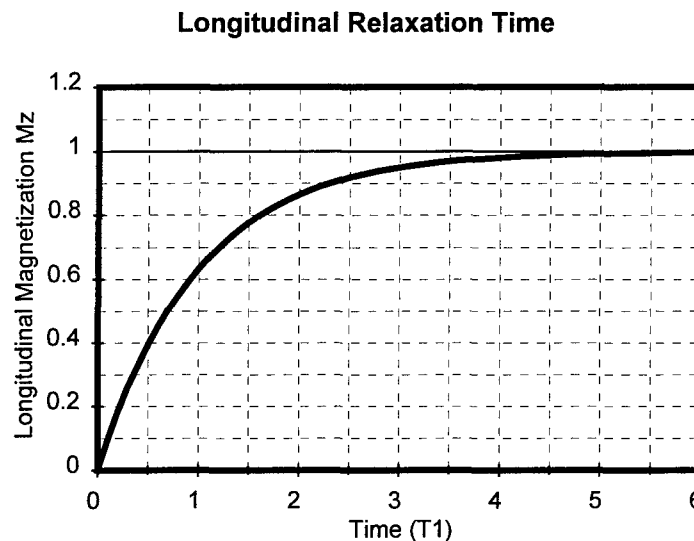
Figure 2-3. Longitudinal Relaxation Time

Many variables influence $T1$. They are [Hill85]: the chemical substance in question and its physical state; the strength of the magnetic field (higher fields cause longer $T1$ times and slower recovery); the temperature (higher temperatures cause longer $T1$ times); and whether the observations are made *in vivo* or *in vitro*. Typical values of $T1$ range from 100 - 400 ms [Beal84]. Some typical values obtained *in vivo* are provided in Table 2-1.

Table 2-1. Typical T1 Values (ms) [Kean86]

Tissue	Magnetic Field Strength (Tesla)			
	0.04	0.08	0.15	1.5
Liver	140-170	172-208	210-270	
Spleen	250-290	371-439	440-580	
Grey Matter	250-275	392-438	340-610	798-944
White Matter	225-250	265-292	220-350	488-542
Cerebrospinal Fluid	350-1000		900-2000	1547-2253
Fat	120-140	131-147		

The transverse relaxation time refers to the rate of decay of the transverse magnetization. Transverse magnetization decay occurs as a result of nuclear magnetic moments losing phase coherence due to their mutual interaction. Hence, transverse relaxation is also referred as *spin-spin relaxation*. It is denoted by the symbol *T2* and is given by

$$M_{xy} = M_0 e^{-\frac{t}{T_2}}$$
(2-3)

where M_{XY} is the transverse component of magnetization (for a field oriented along the z axis), and M_0 is the net equilibrium value of magnetization. Typical values of *T2* in biological tissue range from 50 to 100 ms [Wehr88]. If the external magnetic field were ideally homogeneous, the precessional frequency of all nuclei would be the same and phase coherence would be sustained. However, local field homogeneities cause a local region to map to a range of resonant frequencies, which in turn, cause the decay of

transverse magnetization. Each tissue type in the body has a different *T1* and *T2* time [Soch88]. Therefore these relaxation times are used to differentiate between tissues.

Though the biological mechanisms that influence these times are not fully understood, it is observed that water in tissue that is not bound to the surface of proteins generally has longer *T1* and *T2* times than water that is bound to the surface of proteins [Kean86]. The former is referred to as *free water*. The later is referred to as *bound water*. It is a function of the hydrogen proton density and the *T1* and *T2* relaxation times that yields the contrast information in MRI images [Clin90]. The timing of rf pulses is manipulated so that the relative contributions of *T1*, *T2* and proton density to the final image vary, thereby enhancing selected details in the body and providing a more clinically useful picture [Styt89].

When a nuclei returns to its longitudinal alignment, the rf energy that excited the proton to a higher energy state and was absorbed by the proton, is emitted as electromagnetic energy that is the same frequency as the rf pulse that originally excited it. This energy is emitted by the resonating nuclei and constitutes the signal that must be detected by the MRI receiver in order for cross sectional images of the patient space volume to be generated. A tunable circular coil inside the scanner is generally used as the rf receiver antenna [Youn84]. The signal is typically a few microvolts in amplitude [Rinc93]. The amplitude of the received signal is indicative of the density of hydrogen nuclei that are present in a calculated area of the scanned patient space volume. Since hydrogen is the significant element in water molecules, whose content varies with tissue type, the amplitude of the emitted signal may be correlated to different body tissue types [Soch88].

In order to spatially localize the signal that is emitted as a result of subjecting the patient space hydrogen nuclei to the rf excitation pulse, an MRI scanner has

gradient coils that generate the third component magnetic fields. These fields, called gradient magnetic fields, are superimposed upon the static magnetic field and are intended to vary linearly along a selected direction. Their field strength is generally 2 to 3 orders of magnitude less than the static magnetic field [Bush94], but is designed to be greater than any static field inhomogeneity [Kean86]. Assuming a gradient magnetic field G_x varies linearly along the x direction, then the strength of the resulting magnetic field B(x) may be expressed as a function of x, such that:

$$B(x) = B_o + \dot{G}_x \cdot x \qquad (2\text{-}4)$$

where B(x) is the strength of the resulting magnetic field, B_0 is the strength of the static magnetic field, and $\dot{G}_x$ is the rate of change of the gradient field strength along the x axis [Park90]. The Larmor frequency ω in the presence of a gradient magnetic field in the x direction is also a function of position. It may be written as

$$\omega(x) = (\eta \cdot B_o) + (\eta \cdot \dot{G}_x \cdot x) \qquad (2\text{-}5)$$

Gradient fields may similarly be generated in the y and z directions.

Steeper gradient fields cause the Larmor frequency to change more rapidly as a function of position and therefore may be used to control the thickness of sampled patient space slices, as shown in Figure 2-4.[3] In the figure, note how for a given bandwidth $\Delta\omega$ about the Larmor frequency ω_L, the extent of nuclei along the z axis that are excited is ΔZ_B for the gradient field B, and ΔZ_A for the gradient field A. Thus, the more rapidly changing (steeper) gradient field A results in the reconstruction of a thinner transaxial slice. A disadvantage of selecting thinner slices, however, is fewer

---

[3] Figure 2-4 is adapted from [Star88].
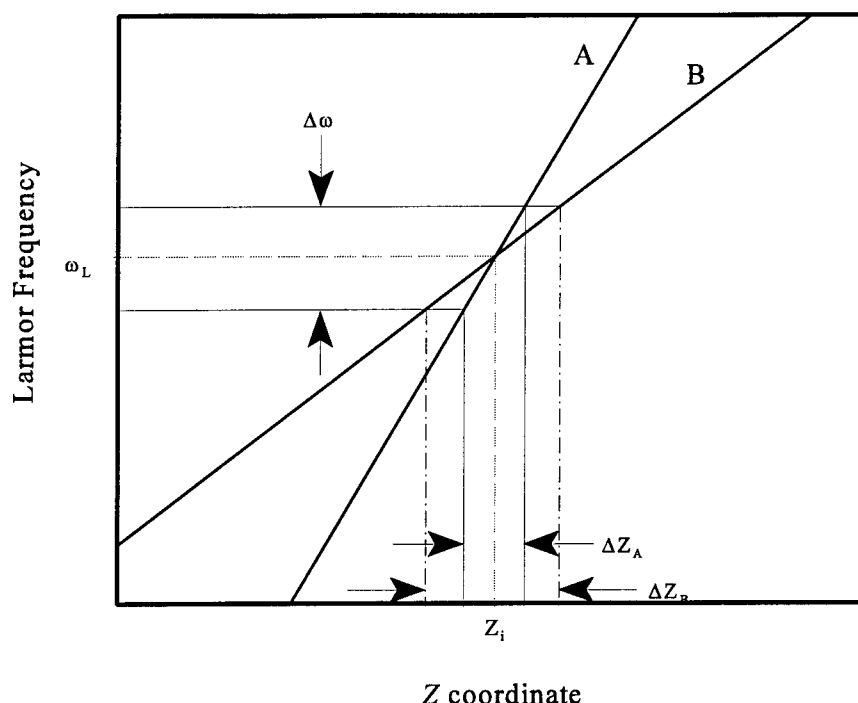
Figure 2-4.   Gradient Field Effect on Slice Thickness

nuclei will respond to the rf signal. This has the effect of lowering the signal-to-noise ratio of the received signal. On the other hand, a shallower gradient field would provide improved signal-to-noise ratios, but at the expense of positional accuracy. Partial volume effects may also become more evident when using shallow gradient fields.

In the presence of magnetic field variations caused by a gradient magnetic field, protons precess at different frequencies, hence position is encoded by frequency. When the signal is subsequently reconstructed into an image of the scanned xy patient space slice, the received time domain signals are transformed into the frequency domain using the Fourier transform. Spectral information is provided by the Fourier transform such that signal strength is given as a function of frequency. Since position is frequency encoded, signal strength can likewise be determined as a function of position. Thus, the frequency and amplitude of the signals that are emitted from the hydrogen nuclei are

respectively used to locate position and to determine nuclei density present at that location [Youn84].

Frequency encoding position also necessitates consideration of the rf pulse bandwidth and shape. If the bandwidth of the rf pulse is well-defined, the slice thickness will be well-defined. Figure 2-5 depicts this relationship.[4] In the figure, note that for a given gradient field the bandwidth about the Larmor frequency ω_L is permitted to be either $\Delta\omega_A$ or $\Delta\omega_B$. The rf pulse with the narrower bandwidth, represented by $\Delta\omega_A$, results in the reconstruction of a transaxial slice that is centered at Z_i and has thickness ΔZ_A. The broader rf pulse bandwidth $\Delta\omega_B$ results in the reconstruction of a slice that is also centered at Z_i, but has thickness ΔZ_B. As the bandwidth of the rf pulse becomes greater, nuclei over a larger area will respond to the pulse, thereby yielding slices that encompass wider regions of the patient space volume.

The shape of the rf pulse must also be considered. The ideal rf pulse would homogeneously excite all nuclei within some intended region of interest that is determined by a bandwidth of precessional frequencies. In the frequency domain, this pulse is a square pulse. In practice, however, ideal bandpass filters do not exist; the rf energy tends to be contained in a Gaussian profile [Kean86]. Gaussian pulses can cause rf energy that is directed towards one slice to excite nuclei from a neighboring slice. As a result, the emissions from the neighboring hydrogen nuclei will distort the received positional proton density information. This undesired excitation is referred to as *cross-excitation* [Rinc93]. Hence, nonideal characteristics of the rf excitation pulse are another source of distortion in MRI.

---

[4] Figure 2-5 is adapted from [Star88].
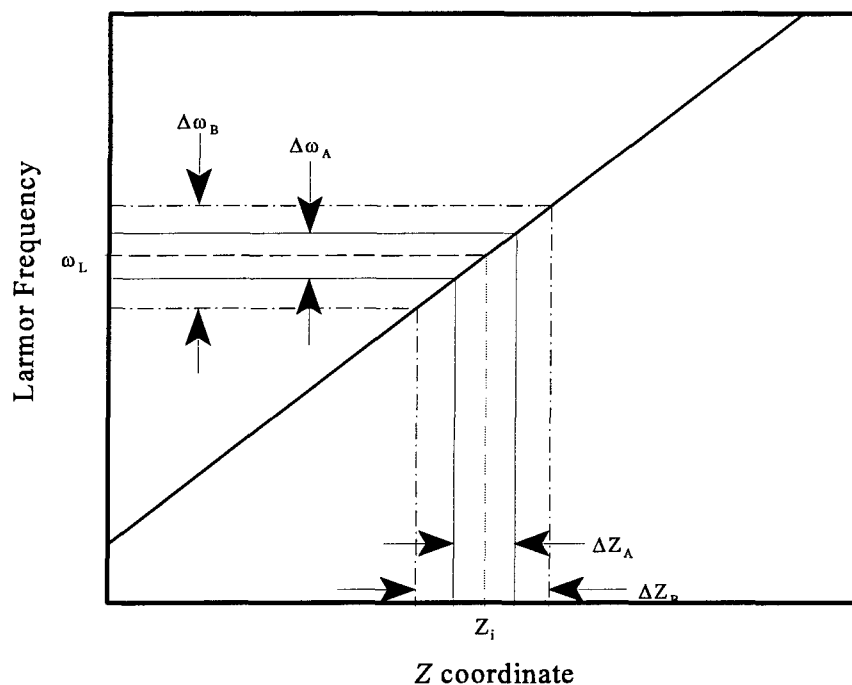
Figure 2-5. Rf Pulse Bandwidth Effect on Slice Thickness

Imaging processes tend to be noise-limited. In MRI, noise is independent of signal strength [Kean86] and is usually gaussian with a spatially independent mean [Chan90]. The signal-to-noise ratio is determined to a large extent by the homogeneity of the static magnetic field. Though the rf signals are spatially encoded, rf noise is not [Star88]. As a result, the amount of rf noise that will be detected can be expected to increase as the bandwidth of the encoded frequencies becomes broader [Kean86].

Other encoding schemes, such as *phase-encoding* [Hill85, Kean86], exist and may be employed. Furthermore, various combinations of applied pulses and gradients in various sequences can be applied to collect MRI information from points, lines, planes, or entire volumes at a time [Mack84]. Regardless of the encoding scheme or combinations and sequences of applied pulses and gradient fields, nonideal characteristics of the three component fields that have been described are sources of

geometric and intensity distortion in MRI. Spatial relationships between patient space voxels can be altered in their modality space reconstruction as a result of the cumulative effects of these sources of distortion.

All three component fields that have been described are controlled in order to be able to spatially localize rf signals of a predetermined range of frequencies that are emitted from the patient space volume. Assuming a sufficiently high sampling rate, a sufficiently large number of quantization levels, an ideal rf pulse with an infinitely narrow bandwidth, a perfectly homogeneous static and linear gradient magnetic fields, the digitized modality space volume would converge to an exact replication of the scanned continuous patient space volume. Given the patient space volume exhibits spatially regionalized properties, it is logical to expect the modality space reconstruction to likewise exhibit the same properties.

However, the real world is not ideal; it involves engineering tradeoffs time after time. Discrete values are modified by tolerances. Ideal rf pulses with square rolloff characteristics are nonexistent. Maximum sampling rates and quantization levels are bounded. Perfectly homogeneous static magnetic fields and perfectly linear gradient magnetic fields cannot be generated. The instability caused by temporal fluctuations in the power supply, offset due to coil placement, and dynamic nonlinearities produced by eddy currents are all examples of sources of deviation [Chan90] from the ideal that result in nonuniform magnetic fields. They have the effect of incorrectly encoding the rf emissions that are received by the scanner receiver and result in distorted modality space representations of patient space volumes. Under these conditions one can no longer assume the distorted modality space representation of a spatially regionalized patient space volume is similarly spatially regionalized.

It is the objective of the research described in Chapter III to analyze simulated distorted MRI modality space volumes of spatially regionalized patient space phantoms to determine if these volumes also exhibit spatial properties. If so, the modality space volumes may be represented by regionalized variables (REVs), their spatial variation can be modeled, and the volume may be interpolated using kriging.

Conventional Methods of Interpolation

In three-dimensional medical imaging the following four primary reasons exist for interpolating scalar values in the volumetric grid of interest [Styt93]: to create a new logical data slice between existing slices, thereby reducing the interslice thickness [Styt90, Udup91]; to increase the number of voxels in the volume along any (or all) dimension(s) for isosurface generation and correct inaccuracies that are caused by isosurface generation techniques, such as those discussed by Wilhelms and Gelder [Wilh90], Cline and others [Clin88], and Parrott and others [Parr92]; to compute scalar values at points within a computational cell, such as Levoy's ray casting technique [Levo88], and Upson and Keeler's V-Buffer method [Upso88]; and to estimate the intersection point of a surface within a voxel, such as is required by the marching cubes algorithm [Lore87] and its derivatives. The techniques that are often employed to accomplish the interpolation include nearest neighbor, averaging and trilinear interpolation.

Nearest neighbor interpolation is the simplest method of interpolation. It assigns a value to a point within a logical slice based upon the closest neighboring sampled point in object space. Since this interpolation method considers only the single sampled value of its nearest neighbor to determine the value of the interpolated point, it is generally

the most imprecise of the interpolation methods described. Rendered images that are obtained using nearest neighbor interpolation have a "block-like" appearance.

The *averaging* method of interpolation improves the estimates of the interpolated values by considering, a neighboring region larger than a single point. It computes each interpolated value by averaging the surrounding nearest sampled values. Application of this technique "smoothes" the block-like appearance that is associated with the nearest neighbor technique, but assumes all neighboring sampled values contribute equally to each interpolated value. A more generalized case of averaging volumetric data is *trilinear interpolation*. Trilinear interpolation is similar to averaging in that it considers adjacent nearest neighboring sampled values to compute each interpolated estimate. However, trilinear interpolation assumes each point to be estimated is most similar to its nearest neighbors. Therefore, to obtain each estimate, trilinear interpolation weights the value of each nearest neighboring voxel based upon its distance from the PTBE.

As discussed by Stytz and others, trilinear interpolation makes the following two critical assumptions in estimating the logical interslice point values: first, it assumes adjacent surrounding sampled values are sufficient to describe the spatial variability of the surrounding data; second, it assumes the data varies linearly between the sampled points [Styt93]. These are simplifying assumptions that enable the application of the technique, but in general are not valid. A structural analysis of spatial variation about each PTBE is necessary to validate these assumptions. Estimates are only be as accurate as the model upon which they are derived. Instances of spatial variation about a PTBE that are not consistent with the interpolation model inevitably yield results that are similarly inaccurate and inconsistent with surrounding data.

Kriging is a method of interpolation that can minimize interpolation accuracies when provided with a model of spatial variation for homogeneous data that is to be interpolated. General kriging methods do not assume any single model of variability. Nor does it assume a fixed number of surrounding voxels contribute to the estimate of an interpolated point. Unlike the deterministic methods of interpolation introduced, kriging provides a measure of error with each interpolated point. Furthermore, the error is minimized relative to the employed model of spatial variation. For these reasons, in an attempt to provide the clinician and radiologist with the most comprehensive and accurate diagnostic information possible, kriging is a candidate for interpolation of volumetric medical data. In the geosciences, kriging is usually applied to data sets of relatively few values that are sampled over large areas with considerable distance between samples.

Using the Variogram to Describe Spatial Variation

Several fields of study, including mining and ore reserve estimation, forest evaluation and hydrology, have applied the kriging to analyze and solve problems of spatial estimation. In these applications the structural traits of the phenomena are often masked by a coexisting and random component. In the analysis of three-dimensional medical data, the radiologist must similarly extract structural characteristics of objects of interest (such as organs, bones, or tumors) in the presence of noise from a limited number of samples of the patient space volume. This process is a specific instance of a more generalized practice known as *structural analysis*. The intent of structural analysis is to analyze structural characteristics of a phenomenon utilizing only fragmentary data of the occurrence. Journel and Huijbregts emphasize

that this prerequisite step is the most important step in any geostatistical study [Jour78].

Matheron introduced regionalized variables to stress the spatial aspect of naturally occurring phenomena [Math63]. A regionalized variable is a random function that varies continuously between points, but cannot be described exactly by a deterministic function due to the complex changes in the variable [Davi86]. A regionalized variable exhibits a spatial correlation between neighboring locations, but only within a finite region. This region is referred to as the *zone of influence*, or *range*. It can be determined using the *variogram* to quantitatively analyze the spatial variation of a regionalized variable. The variogram is the backbone of geostatistical analysis [Omre84]. It is intuitive to think of the variogram as "the variance of the differences [Kerb66]".

Consider a set of values taken by a regionalized variable and define *z(x)* to be the value of the regionalized variable at a point *x*. The variogram 2γ is the mean square of the difference between values at the points *x* and *x+h*. It is represented by *2γ(h)*, such that

$$2\gamma(\hat{h}) = E\{(Z(x+\hat{h}) - Z(x))^2\}. \qquad (2\text{-}6)$$

The *semivariogram* *γ(h)* is sufficient to quantify spatial variation. For the sake of simplicity it is common to refer to the semivariogram *γ(h)* as the variogram [Davi77].

Hence, the variogram is a function of separation distance. In three-dimensional space, separation distance is a vector distance. The variogram is therefore dependent upon direction as well as distance, and must be computed along several directions to comprehensively visualize the spatial variation about a point. *Anisotropies* occur when the extent of a regionalized variable's zone of influence changes as a function of

direction. An interpolation method must account for these anisotropies if it is to provide an estimate that is accurate and consistent with the spatial characteristics of the surrounding neighborhood.

When the distance between a pair of sampled points is zero, a single point is compared with itself. Hence, the variogram $\gamma(0)$ is zero. For very small distances h_{small} one expects the values of the pair of sampled points considered to be very similar since the sampled values are obtained from a continuous biological volume that, with exception of the anatomical boundaries, has been shown to exhibit slowly varying statistics and strong correlations between neighboring areas [Leah91]. In these instances the variogram value $\gamma(h_{small})$ is relatively small. Beyond some greater distance h_{large}, the pairs of sampled points tend not to be related to one another. The square of their difference converges to the variance about the mean value.

The variogram of a regionalized variable can be approximated from a limited number of sample points of the volume of interest. A variogram obtained from physical space in this manner is referred to as an *experimental* variogram. Significant information characterizing the spatial variation of the physical volume is obtained from the shape of an experimental variogram and is summarized by three parameters. The first parameter is the range, or zone of influence. If the variogram converges to a relatively stable horizontal asymptote, one may hypothesize without incurring much risk of error that the regionalized variable possesses a zone of influence [Math89]. Its extent is approximated from the variogram as the distance at which the shape of the variogram plateaus. It is within this extent that the data remain correlated; beyond this range, samples become independent of one another [Clar87]. Figure 2-6 is an example

of an experimental variogram obtained using geological data.[5] From the figure, one can

approximate the range to be about 200 ft.
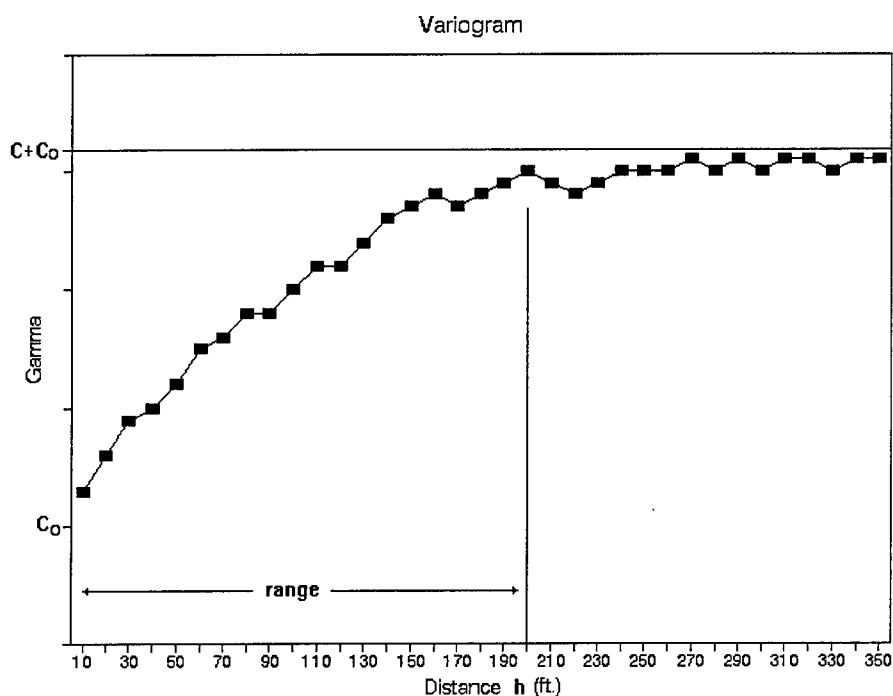
Variogram

Figure 2-6. Variogram of an Iron Ore Deposit

The second parameter is the sampling error, or *nugget effect*. It can be

considered the variance of a totally random component that is superimposed on the

regionalized variable [Davi77]. The nugget effect consists of measurement errors and

microscale variation [Cres88]. The error associated with a given sampling technique

and procedures is considered the measurement error. It may be observed when one

resamples a location and observes that the value of that location differs from its original

sampled value. Microscale variation refers to the rate of change of the phenomenon that

is sampled within a material. For example, in gold ore deposits mineralization typically

occurs as nuggets, or blobs, that cause rapid changes to be sampled over short distances

---

[5] Figure 2-6 is adapted from [Davi77].

[Davi77]. When a nugget effect is present, the variogram curve is shifted upward such that $\gamma(h)$ does not intersect the origin as $|h| \to 0$, even though the value of the variogram computed for a single point is by definition equal to zero. The variogram shown in Figure 2-6 has a nugget effect represented by C_0.

The third parameter that is determined from the variogram is the variance of the samples, or the *sill*. In Figure 2-6, the sill is represented by the value $C+C_0$. Within regions of spatial dependency, the variogram $\gamma(h)$ is small for small distances h. This means sampled points vary near one another are highly correlated. At larger separation distances, sampled points are less correlated between one another and the variogram value $\gamma(h)$ increases. Once the distance h is greater than or equal to the range, the variogram $\gamma(h)$ converges to the variance of the samples [Clar87, Cres88]. That is

$$| \hat{h} | \to \infty , \quad \gamma(\hat{h}) \to VAR\{Z(\hat{x})\} \tag{2-7}$$

where $Z(\hat{x})$ is the random variable that is associated with the regionalized variable that is sampled. Using these three parameters obtained from experimental variograms, the structural characteristics of a physical phenomenon can be characterized.

The experimental variogram is compared to known *variogram models*, searching for a model with similar characteristics to represent the spatial variation of the analyzed data. Variogram models are continuous functions that can be evaluated at any distance. A least-squares fitting algorithm may be used to determine which variogram model most closely represents the experimental variogram. The model that yields the best correlation is selected. David suggests a visual fit is usually sufficient [Davi77]. Zimmerman and Zimmerman have shown a (distance) weighted least squares approach never performs poorly and usually does well [Cres89].

The use of geostatistics in the geosciences indicates that a large number of variogram model functions is not necessary. More than a hundred ore deposits have been estimated using only two models and the tendency is to use only one model, the *spherical model* [Davi77]. The equation for this model is:

$$\gamma(h) = \begin{cases} C[\dfrac{3h}{2a} - \dfrac{h^3}{2a^3}] + C_o \ , & h \leq a \\[3mm] C + C_o \ , & h > a \\[3mm] 0 \ , & h = 0 \end{cases} \qquad (2\text{-}8)$$

where a is the range, C_o represents the nugget effect, and $(C+C_o)$ is the sill. The variogram curve for this model is depicted in Figure 2-7.
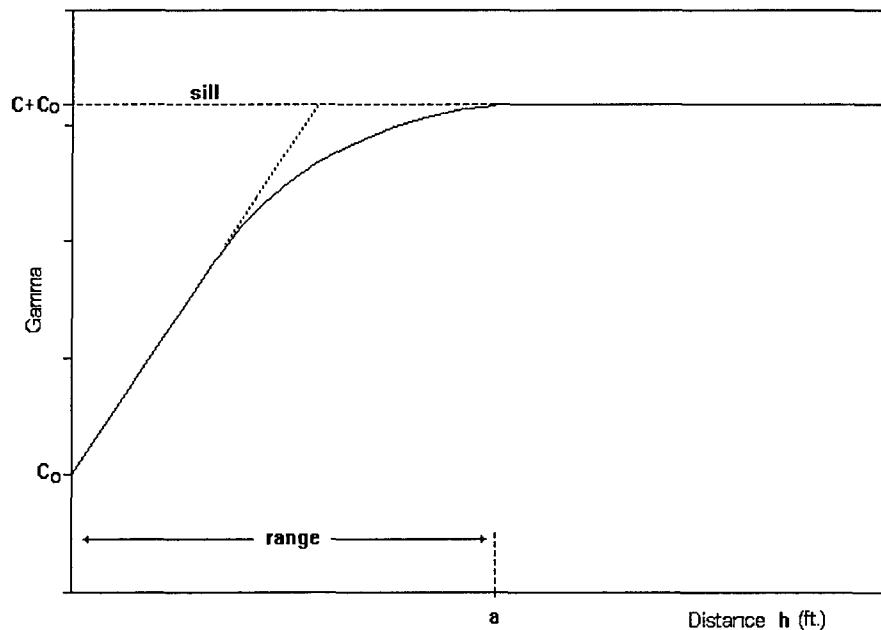
Figure 2-7. The Spherical Model Variogram

Other commonly used models include the linear model, the exponential model, and the gaussian model [Cres91, Davi77, Isaa89]. These models are presented and discussed in more detail in Chapter IV. Once a variogram model and its parameters have been determined to represent the spatial variation about a PTBE, kriging assumes the spatial variability given by the variogram model to obtain an unbiased estimate whose error variance is minimized.

Deriving the Kriging System of Equations

Kriging is a geostatistical method of interpolation recently introduced to the medical imaging community by Stytz [Styt93], Parrott and others [Parr91, Parr93]. The term "kriging" is derived from the name of D. G. Krige, a South African mining engineer [Davi86] who introduced the use of moving averages to avoid systematic overestimation of mining reserves [Delf73]. Kriging was developed to estimate the ore grade thicknesses or accumulations in mining deposits [Math63], but is finding applications in other disciplines that require the analysis of spatially dependent data.

Kriging differs from other statistical interpolation methods in that it does not treat the sampled points as random variables, but as regionalized variables that are spatially dependent upon one another within their zone of influence. Unlike other interpolation methods, kriging does not compute its estimates based upon a fixed size neighborhood of random variables; its estimates are based upon a dynamic neighborhood of regionalized variables. Similar to trilinear interpolation, kriging uses a weighted linear sum of known data values to estimate the value of an unknown point.

That is,

$$\hat{Z} = \sum_i w_i Z_i \qquad (2\text{-}9)$$

where $\hat{Z}$ is the prediction for an unsampled location and w_i represents the weight associated with the ith sample Z_i. However, weights are not selected based solely upon the linear distance between sampled data points of known values and unsampled data points; kriging does not assume the variability of the data to be linear. Weights are chosen to minimize the estimation variance. That is,

$$VAR\{\hat{Z} - Z\} \ minimum \qquad (2\text{-}10)$$

In minimizing the estimation variance, kriging is an *optimal* estimator and is one of the most powerful applications of the notion of estimation variance [Huij73]. In addition to computing a logical estimate, kriging provides a measure of the estimation error associated with estimate.

Kriging weights are also computed to maintain unbiasedness between contributing samples. As an unbiased estimator, kriging's estimation error on the average must equal zero [Huij73]. That is,

$$E\{\hat{Z} - Z\} = 0 \qquad (2\text{-}11)$$

Kriging also satisfies the property of *exactness*. This property is described as the ability to predict a known value with zero error [Davi86]. This occurs when an estimate actually passes through the sampled data points rather than near them [Davi77].

Many, if not most data sets of naturally occurring phenomena are not stationary; that is, they exhibit statistical properties, such as their mean, that varies as a function of time or position. Observances of nonstationarity are classified as either global or

local. *Global drift* is the large-scale trend of a data set mean that varies as a function of position over the entire data set. Global drift must be removed before kriging [Davi77]. Several techniques have been employed (using two-dimensional data) to accomplish the removal of global drift. Grant uses a differencing technique that subtracts the subject data set from an "average" data set obtained by averaging a multitude of data sets that are similar to the subject data set [Gran90]. Brodkin [Brod91], Duckett [Duck91] and McGee [McGe91] fit a second-order polynomial function to the regionalized data using a least squares regression technique to solve for the polynomial coefficients, and subtract this function from the regionalized variable. Cressie [Cres91] describes a (two-dimensional) *median polish* technique of trend removal. Median polishing decomposes data sets into large-scale and small-scale variations by iteratively computing and accumulating median values of rows and columns. Once polished, a data set of residuals remains. The residuals constitute the small-scale variation of the data and are treated as a new intrinsically stationary data set to which a model variogram may be fitted [Cres91]. Cook has explored applying this technique to three-dimensional data [Cook85].

Local drift, on the other hand, is a trend that occurs within a local neighborhood about a point. It may be present even though global drift is removed and an overall stationarity exists. Locally stationary variables have local means that are equal to zero.

Depending upon the assumption of stationarity of the sampled phenomenon, kriging is classified as either *ordinary* or *universal*. Ordinary kriging requires the mean of the regionalized variable is constant, but does not require that it be known. Universal kriging, or what Journel prefers to call "kriging under trend constraints," allows for a variable or nonstationarity mean that is everywhere unknown but is of a known functional form [Jour89]. The form is represented by the sum of a trend

component that is called the *drift* and a random component that is called the *residual*. The drift is a smooth approximation of the regionalized variable of interest. It consists of the expected value of the regionalized variable within some local neighborhood and is nonstationary. The residual is the difference between the actual sampled measurements and the drift [Davi86]. Therefore, if drift is removed from a regionalized variable, the resultant residuals are assumed stationary.

Kriging uses a weighted linear sum of sampled values to estimate the value of an unknown point. Linearity assumes each weight is of the first power. Unbiasedness implies the weights must sum to one and no trend exists. In the presence of a trend a linear estimator is no longer unbiased. Therefore, to apply kriging to this situation, three operations must be performed [Davi86]: to produce stationary residuals the drift must be estimated and removed; the stationary residuals are kriged to obtain the needed estimates; and the estimated residuals are combined with the drift to obtain the logical estimates of the surface of interest. Hence, as suggested by Journel [Jour89], universal kriging reduces to an ordinary kriging system once drift is removed.

Ordinary Kriging

Assuming the unknown value z_0 at a point p_0 is estimated as $\hat{z}_0$ by a linear combination of n sampled values plus an offset parameter w_0, the estimate $\hat{z}_0$ is written as

$$\hat{z}_0 = w_0 + \sum_{i=1}^{n} w_i z_i \qquad (2\text{-}12)$$

The linear combination of n random variables is itself a random variable, called an *estimator*. The estimator $\hat{Z}_0$ is

$$\hat{Z}_0 = w_0 + \sum_{i=1}^{n} w_i Z_i \qquad (2\text{-}13)$$

The actual error of estimation induced by each estimate is $|z_0 - \hat{z}_0|$, and in general is not known. The error associated with the random variable estimator is $|Z_0 - \hat{Z}_0|$.

Assume the mean m_i of each random variable Z_i is known and stationary. Then

$$E\{Z_i\} = m_i = m \; ; \quad i = 0, ..., n \qquad (2\text{-}14)$$

Then the expected value of the random variable estimation error is

$$
\begin{aligned}
E\{Z_0 - \hat{Z}_0\} &= E\{Z_0\} - E\{\hat{Z}_0\} \\
&= E\{Z_0\} - E\{w_0 + \sum_{i=1}^{n} w_i Z_i\} \\
&= E\{Z_0\} - w_0 - E\{\sum_{i=1}^{n} w_i Z_i\} \\
&= E\{Z_0\} - w_0 - \sum_{i=1}^{n} w_i E\{Z_i\} \\
&= m_0 - w_0 - \sum_{i=1}^{n} w_i m_i \\
&= -w_0 + m(1 - \sum_{i}^{n} w_i)
\end{aligned}
\qquad (2\text{-}15)
$$

Unbiasedness dictates the expected value of the random variable estimation error is zero, regardless of the value of the mean m. Therefore, under the condition of unbiasedness

$$w_0 = m\left(1 - \sum_{i=1}^{n} w_i\right) \qquad (2\text{-}16)$$

This is true only if

$$w_0 = 0 \quad and \quad \sum_{i=1}^{n} w_i = 1. \qquad (2\text{-}17)$$

Substituting into equation (10), an unbiased linear estimator of Z_0 may be written as

$$\hat{Z}_0 = \sum_{i=1}^{n} w_i Z_i \quad where \quad \sum_{i=1}^{n} w_i = 1. \qquad (2\text{-}18)$$

In addition to unbiasedness, an optimal estimator minimizes estimation error variance. The estimation error variance σ_E^2 of the estimator $\hat{Z}_0$ is calculated as follows:

$$\begin{aligned} \sigma_E^2 &= VAR\{Z_0 - \hat{Z}_0\} \\ &= VAR\{Z_0 - \sum_{i=1}^{n} w_i Z_i\} \end{aligned} \qquad (2\text{-}19)$$

Define $a_0 = 1$ and $a_i = -w_i$ for $I = 1,...,n$, then equation (2-19) may be rewritten as

$$\begin{aligned} \sigma_E^2 &= VAR\{a_0 Z_0 + \sum_{i=1}^{n} a_i Z_i\} \\ &= VAR\{\sum_{i=0}^{n} a_i Z_i\} \end{aligned} \qquad (2\text{-}20)$$

For any random variable the covariance $COV\{Y,Y\}$ equals the variance $VAR\{Y\}$ [DeGr89]. Therefore, the estimation error variance is rewritten as

$$
\begin{aligned}
\sigma_E^2 &= COV\{\sum_{i=0}^{n} a_i Z_i, \sum_{j=0}^{n} a_j Z_j\} \\
&= \sum_{i=0}^{n} \sum_{j=0}^{n} a_i a_j COV\{Z_i, Z_j\} \\
&= \sum_{i=0}^{n} \sum_{j=0}^{n} a_i a_j \sigma_{ij}
\end{aligned}
\qquad (2\text{-}21)
$$

where $\sigma_{ij} = COV\{Z_i, Z_j\}$. This result is consistent with the findings of Journel [Jour89].

The estimation error variance σ_E^2 must be minimal for the estimator $\hat{Z}_0$ to be optimal. To minimize the variance σ_E^2, the n partial derivatives of σ_E^2 with respect to a_i for $I=1,...,n$ are set to zero, as follows:

$$
\begin{aligned}
\frac{\partial(\sigma_E^2)}{\partial a_i} &= -\frac{\partial(\sigma_E^2)}{\partial w_i} = 0 \\
&\Rightarrow \frac{\partial(\sigma_E^2)}{\partial w_i} = 0 \quad for\ i = 1,...,n
\end{aligned}
\qquad (2\text{-}22)
$$

From equation (2-21) the partial derivative of σ_E^2 with respect to a_i is equated as

$$
\begin{aligned}
\frac{\partial(\sigma_E^2)}{\partial a_i} &= 2\sum_{j=0}^{n} a_j \sigma_{ij} \\
&= 2a_0\sigma_{i0} + 2\sum_{j=1}^{n} a_j \sigma_{ij}
\end{aligned}
\qquad (2\text{-}23)
$$

Substituting $w_i = a_i$ for $I = 1,...,n$; and $a_0 = 1$:

2-31

$$\frac{\partial(\sigma_E^2)}{\partial w_i} = 2\sigma_{i0} - 2\sum_{j=1}^{n} w_j\sigma_{ij} \qquad (2\text{-}24)$$

Setting equation (2-24) equal to zero minimizes the estimation error variance such that

$$-2\sigma_{i0} = -2\sum_{j=1}^{n} w_j\sigma_{ij}$$

$$\sigma_{i0} = \sum_{j=1}^{n} w_j\sigma_{ij} \qquad (2\text{-}25)$$

This sum is expanded for each w_j to produce the following n equations with n unknowns:

$$
\begin{aligned}
w_1\sigma_{11} + w_2\sigma_{12} + \cdots + w_n\sigma_{1n} &= \sigma_{10} \\
w_1\sigma_{21} + w_2\sigma_{22} + \cdots + w_n\sigma_{2n} &= \sigma_{20} \\
w_1\sigma_{31} + w_2\sigma_{32} + \cdots + w_n\sigma_{3n} &= \sigma_{30} \\
&\;\;\vdots \\
w_1\sigma_{n1} + w_2\sigma_{n2} + \cdots + w_n\sigma_{nn} &= \sigma_{n0}
\end{aligned}
\qquad (2\text{-}26)
$$

Additionally, to ensure the solution is unbiased, the weights must be constrained to sum to unity; that is,

$$w_1 + w_2 + w_3 + \cdots + w_n = 1 \qquad (2\text{-}27)$$

Thus, $n+1$ equations describe n unknowns. The complete set of simultaneous equations is described utilizing a Lagrange multiplier λ, as follows:

$$
\begin{aligned}
w_1\sigma_{11} + w_2\sigma_{12} + \cdots + w_n\sigma_{1n} + \lambda &= \sigma_{10} \\
w_1\sigma_{21} + w_2\sigma_{22} + \cdots + w_n\sigma_{2n} + \lambda &= \sigma_{20} \\
w_1\sigma_{31} + w_2\sigma_{32} + \cdots + w_n\sigma_{3n} + \lambda &= \sigma_{30} \\
&\;\;\vdots \\
w_1\sigma_{n1} + w_2\sigma_{n2} + \cdots + w_n\sigma_{nn} + \lambda &= \sigma_{n0} \\
w_1 \quad\;\; + w_2 \quad\;\; + \cdots + w_n \quad\;\; + 0 &= 1
\end{aligned}
\qquad (2\text{-}28)
$$

The kriging system of equations in equation (2-28) is rearranged in general matrix from as

$$[A] \cdot [W] = [B] \qquad (2\text{-}29)$$

which is equivalent to the following expanded form:

$$
\begin{vmatrix}
\sigma_{11} & \sigma_{12} & \cdots & \sigma_{1n} & 1 \\
\sigma_{21} & \sigma_{22} & \cdots & \sigma_{2n} & 1 \\
\vdots & & & \vdots \\
\sigma_{n1} & \sigma_{n2} & \cdots & \sigma_{nn} & 1 \\
1 & 1 & \cdots & 1 & 0
\end{vmatrix}
\cdot
\begin{vmatrix}
w_1 \\
w_2 \\
\vdots \\
w_n \\
\lambda
\end{vmatrix}
=
\begin{vmatrix}
\sigma_{10} \\
\sigma_{20} \\
\vdots \\
\sigma_{n0} \\
1
\end{vmatrix}
\qquad (2\text{-}30)
$$

To determine the vector of unknown weights w_i, equation (2-30) is rearranged such that

$$[W] = [A]^{-1} \cdot [B] \qquad (2\text{-}31)$$

Once the weights are computed, equation (2-18) is used to calculate an estimate $\hat{Z}_0$ at point p_0; that is,

$$\hat{Z}_0 = \sum_{i=1}^{n} w_i Z_i \qquad (2\text{-}32)$$

Calculation of the estimation error variance σ_E^2 is then relatively straightforward; it is the weighted sum of the semivariances for the distances from the sampled points to the location of the point that is being estimated [Davi86]. That is,

$$\sigma_E^2 = [W]^T \cdot [B] \qquad (2\text{-}33)$$

Universal Kriging

Ordinary kriging assumes a stationary regionalized variable, one in which the mean does not vary with position. Universal kriging does not assume the data is locally stationary, nor the mean known. It does assume, however, the local nonstationarity can be modeled within a neighborhood about the PTBE. A first or second-order polynomial may be used [Davi86]. For instance, the drift M at a point p, assuming a first-order drift polynomial, is represented as

$$M_p = \alpha_1 x_i + \alpha_2 y_i \qquad (2\text{-}34)$$

where x_i and y_i are the coordinates of the ith sampled point (in two-dimensions); and α_1 and α_2 are the drift coefficients for each associated x and y coordinate, respectively. In universal kriging, these unknown coefficients are solved in addition to solving the kriging weights. Also, the neighborhood size and drift expression are determined through a structural analysis of the sampled modality space data.

Incorporating the drift expression into the kriging system of simultaneous equations to determine the kriging weights produces a set of weights for the kriged estimate that include the effect of the modeled drift within a specified neighborhood [Davi86]. The resulting system of equations in matrix form, assuming a first-order drift model, would appear as follows:

$$
\begin{vmatrix}
0 & 0 & 0 & 1 & 1 & \cdots & 1 \\
0 & 0 & 0 & x_1 & x_2 & \cdots & x_n \\
0 & 0 & 0 & y_1 & y_2 & \cdots & y_n \\
1 & x_1 & y_1 & \sigma_{11} & \sigma_{12} & \cdots & \sigma_{1n} \\
1 & x_2 & y_2 & \sigma_{21} & \sigma_{22} & \cdots & \sigma_{2n} \\
\vdots & & & & & & \vdots \\
1 & x_n & y_n & \sigma_{n1} & \sigma_{n2} & \cdots & \sigma_{nn}
\end{vmatrix}
\cdot
\begin{vmatrix}
\lambda \\ \alpha_1 \\ \alpha_2 \\ w_1 \\ w_2 \\ \vdots \\ w_n
\end{vmatrix}
=
\begin{vmatrix}
1 \\ x_p \\ y_p \\ \sigma_{10} \\ \sigma_{20} \\ \vdots \\ \sigma_{n0}
\end{vmatrix}
\qquad (2\text{-}35)
$$

where x_0 and y_0 are the coordinates of the point that is being estimated; x_i and y_i are the coordinates of the ith sampled point; the α_i's are the unknown drift coefficients; and σ_{ij} is the covariance between sampled points i and j.

Other Kriging Research Related to Medical Imaging and Biological Sciences

The introduction of kriging to the mining industry dates back to the early 1960s. Its use in other sampling applications has been emphasized time and again, but estimating ore reserves in mining continues to be its most well known application [Clar79]. Since its introduction kriging has also been used to characterize natural resources in the fields of forest evaluation and hydrology. Only recently has kriging been introduced to the medical imaging and biological science communities.

Parrott [Parr91], Stytz [Styt93], and others [Parr92, Parr93] apply kriging to medical imaging data to provide interpolated estimates that are, in general, as accurate as linear interpolation techniques. These medical imaging researchers demonstrate kriging's viability as a candidate medical imaging interpolation technique. The scope of their effort constrained kriging to behave like conventional interpolation techniques.

Consistent with this scope and without the benefits of a structural analysis, these researchers obtained estimation accuracies similar to those that conventional linear techniques provide.

Grant applied kriging to data sets of human subjects as early as 1990, though his research is not specifically oriented to obtaining interpolating medical images. Rather, Grant applies kriging in two-dimensional space to analyze and effectively average facial anthropometric surface data [Gran90]. The source data for his research is a series of cylindrically mapped laser scans of the surface of the heads of human subjects. His research demonstrates how to obtain an optimal average representation of the anthropometric data of a large number of subjects to support improvements in the design of aerospace flight equipment.

Brodkin employs the use of kriging to reduce the size of large two-dimensional data sets such that the estimation variance of a reconstructed image does not exceed a predefined maximum threshold [Brod91]. Brodkin uses two-dimensional MRI data to demonstrate his data compression technique.

This research is most closely related to that of Stytz [Styt93], Parrott [Parr91] and others [Parr92, Parr93] since it uses kriging to obtain estimates of interpolated modality space medical data. It begins where their research ends. It differs from their research by having removed the assumptions they made and by structurally analyzing the data in an effort to obtain linear, unbiased, interpolated estimates that are, in general, more accurate than those provided by conventional linear techniques.

Chapter III

SPATIAL VARIATION OF MRI DATA

The transition of a patient space volume to a modality space volume is inherently accompanied by several sources of distortion that can alter the intensity and position of patient space voxels in their modality space reconstruction. When a patient space volume is sampled using an MRI scanner, the acquired modality space data set undergoes a distortion that is primarily dependent upon the inhomogeneity of the static magnetic field, the nonlinearity of each gradient magnetic field, and characteristics of the rf excitation pulse. Generally, the modality space volume is interpolated to obtain an image space representation with finer resolution than modality space. The process of interpolation can further distort the representation of patient space by incorrectly assuming the variability of the patient space data.

Linear interpolation techniques, for instance, assume patient space data varies linearly between points as a function of distance. If the spatial variation about a point to be estimated were to vary in accordance with a gaussian model, then a linear interpolator would incorrectly underestimate the contribution of nearby samples in computing its estimate, resulting in a distorted representation of the actual patient space value at the estimated point.

The geostatistical interpolation technique of kriging does not assume the patient space volume varies in accordance with one model or another as do conventional linear methods. When kriging is accomplished in conjunction with a structural analysis of the data that is to be interpolated, kriging has the advantage over conventional interpolation methods because it can minimize and quantify the interpolation error that

is introduced to the image space representation of the patient space volume. Kriging assumes, however, the data to be interpolated possess spatially dependent characteristics and can be represented by regionalized variables (REVs).

Patient space volumes clearly exhibit spatially localized characteristics in the realization of different tissues of human anatomy. For instance, bone and muscle tissue each possess characteristics - color, hardness, elasticity, water content - within the extent of their borders that enable distinguishing one from another. To justify the use of kriging as a valid interpolation technique, it is necessary to show that modality space volumes also exhibit characteristics that can be modeled by spatially regionalized variables.

The scope of this research is therefore limited to a single modality - magnetic resonance imaging (MRI). Practical considerations drove a decision to simulate the acquisition and reconstruction processes of an MRI scanner to accomplish this task. A computer simulation facilitates the determination of modality space regionalization by providing unlimited access to a virtual MRI scanner and by granting the researcher absolute control over the scanner field nonuniformities that are simulated by the computational model. The MRI scanner simulation models scanner field nonuniformities that distort the representation of a patient space volume. The use of mathematical patient space phantoms removes measurement uncertainties that are otherwise associated with living test subjects. Figure 3-1 depicts examples of the two domains that are analyzed. Representing patient space is a photographic slice through the thorax of a cadaver; modality space is represented by an MRI image of the same anatomical area as the cadaver slice.[1]

---

[1] Scanned from [Bo90].
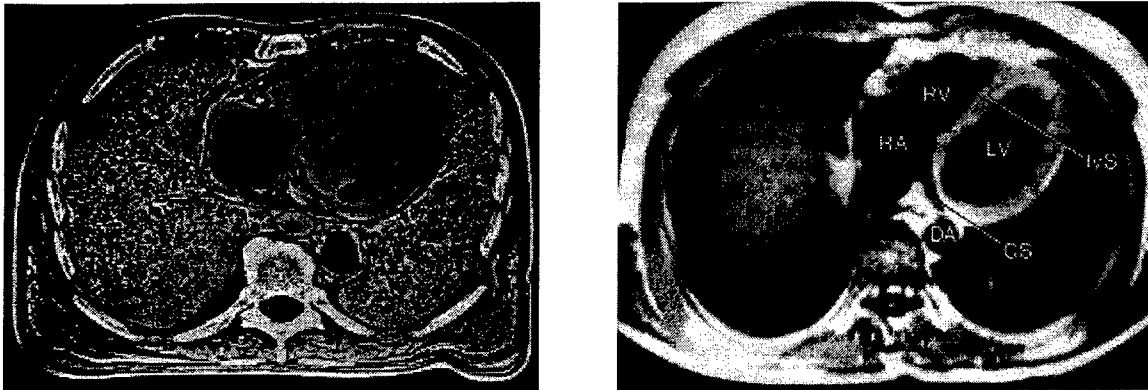
Figure 3-1.   Patient Space Cadaver Thorax Slice (left) and Modality Space T1 MRI Image (right)

Three different three-dimensional phantom objects, each with spatially localized constant media regions, are simulated as having been scanned by an MRI scanner. A modality space volume is reconstructed for each simulated MRI scan. The reconstructed volume is consistent with geometric and intensity distortion effects that would be experienced in a real world scenario. The spatial variation of the reconstructed modality space volumes are then analyzed to determine if they can be modeled using regionalized variables. If so, kriging can be used to interpolate the reconstructed volumes.

Simulating the Effects of MRI Distortion Upon Spatially Regionalized Data

The primary objective in developing the MRI Scanner Distortion Model is to facilitate the determination of whether or not an MRI modality space volume exhibits regions of spatial dependency whose variation and extent can be described using regionalized variables. Unless MRI modality space data *can* be represented using regionalized variables, this research cannot apply kriging as a valid interpolation technique. Kriging requires that the spatial variation of the data that is to be interpolated be described using continuous, deterministic functions. Kriging does not presume nor require, however, that any observed modality space regionalization be

3-3

similar to the corresponding patient space. If the acquisition of MRI data introduces errors of a magnitude such that the similarity in spatial variability between modality space and patient space is no longer significant, as long as regions of modality space spatial dependency can be located, the distortion would not invalidate kriging as a candidate estimation technique. It would, however, require the acknowledgment that the kriged estimate, like any other linear estimate, would be biased by the presence of the distortion. In other words, kriging cannot remove the distortion effects of the scanner used in the acquisition process.

Assuming the primary objective is satisfied, a secondary goal in developing the MRI Scanner Distortion Model is to gain insight as to whether or not the modality space representation of a scanned patient space volume exhibits spatially regionalized characteristics that are similar to those in patient space. Similarity would be assessed in terms of observed correlation trends between modality space and patient space voxels, as well as in terms of the extent of spatial dependency observed about identical locations in modality space and patient space. Once again, kriging requires the existence of regionalized spatial dependency about a point to be estimated; it does not require that spatial characteristics of patient space variability be preserved in an modality space representation of that volume. Providing an exhaustive analysis that relates modality space regionalization to patient space regionalization is beyond the scope of this research. This research simply intends to provide evidence to suggest that characteristics of spatial variability in patient space either are or are not preserved in their modality space representation.

To meet these objectives, two specific tasks were completed. First, the general acquisition and reconstruction processes of an MRI scanner was modeled so that the

geometrical and intensity distortion that occurs to a frequency-encoded modality space representation of a patient space volume in the presence of system noise could be simulated and studied. The model transforms a patient space volume into its modality space representation, distorting the patient space volume in accordance with simulated component magnetic and rf fields. Mathematical functions describe an inhomogeneous static magnetic field and nonlinear x, y and z gradient magnetic fields. Frequency roll-off characteristics of the rf excitation pulses are also simulated and under user control. Thus, the MRI scanner model enables the spatial resolution of the reconstructed volume to be altered dependent upon the parameters that are specified for these three fields. Artifacts due to magnetic susceptibility of the patient space volume are not considered, since these are a function of the patient space material composition rather than of the physics of the scanner.

Second, patient space phantom volumes that include spatially dependent regionalized areas are generated, input to the scanner model and processed using the modeled reconstruction transformations of an MRI scanner. For each patient space phantom volume, the scanner distortion model generates volumetric modality space data that is structurally analyzed along with the patient space source data using semivariograms to compare the spatial variation between the two volumes. One is therefore able to observe how the local regionalization about a given point in patient space is altered in its modality space representation.

In a one-dimensional case along the x direction, consider the ideal profile of the combined static and x gradient magnetic fields, shown by the dashed line in Figure 3-2. Assume that the combined effect of an inhomogeneous static magnetic field and a nonlinear x gradient magnetic field produce the gradient encoding field strength profile
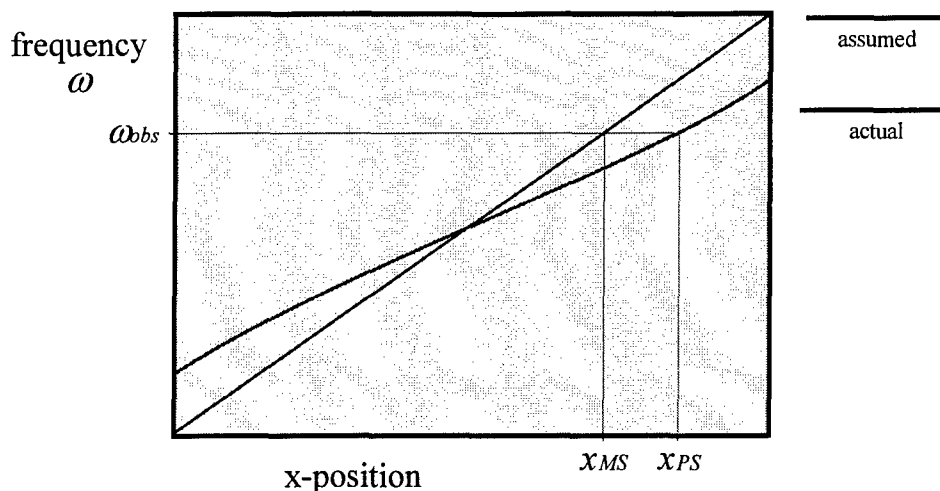
Figure 3-2. Reconstruction Distortion

shown by the solid line. The ordinate is labeled in terms of frequency ω since the precessional frequency is a function of and directly proportional to the magnetic field strength. Though modality space reconstruction algorithms assume ideal profiles, such as that illustrated by the dashed line, frequency-encoding of the modality space image is dependent upon the actual strength of the combined fields and therefore is accomplished using a function such as that given by the solid line. As a result, the rf emission of frequency ω_{obs} from hydrogen nuclei precessing at position x_{PS} in the patient space data would be registered at position x_{MS} in the modality space image. When there is no gradient field distortion, the two lines of Figure 3-2 coincide and a continuous modality space reconstruction exactly replicates the patient space volume aside from any introduced system noise.

If a gradient encoding field distortion exists, as long as the field is strictly monotonic, then a one-to-one correspondence from the actual gradient encoding field strength to the assumed linear gradient field strength is maintained. Under this condition spatial relativity of the continuous patient space volume is preserved in a

continuous modality space reconstruction; however, voxel positions shift and a compression occurs in the modality space representation of patient space. Voxels lying in regions of maximum nonlinearity shift the greatest distances towards the center of the magnetic field of view where the assumed and actual gradient encoding fields are shown to be equal.

In addition to simulating a nonlinear x gradient field superimposed upon an inhomogeneous main static magnetic field to reconstruct positional information along the x coordinate axis, the scanner model similarly simulates nonlinear y and z gradient magnetic fields to encode and reconstruct patient space data along the y and z axes.

Several factors are considered in the derivation of the simulated magnetic fields employed in the MRI scanner distortion model. Though significant distortion effects must be analyzed, it is not the intent to simulate magnitudes of distortion so great that they would not be encountered in a clinical environment. In general, the gradient magnetic field strengths should be designed to be greater than any main field inhomogeneity, and the gradient field variation should be approximately two orders of magnitude greater than the main static field [Kean86]. Resistive magnet MRI scanners, known for their relative poor field uniformity, may produce field inhomogeneities of 50 parts per million [Bush94], or 0.005%. Other researchers have observed modality space geometric distortion of 3-5 mm in phantom studies as well as theoretical analysis for clinically-tuned systems [Chan92]. Assuming a 40 cm field of view, this corresponds to a geometric distortion of 1.25%, or greater than one voxel in a field of view that is 128 voxels on a side. Though it is recognized that these figures exceed those of a carefully shimmed commercial MRI scanner, they are utilized in the derivation of our simulated

fields so that modality space data that is reconstructed under relatively poor conditions may be spatially analyzed.

In actuality, the magnitudes of simulated field nonuniformities are orders of magnitude greater than those expected in a commercial system due to the limited resolution of our simulation. Practical execution times dictate the simulations be run using patient space volumes that are 130x130x130 to generate modality space volumes that are 65x65x65. Field nonuniformities therefore had to be scaled to ensure that some number of modality space voxels would be positionally shifted from their patient space location by at least one voxel so that distortive effects could be observed. It is the resulting geometric and intensity distortion that would be the primary cause of spatial continuity deterioration in an modality space volume.

Static and gradient magnetic field functions are entered into our model scanner in terms of the field of view resolution that is desired. Consistent with simulated fields used by MRI researchers investigating MRI distortion correction algorithms and consistent with the aforementioned typical magnitudes of field nonuniformities, results were obtained using a static field inhomogeneity modeled by

$$B_0(x,y) \ = \ 0.33\,(x^2 + y^2)/(2n+1)^2 \qquad (3\text{-}1)$$

and x and y gradient fields characterized by:

$$
\begin{aligned}
G_x(x \geq 0, y) \ &= \ (0.8\,x + 0.00005\,x/(2n+1)^2)\,(1.6 - 0.025\,y^2/(2n+1)^2)\,, \\
G_y(x, y \geq 0) \ &= \ (0.8\,y + 0.00015\,y^2/(2n+1)^2)\,(1.4 + 0.003\,x^2/(2n+1)^2)\,, \\
G_x(x < 0, y) \ &= \ -G_x(x > 0, y)\,, \\
G_y(x, y < 0) \ &= \ -G_y(x, y > 0)\,.
\end{aligned}
\qquad (3\text{-}2)
$$

where x and y are the spatial coordinates measured in voxel units; and the field of view is $(2n+1)$x$(2n+1)$x$(2n+1)$ voxels, where $n=32$ for the results published herein. The contour map of a transaxial slice of the static magnetic field $B_0(x,y,z=0)$ used in our simulation and generated by the above equation is illustrated in Figure 3-3. Contour maps of transaxial slices of the magnetic fields $B_x(x,y,z=0)$ and $B_y(x,y,z=0)$ that result when the static field is combined with the x and y gradient fields are illustrated in Figure 3-4 and Figure 3-5, respectively. Though the modality space image reconstruction presumes a homogeneous static and linear gradient fields, it is the resulting magnetic field $B(x,y,z)$ that determines the frequency-encoded spatial mapping of the patient space data.
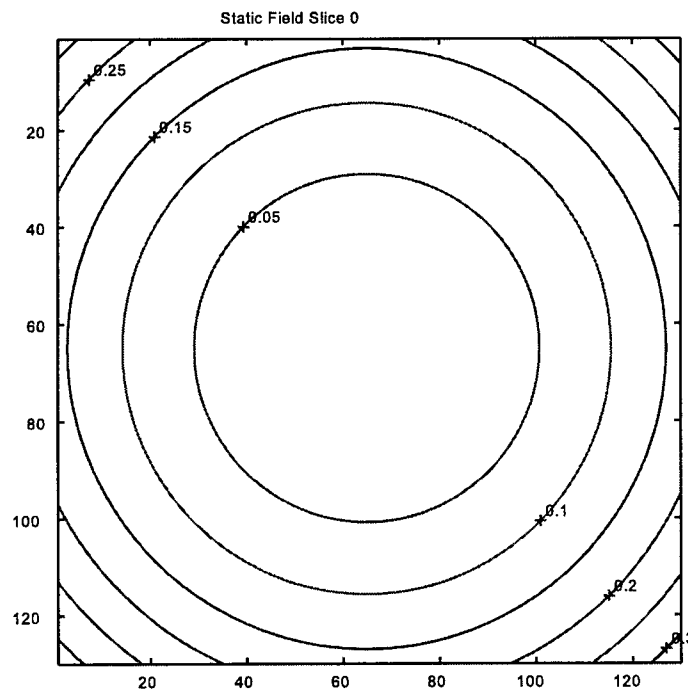
Figure 3-3. Static Field $B_0(x,y,z=0)$
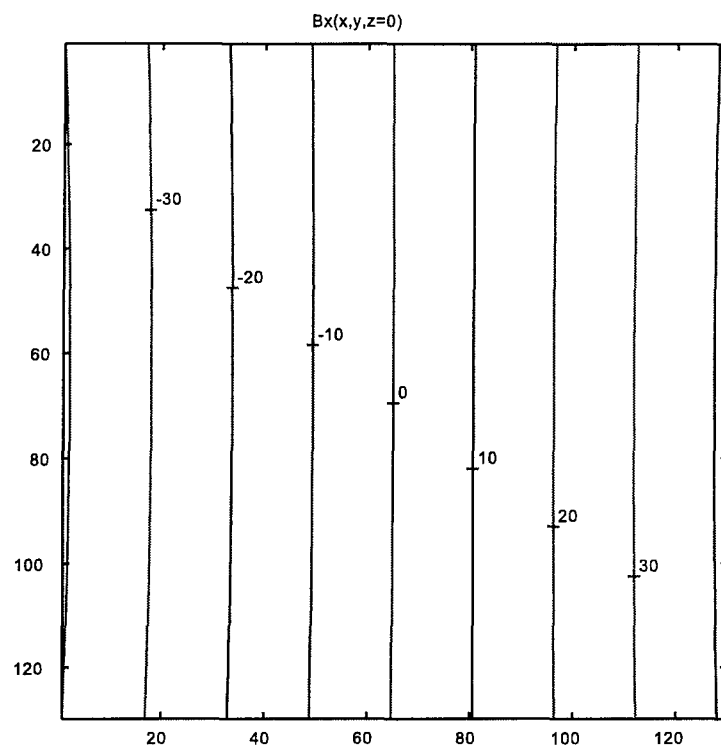
Figure 3-4. Gradient Field $B_x(x,y,z=0)$
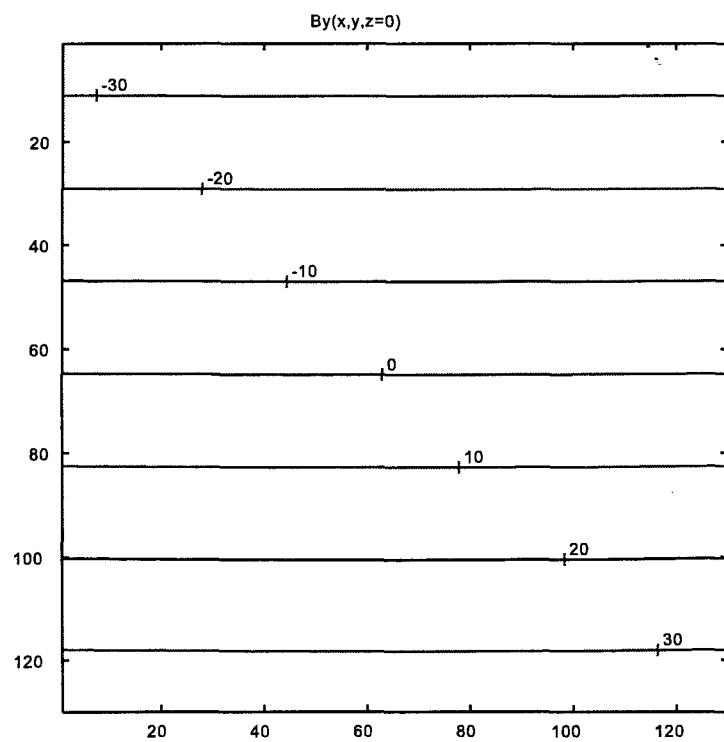
Figure 3-5. Gradient Field $B_y(x,y,z=0)$

In this simulation the z gradient field G_z is characterized by the same function as the x gradient field G_x, only positional encoding along the z axis is computed differently than along the x axis because the slopes of the assumed ideal gradient fields are different with the slope of $G_{z(ideal)}$ being less than the slope of $G_{x(ideal)}$. Table 3-1 lists the mean and maximum percent deviation of each of the simulated nonlinear gradient fields superimposed upon the inhomogeneous static field from their assumed linear counterparts. These values are significant because, based upon the mean nonlinearities and the range of gradient field strengths recorded for the 65x65x65 field of view employed, voxel shifts will not occur in the modality space reconstruction of a patient space volume. However, voxels that lie in locations that experience the maximum nonlinearities will be displaced and summed to an adjacent voxel position in the modality space reconstruction of the patient space volume. These voxel shifts are a primary source of distortion in MRI modality space volumes.

Table 3-1. Simulated Gradient Encoding Field Nonlinearities

% Nonlinearity	B_x	B_y	B_z
mean	0.174832	0.183802	0.159647
maximum	0.793270	0.850113	0.987886

The rf excitation pulse acts as an rf notch filter determining the frequencies of precession and the spatial extent of the hydrogen nuclei that will be misaligned by the rf interrogation. The bandwidth and rolloff characteristics of the rf excitation pulse may be specified in the simulation, thereby enabling different partial volume effects to be analyzed.

The bandwidth of the rf pulse dictates the range of resonant frequencies that excite patient space nuclei. Each frequency spatially maps to a unique position in the patient space volume and the amplitude of each discrete frequency in the pulse bandwidth proportionally determines the gain of the received signal from resonating nuclei. Characteristics of the rf pulse are spatially specified in this simulation such that any induced crosstalk will not extend beyond 1 voxel in any direction from the intended sampling location, except perhaps at the periphery of the simulated field of view.

An *on center* weighting factor indirectly specifies the width of the simulated pulse bandwidth. The results in this chapter were computed using an on center weighting of 0.9; that is, 90% of the received signal originates from nuclei bounded by the intended voxel to be sampled. The remaining 10% of the received signal is a weighted average of emissions that would be received from nuclei that had been approximated to lie in a three-dimensional gaussian envelope about the intended sampled voxel.

To simulate the discrete modality space sampling of a continuous patient space volume, all spatial effects of nonlinear magnetic fields and finite bandwidth, gaussian shaped rf pulses are determined in a coordinate space that is twice the desired resolution of the resulting modality space volume. This difference in coordinate space resolutions enables the observation of smoothing effects that are visible in modality space as a result of rf emissions from neighboring voxel nuclei about an intended point in patient space. This blurring is observed in Figure 3-1 as a loss of clarity in the modality space image when compared to the corresponding patient space cadaver slice.

McVeigh and others showed that noise in unfiltered MR images is spatially invariant, normally distributed white noise [McVe85]. Consistent with these findings, scanner-induced noise is simulated by summing a gaussian noise volume to each patient

space volume during the reconstruction process. The noise volume is given by the following equation

$$i_{noise} = randn(n) * \sigma_{noise} \qquad (3\text{-}3)$$

where *randn(n)* is a function that returns an *n x n x n* array of values between *-1* and *1* with a zero-mean gaussian distribution, and σ_{noise} is the standard deviation scaling factor. The data presented in this chapter use $\sigma_{noise}= 0.01$. The magnitude of the noise that is associated with the spatial coordinate *(x,y,z)* of the patient space volume is represented by $i_{noise}(x,y,z)$.

When a patient space volume is introduced to the scanner model, each voxel value is smoothed by values of neighboring regions, its position is potentially repositioned in accordance with the inhomogeneous static and nonlinear gradient magnetic fields and its intensity value is subject to additive system noise. This process is graphically summarized in Figure 3-6 and is described in further detail in the following paragraphs.

MRI Scanner Distortion Simulation Description

Each patient space-to-modality space simulation follows the process depicted in Figure 3-6. To generate a modality space field of view that is *nxnxn* voxels, a patient space volume that is *(2n+1)*x*(2n+1)*x*(2n+1)* voxels must be generated and loaded into the MRI Scanner Distortion Model. The results in this chapter are generated using patient space phantoms that lie within a 130x130x130 field of view. Using the static magnetic field function given by $B_0(x,y)$ in equation (3-1), a magnetic field contour map is

3D MRI Scanner Distortion Model
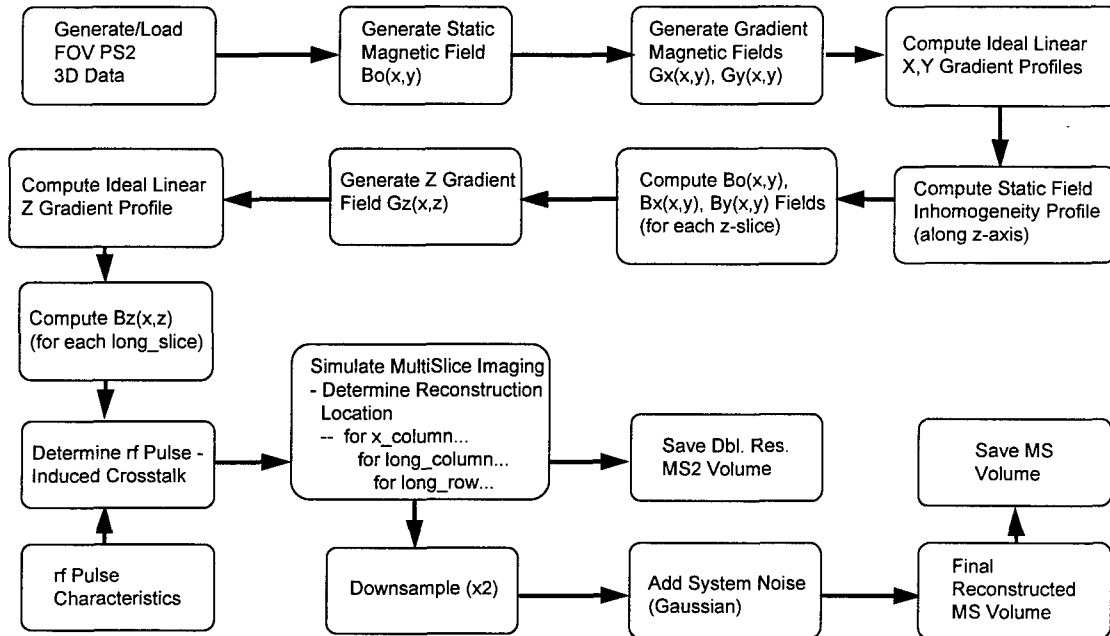
Figure 3-6. 3D MRI Distortion Model

computed corresponding to the transaxial slice at $z=0$ that is midway through the phantom volume. This contour map is plotted in Figure 3-3.

Gradient magnetic fields along the x, y and z directions are characterized by the equations of (3-2). The magnetic field strength simulated at the location given by the patient space coordinates $(x,y,z=0)$ are obtained by the algebraic superposition of the static magnetic field $B_0(x,y,z=0)$ and the x and y gradient magnetic fields, $G_x(x,y,z=0)$ and $G_y(x,y,z=0)$, respectively.

Under ideal conditions, the magnetic field along the longitudinal z direction would be perfectly homogeneous and each transaxial magnetic field contour map would be identical for all values of z. Although the MRI Scanner Distortion Model accounts for

3-14

static field nonuniformities along the z direction, the results of this chapter assume a sufficiently homogeneous static magnetic field along the z direction for the field of view of interest.

For localization along the z axis, however, a nonlinear z gradient magnetic field $G_z(x,y)$ is simulated. The function used to characterize this field is similar to the function G_x that is used to model the x gradient magnetic field, only the slope of the ideal linear profile is different for each gradient field. Their distortive effects are therefore different.

Given each gradient field is assumed to be perfectly linear and the static magnetic field perfectly homogeneous, each patient space voxel is registered in the modality space reconstruction in accordance with the principles previously described and depicted in Figure 3-2. Nonideal rf excitation pulses are simulated in terms of their corresponding spatial extent. They have the effect of exciting nuclei in proximity to the intended sampling point. As a result, each reconstructed modality space voxel value represents not the value of a discrete patient space point, but rather a distance-weighted average response of a spherically distributed region about a discrete patient space point.

The MRI Scanner Distortion Model therefore spatially expands and compresses patient space voxels in their modality space reconstruction as a function of the inhomogeneity of the static magnetic field and the nonlinear characteristics the gradient magnetic fields. In addition to this spatial distortion, the value of each patient space voxel can only be represented as an intensity averaging of the surrounding patient space region. The magnitude of this distortion is a function of nonideal characteristics of the rf excitation pulses that are simulated.

After the scanning of each patient space voxel has been simulated and modality space reconstructed, the resolution of the modality space volume is reduced by a factor of two by averaging each consecutive 2x2x2 voxel subvolume. This resolution reduction simulates the discrete modality space sampling of a continuous patient space volume. Before each simulated modality space reconstruction is saved for subsequent analysis, gaussian noise is added to simulate system noise.

MRI Distortion Simulation Results

In this section the results of three phantom simulations are discussed. Phantom patient space data sets are used so that voxel values of resulting modality space volumes may be compared to their corresponding *true* values. For each volume, spatial variation is analyzed using variograms. Variograms are computed for subvolumes about each patient space sample and for the associated modality space subvolume. Each pair of variograms are compared to one another to determine if the spatial regionalization exhibited in patient space is also present in modality space.

All three simulations were processed with the simulated magnetic fields and rf pulse characteristics previously described. Though it is desired that the patient space resolution be as great as possible to approximate the continuous nature of patient space data, the resolution is limited because the computation of three-dimensional variograms is cpu intensive. Each doubling of resolution necessitates an eightfold increase in the number of computations required. The x, y, and z dimensions of the field of view of the patient space volume each range from -64 to +65, totaling 130^3 voxels. The x, y, and z dimensions of the resulting modality space volume range from -32 to +32, totaling 65^3 voxels. Each voxel has a value that represents one of 2^{10} possible gray levels.

Dimension aspect ratios for each volume are 1.0:1.0:1.0. The three phantoms are a constant media cube, a dual media sphere, and a crosshatch pattern, respectively.

Accompanying each simulation are variogram curves that describe the relationship between patient space and modality space spatial variation along each of thirteen noncomplimentary directions for a given modality space coordinate location. Two modality space locations are analyzed for each phantom volume simulation. The locations analyzed are chosen to be located in regions where the spatial variation of the phantom volume is known to vary.

The key to the variogram information that is plotted is shown in Figure 3-7. Each variogram pair plot is titled above with two coordinate triplets. The first coordinate triplet is enclosed by parentheses and specifies the x, y, and z location in modality space coordinates of the point for which spatial variation is analyzed. The
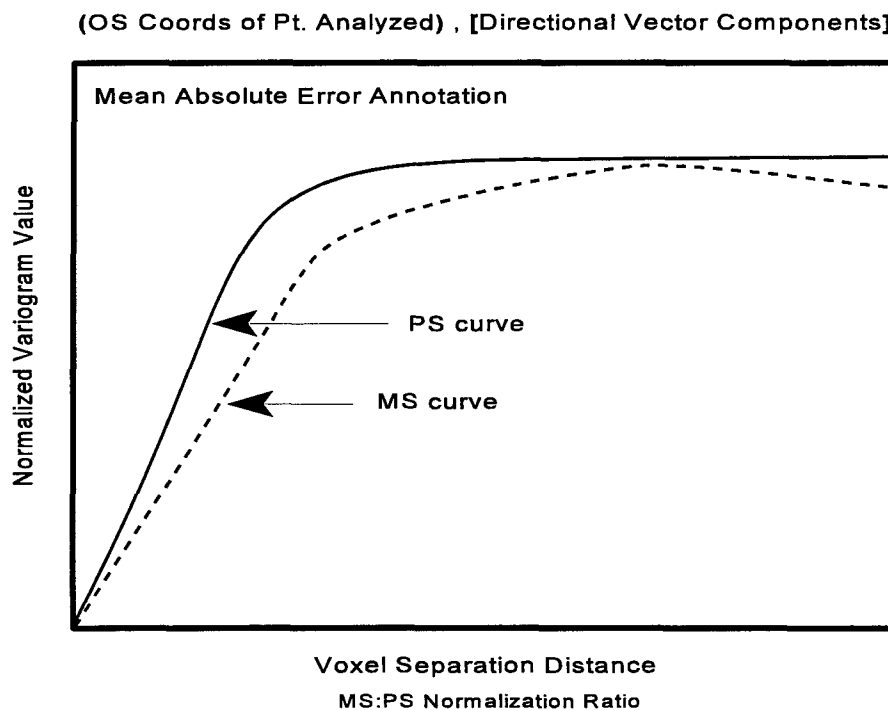
Figure 3-7. Variogram Key

3-17

second coordinate triplet is enclosed by brackets; it provides the x, y, and z relative coordinates from the analyzed point to specify the direction for which the variogram is computed. Each point is analyzed along thirteen different directions using the variogram as the analysis tool. This is equivalent to structurally analyzing the region about a point in 26 different directions, since variogram values that are calculated for a given direction are equivalent to the values that would be computed in the opposite direction. Along a given direction, the variogram is a function of the separation distance between contributing voxels, regardless of whether the direction is positive or negative.

Normalized variogram values are plotted along the ordinate and separation distances are plotted along the abscissa of each plot. The variogram curve that corresponds to the patient space volume is plotted with a solid line. The variogram curve that corresponds to the modality space volume is plotted with a dotted line. Each variogram curve is normalized to a maximum value of 1.

The modality space:patient space ratio below each plot is the modality space-to-patient space ratio of normalization factors that are used to obtain each normalized variogram curve. For instance, a modality space:patient space ratio of 2 indicates that the factor used to normalize modality space variogram values is 2 times greater than the factor used to normalize patient space variogram values. Even though normalized patient space and modality space variograms may be approximated using the same model, the modality space:patient space ratio is necessary to differentiate between variograms whose non-normalized values are significantly different.

The mean absolute error between the two normalized variogram curves is annotated in the upper left corner of each plot. This error is defined to be the mean of the absolute values of the differences between the two curves and computed for each

plotted separation distance. In addition to the mean absolute error, a *weighted* mean error is computed for each plot. This error is similar to the mean absolute error except the error for each plotted separation distance is weighted depending upon the number of contributing pairs of values that determined each variogram value. If one assumes the region about a point is analyzed using a finite number of regularly-space samples, then variogram values that are associated with large separation distances will be computed from fewer pairs of patient space and modality space values than will variogram values that are associated with small separation distances. As a result, the errors for small separation distances will be weighted more heavily in the computation of the weighted mean error than will errors for large separation distances.

Phantom Cube Simulation Results

This simulation processed a phantom cube whose faces are aligned with each of the three orthogonal cartesian coordinate planes. The cube is centered within the 130x130x130 patient space field of view and is 113 units on each side. It is a constant medium object whose gray level intensity is 60% of the simulation maximum. The 65x65x65 field of view of the simulated MRI modality space output maps to the patient space field of view. A rendering of the original patient space cube (mapped to modality space coordinates) is shown in Figure 3-8. Figure 3-9 through Figure 3-11 depict how the constant medium patient space volume is distorted in its MRI modality space reconstruction. The modality space reconstruction of the patient space volume is rendered in Figure 3-9. A cutaway rendition of the modality space volume is shown in Figure 3-10. The extraction of three orthogonal slices of the modality space cube along
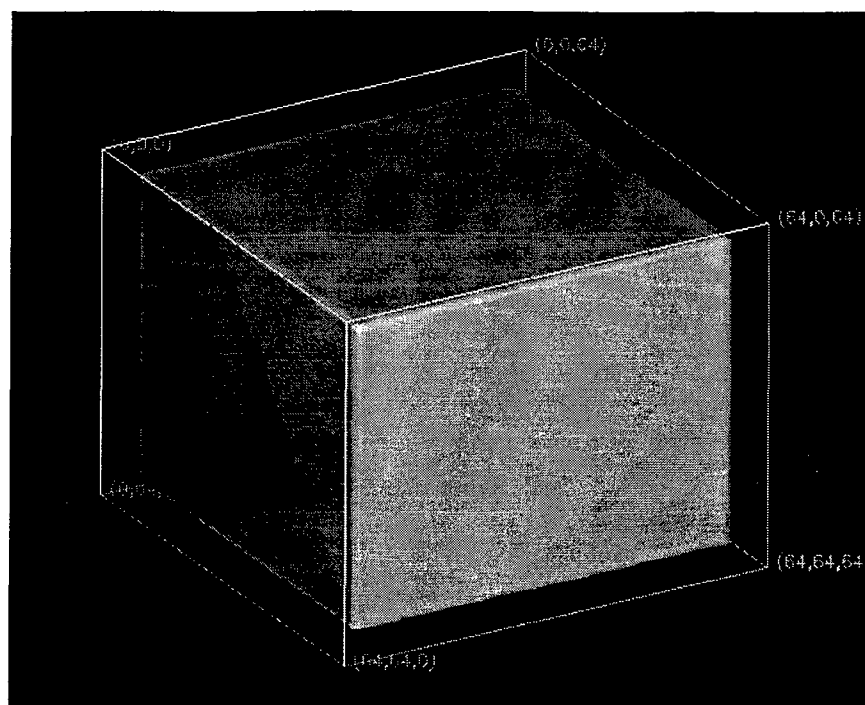
Figure 3-8. Patient Space Cube
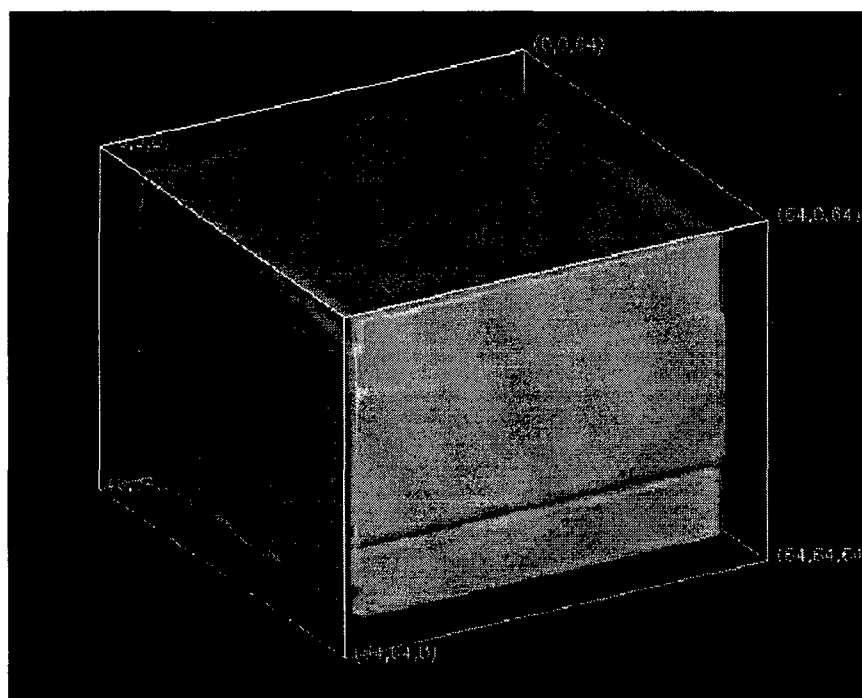
Figure 3-9. Modality Space Cube
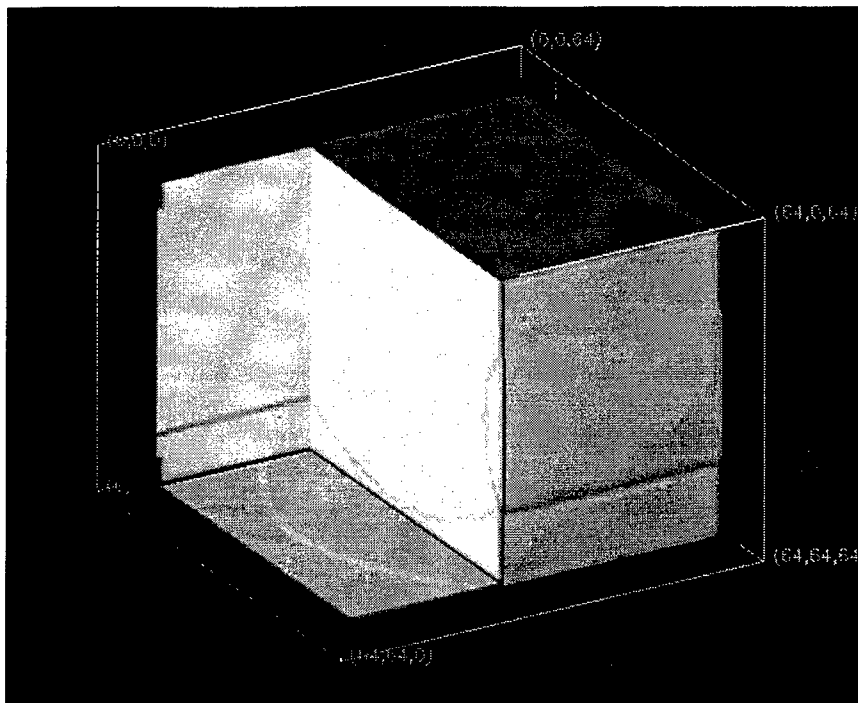
Figure 3-10. Modality Space Cube Cutaway
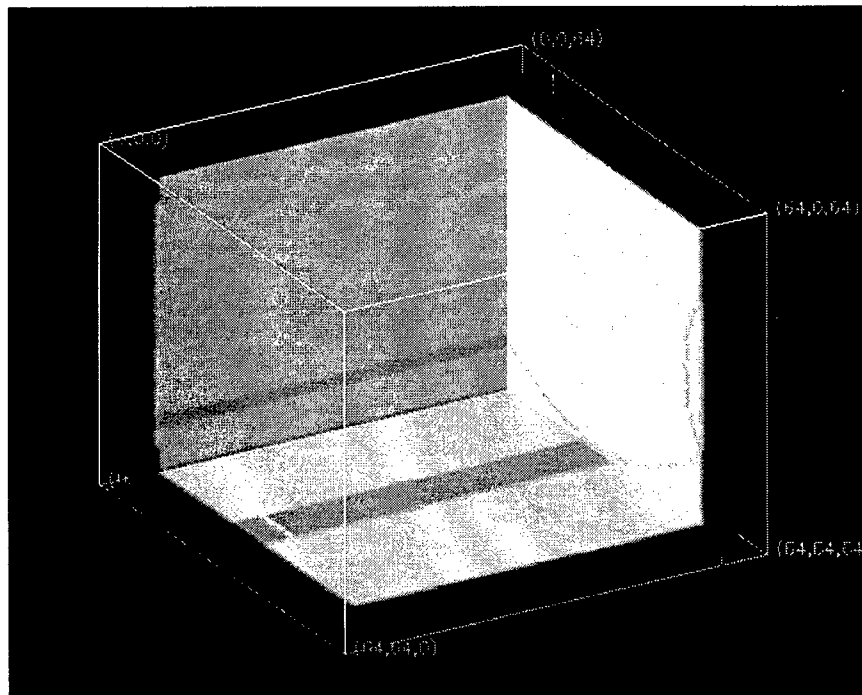
Figure 3-11. Modality Space Cube Perimeter Slices

its perimeter is shown in Figure 3-11. These figures depict the significant intensity and geometric distortion that occurs within reconstructed modality space volumes.

Figure 3-12 through Figure 3-15 are obtained by analyzing the spatial variation of the phantom volume along thirteen noncomplimentary directions about modality space coordinate (4,4,4), which corresponds to a corner of the patient space phantom cube. Figure 3-16 through Figure 3-19 are obtained by analyzing the spatial variation at modality space coordinate (60,60,60), which corresponds to the opposite diagonal corner of the patient space cube.

Natural objects generally do not exhibit perfectly planar surface characteristics like a cube. Their organic composition, in general, is not perfectly homogeneous. Therefore, discriminating intensity and geometric distortion effects upon these objects from their naturally occurring characteristics may be difficult. For this reason, this simulation processed a constant media phantom cube using the MRI Scanner Distortion Model.

Since thirteen directions about each identified point are analyzed, thirteen plots are provided for each identified point. Each direction is specified by the directional vector whose x, y and z components are provided in the right triplet above each variogram plot. The x, y and z modality space coordinates of each analyzed point is given by the left triplet above each variogram plot. These triplets and their position above each plot is shown in the variogram key in Figure 3-7. Four plots are provided for each figure. Part A results depict the first four plots obtained about the given modality space coordinate; Part B results depict the second four plots; Part C the third four plots; and Part D the last, or thirteenth plot.
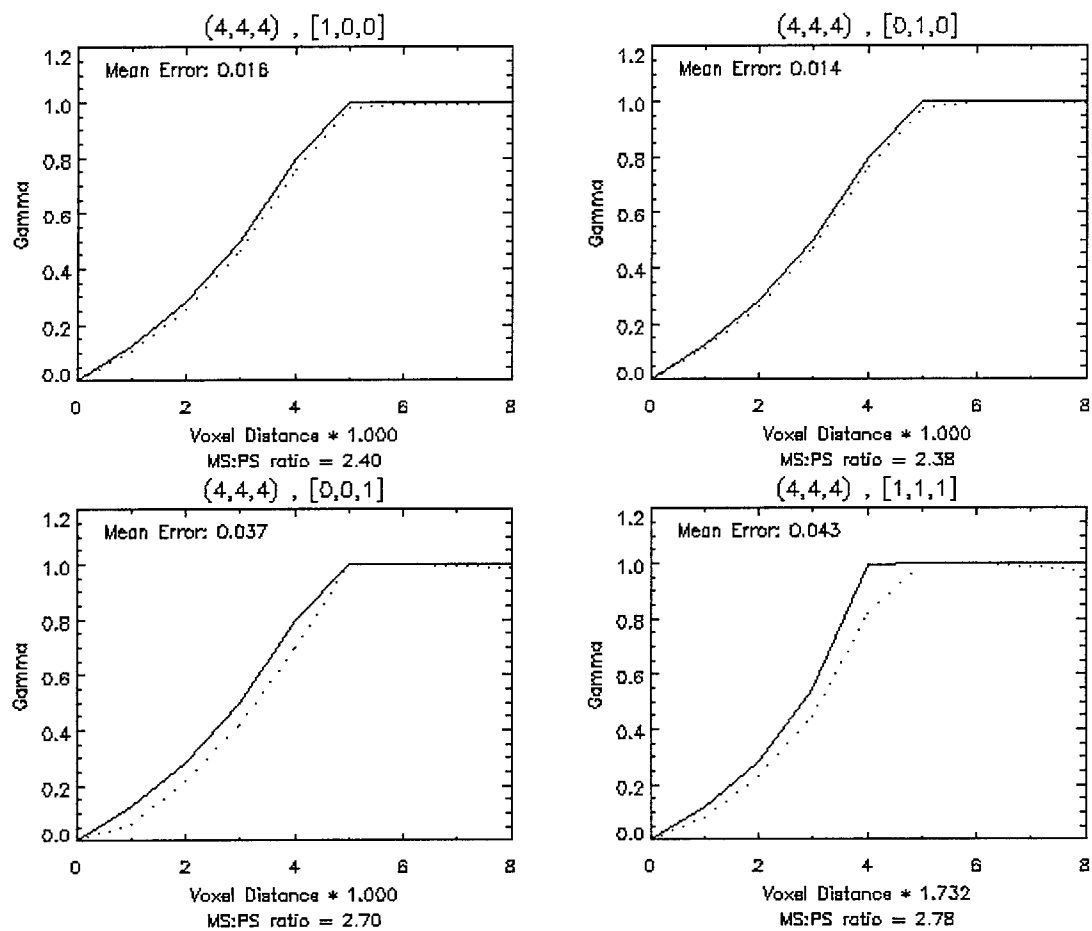
Figure 3-12. Phantom Cube Variograms About (4,4,4), Part A
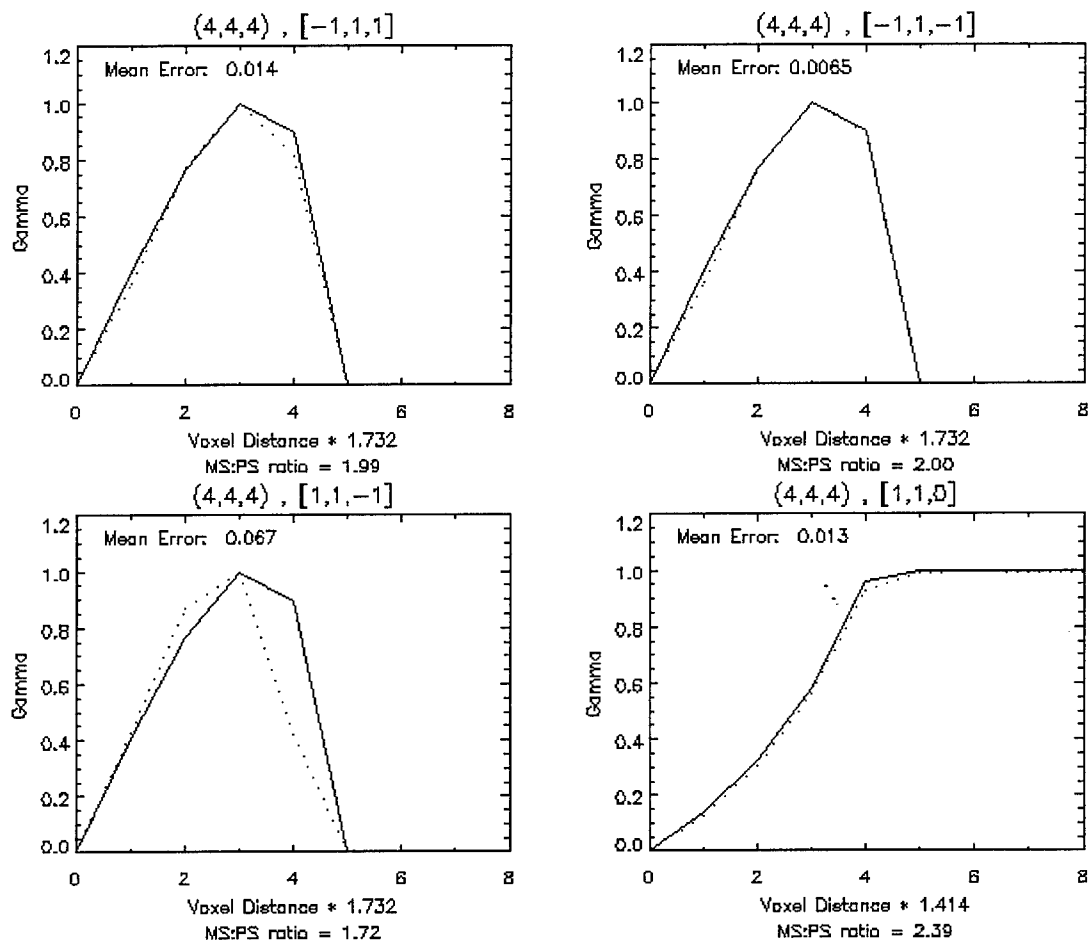
Figure 3-13. Phantom Cube Variograms About (4,4,4), Part *B*
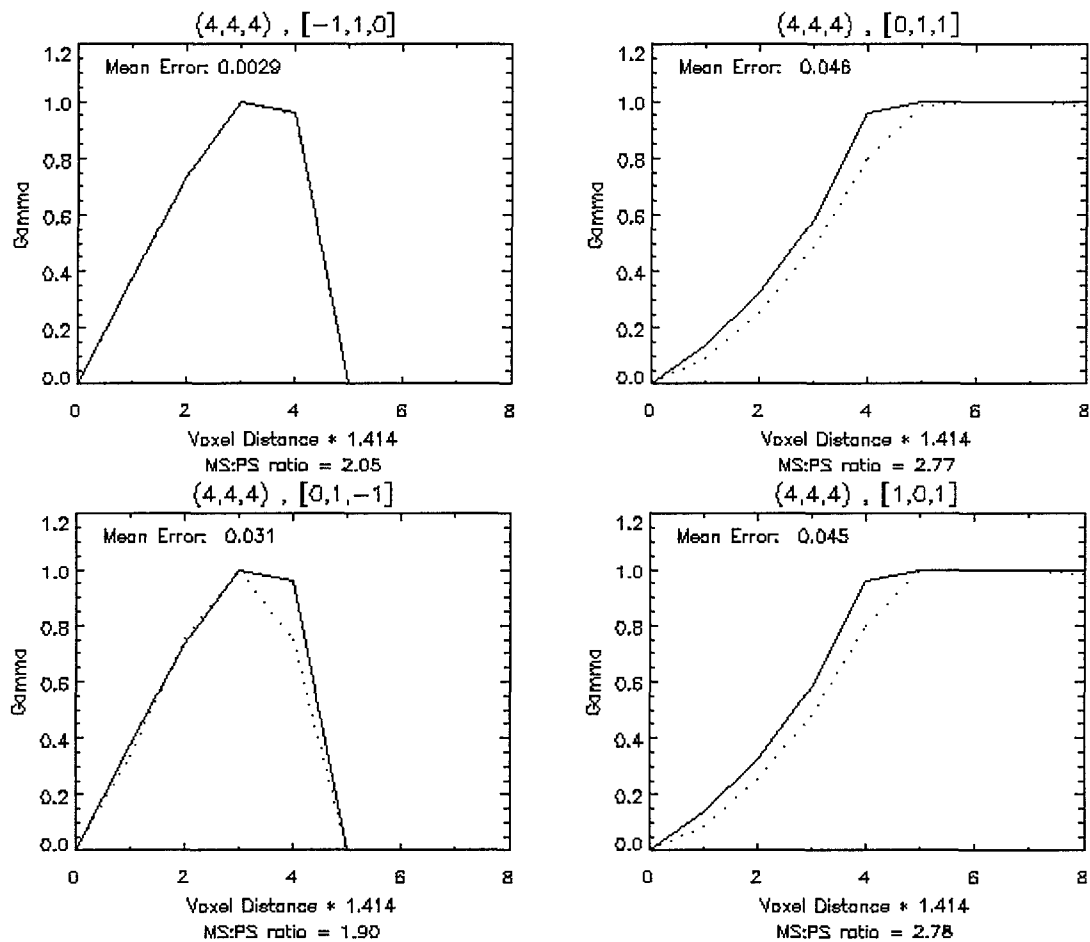
Figure 3-14. Phantom Cube Variograms About (4,4,4), Part C
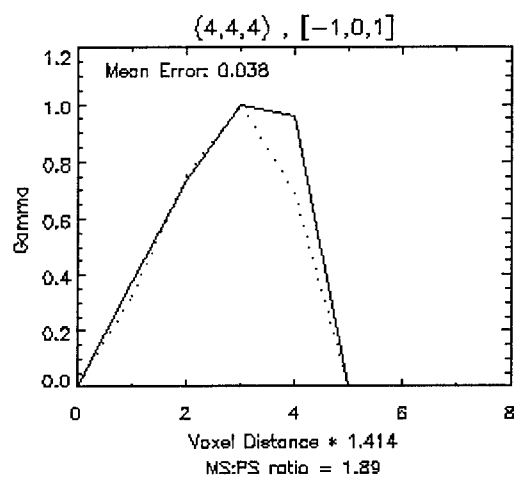
Figure 3-15. Phantom Cube Variograms About (4,4,4), Part *D*
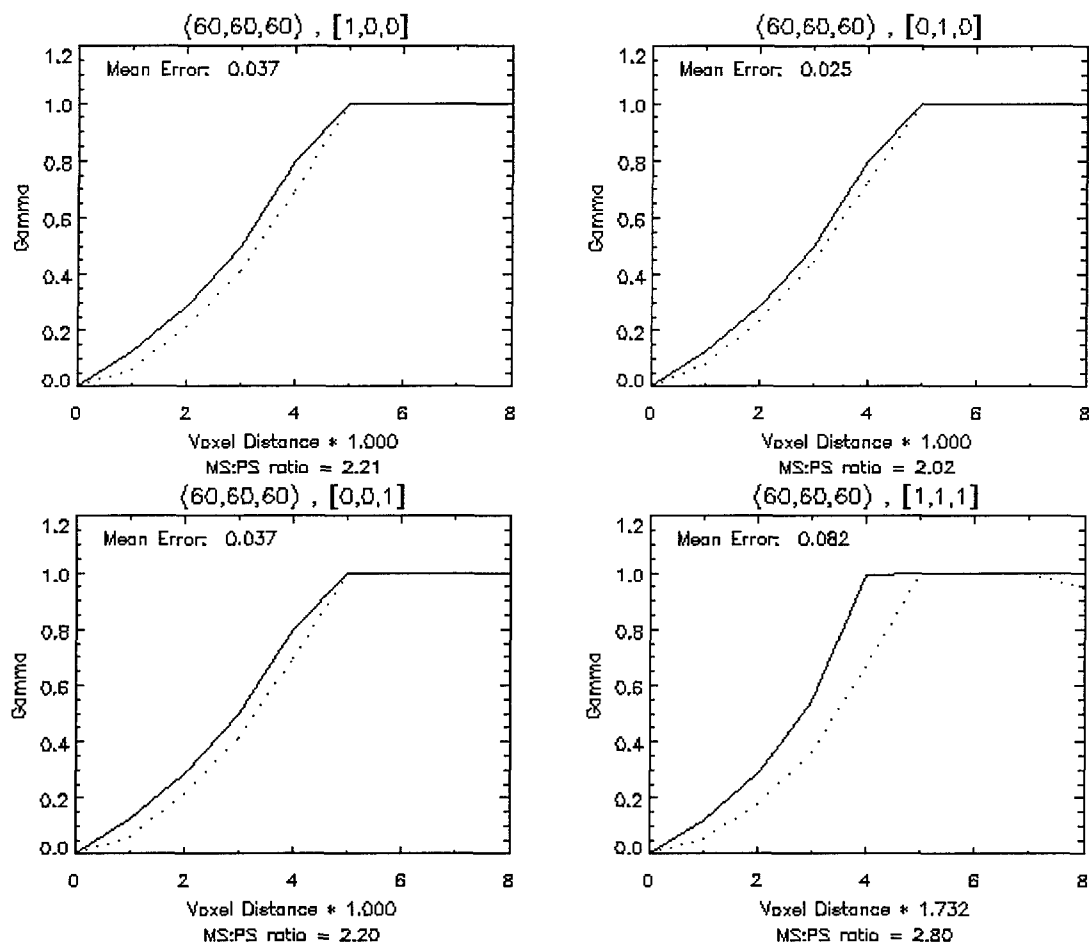
Figure 3-16. Phantom Cube Variograms About (60,60,60), Part *A*
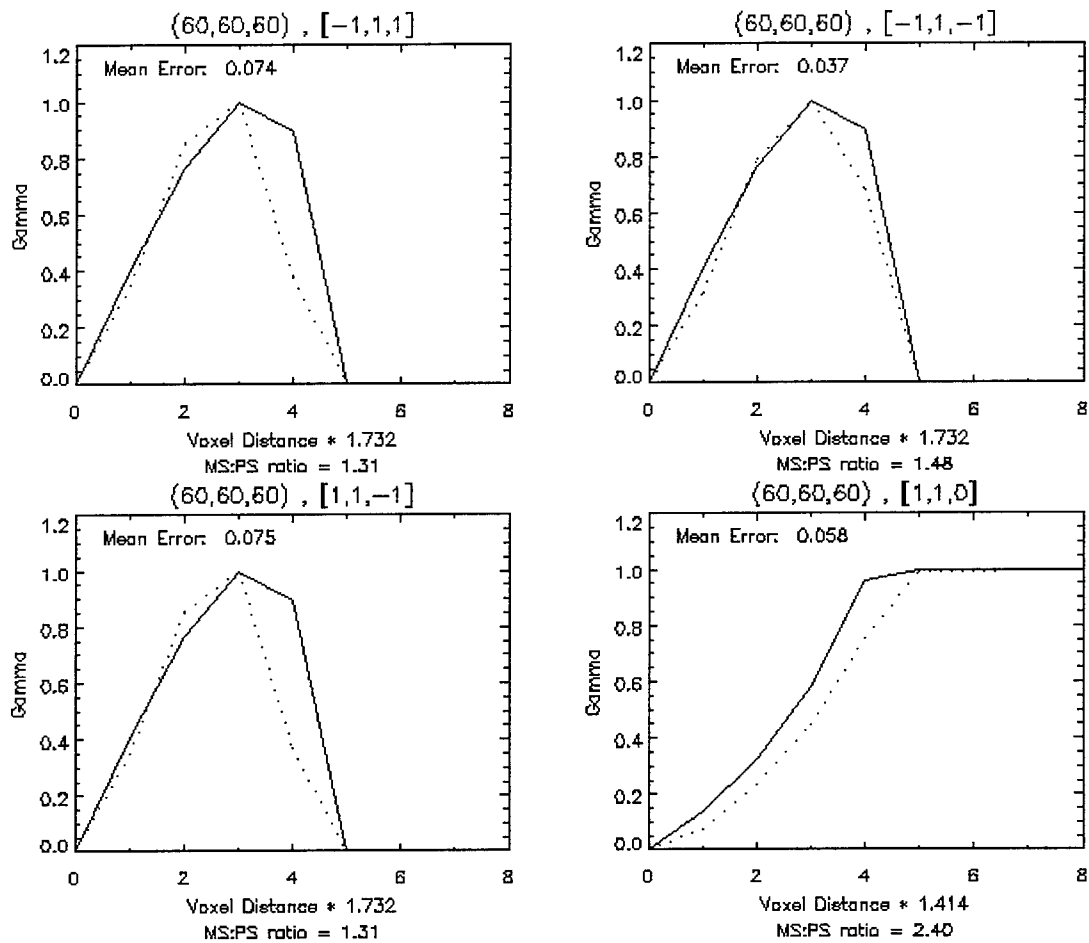
Figure 3-17. Phantom Cube Variograms About (60,60,60), Part *B*
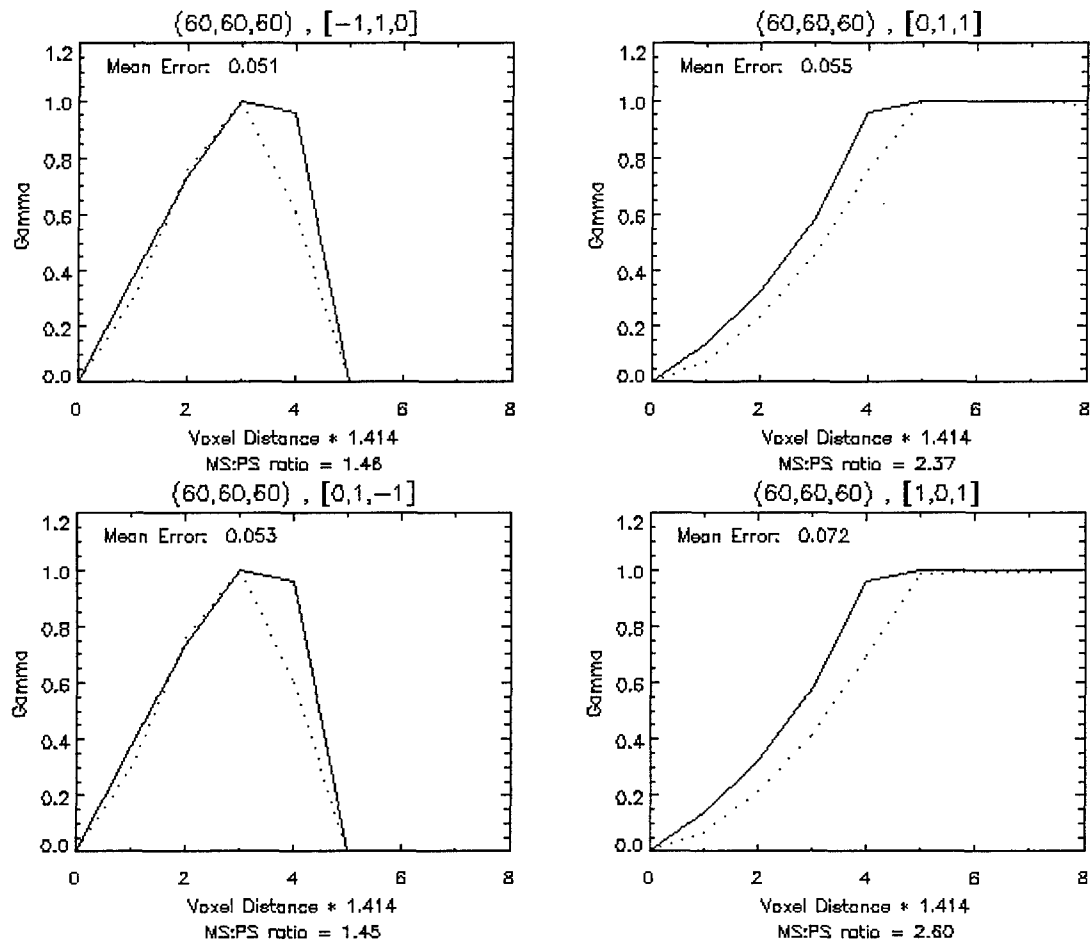
Figure 3-18. Phantom Cube Variograms About (60,60,60), Part *C*
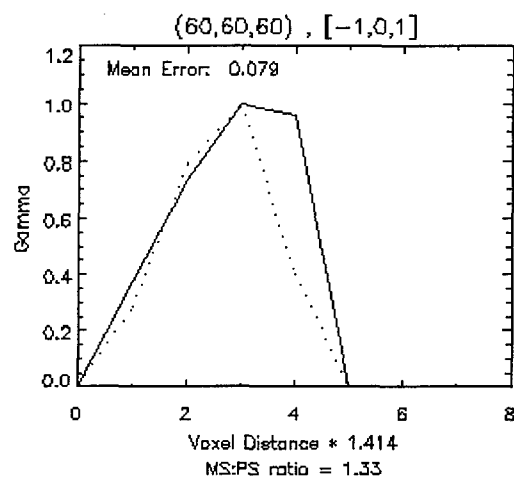
Figure 3-19. Phantom Cube Variograms About (60,60,60), Part *D*

Each variogram pair that is plotted in this chapter may be interpreted in a manner similar to that which follows. Figure 3-12 through Figure 3-15 are obtained by analyzing the spatial variation of the phantom cube about the modality space coordinate (4,4,4), which corresponds to a corner of the patient space cube. No more than four variogram pairs are plotted on a page. One variogram pair is plotted for each of the thirteen noncomplimentary directions analyzed. For example, the four variogram pairs plotted in Figure 3-12 Are for the directions specified by the vectors [1,0,0], [0,1,0], [0,0,1], and [1,1,1], respectively.

In addition to the modality space coordinate and direction analyzed, each variogram pair is annotated with the mean error between the modality space and patient space normalized variograms, the distance scaling factor for the specified direction, and the ratio of the normalization factors that are used to obtain each normalized variogram curve. The mean error is defined as the mean of the absolute values of the differences between the normalized modality space and patient space variograms for a given modality space coordinate and along a specified direction. The distance scaling factor is the factor that abscissa distance units are multiplied by to derive absolute distances from each analyzed point. The modality space:patient space ratio below each plot is the ratio of normalization factors that are used to obtain each normalized variogram curve. Each variogram curve is normalized so that its maximum value is 1. This facilitates comparison of the modality space and patient space variograms.

For instance, consider the upper left plot in Figure 3-12, Part A. It consists of modality space and patient space normalized variogram curves whose mean error is 1.6%. This implies that the spatial variation of the modality space volume along the

direction specified by the vector [1,0,0] can be approximated by the patient space variogram such that the mean error between corresponding modality space and patient space variogram values is 1.6%. However, this does not imply that the rate of spatial variation change between corresponding modality space and patient space regions is equivalent. To the contrary, the modality space:patient space ratio of 2.40 indicates that modality space voxel pairs are 2.4 times less correlated than the corresponding patient space voxel pairs.

In general, the patient space and modality space normalized variogram curves are quite similar. Table 3-2, which lists the computed fractional errors for the phantom cube simulation, quantifies this observation. The observed maximum mean error of modality space variograms compared to their patient space counterparts is less than 8.3%. The average mean error is less than 4.3% with a standard deviation of less than 2.3%. In other words, the spatial correlation between modality space and patient space voxel values differs by an average of these observed values. Given the aliasing effects present in the patient space. The maximum weighted mean error is computed to be less than 11.6%, while the average weighted mean error is less than 6.3% with a standard deviation less than 3.4%.

Modality space:patient space ratios greater than 1.0 indicate an overall decrease in correlation between modality space voxels as compared to patient space voxels for a given separation distance. Nonetheless, the similarity between each pair of patient space and modality space variogram curves indicates that although pairs of voxels may exhibit less correlation in modality space than in patient space, the *change* in correlation as a function of separation distance tends to follow the same characteristic trend.

Table 3-2. Errors of modality space Phantom Cube Variograms

Cube Normalized Variogram Statistics			
OS Position	Direction	Mean Error	Weighted Mean Error
(4, 4, 4)	[1, 0, 0]	0.0163	0.0229
	[0, 1, 0]	0.0139	0.0189
	[0, 0, 1]	0.0367	0.0552
	[1, 1, 1]	0.0432	0.0603
	[-1, 1, 1]	0.0144	0.0232
	[-1, 1,-1]	0.0065	0.0084
	[1, 1,-1]	0.0671	0.0942
	[1, 1, 0]	0.0130	0.0180
	[-1, 1, 0]	0.0029	0.0039
	[0, 1, 1]	0.0460	0.0708
	[0, 1,-1]	0.0312	0.0426
	[1, 0, 1]	0.0454	0.0719
	[-1, 0, 1]	0.0383	0.0525
(60,60,60)	[1, 0, 0]	0.0371	0.0573
	[0, 1, 0]	0.0252	0.0386
	[0, 0, 1]	0.0375	0.0576
	[1, 1, 1]	0.0822	0.1151
	[-1, 1, 1]	0.0744	0.1063
	[-1, 1,-1]	0.0368	0.0489
	[1, 1,-1]	0.0749	0.1070
	[1, 1, 0]	0.0575	0.0928
	[-1, 1, 0]	0.0513	0.0704
	[0, 1, 1]	0.0551	0.0891
	[0, 1,-1]	0.0526	0.0722
	[1, 0, 1]	0.0720	0.1139
	[-1, 0, 1]	0.0791	0.1083
	mean	0.0427	0.0623
	max	0.0822	0.1151
	std dev	0.0229	0.0334

Visual inspection of Figure 3-12 through Figure 3-19 reveals that in 73% of the cases, the range at which minimal spatial dependency is reached is approximately the same for patient space and modality space. In the remaining 27% of the cases analyzed, the separation distance associated with minimal spatial dependency shifted by approximately one distance unit (directions specified by [1,1,1], [0,1,1] and [1,0,1] about coordinate (4,4,4) in Figure 3-12 and Figure 3-14; and by [1,1,1], [1,1,0], [0,1,1] and [1,0,1] about coordinate (60,60,60) in Figure 3-16 through Figure 3-18).

Since these results compare normalized variogram pairs, one cannot draw conclusions regarding the rate at which spatial dependency between modality space and patient space voxels change without considering the modality space:patient space normalization ratio. Even though a spatial regionalization exists and can be modeled, the modality space and patient space model parameters are different. Therefore, an interpolation method that optimizes its estimates based upon the spatial variation of modality space cannot, in general, generate estimates that are optimal with respect to patient space; optimality is satisfied with respect to modality space.

Phantom Sphere Simulation Results

The phantom cube had been processed through the MRI Scanner Distortion Model to analyze the modality space reconstruction of an object with spatial characteristics that facilitate differentiating distortive effects from naturally occurring characteristics. This simulation processed a dual medium phantom sphere. This phantom object has a smooth flowing, non-planar, yet well-defined surface that is more representative of an organ tissue surface than the previous phantom. The sphere is centered within the 130x130x130 patient space field of view. The outer radius of the sphere is 60 units while the radius of the concentric inner media is 40 units. The outer medium gray level intensity is 80% of the simulation maximum. The inner medium (for $r \leq 40$) gray level intensity is 40% of the simulation maximum. To anti-alias the inner and outer media surfaces of the patient space sphere, it is generated at twice the desired patient space resolution and is then downsampled by a factor of 2 using a local neighborhood averaging technique. A rendering of the patient space sphere (mapped to modality space coordinates) is shown in Figure 3-20. A cutaway rendition of the patient space sphere is shown in Figure 3-21.[2]

Figure 3-22 and Figure 3-23 depict how the dual media patient space volume is distorted in its modality space reconstruction. The modality space reconstruction of the patient space volume is rendered in Figure 3-22. A cutaway rendition of the modality space volume (similar to the patient space volume in Figure 3-21) is shown in Figure 3-23.

---

[2] The dark intensity edge observed at the intersection of the cutaway slice with the outer surface of the sphere is an anomaly of the visualization software.
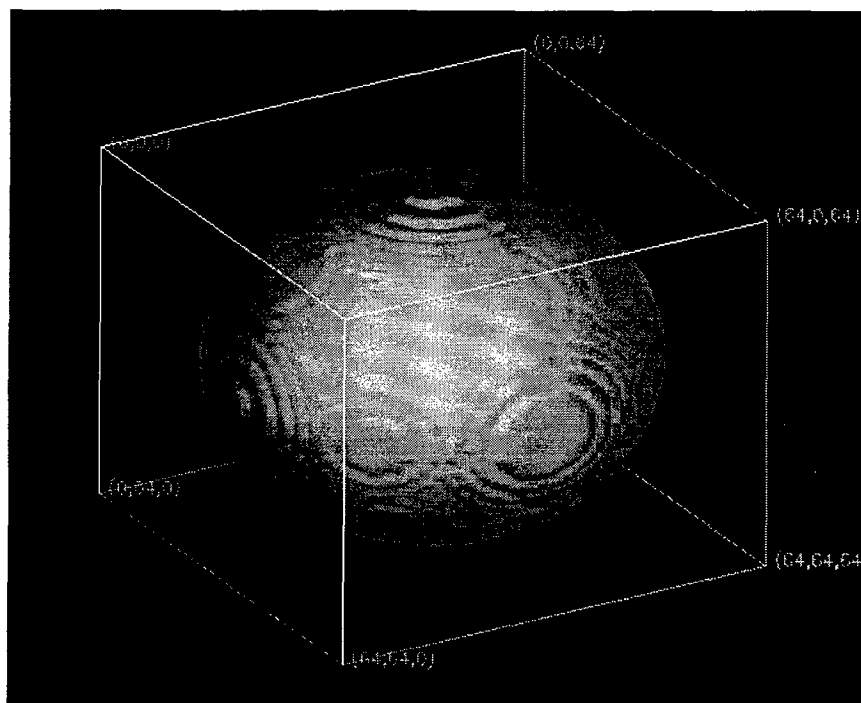
Figure 3-20. Patient Space Sphere
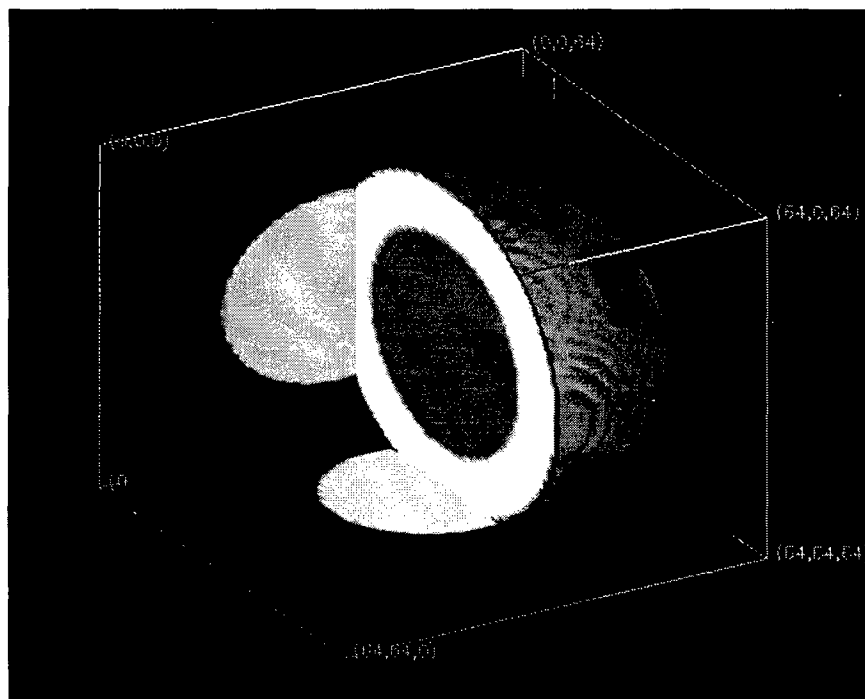
Figure 3-21. Patient Space Sphere Cutaway
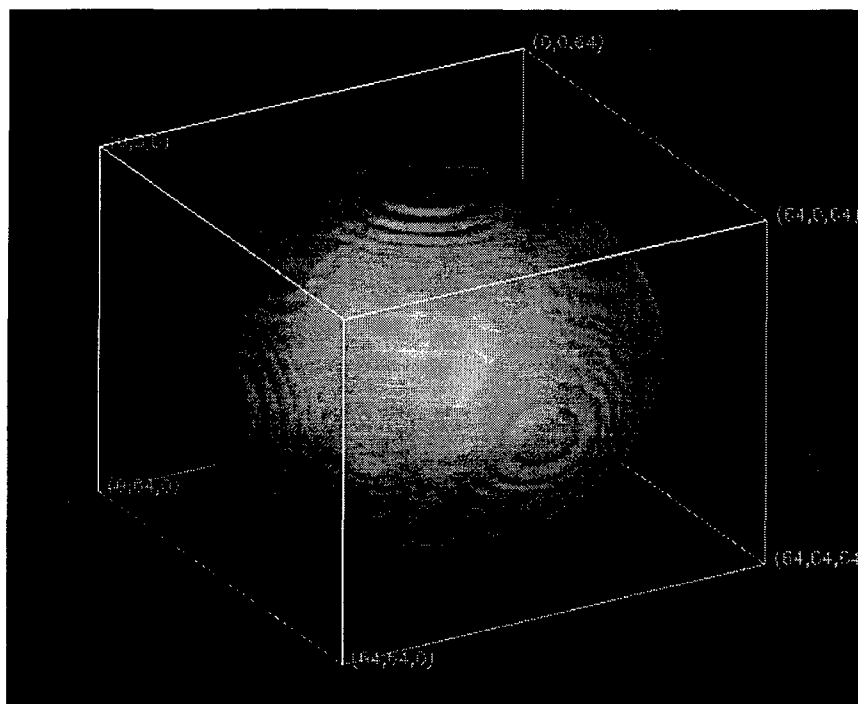
Figure 3-22. Modality Space Sphere
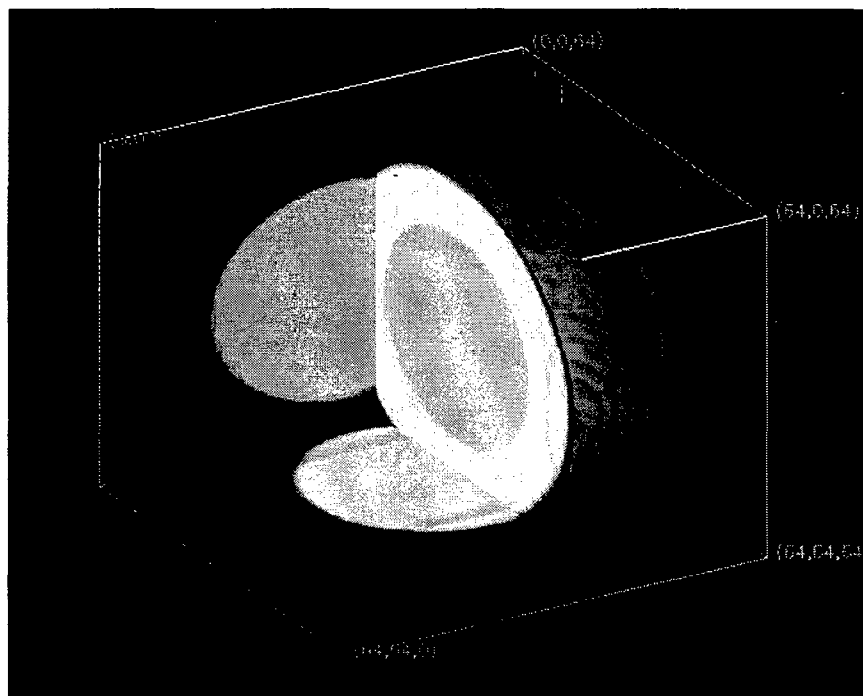
Figure 3-23. Modality Space Sphere Cutaway

Figure 3-24 through Figure 3-27 are obtained from analyzing the spatial variation about the modality space coordinate (18,18,32). This location is midway along the z axis of the volume and is in proximity to where the inner and outer media converge. It is intended to represent a point in patient space where two tissues meet. Figure 3-28 through Figure 3-31 are obtained from analyzing the spatial variation about the modality space coordinate (32,32,12). This location coincides with a voxel that lies on the outer surface of the sphere and also lies along a longitudinal axis that intersects the origin of the volume and is parallel to the z axis. It is intended to represent a point that lies near the surface of a patient space body, but is situated at the periphery of the scanner field of view.

Since thirteen directions about each identified point are analyzed, (the x, y, and z components of each direction given by the right triplet above each variogram plot, as shown in Figure 3-7), thirteen plots are provided for each point that is analyzed. (The x, y, and z modality space coordinates are given by the left triplet above each plot, as shown in Figure 3-7). Part A results depict the first four plots obtained about the given modality space coordinate; Part B results depict the second four plots; Part C the third four plots; and Part D the last, or thirteenth plot.

(18,18,32) , [1,0,0]

Mean Error: 0.019

Gamma

Voxel Distance * 1.000
MS:PS ratio = 0.286

(18,18,32) , [0,1,0]

Mean Error: 0.013

Gamma

Voxel Distance * 1.000
MS:PS ratio = 0.277

(18,18,32) , [0,0,1]

Mean Error: 0.14

Gamma

Voxel Distance * 1.000
MS:PS ratio = 0.189

(18,18,32) , [1,1,1]

Mean Error: 0.031

Gamma

Voxel Distance * 1.732
MS:PS ratio = 0.291
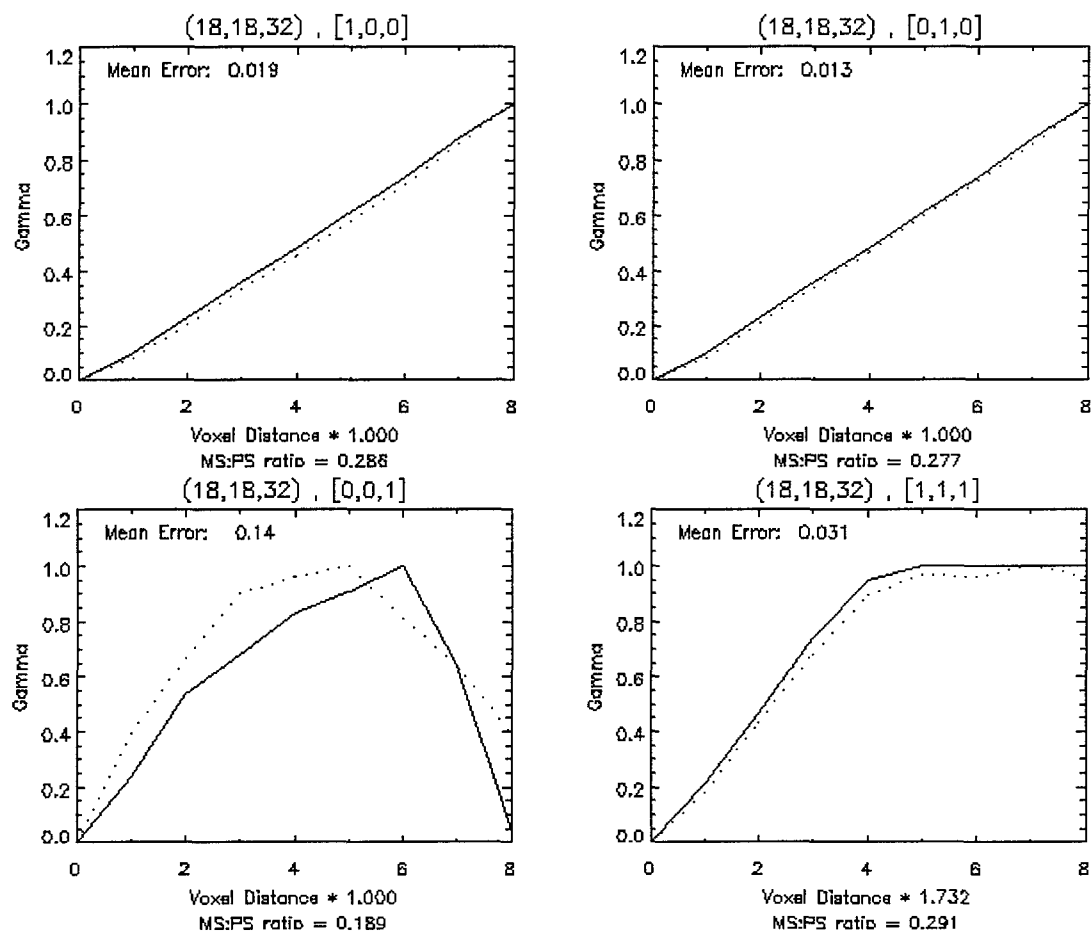
Figure 3-24. Phantom Sphere Variograms About (18,18,32), Part *A*
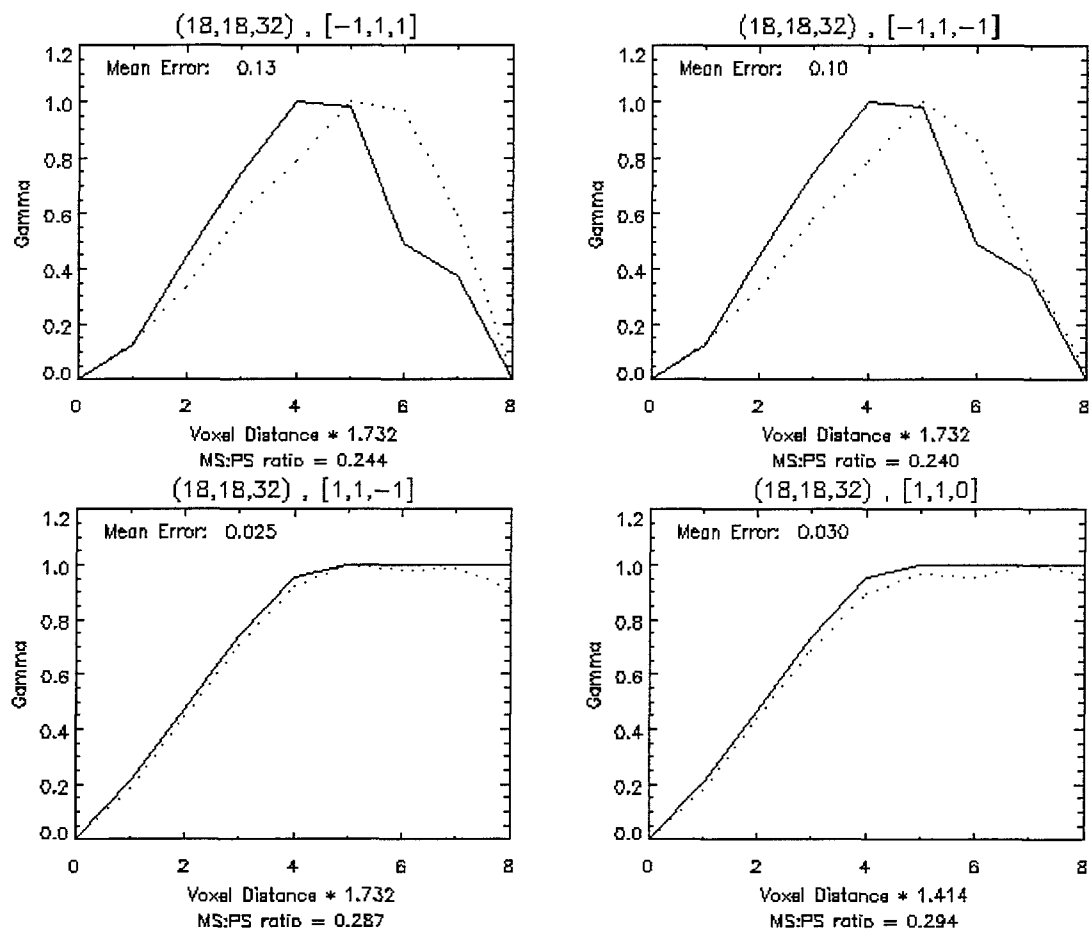
Figure 3-25. Phantom Sphere Variograms About (18,18,32), Part *B*
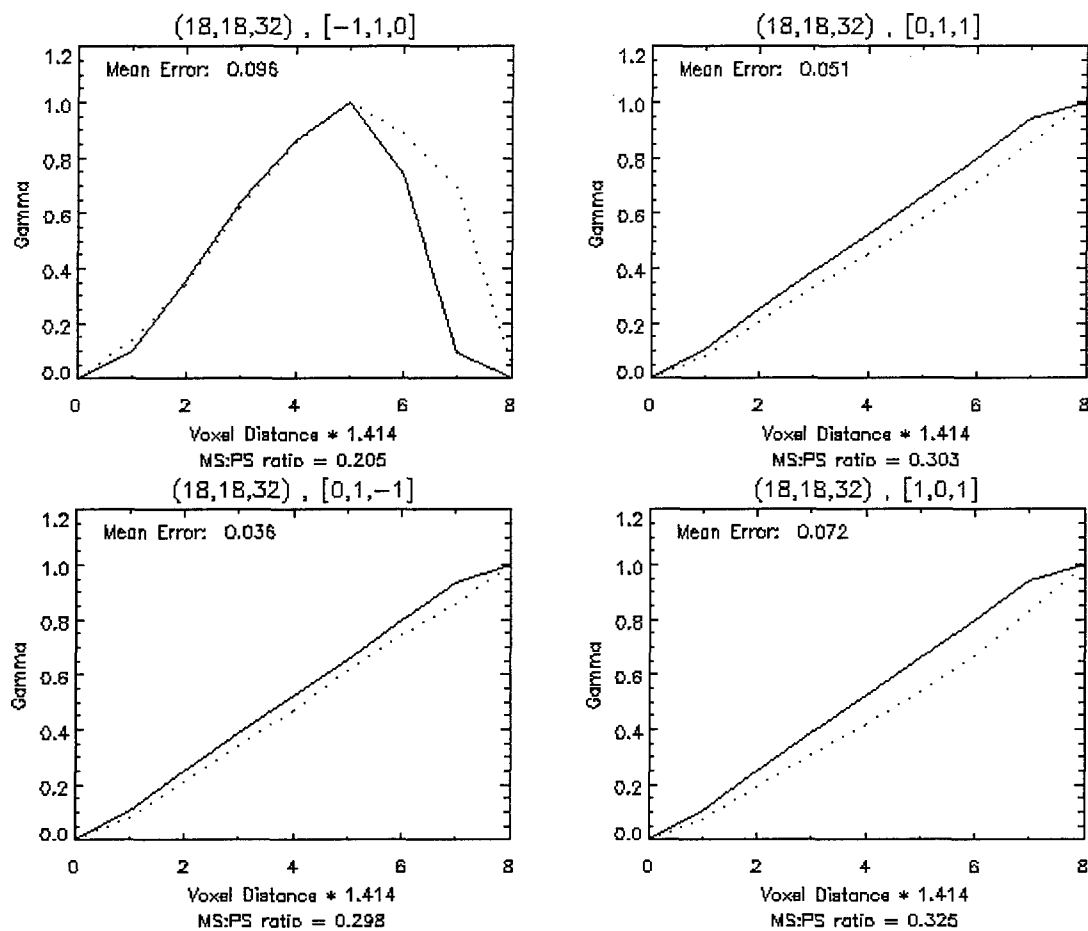
Figure 3-26. Phantom Sphere Variograms About (18,18,32), Part C
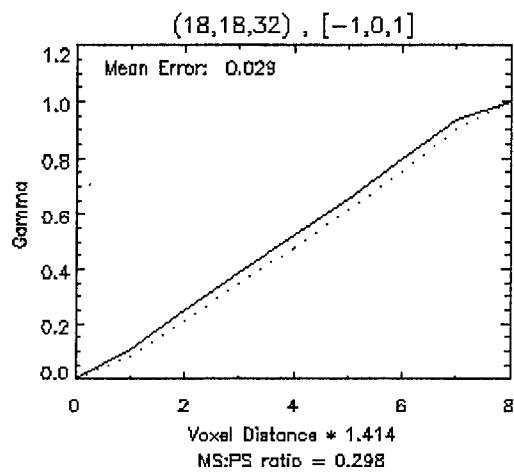
Figure 3-27. Phantom Sphere Variograms About (18,18,32), Part *D*
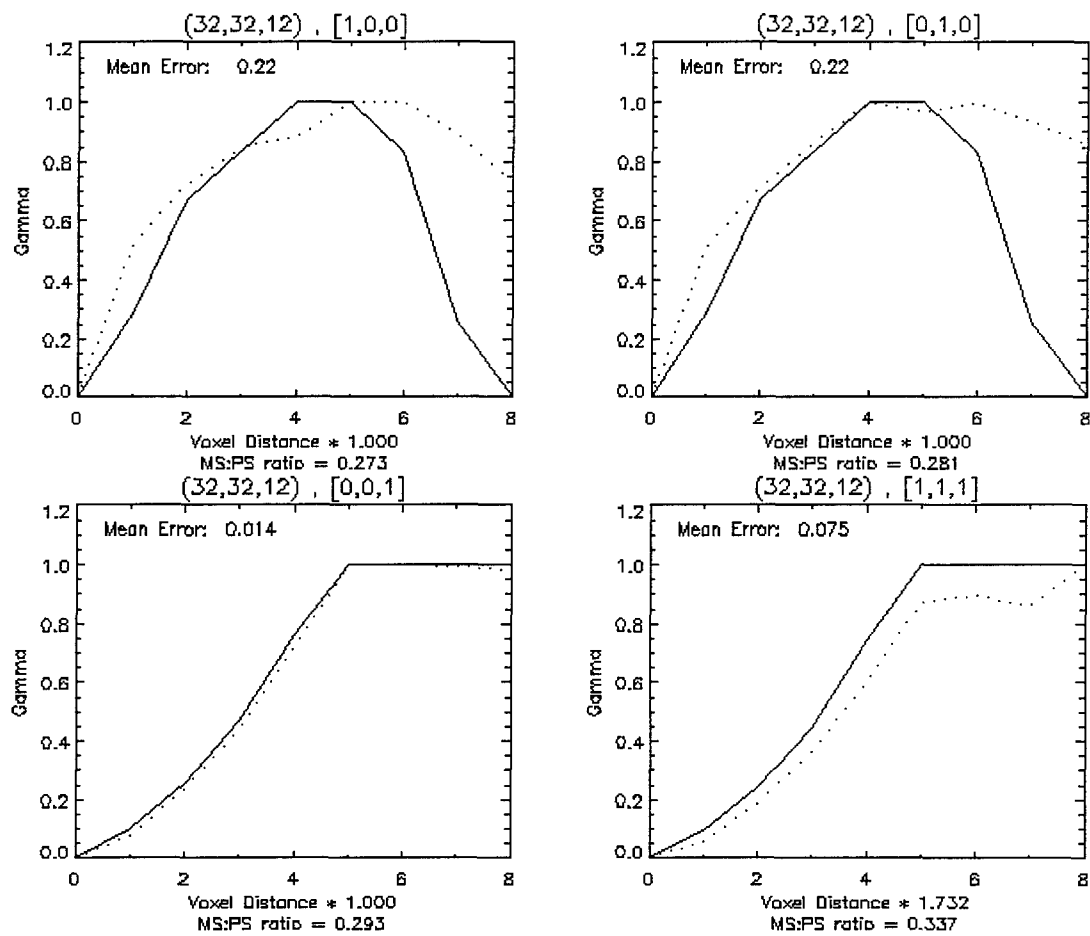
Figure 3-28. Phantom Sphere Variograms About (32,32,12), Part *A*
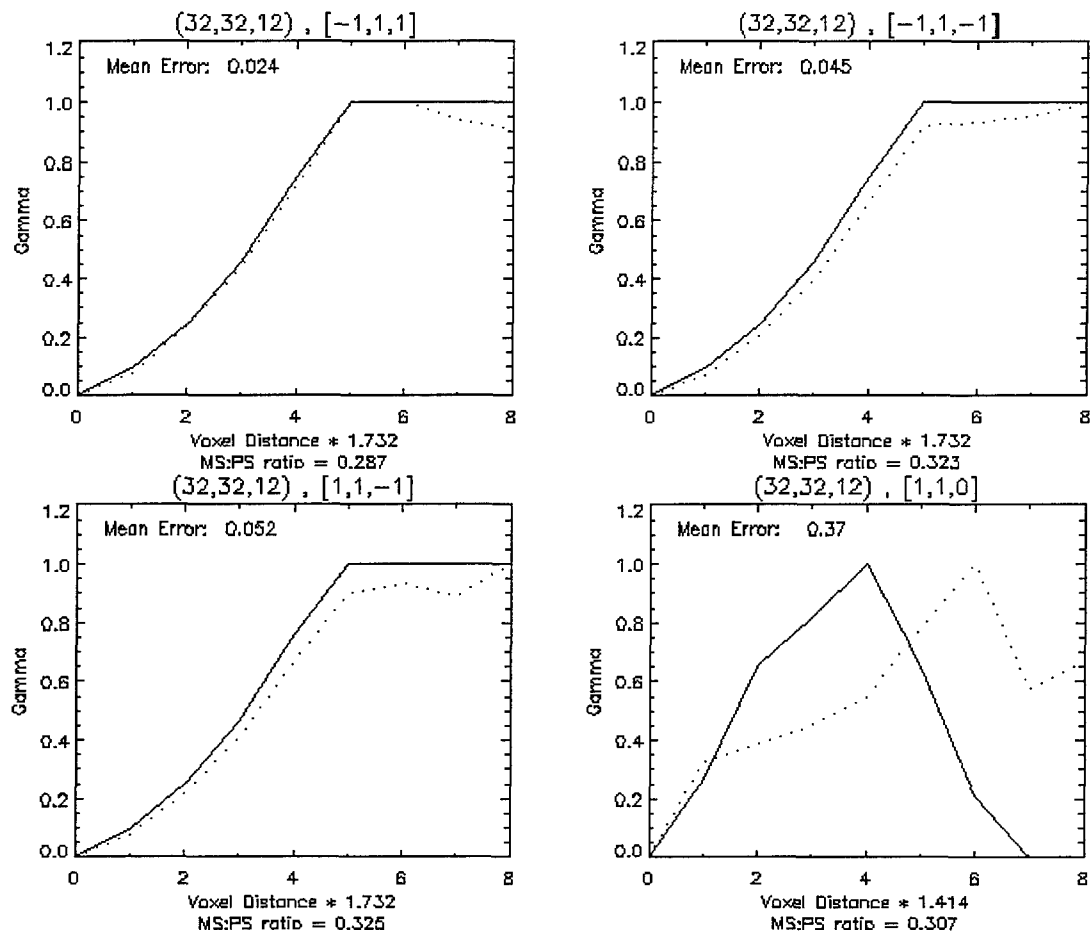
Figure 3-29. Phantom Sphere Variograms About (32,32,12), Part *B*
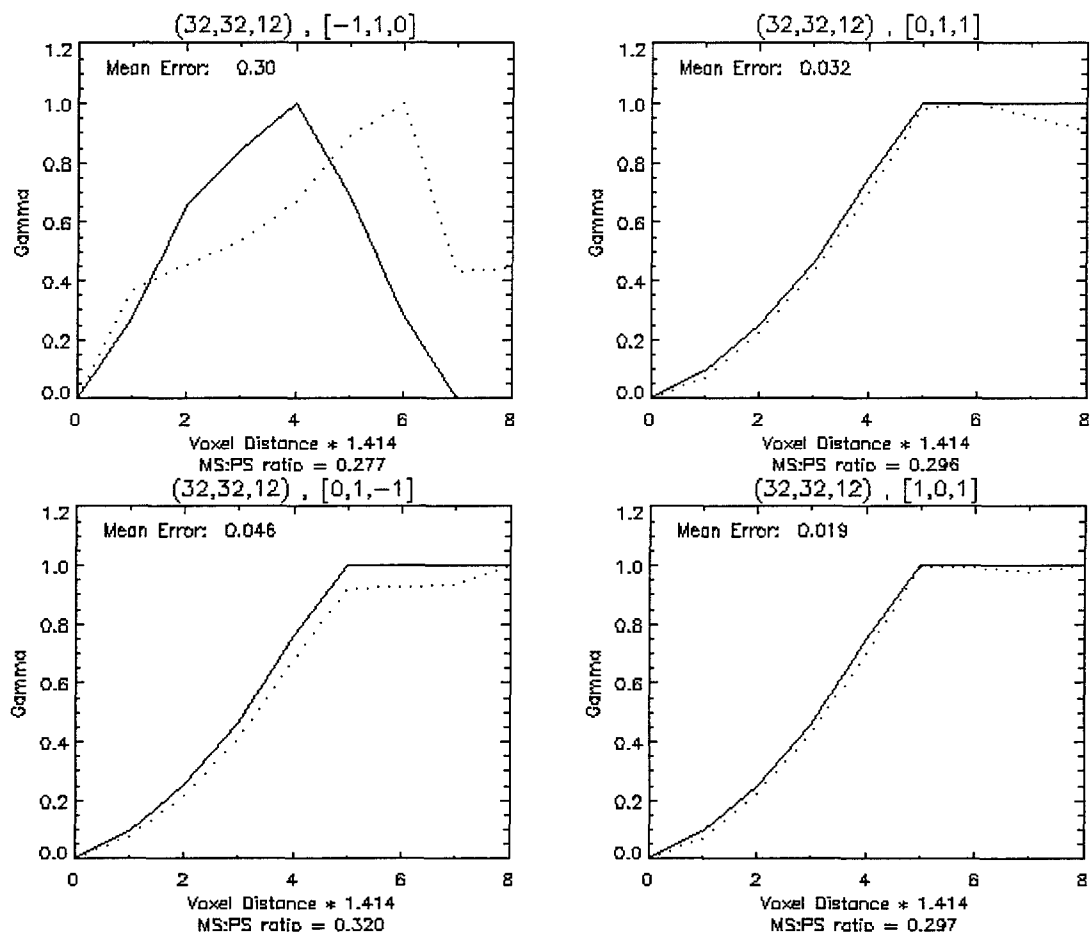
Figure 3-30. Phantom Sphere Variograms About (32,32,12), Part *C*
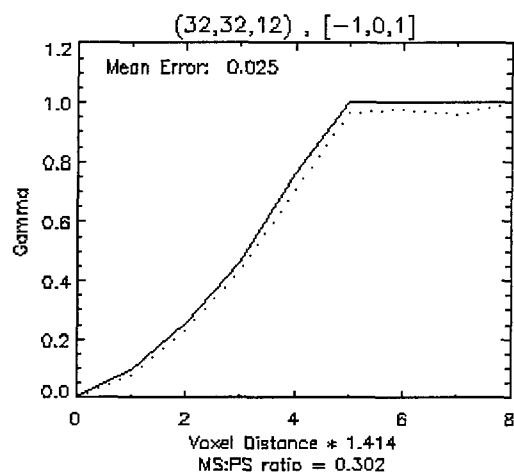
Figure 3-31. Phantom Sphere Variograms About (32,32,12), Part *D*

Table 3-3 is a compilation of the fractional errors observed in Figure 3-24 through Figure 3-31. The observed average mean error of modality space variograms compared to their patient space counterparts is less than 9.8%, while the average weighted mean error is less than 7.7%. The standard deviation of the average of the weighted mean errors is 23% less than the standard deviation of the average of the nonweighted errors. In all observed instances the weighted mean error is less than 30%.

Table 3-3. Errors of modality space Phantom Sphere Variograms

Sphere Normalized Variogram Statistics			
OS Position	Direction	Mean Error	Weighted Mean Error
(18,18,32)	[1, 0, 0]	0.1945	0.0241
	[0, 1, 0]	0.0129	0.0166
	[0, 0, 1]	0.1416	0.1519
	[1, 1, 1]	0.0308	0.0363
	[-1, 1, 1]	0.1328	0.1157
	[-1, 1,-1]	0.1042	0.1259
	[1, 1,-1]	0.0254	0.0246
	[1, 1, 0]	0.0299	0.0357
	[-1, 1, 0]	0.0962	0.0726
	[0, 1, 1]	0.0509	0.0510
	[0, 1,-1]	0.0361	0.0414
	[1, 0, 1]	0.0719	0.0696
	[-1, 0, 1]	0.0287	0.0351
(32,32,12)	[1, 0, 0]	0.2170	0.1510
	[0, 1, 0]	0.2246	0.1413
	[0, 0, 1]	0.1447	0.0194
	[1, 1, 1]	0.0752	0.0638
	[-1, 1, 1]	0.0244	0.0154
	[-1, 1,-1]	0.0451	0.0555
	[1, 1,-1]	0.0524	0.0512
	[1, 1, 0]	0.3682	0.2616
	[-1, 1, 0]	0.3038	0.2901
	[0, 1, 1]	0.0318	0.0290
	[0, 1,-1]	0.0457	0.0531
	[1, 0, 1]	0.0190	0.0275
	[-1, 0, 1]	0.0252	0.0298
	mean	0.0974	0.0765
	max	0.3682	0.2901
	std dev	0.0926	0.0710

Though these results may be hastily interpreted to suggest that the distortion experienced upon an object is a function of its shape, one is cautioned against drawing this premature conclusion. Different modality space locations were analyzed for each simulation trial. Furthermore, too few points were analyzed for each phantom object to compare the results of one to those of the other.

There are phantom sphere results that are, in general, similar to those results observed for the phantom cube. Though the magnitude of the spatial correlation may be significantly different between each modality space and patient space analysis, (indicated by non-unity modality space:patient space ratios for each variogram pair that is plotted), the change in spatial dependency between voxels of a given separation distance tends to adhere to the same continuous model.

The most significant tabulated errors occurred when spatially analyzing the region about modality space coordinate (32,32,12) for the directions specified by the vectors [1,0,0], [0,1,0], [1,1,0] and [-1,1,0]. These results are plotted in Figure 3-28 through Figure 3-30. Each of these cases depict a modality space variogram curve that appears warped compared to the corresponding patient space variogram curve. That is, at some separation distance the normalized modality space variogram exhibits a spatial dependency that is maintained longer than observed on the corresponding patient space variogram curve, but then at some larger separation distance again approximately follows the trend of the patient space variogram curve. In spite of this lag, characteristics of the patient space variogram curve can be recognized in the associated modality space variogram curve. Note that although the errors between the normalized patient space and modality space variogram curves are greatest for the four directions (specified by the directional vectors [1,0,0], [0,1,0], [-1,1,0] and [1,1,0]), the minimum

correlation exhibited by modality space voxels is approximately 40 to 90 times greater than that exhibited by modality space voxels along the other nine directions analyzed. The maximum modality space variogram values for each direction analyzed about the point (32,32,12) are used to compute this statistic and are given in Table 3-4.

Table 3-4.　　Modality Space Sphere
Variogram Values

Modality Space Sphere Variogram Values		
OS Position	Direction	Max Value
(32,32,12)	[1, 0, 0]	586
	[0, 1, 0]	603
	[0, 0, 1]	49290
	[1, 1, 1]	56584
	[-1, 1, 1]	48235
	[-1, 1,-1]	54241
	[1, 1,-1]	54714
	[1, 1, 0]	1192
	[-1, 1, 0]	1015
	[0, 1, 1]	49679
	[0, 1,-1]	53745
	[1, 0, 1]	49969
	[-1, 0, 1]	50700

In all cases observed, the modality space:patient space ratio is less than 1.0 for simulation trials of the phantom sphere. This tends to indicate an overall increase in correlation between modality space voxels compared to patient space voxels for a given separation distance. Recall that he modality space:patient space ratio was greater than 1.0 for simulation trials of the phantom cube. Once again, conclusions should not be hastily drawn; that is, the modality space:patient space ratio is not to be concluded to be a function of simply the shape of the scanned object. Other factors, such as the inhomogeneity and nonlinearity of the (simulated) magnetic fields that coincide with

each analyzed location, must be considered. Assessing these relationships is beyond the scope of this effort and is therefore not investigated further.

The primary objective of these simulations has been to determine whether or not MRI modality space volumes exhibit regions of spatial dependency whose variation and extent can be modeled using regionalized variables. Thus far, phantom cube and phantom sphere simulation results satisfy the primary objective and support the conclusion that MRI modality space data can be represented using regionalized variables.

In spite of the change in absolute correlation between patient space and modality space, visual inspection of Figure 3-24 through Figure 3-31 reveals that in all but six instances the range at which minimal spatial dependency is reached is approximately the same for patient space and modality space. For the six exceptions, four instances indicate a shift of approximately 1 distance unit (directions specified by [0,0,1], [-1,1,1] and [-1,1,-1] about coordinate (18,18,32) observed in Figure 3-24 and Figure 3-25; and by [1,1,0] about coordinate (32,32,12) observed in Figure 3-29), and 2 instances indicate a shift of approximately 2 distance units (directions specified by [1,1,0] and [-1,1,0] about coordinate (32,32,12) observed in Figure 3-29 and Figure 3-30).

As previously stated with regard to the phantom cube simulation results, it is evident that spatial regionalization exists in the reconstructed modality space phantom sphere volume. However, in the cases where the patient space and modality space normalized variogram curves significantly differ, an interpolation method that is based upon the spatial variation of modality space can only estimate voxel values that are consistent with the distorted modality space. It is not an objective of this research to correct scanner-induced distortion. Rather, the objective of this research is to minimize

interpolation-induced distortion. Cases in which the modality space-patient space variogram pairs (plotted in the figures in this chapter) differ significantly from one another indicate instances when significant scanner-induced distortion errors can occur, even when modality space is reconstructed using an optimal interpolation technique.

Phantom Crosshatch Simulation Results

This simulation processes a phantom crosshatch that is aligned with the three cartesian coordinate axes and occurs every 40 units along the x and y axes of the patient space field of view and extends along the entire z axis. Each crosshatch is 1 unit wide in the x and y dimensions, thereby simulating a patient space feature that is smaller (in two dimensions) than the modality space voxel. Each patient space crosshatch has a gray level intensity that is 60% of the simulation maximum. The 130x130x130 patient space field of view maps to a 65x65x65 modality space field of view.

This phantom simulation was conducted to analyze the spatial variation of objects such as capillaries, whose dimension along one axis is small relative to the resolution of the scanning device, and along another axis, extensive. The patient space crosshatch is rendered in Figure 3-32. Figure 3-34 and Figure 3-36 are cutaway views of an xy plane transaxial slice and an xz plane coronal slice of mid regions of the patient space volume, respectively. Figure 3-33, Figure 3-35 and Figure 3-37 are the corresponding modality space renderings the previous patient space renditions. Note how the intensity of each crosshatch line in the modality space cutaway views (Figure 3-35 and Figure 3-37) is reduced due to the regional spatial averaging that accompanies the simulated nuclei rf emissions. Figure 3-38 shows the nonuniform distortion that is evident in modality space xy transaxial slices that exist at extremes of the field of view.
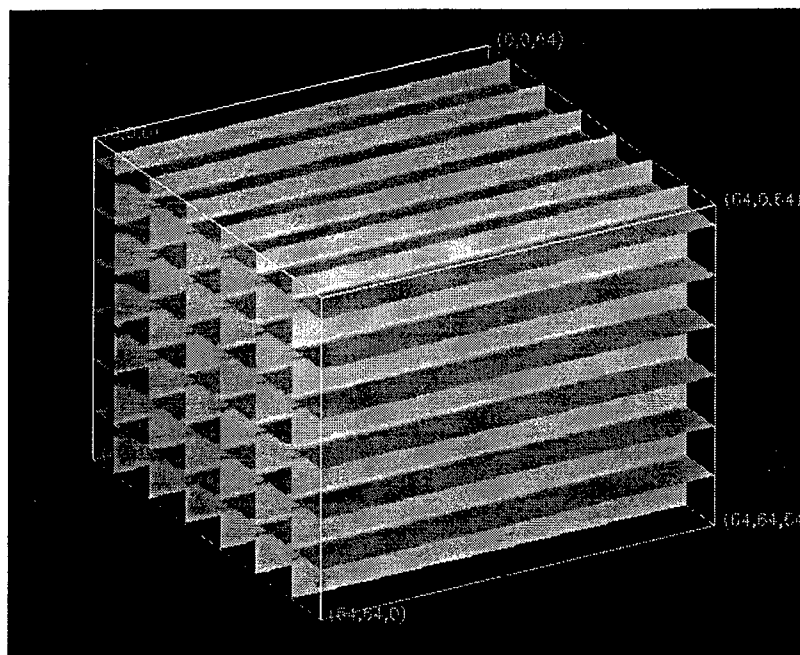
Figure 3-32.   Patient Space Crosshatch
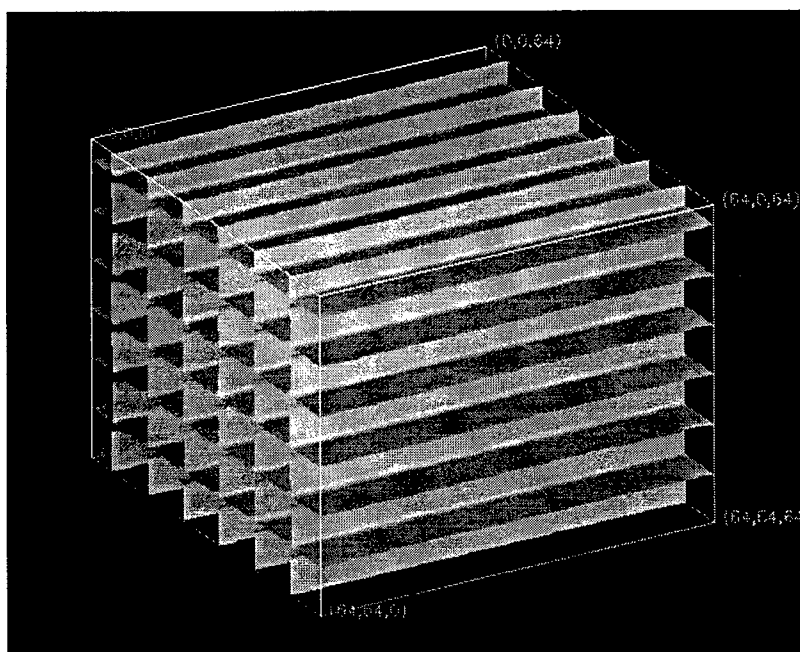
Figure 3-33.   Modality Space Crosshatch
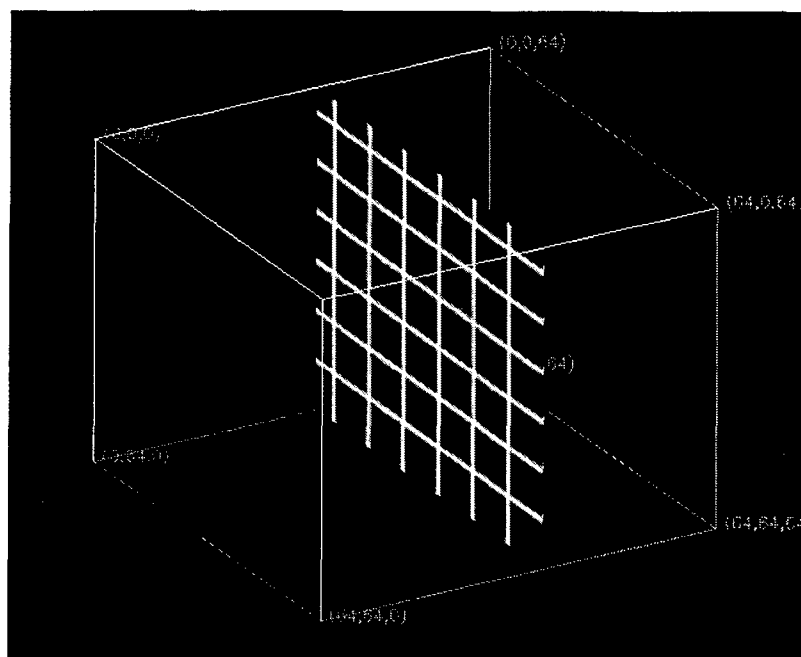
Figure 3-34. Patient Space Crosshatch
XY Cutaway
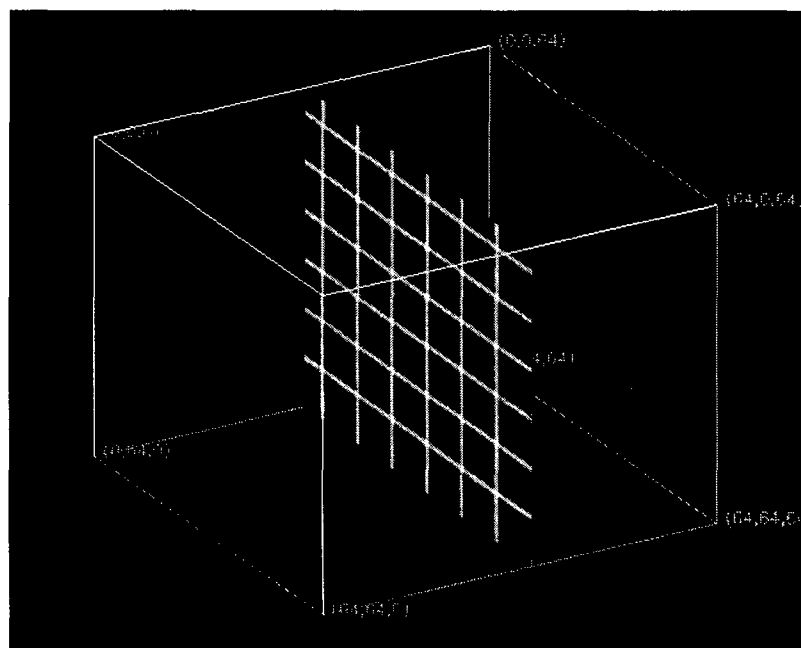
Figure 3-35. Modality Space Crosshatch
XY Cutaway
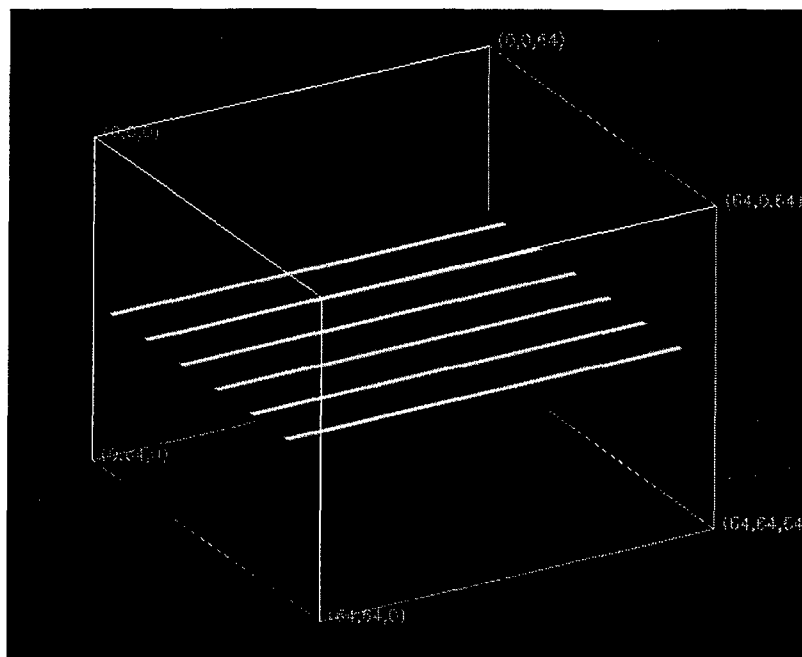
Figure 3-36.   Patient Space Crosshatch
XZ Cutaway
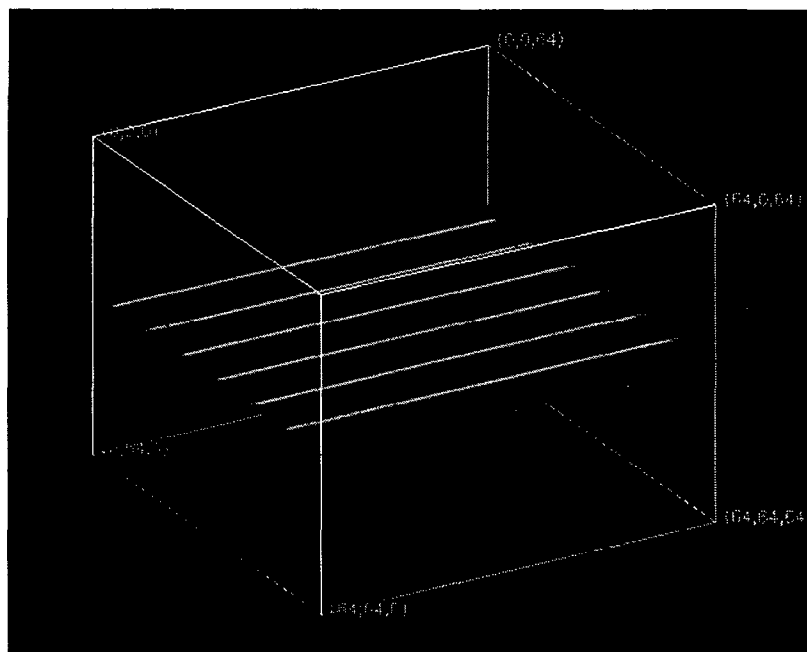
Figure 3-37.   Modality Space Crosshatch
XZ Cutaway

3-54
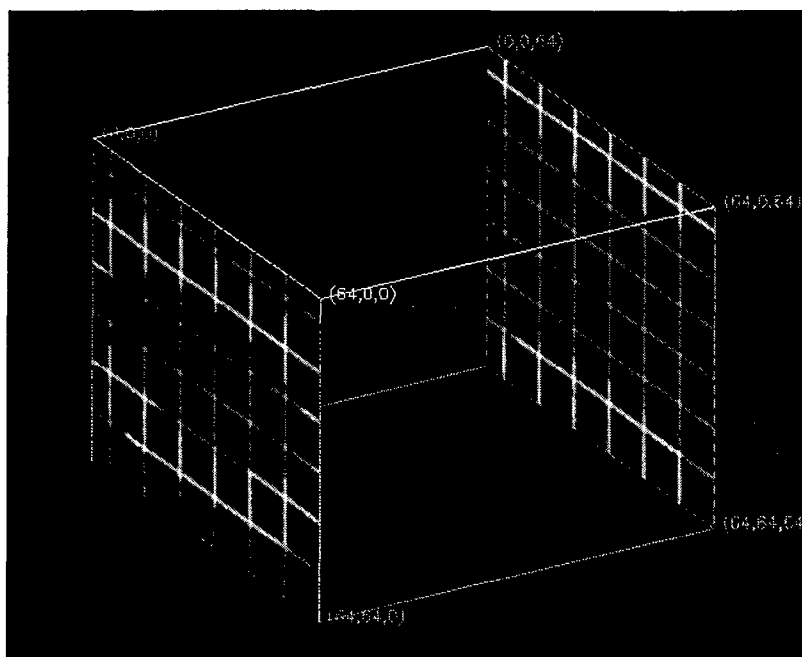
Figure 3-38. Modality Space Crosshatch
XY Cutaways

Since thirteen directions about each identified point are analyzed, (the x, y, and z components of each direction given by the right triplet above each variogram plot, as shown in Figure 3-7), thirteen plots are provided for each point that is analyzed. (The x, y, and z modality space coordinates are given by the left triplet above each plot, as shown in Figure 3-7). Part A results depict the first four plots obtained about the given modality space coordinate; Part B results depict the second four plots; Part C the third four plots; and Part D the last, or thirteenth plot.

Figure 3-39 through Figure 3-42 are normalized patient space and modality space variograms that are obtained by analyzing the spatial variation of the phantom volume about the modality space coordinate (4,4,4). Figure 3-43 through Figure 3-46 are obtained by analyzing the spatial variation about the modality space coordinate (18,18,32) which is midway along the longitudinal z axis of the phantom volume. These locations were arbitrarily chosen to coincide with coordinates selected in the phantom

cube and sphere simulations. Note the flat modality space variogram (Gamma(h) = 0.0) for the direction specified by the vector [0,0,1], (reference Figure 3-39). This is anticipated since all patient space phantom crosshatch voxel values along a direction parallel to the z axis have the same value for all separation distances.
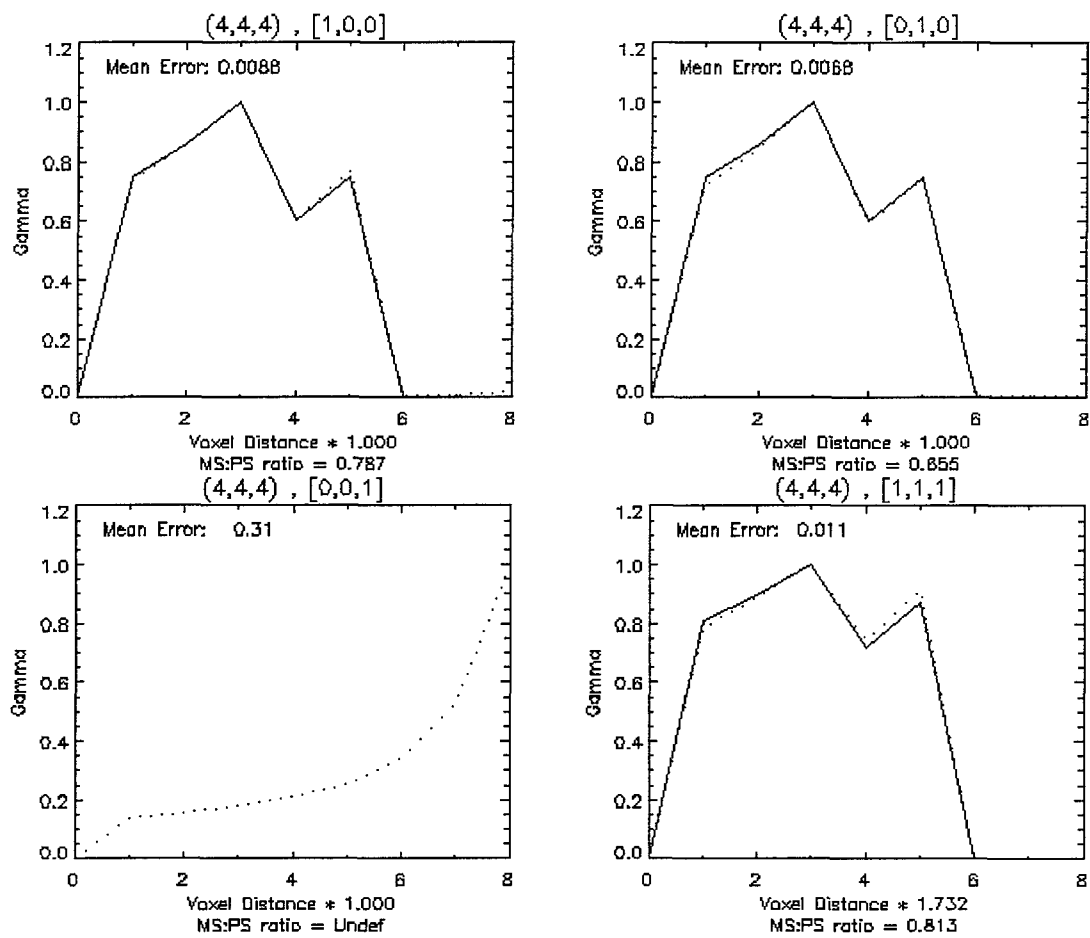
Figure 3-39. Phantom Crosshatch Variograms About (4,4,4), Part *A*
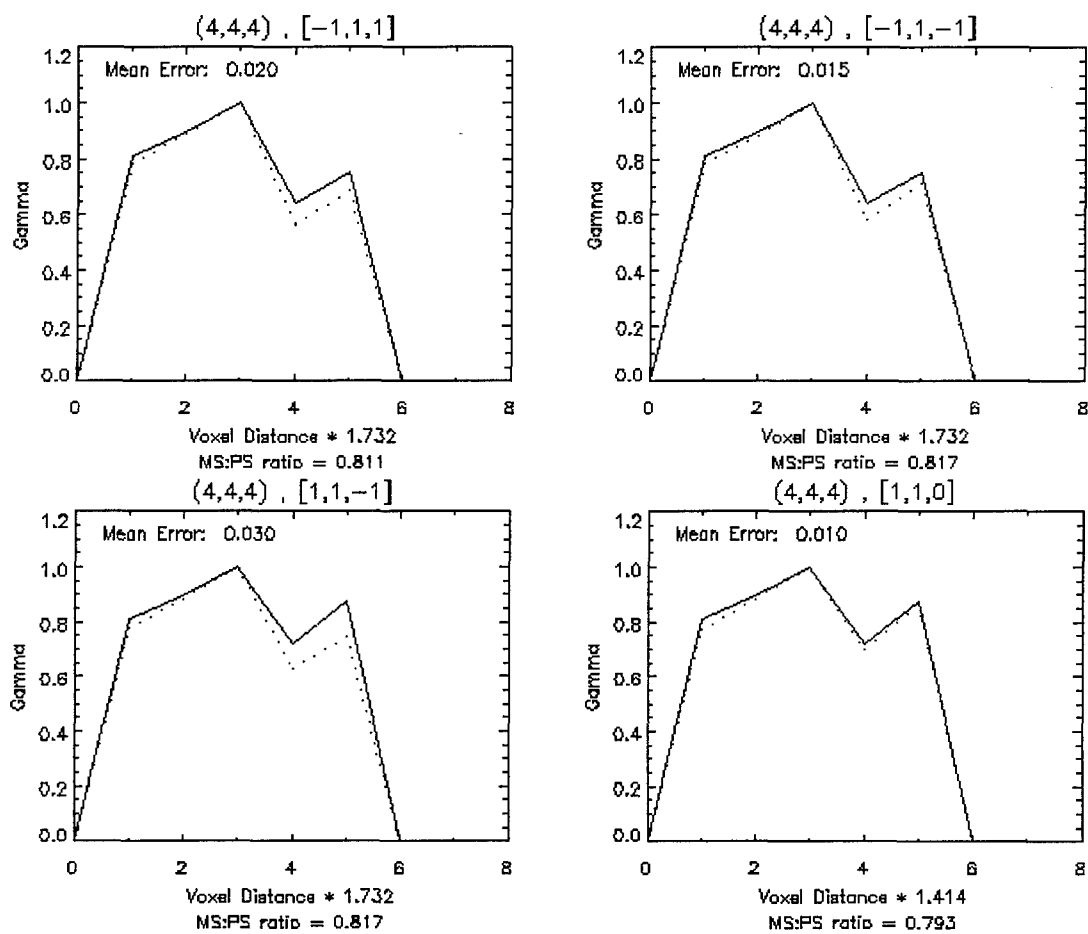
Figure 3-40. Phantom Crosshatch Variograms About (4,4,4), Part *B*
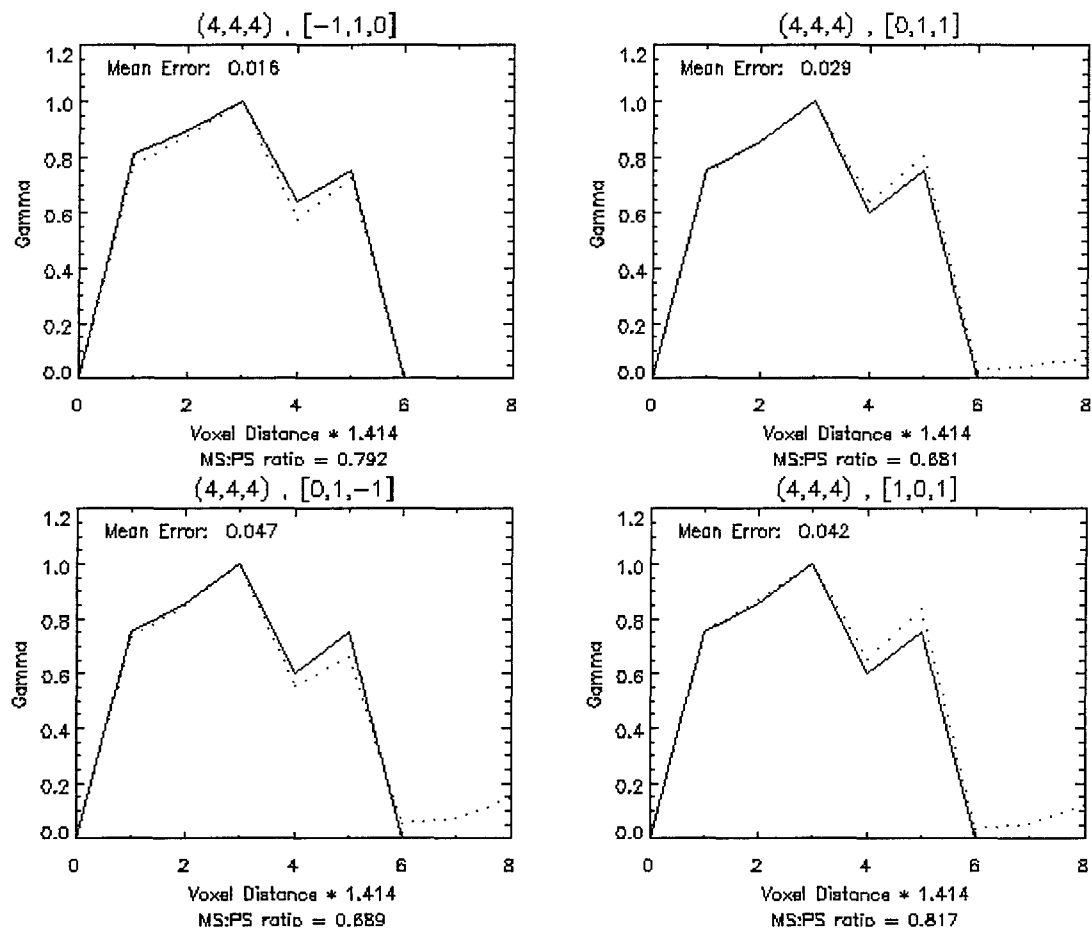
Figure 3-41. Phantom Crosshatch Variograms About (4,4,4), Part C
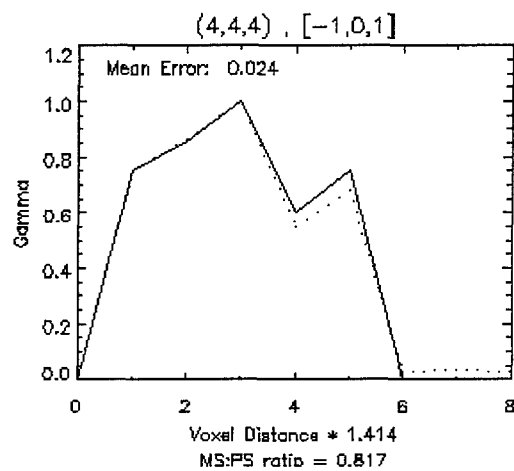
Figure 3-42. Phantom Crosshatch Variograms About (4,4,4), Part D
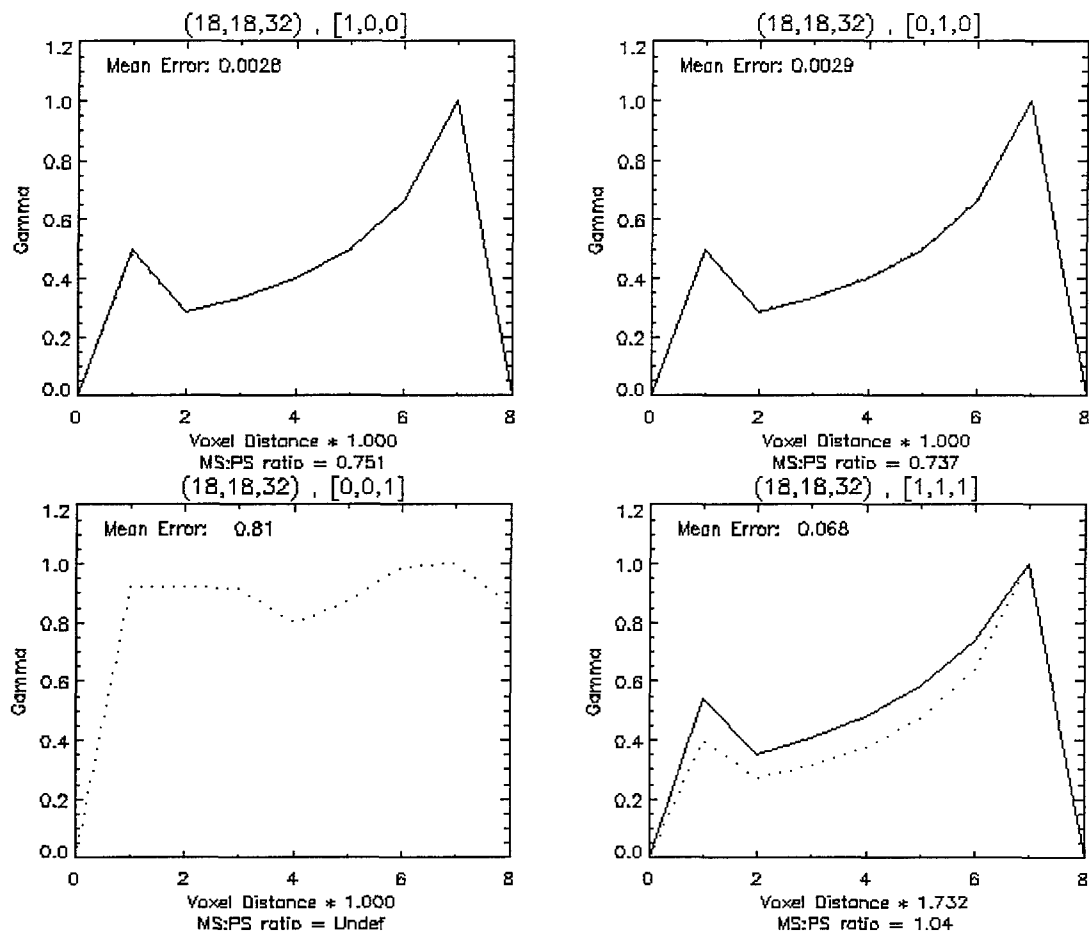
Figure 3-43. Phantom Crosshatch Variograms About (18,18,32), Part *A*
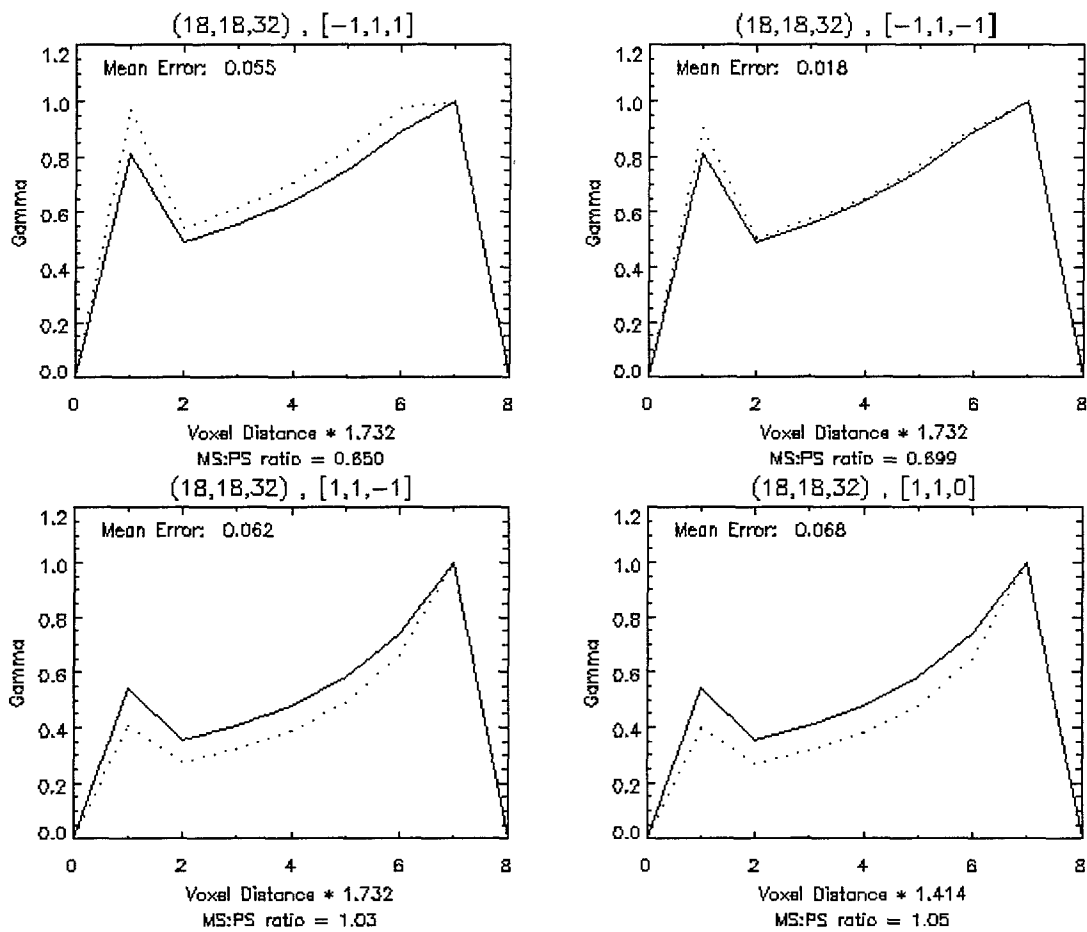
Figure 3-44. Phantom Crosshatch Variograms About (18,18,32), Part B
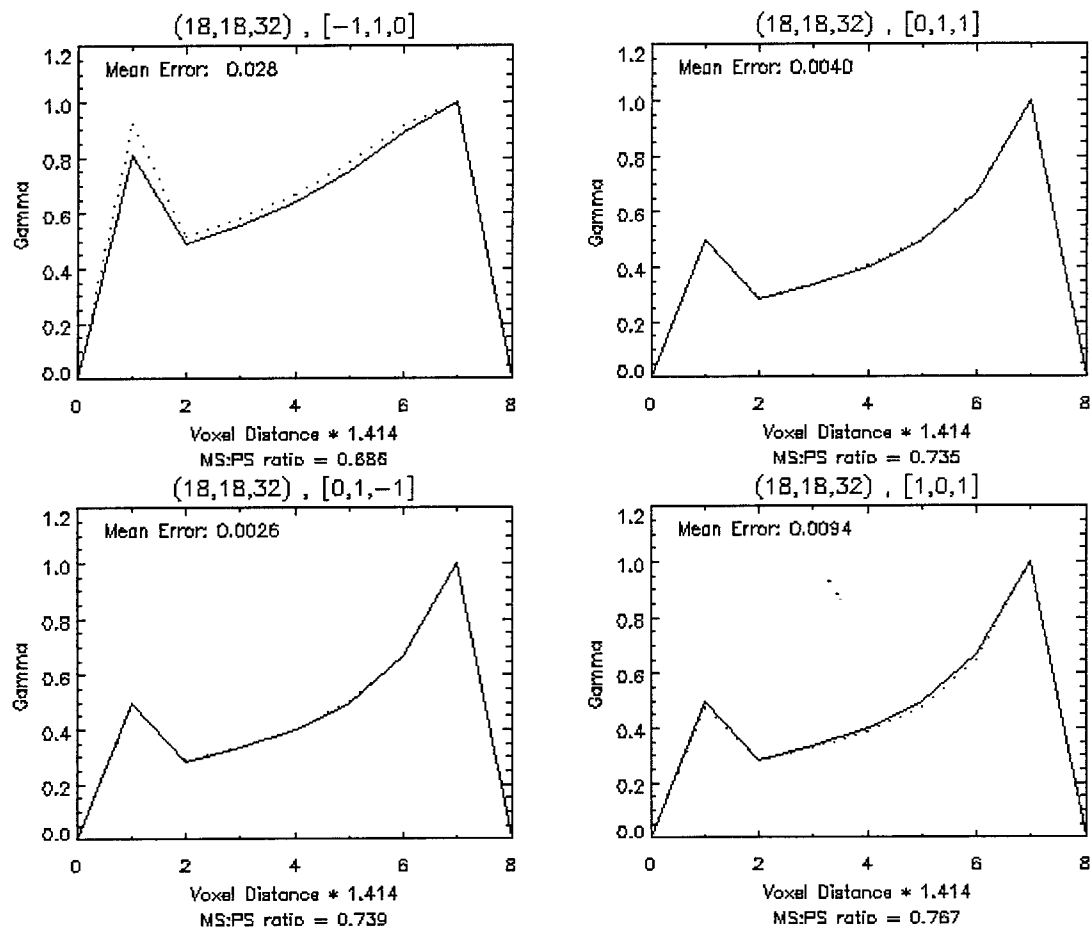
Figure 3-45. Phantom Crosshatch Variograms About (18,18,32), Part C
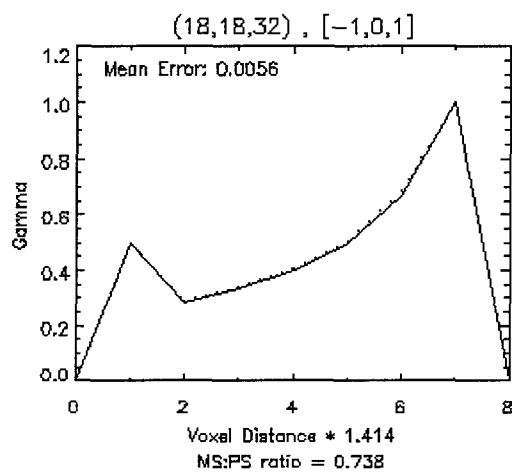
Figure 3-46. Phantom Crosshatch Variograms About (18,18,32), Part D

Table 3-5 is a compilation of the fractional errors observed in Figure 3-39 through Figure 3-46. The average mean error of modality space variograms compared to the corresponding patient space variograms is less than 6.6% and the average weighted mean error is less than 7.3%. These values are biased by variogram values computed for directions that are parallel to the z axis (specified by the directional vector [0,0,1]). Along this direction the patient space variogram curve is flat with a constant value of 0 for all separation distances within the field of view. No change in intensity is observed along this direction. Therefore, the patient space variogram cannot be normalized using as a factor the maximum value of the given variogram curve. As a result, mean and weighted mean errors are not indicative of the similarity or dissimilarity between the modality space and patient space variogram curves.

In response, two actions were taken. First, the crosshatch error statistics were recomputed excluding the effects observed in directions that are parallel to the z axis (specified by the directional vector [0,0,1]). These results are listed in Table 3-6. Second, to obtain insight to the absolute degree of correlation between the spatial variation in modality space and patient space for any given direction, the modality space normalization factor that is used to obtain modality space normalized variogram values is provided. It is labeled as the *MS Max Value* in Table 3-6.

From the table it is evident that the data represented by the normalized modality space variograms that are computed for directions parallel to the z axis are significantly more correlated than for all other directions plotted. When comparing the modality space normalization factors (represented by the column *MS Max Value* in Table 3-6), it can be seen that the factors for directions that are parallel to the z axis are

Table 3-5. Errors of modality space Phantom Crosshatch Variograms

Crosshatch Normalized Variogram Statistics			
OS Position	Direction	Mean Error	Weighted Mean Error
(4, 4, 4)	[1, 0, 0]	0.0088	0.0083
	[0, 1, 0]	0.0068	0.0088
	[0, 0, 1]	0.3116	0.2340
	[1, 1, 1]	0.0109	0.0164
	[-1, 1, 1]	0.0201	0.0263
	[-1, 1,-1]	0.0150	0.0196
	[1, 1,-1]	0.0297	0.0365
	[1, 1, 0]	0.0104	0.0204
	[-1, 1, 0]	0.0164	0.0228
	[0, 1, 1]	0.0289	0.0150
	[0, 1,-1]	0.0470	0.0373
	[1, 0, 1]	0.0417	0.0214
	[-1, 0, 1]	0.0242	0.0239
(18,18,32)	[1, 0, 0]	0.0028	0.0040
	[0, 1, 0]	0.0029	·0.0039
	[0, 0, 1]	0.8081	0.9051
	[1, 1, 1]	0.0684	0.1078
	[-1, 1, 1]	0.0553	0.0865
	[-1, 1,-1]	0.0184	0.0236
	[1, 1,-1]	0.0619	0.0944
	[1, 1, 0]	0.0684	0.1045
	[-1, 1, 0]	0.0279	0.0395
	[0, 1, 1]	0.0040	0.0051
	[0, 1,-1]	0.0026	0.0031
	[1, 0, 1]	0.0094	0.0126
	[-1, 0, 1]	0.0056	0.0065
	mean	0.0657	0.0726
	max	0.8081	0.9051
	std dev	0.1597	0.1737

Table 3-6. Errors of modality space Phantom Crosshatch Variograms

Crosshatch Normalized Variogram Error Statistics (Excludes [0,0,1] Entries)				
OS Position	Direction	Mean Error	Weighted Mean Error	MS Max Value
(4, 4, 4)	[1, 0, 0]	0.0088	0.0083	87,866
	[0, 1, 0]	0.0068	0.0088	73,167
	[0, 0, 1]	******	******	15,994
	[1, 1, 1]	0.0109	0.0164	153,180
	[-1, 1, 1]	0.0201	0.0263	152,806
	[-1, 1,-1]	0.0150	0.0196	153,961
	[1, 1,-1]	0.0297	0.0365	153,958
	[1, 1, 0]	0.0104	0.0204	149,430
	[-1, 1, 0]	0.0164	0.0228	149,334
	[0, 1, 1]	0.0289	0.0150	76,093
	[0, 1,-1]	0.0470	0.0373	76,997
	[1, 0, 1]	0.0417	0.0214	91,234
	[-1, 0, 1]	0.0242	0.0239	91,253
(18,18,32)	[1, 0, 0]	0.0028	0.0040	125,910
	[0, 1, 0]	0.0029	0.0039	123,549
	[0, 0, 1]	******	******	223
	[1, 1, 1]	0.0684	0.1078	293,733
	[-1, 1, 1]	0.0553	0.0865	122,493
	[-1, 1,-1]	0.0184	0.0236	131,820
	[1, 1,-1]	0.0619	0.0944	290,019
	[1, 1, 0]	0.0684	0.1045	295,584
	[-1, 1, 0]	0.0279	0.0395	129,219
	[0, 1, 1]	0.0040	0.0051	123,110
	[0, 1,-1]	0.0026	0.0031	123,841
	[1, 0, 1]	0.0094	0.0126	128,561
	[-1, 0, 1]	0.0056	0.0065	123,584
	mean	0.0245	0.0312	142,529
	max	0.0684	0.1078	
	std dev	0.0210	0.0319	62,247

approximately 1-3 orders of magnitude less than the average modality space normalization factor for all other directions.

Not incorporating error computations for directions parallel to the z axis, (from Table 3-6) the average mean error of modality space normalized variograms compared to their corresponding patient space variograms is less than 2.5% with a standard deviation of 2.1%. The average weighted mean error is less than 3.2% with a standard deviation of less than 3.2%. These results indicate, for the points that have been evaluated, that the secondary objective of this research is satisfied; that is, the modality space representation of the scanned patient space volume does exhibit spatially regionalized characteristics that are similar to those in patient space.

In all cases observed, the modality space:patient space normalization ratio (for directions for which it can be defined) lies between 0.65 and 1.05. In only 3 of 24 cases is the ratio greater than 1. This indicates that in the majority of cases, modality space voxels tend to be slightly more correlated than patient space voxels of the same separation distances. Visual observation of Figure 3-39 through Figure 3-46 reveals the range of spatial dependency associated for the 24 cases is approximately the same in modality space as it is in patient space.

Even though the variograms that have been computed for the phantom crosshatch simulation trials are more complex in terms of the model order required to represent them than those observed for the phantom cube or phantom sphere simulations, in general, the results satisfy the primary objective of the simulations. That is, modality space MRI volumes can be represented using regionalized variables modeled by continuous, deterministic functions.

Concluding MRI Data Can Be Represented Using Regionalized Variables

As stated earlier, the primary purpose for MRI scanner modeling was to process patient space phantom objects using the model to obtain distorted modality space representations of the phantoms that are consistent with typical scanner field nonuniformities so that it can be determined if MRI modality space volumes can be represented using regionalized variables. If this is true, kriging can be applied to modality space data to compute minimal error, interpolated representations of the MRI data.

This chapter provides the empirical results obtained from processing three different three-dimensional phantom patient space objects through the MRI Scanner Distortion Model. Each phantom object is subject to the same simulated fields effects of an MRI scanner and a modality space reconstruction is generated for each simulation trial. A spatial analysis is conducted for both the patient and modality space volumes for a small sampling of identical points within each volume along thirteen noncomplimentary directions. The locations of the patient and modality space points are chosen to lie in close proximity to regions of each volume where surfaces of each phantom are known to exist, knowing that voxels about these locations would prove to be the most difficult to interpolate accurately using an interpolator that bases its prediction upon the spatially regionalized characteristics of the surrounding data.

None of the cases analyzed revealed random or nondeterministic patterns of spatial variability. Each variogram analyzed shows the existence of spatial continuity. That is, the correlation between voxels of a given separation distance is most similar to the correlation between voxels of an incrementally larger separation distance. As the correlation of a given separation distance is compared to the correlation between voxels

of larger and larger, or smaller and smaller separation distances, generally the variogram values become more and more dissimilar, indicating a lessening in correlation. This behavior is characteristic of regionalized variables. It is therefore concluded that MRI modality space data can be represented using REVs. This result is the basis upon which kriging is applied to MRI data.

With the primary objective satisfied, a secondary goal in developing the MRI Scanner Distortion Model was to gain insight to the similarity that is exhibited between spatially regional characteristics of a modality space representation of a patient space volume and the original patient space volume. To reach this determination, variograms were computed, normalized and plotted for thirteen noncomplimentary directions for each of three patient space and modality space phantom volumes. Mean absolute errors and weighted mean errors are computed for each patient space and modality space pair of directional variogram curves.

The mean modality space:patient space normalization ratio (for directions for which it can be defined) was computed to be 1.065 with a standard deviation less than 8.3%. This mean ratio indicates that for a given separation distance the correlation between modality space voxels may be greater than or less than corresponding patient space voxels, but on average is approximately the same. Excluding the 2 of 78 cases when the patient space variogram curve is constant and zero, the average mean error of modality space normalized variograms in comparison to the corresponding patient space variograms is less than 5.6% with a standard deviation less than 6.5%. The average weighted mean error is less than 5.8% with a standard deviation less than 5.3%. Contributing to these errors are 13 of 76 cases where the extent of spatial dependency is observed to increase from their patient space values. However, only in

2 of these 13 instances did the shift map beyond the dimension of one voxel. In 83% of the cases studied, though the absolute correlation between neighboring voxels of a given separation distance changed, the range of spatial dependency remained the same.

Of noteworthy significance is the fact that these statistics are computed from modality space data that is generated using simulated magnetic fields that are far worse in terms of nonuniformity than any that would be experienced in a real life clinical scenario. These simulations may be classified as worse case scenarios. Nonetheless, the resulting statistics suggest that not only does spatial continuity exist in modality space, but the spatial variation of modality space data shares regional characteristics that are similar to those present in the source patient space volume. In general, the results indicate that the relative spatial variability that is present in patient space is preserved in an MRI modality space representation of patient space. The same spatial model that describes patient space is shown within an acceptable margin of error to accurately describe the MRI modality space representation of patient space.

In summary, I have described in this chapter how typical field nonuniformities of an MRI scanner can be modeled so that distorted modality space representations of phantom patient space objects can be obtained and their spatial variation analyzed. I proceeded to show how the variogram could be used to accomplish the spatial analysis of MRI modality space data and how its characteristics support the prerequisite that MRI modality space data can be represented using regionalized variables. Therefore, I have justified the use of kriging to interpolate MRI modality space data.

Chapter IV

DESIGNING THE AFIT KRIGING ALGORITHM
TO INTERPOLATE MRI VOLUME DATA

The mining engineer's challenge to visualize the structure of natural phenomena beneath the earth's surface is likened to similar challenges faced by the radiologist in trying to visualize structure inside the human body. Similarities between the interpolation problem encountered in each field motivated this research. Each field requires estimates of a three-dimensional physical world be obtained based upon a limited number of samples of physical space. Individuals in the mining industry recognized that phenomena of interest vary gradually over a finite extent in their physical space. In response, they introduced the theory of regionalized variables and kriging to improve estimates of thee phenomena sampled.

Though seemingly similar, a notable difference exists between the data sets that are interpolated in each case. The mining engineer obtains physical space samples that are analogous to patient space samples in the medical imaging field. The radiologist does not obtain patient space samples; rather, samples are obtained that have undergone a transformation to another space - modality space. Therefore, before the modality space data can be justifiably interpolated using kriging, it is necessary to show that modality space can be represented by regionalized variables. This analysis has been satisfied for MRI modality space representations of spatially regionalized patient space volumes and is described in Chapter III. Confident that MRI modality space exhibits spatially regionalized properties, the objective of the research described in this chapter was to develop an algorithm that applies kriging to three-dimensional medical

data to produce more accurate modality space estimates than those obtained using trilinear interpolation.

As patient space samples are collected and reconstructed into a modality space volume, errors are inevitably introduced resulting in a distorted patient space representation. Since diagnoses are often made based upon modality space renditions of patient space, a goal of medical imaging should be to minimize errors across the entire scanning and imaging process. An important step in this process is interpolation. Kriging offers the opportunity to minimize and quantify errors that are introduced during interpolation. Previous research has shown kriging to be a candidate medical imaging interpolation method [Parr92, Parr93, Styt93]. However, if *best* estimates are to be obtained that minimize estimation error variance, the assumptions previously made by researchers who compared kriging to other deterministic interpolation methods must be examined. That is, drift must be assumed to exist, the model variogram cannot necessarily be assumed to be known, and the neighborhood size about the point to be estimated (PTBE)[1] cannot be assumed to be known, nor can it be assumed to have symmetrical cubic dimensions.

This research proposes to apply kriging for the first time to volumetric medical data for producing modality space voxel estimates that may be considered to be optimal, linear, and unbiased with respect to the spatial variation that is modeled about each PTBE. This objective requires that a structural analysis of the volumetric data be conducted and incorporated into the interpolation process. Previous medical imaging research has suggested that the structural analysis of three-dimensional medical data is the barrier that must be overcome before kriging can produce optimal estimates

---

[1] Voxel values are referenced in terms of coordinate points on a three-dimensional grid and in this research are interchangeably described as *points to be estimated*.

[Styt93]. However, previous medical imaging research efforts have not accomplished nor integrated a comprehensive structural data analysis into their methodologies. The structural analysis demonstrated in this research removes regional drift, computes an ellipsoid neighborhood about the PTBE, and determines a reasonable model variogram that shares similar characteristics with its experimentally obtained counterpart. Neighborhoods of spatial dependency about each PTBE are determined from the structural analysis and are utilized to obtain kriged estimates and estimation errors that are based upon the modeled spatial variation. The first section of this chapter provides a top level description of the algorithm designed to accomplish these tasks in an unsupervised manner. Reasons are also given stating why the employed approach is pursued. Subsequent sections of this chapter provide expanded task by task descriptions of the algorithm.

Top Level Decomposition of the AFIT Kriging Algorithm

A top level description of the algorithm is given in the following paragraphs and is summarized in Table 4-1. The corresponding top level flowchart is provided in Figure 4-1. Readers who desire more detail than is provided in this section are referred to subsequent sections of this chapter, each which corresponds to a task of the Air Force Institute of Technology (AFIT) Kriging Algorithm.

To demonstrate the AFIT Kriging Algorithm, an (nx) x (ny) x (nz) modality space volume is interpolated to $(2nx-1)$ x $(2ny-1)$ x $(2nz-1)$. The interpolation process proceeds in an unsupervised manner after system initialization parameters are provided. Once estimates are obtained, it is necessary to determine the error associated with each estimate. Ideally, interpolated modality space voxel values equal their actual, or true,

patient space value. Therefore, the corresponding true value of each estimated location
must be known to compute the error of each estimate.

Table 4-1. The AFIT Kriging Algorithm

Task	Task Name	Description
1.	Generate Validation Data	Generate a reduced resolution MRI data set by removing every other column, row, and slice of an original 3D MRI data set.
2.	Identify Border Regions	Locate voxels that lie in high gradient regions. Krige only these voxels.
3.	Structurally Analyze and Krige	For each PTBE, structurally analyze the spatial variation of surrounding voxels to determine the neighborhood of voxels whose values contribute to each kriged estimate.
Subtask	Subtask Name	Description
3.1.	Characterize and Remove Drift	Characterize and remove large scale variations from the local region about the PTBE, thereby leaving behind stationary residuals.
3.2.	Compute Experimental Variogram	Compute the semivariogram curves for each specified directions.
3.3.	Assign Variogram Model	Determine if majority of directional variograms about the PTBE are best characterized by a gaussian, exponential, or spherical model.
3.4.	Determine Local Neighborhood	Determine ellipsoid region about the PTBE for which included voxels are determined to be spatially dependent upon one another.
3.5.	Generate Mathematical Model of Spatial Variation	Generate a mathematical model to predict the value of the modeled variogram as a function of volume coordinates.
3.6.	Krige Neighborhood Voxels	Estimate the value of the PTBE using the mathematical model to generate a system of ordinary kriging equations that are based upon voxels within the local neighborhood.

THE AFIT KRIGING ALGORITHM
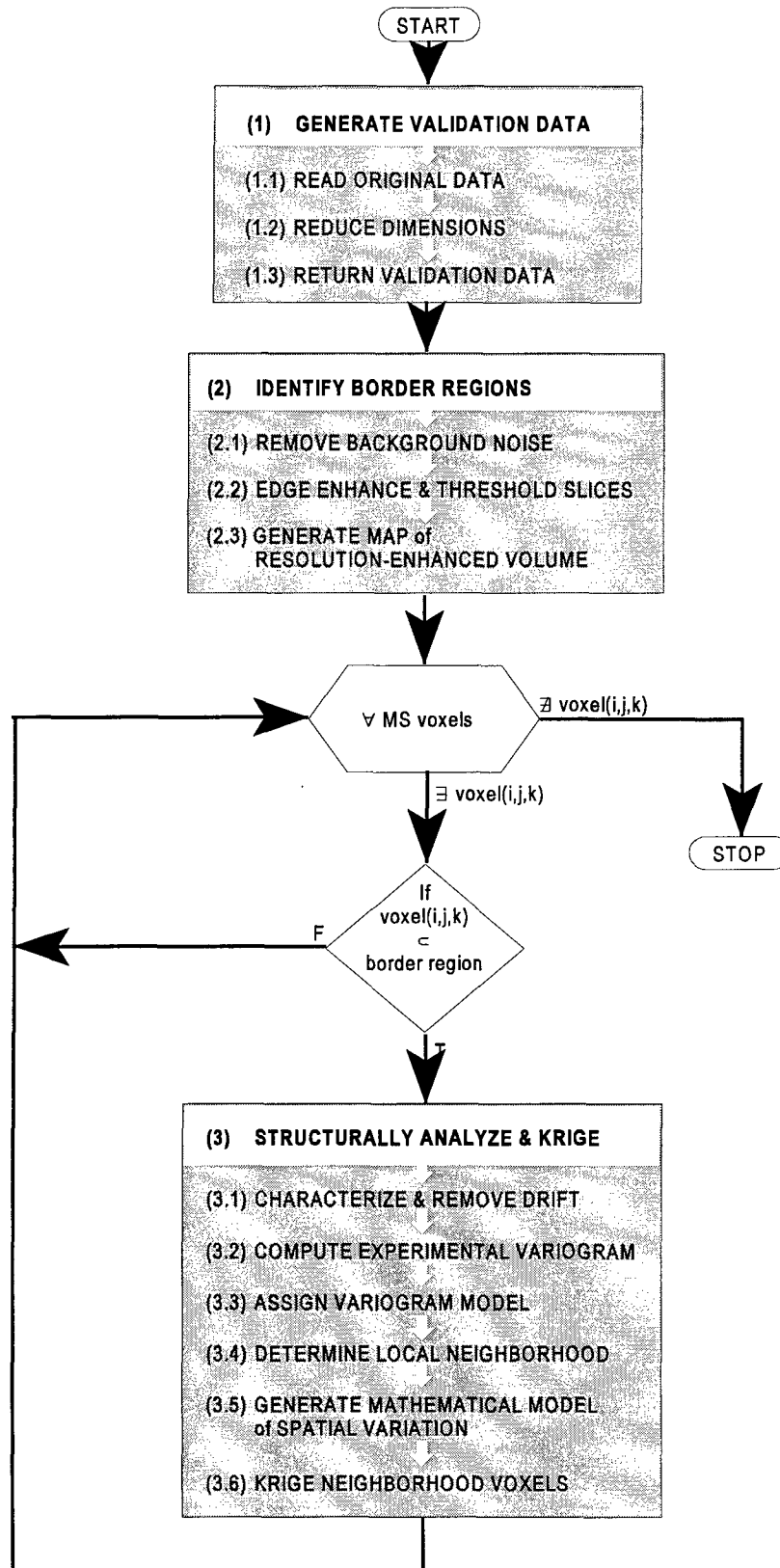
Figure 4-1. The AFIT Kriging Algorithm Flowchart

To accomplish this comparison, the top level task *Generate Validation Data Set* of the AFIT Kriging Algorithm removes voxels of every other sampled column, row, and slice of the original MRI data set. The resulting volume is herein referred to as the *validation data set*. The *Generate Validation Data Set* task is a preprocessing task necessary for this research to enable the computation of actual estimation errors. This task would not be exercised in a real world clinical implementation. The AFIT Kriging Algorithm proceeds to compute estimates between every other column, row, and slice of the validation data set in order to reconstruct the original MRI data set. The task, *Generate Validation Data Set*, is portrayed in Figure 4-2.
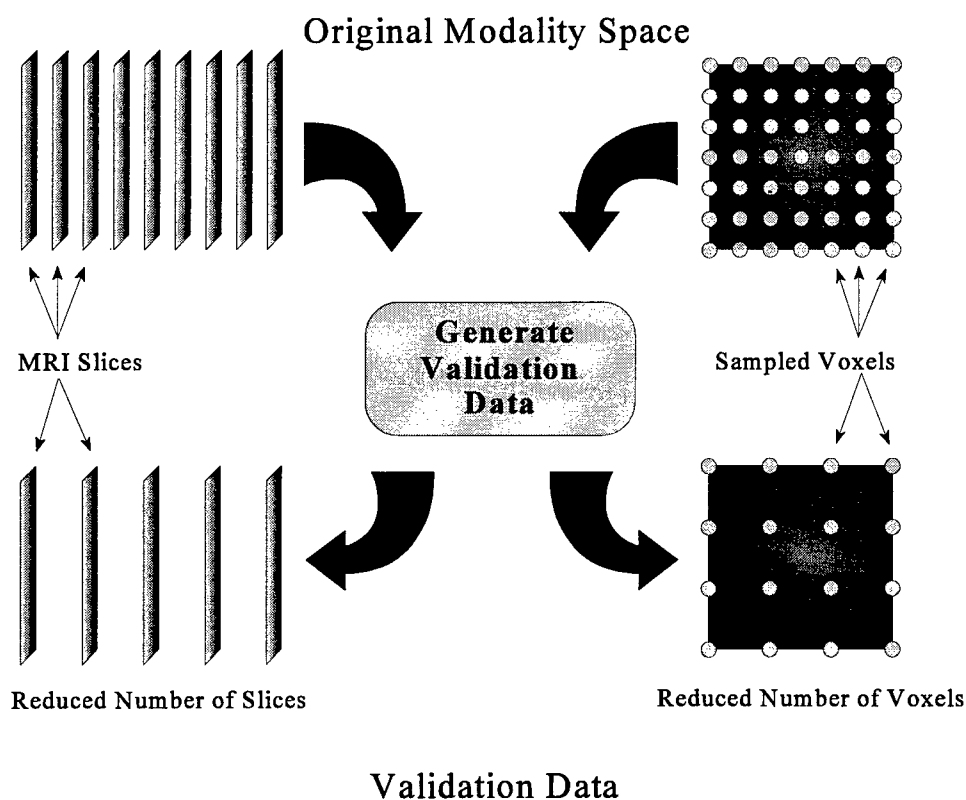
Figure 4-2. Generate Validation Data

Computational costs when using kriging as an interpolator are high when compared to conventional interpolation techniques. Kriging can easily require more than two orders of magnitude more operations to compute a volumetric estimate than does trilinear interpolation. As a matter of practicality, it is not the intent to employ kriging to estimate every unsampled voxel of a volume whose resolution is to be enhanced by some factor. Even simple interpolation techniques such as nearest neighbor or mean averaging yield fairly accurate estimates in homogeneous regions where the data varies slowly. Therefore, only voxels that lie in regions whose local gradient is sufficiently high shall be estimated using kriging. Such regions are found to spatially correspond to regions where multiple tissues or medium coexist. These regions are referred to as *border regions*. Unsampled voxels that lie in the border regions of a volume of interest are identified in the AFIT Kriging Algorithm task, *Identify Border Regions*.

Conventional geostatistical applications of kriging assume that the region surrounding the PTBE is homogeneous with respect to the sampled feature. The simulation presented in Chapter III indicates that a spatial dependency exists in MRI modality space data such that the closest voxels of a local region exhibit the highest degree correlation. In this sense, medical data is similar to geoscience data. The approach used to krige medical data in this research is unique in that the points to be interpolated lie in the least homogeneous regions of the volume. The motivation for focusing the interpolation on these least homogeneous regions is twofold. First, it is based on Miller's observation that information density increases as variance increases [Mill56]. Information density of a scene is greatest in regions where the variance, or contrast, is greatest. Second, it is out of a consideration of practicality. Though the development of the AFIT Kriging Algorithm adheres to standard software engineering

practices, optimization of the algorithm is not an objective of this research. The identification of points that lie in border regions occurs independent of the estimation process and serves to constrain the points that are kriged to those deemed most challenging to estimate. Given variability is greatest in the border regions, estimation errors are expected to be the largest for interpolated voxels that lie in these regions. In general, estimation methods tend to suffer from high variability and benefit from low variability [Isaa89]. The inclusion of only voxels that lie in border regions provides, in general, worst case estimates in terms of error magnitude.

Stationarity is a necessary condition for a linear estimator, such as kriging, if the weights of the estimator are to be unbiased. In the limit converging about a PTBE, one may obviously assume stationarity; that is, for the given number of discrete values that the data may assume, no change in value is discernable. As the region of consideration expands about that same point, homogeneity of the region likely lessens and stationarity may no longer be satisfied. For this reason, only the closest, most similar neighboring voxels about each PTBE contribute to each kriged, linear estimate. Additionally, the local drift observed within the local region about each PTBE is modeled and removed. The local drift accounts for a significant source of nonuniformity. Therefore, once removed, stationary residual voxel values remain.

Another factor that supports the stationarity assumption when considering neighboring voxels about a PTBE is specific to MRI modality space data. The physics of magnetic resonance imaging imply the modality space data encompasses rf returns that are a function of neighboring voxel values due to gradient magnetic fields and rf excitation pulses that unavoidably excite neighboring nuclei. The contribution of neighboring nuclei inherently implies a spatial dependency even in border regions of a

volume of interest. For all of these reasons, stationarity about each PTBE is satisfied. Stationarity is a necessary condition to obtain unbiased, linear estimates.

For each voxel whose value is to be estimated using kriging, a structural analysis of the surrounding region is carried out in the task, *Structurally Analyze and Krige*. The structural analysis is adaptive in the sense that dimensions of the regions analyzed are dependent upon the spatial characteristics that are observed for each iteration of the analysis. The regions about a PTBE expand with each iteration of the analysis until the extent of spatial dependency about the PTBE is reached. With each iteration, the data that surrounds a PTBE is structurally analyzed to derive a mathematical description of the spatial variation that can be used in the kriging system of equations. When incorporated into the kriging system of equations, the derived mathematical model has the effect of weighting voxels that exhibit high degrees of correlation more heavily in computing an estimate than those voxels that exhibit lesser degrees of correlation.

Since medical data is observed to have a varying component even within regions of same tissue type [Leah91], it cannot be assumed the modality space REV is stationary. Therefore, the structural analysis begins with the characterization and removal of observable drift in the task, *Characterize and Remove Drift*. The drift is analyzed using neighboring samples about the PTBE and in this sense may be considered *local* drift with respect to the global volume. However, since the local neighboring samples (hereafter referred to as the *subvolume* about the PTBE) are the domain of samples that are permitted to contribute to the estimate, the drift is in fact *global* with respect to the subvolume. Drift is removed from each subvolume so that it can be considered stationary with a constant mean.

Two kriging approaches are considered to contend with drift that is present about a PTBE - ordinary kriging and universal kriging. Ordinary kriging assumes the data

is stationary with a constant mean. Medical data is not, in general, stationary. Different anatomical regions elicit different modality space characteristics when scanned. These changing characteristics must be characterized and removed prior to kriging. With the drift removed the stationary residual data may be kriged using ordinary kriging to obtain residual estimates. The residual estimates can be added to the value of the drift at each estimated location to obtain modality space estimates.

The other method that accounts for drift is universal kriging. Universal kriging allows for a nonstationary mean, but requires that it be characterized, for instance as a first or second-order polynomial. The expression used to characterize the drift must be incorporated into the kriging system of simultaneous equations. Weights and estimates obtained using universal kriging include the effect of the modeled drift.

The selection of either method requires the drift be characterized. However, if universal kriging is used, then the number of simultaneous equations to be solved can more than double compared to the number required using ordinary kriging. Each drift coefficient adds another column and row to the covariance matrix in the matrix form representation of the ordinary kriging system of equations when using universal kriging. Furthermore, it has been observed that estimates obtained using ordinary kriging on median polished residuals are nearly identical to those obtained when universal kriging is employed [Cres91]. For these reasons, the AFIT Kriging Algorithm characterizes and removes drift from the modality space volume using a three-dimensional median polish algorithm, and ordinary kriging is applied to the stationary residuals to obtain a residual estimates. Each residual estimate is summed to the value of the drift at that location to obtain the each modality space estimate.

The median polish algorithm iteratively computes and accumulates the median values of each column, row and slice of a subvolume. When polishing is complete, the

median effects are removed from each subvolume. The residual subvolume that remains is stationary with a constant zero mean. The decomposition of any element of the subvolume can be represented as follows:

$$subvol(i,j,k) = vol\_med + col\_med(i) + row\_med(j) + slice\_med(k) + residual(i,j,k) \qquad (4\text{-}1)$$

where $subvol(i,j,k)$ is the element of the ith column, j^{th} row, and k^{th} slice of the subvolume; vol_med is a scalar and col_med, row_med, and $slice\_med$ are vectors containing the median main effects of the subvolume and of each column, row, and slice of the subvolume, respectively; and $residual(i,j,k)$ is a three-dimensional array whose elements represent the stationary residuals that remains after all median main effects have been removed from the corresponding subvolume element, $subvol(i,j,k)$. All subsequent structural analysis tasks operate on the stationary residual subvolume.

Given that the voxels of local regions about each PTBE are stationary and assumed to be spatially dependent, the next step of the top level task, *Structurally Analyze and Krige*, is to analyze the spatial variation about each PTBE so that it can be modeled and incorporated into the kriging equations. The subtask, *Compute Experimental Variogram*, accomplishes this analysis. *Compute Experimental Variogram*, computes semivariogram curves along each of a specified number of directions about the PTBE. The semivariogram for a specific vector distance $\bar{h}$ is given by:

$$\gamma(\bar{h}) = \frac{1}{2N(\bar{h})} \sum_{i=1}^{N(\bar{h})} [Z(p_i + \bar{h}) - Z(p_i)]^2 \qquad (4\text{-}2)$$

where there are $N(\bar{h})$ pairs of data samples that are a vector distance $\bar{h}$ apart, $Z(p)$ is the value at the point p, and $Z(p+\bar{h})$ is the value at the point $(p+\bar{h})$. This conventional

definition of a variogram applies to variograms that are referred to in this research as *discrete* directional variograms, because it describes the spatial variation of sampled points that lie along a specific, discrete direction.

The decision to interpolate voxels that lie in the least homogeneous regions of a volume implies that the extent of spatial dependency about a PTBE is minimal. Due to fewer number of sampled voxels that lie in the relatively small regions established by a minimal spatial dependency, the variability of the variograms was anticipated and shown to be significantly and undesirably high. This limits the precision with which models can be fit to or ranges can be extracted from the variograms. In response, *composite* directional variograms are introduced.

A composite directional variogram is different from a discrete directional variogram in that it allows an angular tolerance about the direction specified for the discrete directional variogram. All pairs of sampled points that lie along directions that fall within the permitted angular tolerance are considered in the computation of composite variogram values (as a function of separation distance). It is hypothesized that for a given subvolume, the increased number of points that a composite variogram considers produces a variogram curve that is less variable than the discrete variogram computed along the same direction. The precision with which model variogram coefficients can be determined therefore increases.

Once the semivariogram curve is computed for all possible pairs of values of the residual subvolume along all specified directions, one of five theoretical model types is chosen to reasonably represent the semivariogram curve characteristics. They are: linear, spherical, exponential, gaussian, or hole-effect. These five functions constitute the domain from which a variogram model is selected. Their reoccurring use in geostatistics to model the spatial variability of natural phenomena of the earth sciences

is the basis for their use in the AFIT Kriging Algorithm. From these five functions, variograms are categorized depending upon the presence or absence of the following traits: no sill; an asymptotic sill; a flat sill; parabolic behavior; and an inflection point near the origin. Based upon these categorized traits, the five functions sufficiently describe the gestalt of an experimental variogram.

The purpose for structurally analyzing the data is ultimately to enable the derivation of a mathematical description of the same. The complexity of the variogram and mathematical modeling algorithms is reduced by constraining the algorithms to *simple* models; that is, by not incorporating the logic to generate models of compound nested structures. This decision is a reasonable initial approach towards automating the three-dimensional kriging interpolation process. It is made with knowledge that researchers in the field of geostatistics recommend the use of simple models over complex models, assuming the major features of the variogram can be captured by simple models [Isaa89].

If the experimental variogram curve exhibits characteristics that suggest a linear behavior, it is assumed that the subvolume about the PTBE does not extend far enough from that point such that spatial independence may be observed on the plotted variogram curve. In these instances the subvolume dimensions about the PTBE are increased and the execution of the task, *Structurally Analyze and Krige*, starts over.

A hole-effect model is employed to characterize data with periodic spatial characteristics. This type of data model is encountered when one material is embedded within another in the analyzed subvolume. Initially, the data is highly correlated, but the correlation lessens as the separation distance increases. At some separation distance, however, minimum correlation is reached and the trend reverses; that is, the data becomes more correlated with increasing separation distance. The trend may

again reverse itself, following a damped periodic cycle. The hole-effect model described

is shown in Figure 4-3 and is given by equation (4-3):

$$\gamma(h) = \left[1 - \frac{\sin(ah)}{ah} \right] \qquad (4\text{-}3)$$

where h is the separation distance and a is the range.

Consistent with the approach of representing experimental variograms using

only simple models, the spherical variogram model is fit to experimental variograms

that indicate a hole-effect spatial variation. Modeling error is minimized by fitting only

the variogram values of the smallest separation distances up to and including the

maximum variogram value. Values beyond this separation distance are truncated and

the resulting neighborhood of spatial dependency may be modeled reasonably well using

Hole-Effect Variogram Model
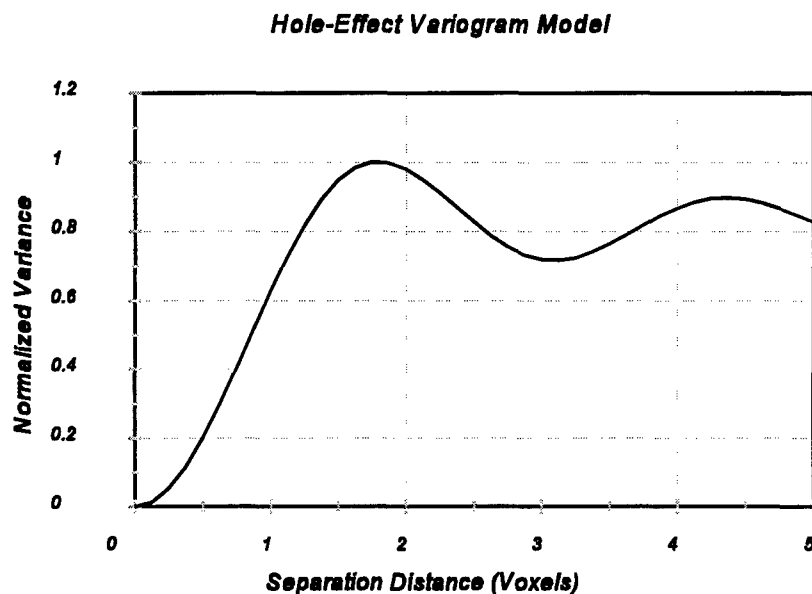
Figure 4-3. Hole-Effect Model

4-14

a spherical function. Since a single model type is eventually selected to best represent the spatial variation for all directions about a PTBE, the hole-effect model is handled as a spherical model whose extent is equivalent to the distance associated with minimal spatial correlation. To handle otherwise would jeopardize the validity of the stationarity argument.

The interim assignment of a linear model to a variogram indicates that the extent of spatial dependency, the separation distance for which voxels exhibit no dependency upon one another, is not achieved. In such instances the local region under analysis is extended along the direction of interest and the *Structurally Analyze and Krige* subtasks are reinitiated.

Ultimately, the *Assign Variogram Model* task assigns one of three variogram model types to each direction that is spatially analyzed: spherical, gaussian, or exponential. These functions have been shown to work well to describe the naturally occurring phenomena of the earth sciences [Davi77, Isaa89]. These functions also each satisfy the additional requirement that they be positive definite. This property ensures the solution to the kriging equations not only exists, but that it is unique and stable. It ensures a non-negative variance regardless of the sign of the kriging weights.

Once all directions of interest have been analyzed, the model type that occurs most frequently among the analyzed directions is assigned as the *common model* that will be used to describe the spatial variation about the PTBE. The spatial continuity about the PTBE is further analyzed in the task, *Determine Local Neighborhood* to determine the local neighborhood for which a spatial dependency is shown to exist. The neighborhood is approximated as an ellipsoid that is centered about the PTBE. The ellipsoid does not imply a spherical variability. Radii of the ellipsoid establish the surface whose interior encloses spatially dependent voxels that contribute to the kriged

estimate. The radii are determined from the ranges that are extracted from variograms along orthogonal directions of spatial continuity. Contributing weights of the neighborhood voxels are determined by the assigned variogram model.

The orientation of the ellipsoid superimposed upon the analyzed subvolume is determined by a lower level task within, *Determine Local Neighborhood*. Changes in range are analyzed relative to changes in direction in order to determine the anisotropy of spatial continuity evident in the local region. The ellipsoid is then oriented with its major axis aligned to the computed direction of maximum continuity. The orthogonal minor axis of the ellipsoid is similarly aligned as closely as possible with the direction of minimum continuity. Using these axes, a rotational transformation is computed which, when applied to the residual subvolume, aligns the major and minor axes of continuity of the subvolume with the y and x coordinate axes, respectively.

With the axes of continuity aligned to the coordinate axes, a mathematical model of spatial variation is generated in the task, *Generate Mathematical Model*. This mathematical model uses model type, directions of continuity, and the range along each direction of continuity to predict, as a function of subvolume coordinate position, the semivariogram value between the PTBE and any other point in the residual subvolume.

Krige Neighborhood Voxels considers all subvolume values that are contained within the computed ellipsoid neighborhood and generates the set of ordinary kriging equations (in matrix form) similar to that shown in equation (4-4),

$$
\begin{bmatrix}
C_{11} & \cdots & C_1n & 1 \\
\vdots & \ddots & \vdots & \vdots \\
C_{n1} & \cdots & C_{nn} & 1 \\
1 & \cdots & 1 & 0
\end{bmatrix}
\begin{bmatrix}
w_1 \\
\vdots \\
w_n \\
\mu
\end{bmatrix}
=
\begin{bmatrix}
C_{10} \\
\vdots \\
C_{n0} \\
1
\end{bmatrix}
\tag{4-4}
$$

where C_{ij} is the semivariance between the ith and j^{th} subvolume values contained within the ellipsoid neighborhood and w_i is the weight of the ith value of the subvolume. The weight matrix also contains the Lagrange parameter which enables conversion of the kriging set of equations into an unconstrained minimization problem and is useful for calculating the resulting estimation error variance.

Once matrices have been generated, an estimate is computed. This estimate, recall, is a residual estimate and therefore must be summed to the drift at that location in order to derive a modality space estimate of the point. The top level task, *Structurally Analyze and Krige*, is repeated for each border region voxel. The relationship between high level tasks of the AFIT Kriging Algorithm that have been presented in this section are depicted in a flowchart in Figure 4-1. For ease of cross-reference, task numbers in parentheses in Figure 4-1 are the same as those used in tables throughout this chapter. Implementation details of each of these tasks are provided in the chapter sections that follow.

Note the AFIT Kriging Algorithm developed as part of this research and described in this chapter provides a capability that is consistent with three-dimensional medical imaging systems. Specifically, the primary use of interpolation is to achieve scene continuity [Styt91], such as when magnifying images or rendering volumes. Hence, the AFIT Kriging Algorithm computes estimates between every other column, row and slice of a validation data set, as depicted in Figure 4-2. A storage requirement reduction is presently made by constraining modality space samples and interpolated locations to be regularly spaced. Limiting the process to regularly spaced data alleviates the need to maintain three-dimensional coordinates of each sample and interpolated value. These coordinates are computed as a function of their three-dimensional Cartesian coordinate indices.

The AFIT Kriging Algorithm could have been designed or can be modified to provide estimates at arbitrary, nonregularly spaced locations. Task objectives would be no different. However, this sort of implementation would require three-dimensional coordinates be stored for each processed location. Integer data types would be insufficient to store the values of the arbitrary locations that may be interpolated. Operational storage requirements would therefore dramatically increase over the requirements of the present implementation. Procedures and functions would also require modification to pass these additional data structures.

Subsequent sections of this chapter address each task of the AFIT Kriging Algorithm in further detail.

Generating Validation Data to Confirm the Accuracy of Interpolated Estimates

The purpose for incorporating this task into the developed kriging algorithm stems from the need to assess the technique's performance in interpolating three-dimensional medical data. In order to assess estimation accuracy, true values of interpolated voxels must be known. Mathematical phantoms could have been substituted for MRI modality space data, but results would have had limited value to the medical community. The scanning of phantom objects could have been accomplished, but the distortion inherent in the modality space reconstruction would have added an uncertainty factor to estimation accuracy computations.

The approach pursued in this research utilizes real MRI modality space data. A validation data set is generated from a subset of an actual MRI modality space volume. This permits interpolated voxel values to be compared to actual modality space values when computing estimation accuracy. A pictorial depiction of *Generate*

Validation Data is shown in Figure 4-2. A high level decomposition of the task is found in Table 4-2.

Table 4-2.   Generate Validation Data

Task	Task Name	Description
1.	Generate Validation Data	Generate a reduced resolution MRI data set by removing every other column, row, and slice of an original 3D MRI data set.
Subtask	Subtask Name	Description
1.1.	Read Original Data	Read the values of an original MRI data set whose dimensions are: $(2nx-1)$ x $(2ny-1)$ x $(2nz-1)$.
1.2.	Reduce Dimensions	Remove every other column, row, and slice of original data set.
1.3.	Return Validation Data	Return the reduced resolution validation data set. Dimensions are (nx) x (ny) x (nz).

The subtask, *Read Original Data*, reads the values of an original modality space data set. The examples and results in this research are based upon modality space volumes extracted from an MRI acquisition of a human head. The column:row:slice aspect ratio of the MRI acquisition was 1:1:1.25.

The subtask, *Reduce Dimensions*, removes every other slice from the modality space volume and from each remaining slice removes voxels of every other column and row. For example, slices 0, 1, and 2 of the resulting volume would map to slices 0, 2, and 4 of the original modality space volume. Columns and rows of each volume would similarly map to each other. Thus, if the dimensions of the original modality space volume are $(2nx-1)$ columns by $(2ny-1)$ rows by $(2nz-1)$ slices, the validation volume

returned in the subtask, *Return Validation Data*, would be *(nx)* columns by *(ny)* rows by *(nz)* slices.

Using kriging to obtain estimates in high gradient regions, the resolution of the validation data set is nearly doubled. The end result is an interpolated reconstruction of the original modality space volume whose *estimated* values could be individually compared to the *actual* values of the original modality space data set. In this manner, error statistics of the kriged data set are obtained.

Identifying Border Regions to Interpolate Using Kriging

Given eight values that represent the sampling of a phenomenon at the corners of a rectangular parallelpiped formed by two adjacent slices of volume data, (as shown in Figure 4-4), estimating a value between the slices using trilinear interpolation requires computing inverse distance dependent weights for each sampled value, multiplying each sampled value by its computed weight, and summing all resultant contributions. Computing the eight weights requires eight division operations and seven addition operations. Computing the contributions from each sampled value requires eight multiplication operations. Obtaining the final estimate requires summing each of the eight contributions. Therefore, computing the trilinear estimate of a point within the parallelpiped using the eight corner values requires 31 operations.

In contrast, assume an estimate of a similar location is desired using kriging. Also assume the subvolume used to structurally analyze the local region about the PTBE extends 2 voxels in each direction about the PTBE, or in other words, includes 64 sampled values (as shown in Figure 4-5). Finally, assume the structural analysis is conducted along thirteen different directions, as is done in this research, given by the directional vectors that are indexed in Table 4-3.
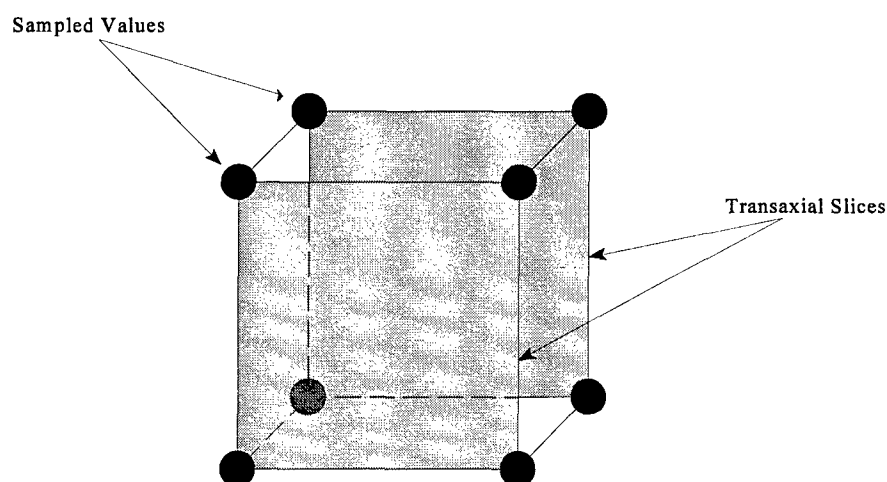
Figure 4-4. Trilinear Sampling

A variogram that is calculated for any specified direction is equal to the variogram that is calculated in the opposite direction. For instance, a variogram computed as a function of the direction specified by the directional vector [-1, 0, 0] produces the same result as the variogram computed for the direction specified by the directional vector [1, 0, 0], given by the vector with index 0 in Table 4-3. Therefore, the directional variograms that are computed for the directions specified by the indexed

Table 4-3. Structural Analysis Directional Vectors

Vector Index	Terminal Coordinates	Vector Index	Terminal Coordinates	Vector Index	Terminal Coordinates
0	[1, 0, 0]	4	[-1, 1, 1]	8	[-1, 1, 0]
1	[0, 1, 0]	5	[-1, 1,-1]	9	[0, 1, 1]
2	[0, 0, 1]	6	[1, 1,-1]	10	[0, 1,-1]
3	[1, 1, 1]	7	[1, 1, 0]	11	[1, 0, 1]
				12	[-1, 0, 1]
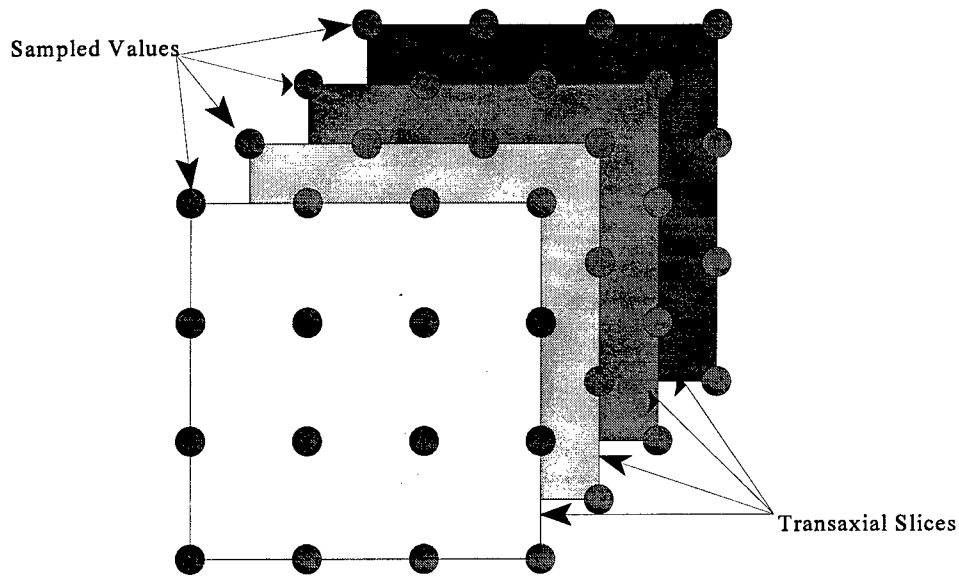
Figure 4-5. Kriging Sampling

directional vectors in Table 4-3 equal the variograms that are computed in directions opposite each indexed directional vector.

Consider the definition of the variogram $\gamma(\bar{h})$ as given in equation (4-5),

$$\gamma(\bar{h}) = \frac{1}{2N(\bar{h})} \sum_{i=1}^{N(\bar{h})} [Z(p_i + \bar{h}) - Z(p_i)]^2 \qquad (4\text{-}5)$$

where there are $N(\bar{h})$ pairs of data samples that are a vector distance $\bar{h}$ apart, $Z(p)$ is the value at the point p, and $Z(p+\bar{h})$ is the value at the point $(p+\bar{h})$. Calculating a single variogram value for a given distance vector $\bar{h}$ that is parallel to one of the coordinateaxes requires the number of computations listed in Table 4-4.

Table 4-4. Variogram Computations

|h|	Number of Operations
1	145
2	97
3	49
total:	291

Computing a variogram curve along a single direction parallel with a coordinate axis would therefore require the computation of 291 operations. Using this number to approximate the number of operations that would need to be computed when all thirteen specified directions are considered increases to over 3,700. This number reflects only the number of operations necessary to conduct a limited structural analysis of the subvolume that surrounds the PTBE. If the subvolume about the PTBE is extended by ±1 voxel in each direction, the number of operations required to structurally analyze all 13 directions increases to over 21,000. If it is conservatively assumed that the local ellipsoid neighborhood about each PTBE contains 12 sampled values, then computing the weights associated with each value within the neighborhood necessitates the multiplication of a 1x13 matrix with a 13x13 matrix. 156 of 182 elements of these matrices are semivariances that are computed based upon a model derived from a structural analysis. The number of computations required for the structural analysis are not even considered here. Nonetheless, the computational costs of using kriging rather than trilinear interpolation is evident. More than two orders of magnitude more

computations are required to obtain the kriged estimate than are required to obtain a trilinear interpolated estimate.

In a practical scenario it may be difficult to justify the computational costs of kriging to obtain estimates in homogeneous regions of low variability where trilinear interpolation likely provides sufficient accuracy. Consistent with this reasoning, the AFIT Kriging Algorithm developed for this research enables the least homogeneous connected regions of a volume to be identified as *border regions*. Only these so called border regions are interpolated using kriging. The top level task of the AFIT Kriging Algorithm, *Identify Border Regions*, accomplishes this identification process. A high leveldecomposition of *Identify Border Regions* is provided in Table 4-5.

Segmenting Background Voxels from the Volume of Interest

The task, *Remove Background Noise*, enables the user to interactively view histograms of selected slices of the volume of interest. The user selects a threshold value to differentiate between background values and values corresponding to the object of interest. This task then creates a binary volume the same size as the modality space volume of interest. Voxels of the modality space volume that lie in a background region are cleared to a value of 0 in the binary volume. All other voxels of the binary volume are set to a value of 1. No voxels whose value is 0 is considered part of the object of interest and, therefore, is not operated on by any subsequent task of the AFIT Kriging Algorithm.

Table 4-5. Identify Border Regions

Task	Task Name	Description
2.	Identify Border Regions	Locate voxels that lie in high gradient regions. Krige only these voxels
Subtask	Subtask Name	Description
2.1.	Remove Background Noise	Threshold volume to segment background from region of interest.
2.2.	Edge Enhance and Threshold Slices	Use Sobel edge enhancement operator on voxels that do not lie in background. Threshold resultant volume to segment heterogeneous regions.
2.3.	Generate Map of Resolution Enhanced Volume	Generate map of enhanced resolution volume that identifies voxels in high gradient regions.

Edge Detection of MRI Slices

Voxels of the modality space volume that do not lie in background regions are edge enhanced to facilitate the localization of border regions. Voxels that correspond to background regions of the volume are cleared to 0. The task, *Edge Enhance and Threshold Slices*, executes the edge enhancement of each slice using a 3x3 Sobel edge detection operator. The Sobel operator is selected over other edge detection and enhancement operators due to its computational simplicity, ease of implementation, and overall ability to detect gradient regions of an image.

Given a pixel *ms(i,j)* that lies in the ith column and j^{th} row of a modality space image slice, neighboring pixels are labeled as shown in Figure 4-6. Using this notation, the corresponding Sobel edge-enhanced pixel value *s(i,j)* is approximated as,

$$s(i,j) = |s\_col| + |s\_row| \tag{4-6}$$

where,

$$s\_col = \{ms(i+1,j-1) + 2ms(i+1,j) + ms(i+1,j+1)\}$$
$$- \{ms(i-1,j-1) + 2ms(i-1,j) + ms(i-1,j+1)\} \qquad (4\text{-}7)$$

$$s\_row = \{ms(i-1,j-1) + 2ms(i,j-1) + ms(i+1,j-1)\}$$
$$- \{ms(i-1,j+1) + 2ms(i,j+1) + ms(i+1,j+1)\} \qquad (4\text{-}8)$$

A gray scale, edge-enhanced representation of the modality space volume is produced in this manner.

$ms(i\text{-}1,j\text{-}1)$	$ms(i,j\text{-}1)$	$ms(i+1,j\text{-}1)$
$ms(i\text{-}1,j)$	$ms(i,j)$	$ms(i+1,j)$
$ms(i\text{-}1,j+1)$	$ms(i,j+1)$	$ms(i+1,j+1)$

Figure 4-6. Neighboring Pixels

Slice histograms are interactively displayed for user evaluation. The histograms reflect voxel values of the edge-enhanced volume. A threshold value is selected to indirectly specify the degree of inhomogeneity that must be present to label voxels as border region voxels. Once a threshold is determined, a binary volume that is the same size as the modality space volume of interest is created. High gradient regions of themodality space volume have their corresponding binary voxel values set to 1.

Generating a Map of the Resolution Enhanced Volume

The previous task designates modality space voxels that lie in high gradient regions. A similar binary volume that is the same size as the final interpolated volume

must be created to indicate the voxels of the interpolated volume that require kriged estimates. The generation of such a volume is accomplished by the subtask, *Generate Map of Resolution Enhanced Volume*. Only voxels of the resolution enhanced volume that map to high gradient regions of the modality space volume are set to the value 1, indicating their estimates are to be obtained using kriging. Voxels whose values are not set during the execution of this task are not considered for interpolation by the AFIT Kriging Algorithm. A high level decomposition of *Generate Map of Resolution Enhanced Volume* is provided in Table 4-6.

Table 4-6. Generate Map of Resolution Enhanced Volume

Task	Task Name	Description
2.3.	Generate Map of Resolution Enhanced Volume	Generate map of enhanced resolution volume that identifies voxels in high gradient regions.
Subtask	Subtask Name	Description
2.3.1.	Expand Binary Volume	Given a *(nx)* x *(ny)* x *(nz)* binary volume, map voxel values to a *(2nx-1)* x *(2ny-1)* x *(2nz-1)* binary volume.
2.3.2.	Dilate Binary Data	Apply morphological dilation to resolution enhanced binary volume to close discontinuities caused by the expansion.
2.3.3.	Crop Binary Volume Perimeter	Do not permit voxels that lie within q voxels of volume perimeter to be estimated using kriging; PTBE must be centered within subvolume from which variograms are computed.

Given an *(nx)* x *(ny)* x *(nz)* modality space volume, the subtask, *Expand Binary Volume*, generates a binary volume whose dimensions are *(2nx-1)* x *(2ny-1)* x *(2nz-1)*. A slice is added between every slice of the modality space volume; a row is added

between every pair of rows; and a column is added between every pair of columns. Voxel values of all added slices, rows and columns are zero. Therefore, any modality space voxel whose value is 1 is surrounded, in the resolution enhanced volume, by voxels whose value are 0. The resulting discontinuities in the resolution enhanced volume are closed by the morphological dilation that occurs in the subtask, *Dilate Binary Volume*.

In *Dilate Binary Volume*, each resolution enhanced volume voxel whose value is 1 has its 26 adjacent voxels reassigned to the value 1. This dilation serves two purposes: it closes discontinuities that are created during the expansion of the thresholded modality space volume; and it "grows" the extent of the border region of the resolution enhanced volume by ±1 voxel in each coordinate direction. Dilating the border region smooths the surfaces that differentiate between voxels that the AFIT Kriging Algorithm interpolates using kriging from those that are interpolated using a conventional interpolation technique.

The subtask, *Crop Binary Volume Perimeter*, imposes the constraint upon the resolution enhanced volume that no voxel whose corresponding modality space position is within q voxels of the border of the modality space volume is estimated using kriging. This constraint is necessary so that a subvolume of values used to compute the directional semivariograms may be centered about the PTBE while not exceeding the perimeter of the original modality space volume. For example, if q assumes the value of 3, then the subvolume that is used to compute the directional variograms is not permitted to exceed ±3 voxels along any coordinate axis about the PTBE. Since objects of interest are generally centered within the scanner field of view and since the voxels that cannot be considered for kriging lie along the perimeter of the acquired modality space volume, in practice, this constraint does not limit the utility of the AFIT Kriging Algorithm developed in this research.

The value of q bounds the extent of the subvolume that is analyzed about a PTBE. Values of q less than 3 are found to generate too few variogram values to determine whether or not spatial independency of voxels beyond the subvolume extent has been reached. On the other hand, values of q greater than 3 exhibit variograms that have undergone a smoothing effect such that their values reflect the contributions of too many nearby voxel values to capture the finer spatial variations that may be occurring about a PTBE. Furthermore, values of q greater than 3 are frequently observed to specify a subvolume whose dimensions significantly exceed the extent of spatial dependency; therefore, the additional voxel contributions that results from structurally analyzing larger subvolumes about a PTBE have the effect of biasing the estimate with voxel values from a spatially independent neighboring region.

The Structural Analysis and Kriging of Border Region Voxels

This task of the AFIT Kriging Algorithm is the primary focus of this research. Preceding tasks are accomplished to provide a means to evaluate the accuracy of kriging when used as a volumetric medical imaging technique. *Structurally Analyze and Krige* is the task that accomplishes the structural analysis and subsequent interpolation of the volumetric data.

Kriging is no different than other linear interpolation techniques in the sense that each estimate is computed from a linear combination of neighboring voxel values. Trilinear interpolation is the most common volumetric linear interpolation technique. Adjacency determines the ensemble of contributing voxels. The weighting of each contributing voxel is strictly a function of the distance from the PTBE. Like trilinear interpolation, kriging weights neighboring voxel contributions as a function of distance from the PTBE, however, distance is not the only factor that is used. Kriging also

considers the local spatial variation about the PTBE when computing the weights that that determine the contributions of neighboring voxels.

Unlike trilinear interpolation, kriging does not limit the membership of contributing voxels to those that are strictly adjacent to each PTBE. Rather, kriging can consider and include any number of relevant voxels. The AFIT Kriging Algorithm determines relevant, dependent voxels to be those that are included within an ellipsoid that is centered about each PTBE. The extent and orientation of the three orthogonal semiaxes of each ellipsoid are calculated to approximate the inclusion of all spatially dependent voxels about each PTBE.

This task utilizes a top-down, three-tiered approach to converge upon the identification of spatially dependent contributing voxels and their weights. Initially, a parallelpiped subvolume is centered about each PTBE to represent a coarse approximation of the spatially dependent region about the PTBE. The axis of the parallelpiped subvolume are parallel to the modality space coordinate axes. The endpoints of the parallelpiped subvolume are incrementally moved apart until experimental variograms indicate spatial independency between subvoxels that are farthest apart.

Once this condition is satisfied, the extent of the three-dimensional, spatially dependent neighborhood is more closely approximated by orienting the major and minor axes of an ellipsoid to most closely align with the directions of maximum and minimum continuity, respectively. Use of the ellipsoid enables anisotropic spatial variation to be factored into the computation of each kriged estimate.

The third level of approximation concentrates on the weights that are computed for each voxel that lies within the spatially dependent ellipsoid neighborhood. The contribution of each voxel value is dependent not only upon the Euclidean distance from

the PTBE, but also upon the spatial variation that is exhibited and modeled about the PTBE. Spatial variation is modeled as a function of the vector distance from each PTBE.

Structurally Analyze and Krige is the task that utilizes the three-tiered approach in its structural analysis to converge upon the spatially dependent region about each PTBE. In addition, this task kriges the spatially dependent voxels using a model that it derives from the same structural analysis. Each linear estimate is guaranteed to be unbiased and optimal with respect to the derived spatial model. The task is repeated for every point that is identified in *Identify Border Regions* to be estimated.

Two opposing factors determine the size of the subvolume of values that are selected about the PTBE for the structural analysis. It is desired that the subvolume be small in comparison to the subject of interest so that stationarity may be assumed. On the other hand, variograms computed from small subvolumes about a PTBE exhibit more variable behavior than do variograms computed from larger subvolumes. The smoothing effect that is noticeable on variograms computed from relatively large subvolumes is far less noticeable on variograms computed from smaller subvolumes. Simple models may be unable to represent the variability of variograms generated from subvolumes whose dimensions are relatively small. Such an occurrence manifests itself in high estimation error variance and broad confidence intervals for the interpolated estimate.

This task is designed in consideration of these opposing factors. Small subvolumes ensure stationarity. Therefore, algorithm iterations of *Structurally Analyze and Krige* begin with small subvolume approximations. Subvolume dimensions are then incrementally expanded to reduce variogram variability and estimation variance. However, incremental subvolume expansions are constrained so that spatially

independent voxels about a PTBE are not included within the surface of the resulting

ellipsoid neighborhood.

The decomposition of the top level task, *Structurally Analyze and Krige*, is

provided in Table 4-7. Surrounding voxels of each PTBE are structurally analyzed to

determine the spatial variation about each point. This analysis consists of:

characterizing and removing drift from the local region; computing experimental

Table 4-7. Structurally Analyze and Krige

Task	Task Name	Description
3.	Structurally Analyze and Krige	For each PTBE, structurally analyze the spatial variation of surrounding voxels to determine the neighborhood of voxels whose values contribute to each kriged estimate.
Subtask	Subtask Name	Description
3.1.	Characterize and Remove Drift	Characterize and remove large scale variations from the local region about the PTBE, thereby leaving behind stationary residuals.
3.2.	Compute Experimental Variogram	Compute the semivariogram curves for each of several specified directions.
3.3.	Assign Variogram Model	Determine if majority of directional variograms about the PTBE are best characterized by a gaussian, exponential, or spherical model.
3.4.	Determine Local Neighborhood	Determine ellipsoid region about the PTBE for which included voxels are determined to be spatially dependent upon one another.
3.5.	Generate Mathematical Model of Spatial Variation	Generate a mathematical model to predict the value of the modeled variogram as a function of volume coordinates.
3.6.	Krige Neighborhood Voxels	Estimate the value of the PTBE using the mathematical model to generate a system of ordinary kriging equations that are based upon voxels within the local neighborhood.

variograms from the stationary residuals along each of several specified directions; determining a variogram model to approximate the neighborhood of spatial dependency about each PTBE and to describe the spatial variation within the local neighborhood; and finally, incorporating the variogram model into the kriging system of equations to obtain an estimate and estimation error variance for each PTBE.

Characterizing and Removing Drift from Modality Space Data

The structural analysis of each subvolume begins by characterizing the drift about the PTBE. There are two reasons why the drift is characterized. First, it must be removed from each subvolume so that the subvolume can be considered stationary with a constant mean. Kriging assumes the data to be interpolated is stationary. Second, after a kriged residual estimate is obtained, the drift that is present at the location of the estimate must be added to the residual estimate to obtain each interpolated modality space estimate. Unless the modality space drift is modeled, its value at an arbitrary location in the resolution enhanced volume will not be known. The task, *Characterize and Remove Drift*, accomplishes the task of modeling and removing the modality space drift associated with the subvolume about each PTBE. A decomposition of *Characterizeand Remove Drift* is provided in Table 4-8. Descriptions of each of its subtasks are provided in the following paragraphs.

The subtask, *Median Polish*, applies a three-dimensional main effects median polish algorithm to each subvolume. The algorithm is an extension of a two-dimensional technique described by Cressie [Cres91]. A median main effect is the median average value of all voxels considered, for instance, along a given direction. The three-dimensional median polish technique iteratively processes a subvolume, and then slices, rows and columns of the subvolume to derive the median main effects that contribute

Table 4-8. Characterize and Remove Drift

Task	Task Name	Description
3.1.	Characterize and Remove Drift	Characterize and remove large scale variations from the local region about the PTBE, thereby leaving behind stationary residuals.
Subtask	Subtask Name	Description
3.1.1.	Median Polish	Apply a 3D main effects median polish algorithm to subvolume about PTBE.
3.1.2.	Model Median Main Effects	Fit a 3rd order polynomial to each column, row, and slice main effects vectors.
3.1.3.	Remove Main Effects	Remove the modeled main effects from the subvolume about the PTBE, resulting in a subvolume of stationary residuals.

to the large scale trends that exist in the subvolume data. The algorithm proceeds as follows: First, the median value of the subvolume is computed, stored, and removed from each element of the subvolume. Second, the median value of each slice is computed from the subvolume, stored, and removed from each element in the corresponding slice. The median value that is associated with each slice is called the slice median main effect. Third, the median value of each row of the subvolume is computed, stored, and removed from each element in the corresponding row. The median values that are associated with each row are called the row median main effects. Fourth, the column median main effects are similarly computed and stored. Once the column median main effects are removed from each element in the corresponding column of the subvolume, a subvolume of stationary residuals remains. The modality space value of any element of the residual subvolume can be represented as:

$$subvol(i,j,k) = vol\_med + col\_med(i) + row\_med(j) + slice\_med(k) + residual(i,j,k) \qquad (4\text{-}9)$$

where $subvol(i,j,k)$ is the element of the ith column, j^{th} row, and k^{th} slice of the subvolume; vol_med is a scalar and col_med, row_med, and $slice\_med$ are single dimension arrays containing the median main effects of the subvolume and of each column, row, and slice of the subvolume, respectively; and $residual(i,j,k)$ is a three-dimensional array whose elements represent the residual that remains after all median main effects have been removed from the corresponding subvolume element, $subvol(i,j,k)$.

Elements of the resulting residual subvolume spatially correspond to the elements of the original modality space subvolume; dimensions of the modality space and residual subvolumes are equal. However, residual estimates obtained using kriging will spatially correspond to locations that lie between existing sampled points. Therefore, it is necessary that the median main effects drift terms be modeled so that main effects terms can be obtained for locations that lie between the sampled modality space points. This modeling is accomplished by the subtask, *Model Median Main Effects*. Figure 4-7 through Figure 4-9 depict examples of column, row and slice median main effects modeling as computed by *Model Median Main Effects*.

Column Main Effects
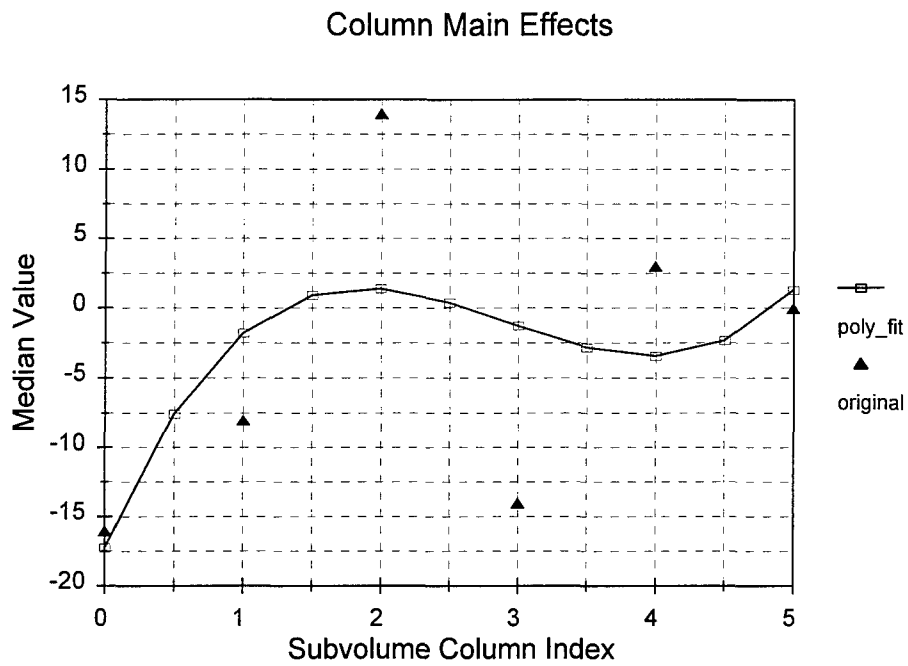
Figure 4-7. Column Main Effects Modeling
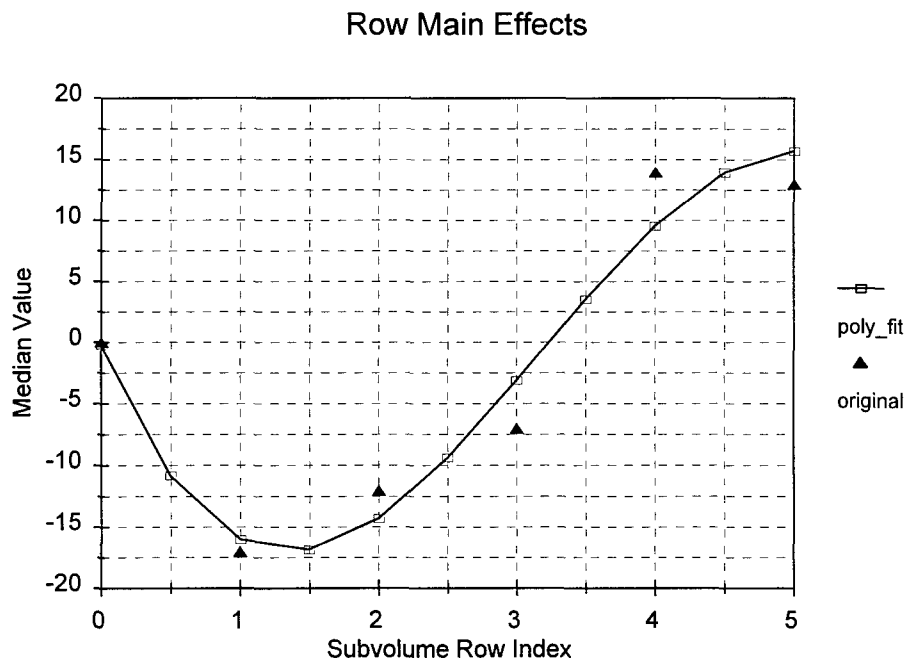
Row Main Effects

Figure 4-8. Row Main Effects Modeling
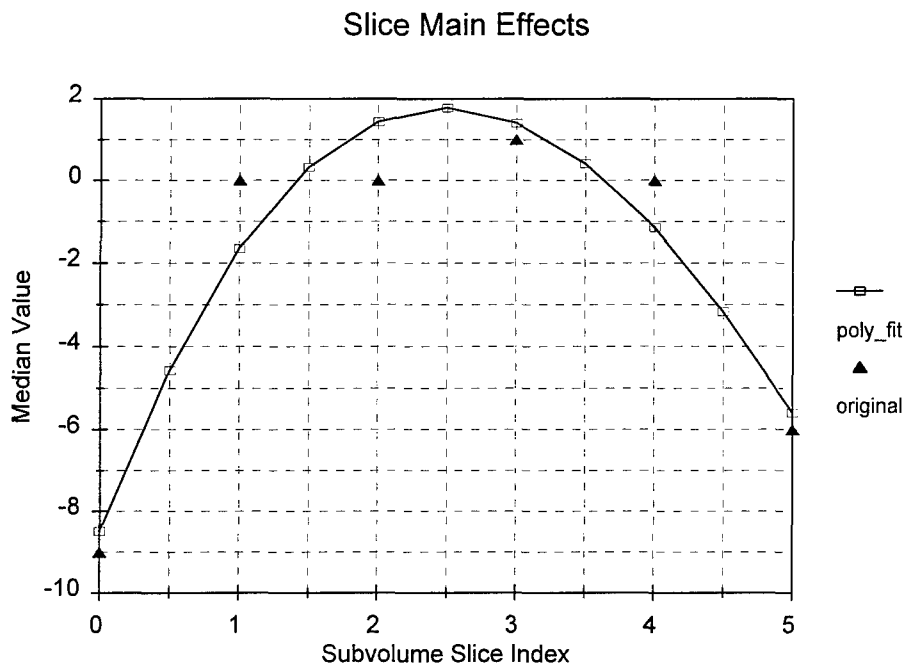
Slice Main Effects

Figure 4-9. Slice Main Effects Modeling

Model Median Main Effects fits a third-order polynomial, depicted by the solid lines in Figure 4-7 through Figure 4-9, to each modality space column, row, and slice main effects values that are obtained in the subtask, *Median Polish*. The actual main effects values are represented by the solid triangles in Figure 4-7 through Figure 4-9. Coefficients of each third-order polynomial are computed using a least squares polynomial fit algorithm. The number of elements in each median main effects array is then increased from n to $(2n-1)$ to account for the resolution enhancement that occurs to the interpolated subvolume. Values of the newly added main effects column, row, and slice elements are obtained by interpolating the original main effects arrays using the third-order polynomial specified by the least squares polynomial fit algorithm. These newly added main effects column, row, and slice elements are represented by the outlined squares in Figure 4-7 through Figure 4-9. Trials fitting fifth, seventh and

ninth-order polynomials were also made, but were judged to react too quickly to data variations, often overshooting or undershooting experimental values. Use of a third-order polynomial was observed and judged to best approximate the large scale variation exhibited by the data.

In general, the polynomial model of each median main effects vector only approximates the discrete values determined by the *Median Polish* subtask. If the median main effects for a given sampled location are estimated using the polynomial model, in general, they do not equal the values obtained by the *Median Polish* subtask. Therefore, the subvolume stationary residuals are recomputed in the subtask, *Remove Main Effects*, using main effects values derived in the subtask *Model Main Effects*. In this manner, drift can be predicted for any location within the subvolume, whether a sampled value is available at that location or not. Drift predictions made at sampled locations now satisfy exactness; that is, the use of modeled main effects drift values ensures equivalence in the modality space residual decomposition equation, equation (4-9). All subsequent structural analysis tasks operate on subvolumes of stationary residuals.

Computing Experimental Variograms from Stationary Residual Volumes

Having characterized and removed the subvolume drift, the structural analysis proceeds using stationary residuals computed from the *Characterize and Remove Drift* task. *Compute Experimental Variogram* computes directional variogram curves along thirteen unique directions about each PTBE to describe the spatial variation of each subvolume. The number of directions chosen for analysis is limited by the number and distribution of available samples within each subvolume. The dimensions of each subvolume are minimized to satisfy the stationarity assumption; they are increased

about the PTBE only to the extent that spatial dependency is observed to reach or converge to a minimum. These conditions are generally observed satisfied (for the MRI data analyzed in this research) when subvolume dimensions are between 4x4x4 and 5x5x5, centered about the PTBE. Because directional variograms computed for two opposite directions are equal, then the maximum number of unique directions along sampled values, such that the minimum separation distance is no greater than the spacing between 1 adjacent voxel, is thirteen. Therefore, in this research, 13 different directions (not including complimentary directions) are considered in the structural analysis of each subvolume. They are given by the indexed directional vectors in Table 4-3 (represented by the x, y, and z coordinates of the terminal point of each vector, assuming the initial point of the vector is at the origin).

In practice, though it often is true that voxel sampling, or spacing, along two of the coordinate axes of an MRI scanner is equal, the voxel sampling, or spacing, along one of the coordinate axes is generally greater than the other two. This nonuniform aspect ratio between the sampling axes is significant and must be considered when determining spatial dependencies in a volume of interest. For instance, if voxels along the z axis are sampled at a rate that is 1.25 times less frequent than the sampling rate along the x or y axes, then the directional vector given by [0, 1, 1] would not specify a direction that is 45° above the xz plane, but rather one that is not quite 39° above the xz plane.

The variogram is the tool used to quantify and describe the spatial variation present along a given direction in a volume of interest. It is given by the following equation:

$$\gamma(\bar{h}) \ = \ \frac{1}{2N(\bar{h})} \sum_{i=1}^{N(\bar{h})} [Z(p_i + \bar{h}) - Z(p_i)]^2 \qquad (4\text{-}10)$$

where there are $N(\bar{h})$ pairs of data samples that are a vector distance $\bar{h}$ apart, $Z(p)$ is

the value at the point p, and $Z(p+\bar{h})$ is the value at the point $(p+\bar{h})$. The directional

vector $\bar{h}$ that appears in equation (4-10) is given by,

$$\bar{h}_i = [x_i, y_i, z_i] \qquad (4\text{-}11)$$

where x_i, y_i, and z_i are the modality space coordinate components of the ith indexed

direction. The algorithm developed in this research assumes that the voxel sampling

along the x and y coordinate directions is equal, but allows for a different sampling rate

along the z axis. Therefore, in terms of patient space coordinates, the directional vector

$\bar{h}$ is given by,

$$\bar{h}_{PS(i)} = [x_i, y_i, (z_i) \cdot (z\text{-}sp)] \qquad (4\text{-}12)$$

where z_sp is the factor that indicates the voxel sampling distance along the z axis

relative to the sampling distance along the x or y axes.

For each specified direction the variogram curve is obtained by computing the

values of the variogram, using equation (4-10), for all integer multiples of $|\bar{h}|$ that are

valid for the dimensions of the subvolume considered. For small values of $|\bar{h}|$, there

is a relatively large number of sampled values that contribute to the value of the

variogram. On the other hand, as $|\bar{h}|$ increases, fewer pairs of sampled values are

separated by that distance within the subvolume considered.

From a statistical viewpoint, the variogram becomes less reliable as the magnitude of $\bar{h}$ becomes large, because fewer pairs of sampled points contribute to the value of the variogram as $|\bar{h}|$ increases. This is why variogram values for distances beyond some application dependent value of $|\bar{h}|$ are usually ignored in geoscience applications. This value is typically on the order of one-half the maximum value of $|\bar{h}|$. The AFIT Kriging Algorithm developed in this research likewise permits portions of experimental variogram curves that are associated with the largest values of $|\bar{h}|$ to be truncated.

Measurement error is unavoidable in the real world. Whether due to patient movement or physical constraints of the MRI scanner, its presence is certain. Unfortunately, the error variance of a sample or estimate at an arbitrary location cannot be statistically computed given only a single acquisition MRI scan. By definition, for a single set of sampled values the value of a variogram corresponding to $\bar{h} = 0$ must be 0. Given the MRI modality space volume analyzed in this research is such a set of sample values, for distances of $\bar{h} = 0$,

$$Z(p_i + \bar{h}) = Z(p_i) \quad \Rightarrow \quad \gamma(\bar{h} = 0) \equiv 0 \tag{4-13}$$

Since the value of all directional variograms is zero at a separation distance of zero, no nugget effect is observed in variograms computed in this research.

Two types of variograms are used in this research to describe spatial variation. The first is the discrete directional variogram, given by equation (4-10). The discrete directional variogram describes the spatial variation of sampled points that lie along a specific, discrete direction. The composite directional variograms is the other type of variogram used in this research. The composite directional variogram also describes spatial variation, but an angular tolerance is allowed about the specified direction. All

pairs of sampled points that lie along directions that fall within the permitted angular tolerance are considered in the computation of composite variogram values. Therefore, directions specified for composite directional variograms are more general than those specified for discrete directional variograms. Composite directional variograms are introduced to increase the number of pairs of sampled values that factor into the computation of the variogram. As a result, composite directional variogram curves are generally less variable than discrete directional variogram curves computed along the same indexed direction. The incorporation of each of these directional variograms into the AFIT Kriging Algorithm is described in the following two sections of this chapter.

Computing Discrete Directional Variograms. The variogram defined by equation (4-10) is referred to in this research as a *discrete* directional variograms, because it describes the spatial variation of sampled points that lie along a specific, discrete direction. The data structure used to store the variogram values for each of the specified discrete directions is a two-dimensional array. Each row of the array corresponds to an indexed direction. The number of columns of the array equals the greatest integer distance magnitude (in modality space coordinates) that can be computed among the variograms for all specified directions. Therefore, given a two-dimensional array to store the variograms about a PTBE, the variogram associated with the ith indexed direction is represented by the ith column vector of the two-dimensional array. Similarly, the variogram value for $|\bar{h}| = 0$ is contained in the first row of each column vector; the variogram value for $|\bar{h}| = 1$ is contained in the second row of each column vector; and so on, where $|\bar{h}|$ represents relative distance in terms of modality space voxel coordinates. To determine absolute distances, the z axis sampling rate must be considered. Elements of the two-dimensional data structure for which no valid

relative voxel coordinate distance exists along any indexed direction are assigned the value *-1*.

Working under the assumption that MRI data exhibits a spatial dependency for small regions about the PTBE, the subvolumes from which the variograms are computed are purposefully relatively small. Unfortunately, this has the undesirable effect of significantly limiting the number of pairs of sampled values that contribute to the value of a discrete variogram for any given distance $\bar{h}$ The situation worsens as the magnitude of $\bar{h}$ increases. These factors often result in variogram curves that exhibit high degrees of variability. Fitting a model variogram that is considered representative of patient space variability through such an experimental variogram curve is challenging. A number of model variograms may often be fit through such a curve. However, without additional information it is not possible to determine which model best approximates reality.

Computing Composite Directional Variograms. *Composite* directional variograms are introduced in response to the undesirable characteristics observed in the discrete directional variograms that are computed. Since the subvolume of sampled values about each PTBE is minimized to satisfy the stationary requirement, only relatively small numbers of discrete variogram values can be computed. Highly variable discrete directional variograms are frequently observed when describing the spatial variation of these small subvolumes. Composite directional variograms do not constrain contributing pairs of sampled points to lie along a discrete direction. All pairs of sampled points that lie along any of several adjacent directions contribute to values of the composite variogram. Adjacent directions are given by directional vectors that are contained within a cone whose vertex is located at the origin, whose longitudinal axis lies along the direction specified by the vector $\bar{h}$, and whose surface is swept by rotating

the vector $(\bar{h} \pm ang\_tol)$ about the longitudinal axis, where ang_tol defines an angular tolerance about the directional vector $\bar{h}$. In the limit, an omnidirectional variogram results if the angular tolerance is $\pm 90^\circ$. An omnidirectional variogram considers only separation distance; its computations are independent of direction. It can be loosely considered an average of all possible directional variograms [Issak89] that can be computed over a given subvolume.

Composite variograms are incorporated into this research to utilize more of the information present in the ensemble of discrete directional variograms of each subvolume, information that would otherwise be ignored if one were to exclusively employ discrete directional variograms. For a given size subvolume, the use of composite directional variograms increases the number of samples that contribute to the computation of each variogram. It is hypothesized that if a larger number of sampled values contribute to each variogram curve, then the precision that a model variogram can fit experimental variogram values increases. The estimation error variance of kriged estimates theoretically decreases as the precision of model fitting is increased since estimates are computed based upon models that are assumed to represent the physical world. Figure 4-10 and Figure 4-11 provide examples of discrete directional variograms and corresponding composite directional variograms computed along the same directions about a PTBE.
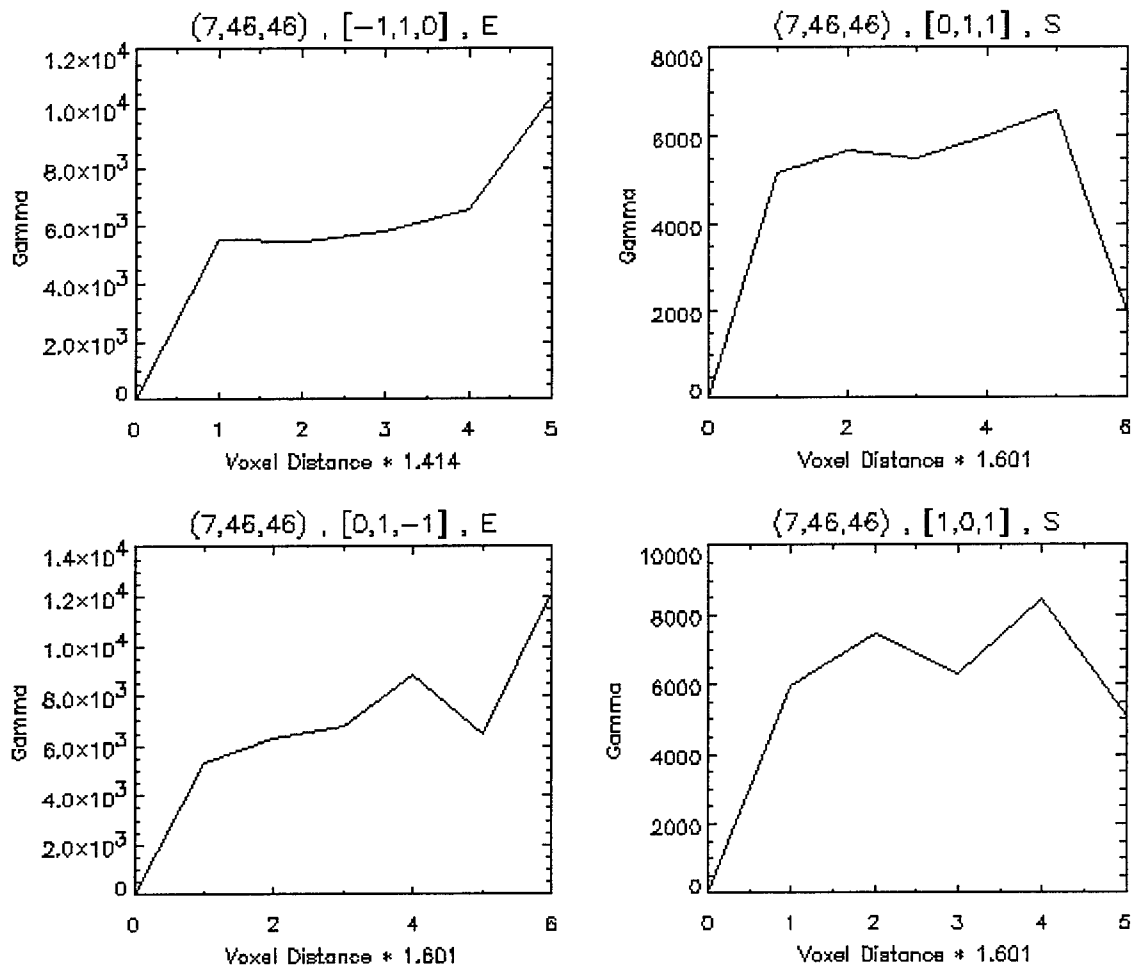
Figure 4-10. Discrete Directional Variograms
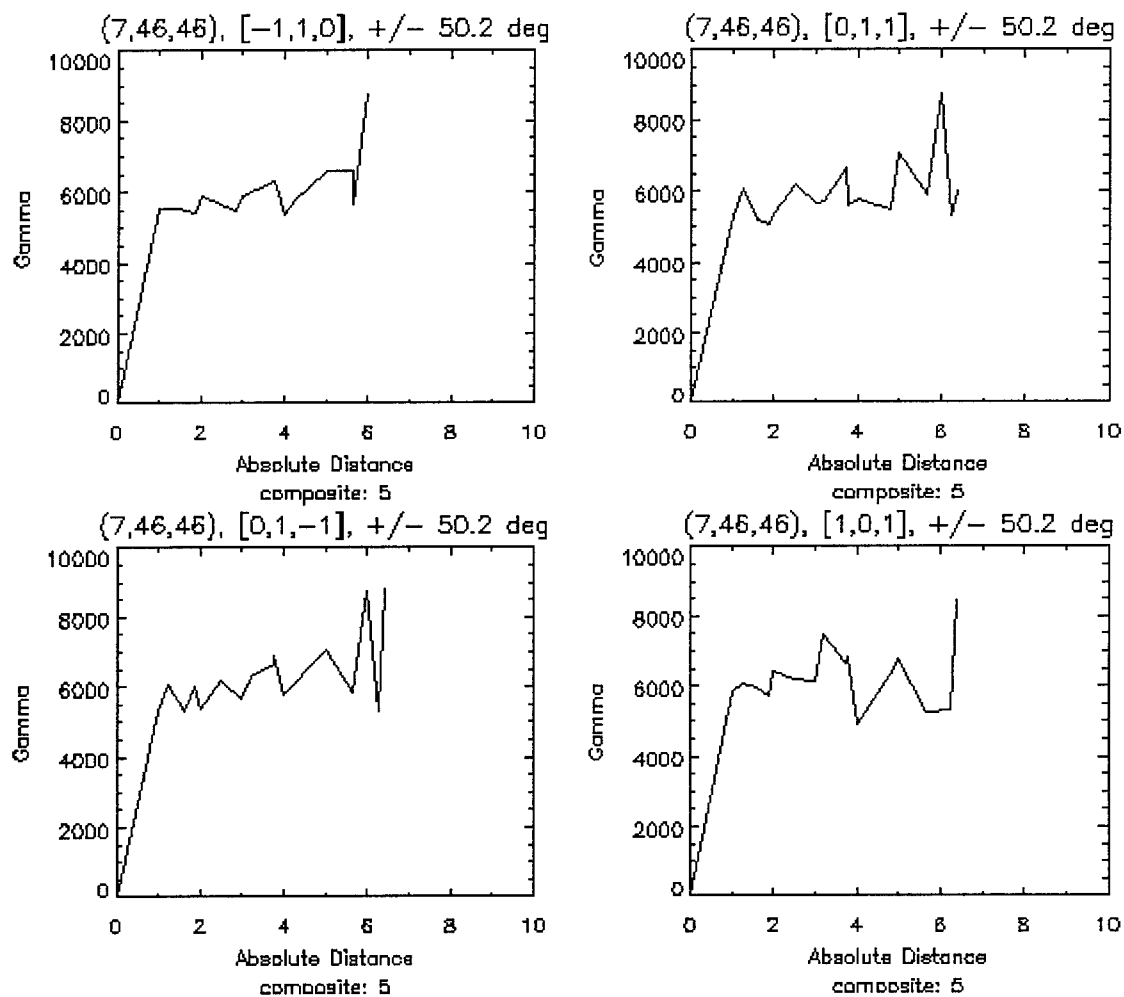
Figure 4-11. Composite Directional Variograms

Another reason for using composite variograms is related to the mathematical model that is constructed to describe the spatial dependency between a PTBE and any other neighboring point. The mathematical model is a function of three variables that specify position relative to three coordinate axes. The coefficients of each variable of the model are derived from the directional variograms whose directions are closest to being parallel with the coordinate axes that have been aligned with the anisotropic axes of the subvolume. Therefore, three directional variograms can predict the spatial variation for any point within the subvolume. This being the case, each of the three directional variograms identified should represent *general* characteristics of variation for the direction given by the corresponding coordinate axis. The use of composite directional variograms satisfies this goal, and in doing so, statistically increases the likelihood of decreasing the variability that is otherwise observed in discrete variograms along the same direction.

The use of composite variograms is also more appropriate when examining the structural analysis for the spatial variation along a direction that is not specified by one of the indexed directional vectors. Using discrete directional variograms, one of several methods must be employed. The variogram that is computed along the direction that is closest to being parallel to the queried direction can be used. Alternatively, the variograms that are computed along several directions that are closest to being parallel to the queried direction can be averaged using a weighted averaging technique to derive an interpolated variogram along the desired direction. On the other hand, the angular tolerance of composite variograms can be chosen so that all possible directions in three-dimensional space are accounted for; no further interpolation or averaging of variograms is required. The process of searching for a directional variogram to represent the spatial variation of a subvolume of interest along an arbitrary direction is required in later

stages of the AFIT Kriging Algorithm when orthogonal axes of continuity must be characterized.

Similar to the approach taken for discrete directional variograms, the data structure used to store composite variogram values for each of the indexed directions is a two-dimensional array. The two-dimensional array has as many columns as there are indexed directions. Discrete directional variograms are computed at regular separation distance intervals. Composite variograms, however, are computed at irregular separation distance intervals. Thus, the number of rows necessary to describe each composite directional variogram equals the number of unique relative distance coordinates that exist in all of the contributing discrete directional variograms. The number of rows of the two-dimensional array is set to the maximum number of unique relative distance coordinates that exists among all of the composite directional variograms that are computed.

For each contributing discrete directional variogram value, two additional two-dimensional arrays are required to store the patient space voxel distance (which takes into account the sampling rate along the z axis) and the number of sampled pairs considered in the computation of each discrete directional variogram value. Each two-dimensional array has the same number of columns and rows as the two-dimensional array that stores the values of each composite variogram. With the information contained in these two additional arrays, the iterative summations that were executed in the computation of each discrete variogram value can be reused, rather than recomputed, in the construction of each composite variogram value. This reduces a significant amount of processing that would otherwise be required to compute each composite directional variogram.

For example, assume t discrete variograms contribute to a given composite variogram. The value of each discrete directional variogram can be computed using equation (4-10) and incorporating the subscript dv to represent each discrete directional variogram, such that $dv = 1, 2, ... t$, as follows:

$$\gamma_{dv}(\bar{h}) = \frac{1}{2N_{dv}(\bar{h})} \sum_{i=1}^{N_{dv}(\bar{h})} [Z(p_i + \bar{h}) - Z(p_i)]^2 \qquad (4\text{-}14)$$

where there are $N_{dv}(\bar{h})$ pairs of data samples that are a vector distance $\bar{h}$ apart in each discrete variogram dv, $Z(p)$ is the value at the point p, and $Z(p+\bar{h})$ is the value at the point $(p+\bar{h})$. For each unique separation distance that is computed among all of the contributing discrete directional variograms for a given subvolume, the value of the composite variogram $\gamma_c(h)$ for a given separation distance h can be written as:

$$2\gamma_c(h) = \frac{1}{N_c(h)} \Big\{ \sum_{i=1}^{N_1(h)} [Z(p_i) - Z(p_i+h)]^2 + \sum_{i=1}^{N_2(h)} [Z(p_i) - Z(p_i+h)]^2 + \ldots$$
$$\ldots + \sum_{i=1}^{N_t(h)} [Z(p_i) - Z(p_i+h)]^2 \Big\} \qquad (4\text{-}15)$$

where,

$$N_c(h) = N_1(h) + N_2(h) + \ldots + N_t(h) \qquad (4\text{-}16)$$

$N_c(h)$ is the sum of the number of sampled pairs that are a distance h apart in each of the t contributing discrete variograms. Rather than recompute all sum of difference squared terms, the following equivalence is substituted into equation (4-15):

$$2\gamma_{dv}(h)N_{dv}(h) = \sum_{i=1}^{N_{dv}(h)} [Z(p_i) - Z(p_i+h)]^2 \qquad (4\text{-}17)$$

An equivalent form of equation (4-15) can therefore be written as:

$$2\gamma_c(h) = \frac{1}{N_c(h)}\left[2\gamma_1(h)N_1(h) + 2\gamma_2(h)N_2(h) + \ldots + 2\gamma_t(h)N_t(h)\right] \qquad (4\text{-}18)$$

where $\gamma_{dv}(h)$ is the value of a contributing discrete variograms at a separation distance h. $N_{dv}(h)$ is the number of sampled pairs that are a distance h apart in the contributing discrete variogram. In this manner, composite directional variograms are constructed from previously computed discrete directional variograms.

Identifying a Common Model to Represent Spatial Variation

When an estimate is obtained using kriging, the inclusion or exclusion of values of points that contribute to the estimate is a result of their membership status in the neighborhood of spatial dependency that exists about the PTBE. Therefore, a prerequisite requirement of the AFIT Kriging Algorithm before an estimate can be kriged is the determination of a subvolume about each PTBE whose dimensions are large enough to contain the neighborhood of spatial dependency about each PTBE. This requirement is accomplished by the task, *Assign Variogram Model*.

Once variograms are computed for each specified direction (regardless whether they are discrete or composite variograms) the next step of the structural analysis requires determining which model variogram most appropriately represents the ensemble of experimental variograms computed for a given subvolume. The subtask, *Assign Variogram Model*, also accomplishes this determination.

There are several reasons why model variograms are chosen to represent experimental variograms. First, model variograms are continuous functions that can be evaluated for any separation distance. Experimental variograms, on the other hand,

are computed for a discrete number of sampled locations and only represent a fraction of all possible separation distances within a subvolume. Second, experimental variograms do not guarantee the existence of a unique solution if incorporated into the ordinary kriging system of equations. The existence and uniqueness of a solution is ensured by fitting to the experimental variograms model functions that are known to be positive definite. By respecting the positive definite condition, one not only guarantees that a unique solution exists, but also that the solution is stable [Isaa89]; that is, weights are not computed which are considerably greater than 1 or considerably less than 0.

As discussed previously, five functions are considered in *Assign Variogram Model* as the domain of candidate models that each experimental variogram is compared to. They are the linear, spherical, gaussian, exponential, and hole-effect models. The successful use of these functions to model spatial variation of natural phenomena of the earth sciences is the basis for their inclusion into the AFIT Kriging Algorithm. Assuming no nugget effect, equations for the first four of these models are:

$$\gamma_{lin}(h) = kh \ , \qquad k = constant \tag{4-19}$$

$$\gamma_{gauss}(h) = C\left[1 - e^{-3\left(\frac{h}{a}\right)^2}\right] \tag{4-20}$$

$$\gamma_{exp}(h) = C\left[1 - e^{-3\frac{h}{a}}\right] \tag{4-21}$$

$$\gamma_{sph}(h) \;=\; \begin{cases} C\left[\dfrac{3h}{2a} - \dfrac{h^{3}}{2a^{3}}\right], & h \le a \\[2ex] C\,, & h > a \\[1ex] 0\,, & h = 0 \end{cases} \qquad\qquad (4\text{-}22)$$

where γ_{lin}, γ_{gauss}, γ_{exp}, and γ_{sph} give the functions for the linear, gaussian, exponential, and spherical variogram models, respectively. C is the value of the sill; h is the separation distance, (the independent variable); and a is the range, beyond which two voxels no longer influence one another. Examples of the gaussian, exponential and spherical models (for range $a = 3$) is provided in Figure 4-12.

From the five functions that have been introduced, variograms are categorized depending upon the presence or absence of the following traits: (1) no sill, likely indicating the extent of spatial dependency exceeds the subvolume field of view; (2) an asymptotic sill, indicating convergence to a minimal spatial dependency; (3) a flat sill,
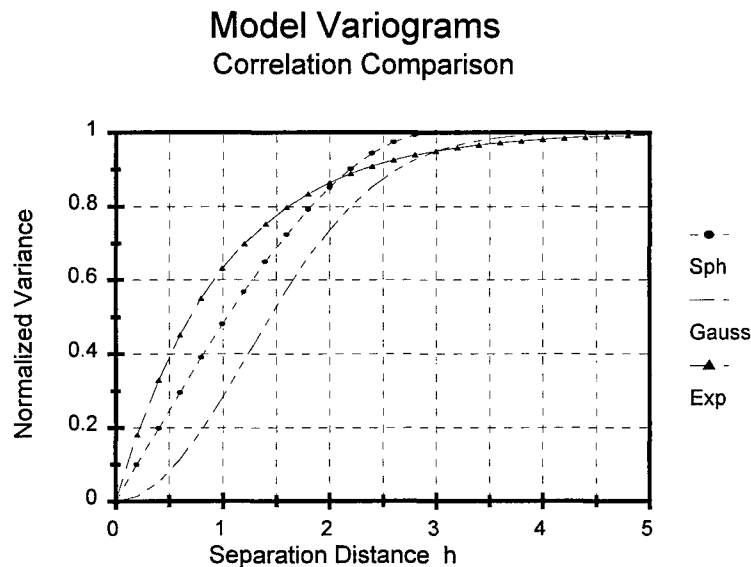
Figure 4-12. Variogram Models

indicating a minimum spatial dependency is reached; (4) parabolic behavior, indicating the existence of zonality with the subvolume; and (5) an inflection point near the origin, indicating extremely continuous phenomenon within the subvolume field of view. These categorized traits are all present in the domain of the five model functions. Similar decisions are made in visually fitting models to variograms.

The subtask, *Assign Variogram Model*, queries each directional variogram to determine if the variogram exhibits a linear behavior. Linear behavior is characterized by the absence of a sill and a trend of increasing variogram values with increasing separation distance. To make its determination, *Assign Variogram Model* analyzes the changes in slope between consecutive segments of the normalized variogram. The task also analyzes changes in slope between the average segment associated with smaller separation distances and the average segment associated with larger separation distances. Sufficiently small differences between these slopes indicates linear behavior. A threshold parameter specifies the maximum difference in the slopes that cannot be exceeded between these segments if the spatial variability is determined to be linear. If the variogram exhibits linear behavior, the AFIT Kriging Algorithm assumes dimensions of the subvolume about the PTBE are not large enough to contain the spatially dependent neighborhood about the PTBE. Therefore, the endpoints of the subvolume are moved by ±1 voxel along each coordinate axis and the structural analysis about the PTBE starts over.

If *Assign Variogram Model* determines that linear behavior is not present, then the variogram is analyzed to determine the presence or absence of a hole-effect. A hole-effect model is employed to characterize data with periodic spatial characteristics. Initially, the data is highly correlated, but the correlation lessens as separation distance increases. At some data dependent separation distance, minimum correlation is reached

and the trend reverses; that is, the data becomes more correlated with increasing separation distance. The trend may again reverse itself, following a damped periodic cycle. The spatial variation of the hole-effect model described is shown in Figure 4-3. Hole-effect behavior may be encountered when one material, or tissue, runs through that of another (within the subvolume and across the direction analyzed), thereby establishing *zones* within the subvolume. An example is shown in Figure 4-13, which depicts a material B embedded within a material A.
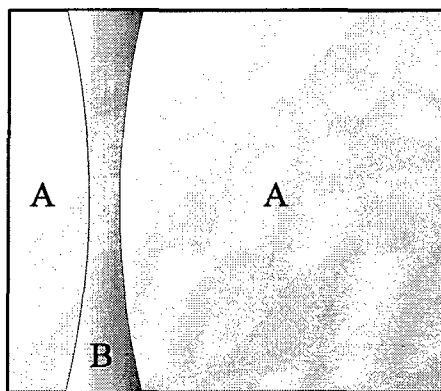
Figure 4-13. Embedded Zones

To determine the presence of a hole-effect, the maximum value of an experimental variogram is compared to the value of the variogram associated with the greatest separation distance within the subvolume, $\gamma(h_{max})$. If $\gamma(h_{max})$ is less than the product of the maximum variogram value and a user-initialized threshold, then the variogram possibly indicates the presence of a hole-effect. If so, the slopes of the last few segments of the normalized variogram are analyzed. The purpose of this additional analysis is to differentiate between a variogram that suggests a hole-effect from one that simply exhibits a high degree of variability due to the limited number of samples

available for analysis. An example of a variogram that requires additional analysis is shown in Figure 4-14. If the slopes are exclusively negative and spatial dependency continues to increase with increasing separation distance, a hole-effect is determined to be present. Otherwise, the hole-effect criteria is not satisfied and the search for a variogram model continues.
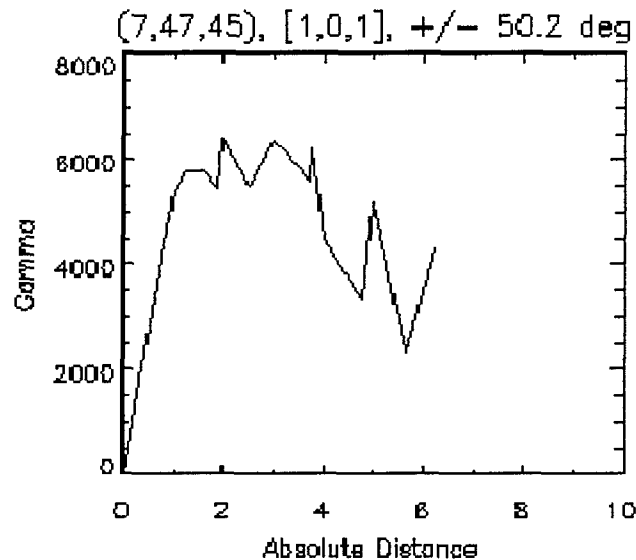
Figure 4-14. Candidate Hole-Effect Variation

Experimental variograms that exhibit a hole-effect are truncated so that only nearest neighbor voxels contribute to the subsequent model variograms. This truncation of variogram values for separation distances greater than that associated with minimum spatial correlation is accomplished for two reasons. First, it is consistent with the stationarity condition that is assumed about each PTBE. Second, it simplifies the derivation of the three-dimensional variogram model. Once variogram truncation occurs, the spatial variation of the nearest neighbor voxels can be modeled as a spherical function.

Since assignment of the linear model only serves to reinitiate the structural analysis using an incrementally larger subvolume about the PTBE, and since hole-effect

4-55

variograms are approximated over a subset of their computed values using the spherical model, the *Assign Variogram Model* task ultimately assigns one of three variogram model types to each direction analyzed: spherical, gaussian, or exponential.

Sampled values of a regionalized variable nearest a PTBE exert the most significant influence on the estimate. For short separation distances (assuming a fixed range and sill), the gaussian model exhibits the highest degree of correlation among the three models considered. (See Figure 4-12). Therefore, *Assign Variogram Model* initially checks an experimental variogram for gaussian characteristics. Unlike the spherical or exponential models, the gaussian model possesses an inflection point near the origin and maintains a higher degree of correlation between voxels with the shortest separation distances. *Assign Variogram Model* determines if a variogram is modeled by a gaussian function depending upon the presence of an inflection point near the origin.

Existence of the inflection point is determined in the following manner. Two user-initialized thresholds specify bounds for the slopes of consecutive segments of the normalized variogram. Though the AFIT Kriging Algorithm can be easily modified to automatically and adaptively determine these threshold values, this process is presently not implemented. The threshold values are entered as hard coded parameters based upon observed spatial statistics. The initial segment slope is not permitted to exceed the first threshold and the trailing segment slope is not permitted to be less than the second threshold. If the slopes of the two consecutive variogram segments satisfy these conditions, then the experimental variogram is modeled using a gaussian function. If the variogram is not gaussian, *Assign Variogram Model* continues further analyzing the subvolume to determine if it exhibits either exponential or spherical characteristics.

Assign Variogram Model distinguishes between the exponential and spherical models based upon their sill. The sill of the spherical model maintains a constant value

once its separation distance exceeds its range. The exponential model, on the other hand, reaches its sill asymptotically; its practical range is defined as the distance at which the variogram value is 95% of the sill [Isaa89]. Exploiting this characteristic, a user-initialized threshold sets a limit on the magnitude of the average slope of the normalized variogram over the largest separation distances. If the average slope of the segments of the normalized variogram beyond the approximated range exceeds this threshold, the variogram is modeled by an exponential function. Otherwise, the variogram is modeled by a spherical function. Beyond this limit the spatial variation of the subvolume is assumed to behave exponentially. Below this threshold the variation is assumed to behave spherically.

In this manner, one of three variogram models is assigned for each direction analyzed about a PTBE to characterize the general spatial variation along a given direction. The model that occurs most frequently about the PTBE is designated the *common model*. Before kriging, *Structurally Analyze and Krige* must generate a single mathematical model to represent spatial variation along any direction as a function of separation distance. The common model specifies the variogram model that is used to reduce all directional variograms about a PTBE to a single, three-dimensional mathematical model. Errors that are introduced when estimating values along a direction whose assigned model of spatial variation was different than the common model will be quantified in the estimation error variance that is obtained as a kriging by product. The spatial variation described as a function of distance by the three-dimensional mathematical model will bias the weights of each of the contributing nearby voxels accordingly.

Determining the Local Neighborhood of Spatial Dependency

Having described the spatial variation about a PTBE along all specified directions using experimental variograms, the structural analysis requires that the information be compiled and a local region, or neighborhood, of spatial dependency about the PTBE be determined. One cannot assume the data varies isotopically about the PTBE. In general, the spatial variation changes at different rates along different directions. The AFIT Kriging Algorithm accounts for these geometric anisotropies in this task by adapting, not only the model of spatial variation, but also the extent and orientation of the spatially dependent neighborhood about each PTBE in accordance with spatial information obtained from the experimental variograms. A decomposition of *Determine Local Neighborhood* is found in Table 4-9. Its three component subtasks are described in the subsections of this chapter that follow.

Table 4-9. Determine Local Neighborhood

Task	Task Name	Description
3.4.	Determine Local Neighborhood	Determine ellipsoid region about the PTBE for which included voxels are determined to be spatially dependent upon one another.
Subtask	Subtask Name	Description
3.4.1.	Extract Range and Sill	The range and sill values of each directional variogram are optimally determined.
3.4.2.	Determine Axes of Continuity	Construct an ellipsoid neighborhood about the PTBE. The major and minor axes of the ellipsoid should approximately align with the directions of the largest and smallest ranges, respectively.
3.4.3.	Align Anisotropic and Coordinate Axes	Compute the rotational transformation necessary to align the anisotropic ellipsoid axes with the orthogonal modality space coordinate system.

Extracting the Range and Sill from Directional Variograms. For each direction that is analyzed about a PTBE, the neighborhood of spatial dependency must be determined. The sill of the associated directional variogram must also computed. The subtask, *Extract Range and Sill*, determines these values for each experimental composite variogram.

Variogram values for a given subvolume that are associated with the largest separation distances are theoretically the most statistically unreliable since the fewest number of pairs of sampled voxels contribute to their values. For this reason, the length of each experimental variogram can be truncated for separation distances that exceed a user-defined threshold. The threshold is defined in terms of a percentage of the maximum separation distance analyzed. After truncation, a variogram model is fit to the experimental variogram to determine the value of the range and sill. The model type is the common model that *Assign Variogram Model* determines occurs most frequently about the PTBE. The common model is optimally fitted to the each experimental variogram using a least squares error fitting algorithm. Each experimental variogram value is statistically weighted by the number of voxel pairs that contributed to its derivation when determining the error between the experimental and model variogram curves.

Approximating the Axes of Spatial Continuity. The purpose of structurally analyzing data about a PTBE is to model the *rate* of spatial variation and the *range* of spatial dependency present in that variation. The rate of spatial variation is modeled by the common model that *Assign Variogram Model* determines, using range and sill parameters for each direction that *Extract Range and Sill* establish. The subtask *Determine Local Neighborhood* models the ensemble of ranges for each experimental

variogram to approximate the local neighborhood of spatial dependency about each PTBE.

The neighborhood of spatial dependency may be rendered as a surface that encloses the PTBE. If the range vectors of each experimental variogram are plotted from the PTBE along their corresponding direction, their terminal endpoints would intersect the surface that specifies the neighborhood of spatial dependency. In general, the surface is not symmetrical. Yet it must be modeled to obtain a spatially dependent neighborhood of points that can be kriged. An ellipsoid is chosen to represent each of these neighborhood surfaces. This does not imply kriging weights of contributing points within the surface are determined in accordance with a spherical model. Rather, the ellipsoid is the geometric surface that segregates voxels that lie within the kriging neighborhood from those that do not.

The AFIT Kriging Algorithm permits the ellipsoid to assume six degrees of freedom to enhance its approximation of each neighborhood of spatial dependency. The radii of each ellipsoid semiaxis is variable, as is its orientation; the ellipsoid may be rotated about any of its three semiaxes. The subtask *Determine Axes of Continuity* determines each of these parameters. The concept to determine them is elementary; the implementation, however, requires a means to resolve ambiguous directions of continuity. The concept is described in the following paragraph.

Given ranges of spatial dependency for each experimental variogram, the radius of the major semiaxis of the ellipsoid is aligned with the range vector corresponding to the direction of maximum continuity. Continuity is defined as the rate of growth of the variogram $\gamma(h)$ for small separation distances, h [Davi77]. The radius length equals the magnitude of the range vector. The direction of maximum continuity is the direction for which the spatial variation is observed to change most slowly. The range of the

associated experimental variogram is the greatest of all directional variograms analyzed about a PTBE. If the range vector corresponding to the direction of minimum continuity is perpendicular to the direction of maximum continuity, then the direction of minimum continuity specifies the radius of the minor semiaxis of the ellipsoid. Its magnitude equals the magnitude of the corresponding range vector. Unfortunately, the implementation is not that straightforward. In general, directions of maximum and minimum continuity are not perpendicular. Furthermore, equivalent maximum or minimum ranges are frequently observed for multiple directions. An example is shown in Figure 4-15.

Range vs Indexed Direction
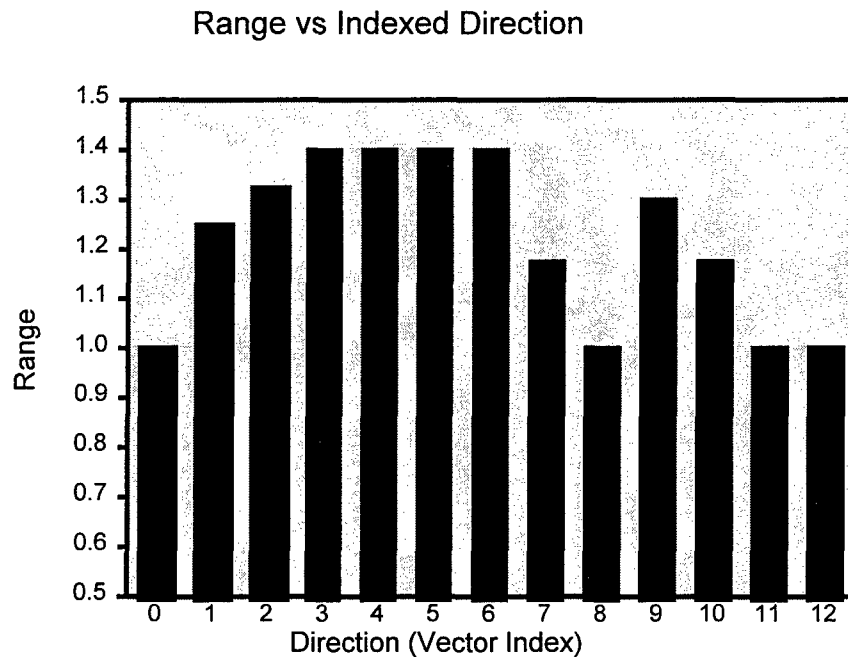
Figure 4-15. Axes of Ambiguity

The maximum range in Figure 4-15 is 1.4 voxel units, but four directional variograms (given by directional vector indices 3, 4, 5 and 6) exhibit this range. Four directional variograms (given by directional vector indices 0, 8, 11 and 12) exhibit an equivalent minimum range. In this and similar instances the ambiguity must be

resolved; unique directions of maximum and minimum continuity must be determined so that the alignment of the ellipsoid best approximates the axes of continuity observed in the experimental variograms.

Determine Axes of Continuity disambiguates multiple and nonperpendicular directions of maximum and minimum continuity by analyzing ranges of neighboring directional vectors that surround the directional vector of interest. *Determine Axes of Continuity* averages the ranges associated with directional vectors that surround the directional vector of interest to determine an average range of continuity for each specified direction. For instance, (referencing the directional vectors indexed in Table 4-3), if the direction of interest lies along the z axis (given by vector index 2), then the ranges associated with directions given by vector indices 9, 10, 11 and 12 are also analyzed and averaged with the range of vector index 2 to arrive at an *average* range for vector index 2. The average ranges for all other directions are similarly computed. The previous example, recomputed using average ranges, is shown in Figure 4-16.

Although the use of average ranges lessens the probability that multiple directions of maximum or minimum continuity exist, it does not eliminate the possibility. Furthermore, there is no guarantee that directions of maximum and minimum continuity (using average ranges) will be perpendicular to one another. This is significant because the objective of *Determine Local Neighborhood* is to approximate the alignment of the orthogonal semiaxes of an ellipsoid with the directions of maximum and minimum continuity that are, in general, not orthogonal. Shearing of the ellipsoid semiaxes to nonorthogonal configurations is not implemented in this implementation of the AFIT Kriging Algorithm. Therefore, to obtain the most accurate approximation of the maximum and minimum axes of continuity, *Determine Axes of Continuity* does not

resolved; unique directions of maximum and minimum continuity must be determined so that the alignment of the ellipsoid best approximates the axes of continuity observed in the experimental variograms.

Determine Axes of Continuity disambiguates multiple and nonperpendicular directions of maximum and minimum continuity by analyzing ranges of neighboring directional vectors that surround the directional vector of interest. *Determine Axes of Continuity* averages the ranges associated with directional vectors that surround the directional vector of interest to determine an average range of continuity for each specified direction. For instance, (referencing the directional vectors indexed in Table 4-3), if the direction of interest lies along the z axis (given by vector index 2), then the ranges associated with directions given by vector indices 9, 10, 11 and 12 are also analyzed and averaged with the range of vector index 2 to arrive at an *average* range for vector index 2. The average ranges for all other directions are similarly computed. The previous example, recomputed using average ranges, is shown in Figure 4-16.

Although the use of average ranges lessens the probability that multiple directions of maximum or minimum continuity exist, it does not eliminate the possibility. Furthermore, there is no guarantee that directions of maximum and minimum continuity (using average ranges) will be perpendicular to one another. This is significant because the objective of *Determine Local Neighborhood* is to approximate the alignment of the orthogonal semiaxes of an ellipsoid with the directions of maximum and minimum continuity that are, in general, not orthogonal. Shearing of the ellipsoid semiaxes to nonorthogonal configurations is not implemented in this implementation of the AFIT Kriging Algorithm. Therefore, to obtain the most accurate approximation of the maximum and minimum axes of continuity, *Determine Axes of Continuity* does not

Average Range vs Indexed Direction

Figure 4-16. Resolution of Directional Ambiguity

estimate the orientation of the ellipsoid semiaxes strictly as a function of the average ranges that are computed for each direction. Rather, a range tolerance is introduced as a disambiguation mechanism to enable the convergence of the approximation to a unique triplet of orthogonal major, minor and mid directions of spatial continuity.

The range tolerance permits pairs of directions whose ranges are near the maximum and minimum average ranges to be considered if each directional pair is closer to exhibiting perpendicularity than the directional pair associated with the maximum and minimum average ranges. Initially the range tolerance is very small so that the directional pair associated with the maximum and minimum average ranges receives consideration first. The closer this directional pair is to being perpendicular, the more likely it will be designated as the pair that is used to align the major and minor semiaxes of the ellipsoid. As this directional pair deviates from perpendicularity, the algorithm iterates and with each iteration the range tolerance increases. As the

range tolerance increase additional directions with ranges that are near to the maximum and minimum average ranges are considered and analyzed for their *closeness* to perpendicularity. The *closeness* of two directions to perpendicularity is measured in terms of the angular distance between each pair of candidate directions.

Three orthogonal axes of continuity define the three semiaxes of the ellipsoid that approximate the neighborhood of spatial dependency about the PTBE. The direction of maximum continuity of the subvolume determines the orientation of the major semiaxis of the ellipsoid. The range associated with the direction of maximum continuity specifies the length of the radius along the major semiaxis of the ellipsoid. The projection of the range vector along the direction of minimum continuity onto a plane that is normal to the major semiaxis determines the minor semiaxis orientation and radius. The mid semiaxis of the ellipsoid is the axis that is orthogonal to the major and minor semiaxes. The radius of the mid semiaxis equals the range of the directional variogram whose direction is closest to parallel to the mid semiaxis. The local kriging neighborhood about the PTBE is therefore defined by an ellipsoid that is centered about the PTBE and whose semiaxes orientation is given by the subvolume axes of maximum, mid and minimum continuity.

Aligning the Neighborhood Axes of Continuity with the Modality Space Coordinate Axes. The previous subtask approximates the local region of spatial dependency about a PTBE by an ellipsoid that is oriented so voxels that exhibit a spatial dependency upon one another are assumed to be enclosed by the ellipsoid surface, and voxels that are spatially independent of the local region about the PTBE lie outside the ellipsoid surface. The *Align Anisotropic and Coordinate Axes* subtask determines the translational and rotational transformations that are necessary to map the coordinate space established by the orthogonal axes of continuity to the modality space coordinate

4-65

space. Modality space voxel positions, on the other hand, are given in modality space coordinates. A mathematical model of spatial variation is to be derived in terms of modality space coordinates so that spatial variability can be modeled for locations that coincide with the sampled modality space data. Measures of modeled spatial variability, given by $\gamma(\bar{h})$, are necessary for each sampled voxel about a PTBE as well as for each PTBE to obtain each kriging estimate. Each coordinate space consists of orthogonal axes that may be translated so that its origin coincides with the PTBE. A three-dimensional rotational transformation suffices to convert the coordinates of one system to the coordinates of the other. The subtask, *Align Anisotropic and Coordinate Axes*, computes the rotational transformation necessary to align the semiaxes of the ellipsoid neighborhood with the x, y, and z axes of the modality space coordinate system.

The target modality space coordinate system is assumed to be a right-handed Cartesian coordinate system such that MRI slices are acquired along the z axis, each parallel to the xy plane. Polar coordinates are given such that a point p_{cart} in Cartesian coordinates is equivalent to the point p_{polar} in polar coordinates; that is,

$$p_{cart}(x, y, z) = p_{polar}(r, \theta_{xz}, \phi_z) \qquad (4\text{-}23)$$

where x, y and z represent Cartesian space coordinates; r is the magnitude of the vector $\bar{p}$ drawn from the origin to the point p; θ_{xz} is the angle the vector $\bar{p}$ rises above the xz plane; and ϕ_z is the angle subtended when the vector $\bar{p}$ is rotated counterclockwise about the y axis from the positive z axis. (See Figure 4-17.)
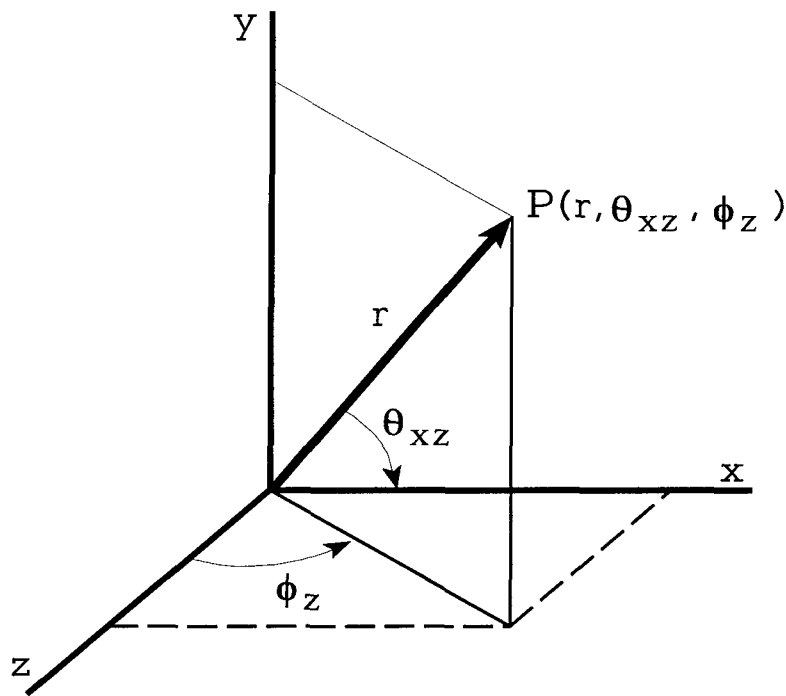
Figure 4-17. Polar Coordinates

The polar coordinates of the vector that describes the range and orientation of the major semiaxis of the ellipsoid neighborhood are computed. Using these coordinates, the major semiaxis of the ellipsoid is aligned with the modality space y axis in the following manner: first, the major semiaxis vector is rotated about the y axis by $-\phi_z{}^\circ$ to align it with the modality space yz plane; then, the major semiaxis vector is rotated about the x axis by $-\theta_y{}^\circ$ to align it with the y axis, such that,

$$\theta_y = (90 - \theta_{xz}).$$
(4-24)

The vector that describes the range and orientation of the minor semiaxis of the ellipsoid neighborhood undergoes the same rotations described above before its equivalent polar coordinates are computed. Once the angular displacement of the minor

4-67

semiaxis vector from the x axis is determined, the minor semiaxis vector is rotated by this amount about the y axis to align it with the x axis. Since the major ellipsoid semiaxis vector is already aligned with the y axis, this last rotation about the y axis will not alter the position of the major semiaxis vector. By definition of orthogonality, the mid semiaxis vector must align with the z axis. Therefore, with knowledge of the polar components θ and ϕ for the major semiaxis, and of ϕ for the minor semiaxis, the necessary rotational transformation to align the orthogonal axes of continuity with the modality space Cartesian coordinate system is computed.

Generating a Three Dimensional Mathematical Model to Describe Modality Space Spatial Variation

All information necessary to generate a three-dimensional modality space mathematical model of the spatial variation about a PTBE is obtained in the previous subtasks of *Structurally Analyze and Krige*: (1) drift is removed from each modality space subvolume; (2) directional variograms are computed along several directions using stationary residual data; (3) a variogram model characterizes the ensemble of experimental variograms; (4) directions of maximum and minimum continuity are identified; (5) an ellipsoid surface is scaled and oriented to approximate the neighborhood of spatial dependency; and (6) a three-dimensional rotational transformation to align the semiaxes of the ellipsoid neighborhood with the modality space coordinate axes is derived. The subtask *Generate Mathematical Model*, accomplishes the final step necessary before an estimate can be kriged. A three-dimensional mathematical model is generated to describe the spatial variation of the local neighborhood about a PTBE as a function of modality space coordinates.

In general, modality space data is not isotropic; the rate of spatial variation varies as a function of direction. The AFIT Kriging Algorithm accounts for such spatial variability, but assumes any such variability is strictly geometric. That is, the range of spatial dependency changes as a function of direction, but the sill of each variogram is constant. This assumption simplifies the derivation of the three-dimensional mathematical model by excluding the need to incorporate nested structures into the model. The assumption does not affect the value of kriged estimates because it does not change the range computed along each direction. Kriging weights are sensitive to changes in the range of spatial dependency; they are unaffected by variogram scaling operations that change the sill of a variogram.

Using the rotational transformation from *Align Anisotropic and Coordinate Axes*, the major, mid and minor semiaxes of the ellipsoid neighborhood are aligned with the y, z, and x modality space coordinate axes, respectively. The variogram models that correspond to each semiaxis of the ellipsoid neighborhood now correspond to each modality space coordinate axis. *Generate Mathematical Model* calculates the ratios between the ranges of spatial dependency along each modality space axis to establish a relationship between the rates of variation along each of the axes. This relationship enables a standard model to represent spatial variation along any direction. Using this relationship, range-normalized variograms are computed from the variogram models associated with each modality space coordinate axis[2] Range-normalized variograms are obtained by substituting the separation distance variable h with a reduced distance variable h/a, where a represents the range of a given variogram.

---

[2] The range of a range-normalized variogram is the value 1.

For example, consider the three directional variogram models depicted in Figure 4-18. The three variograms correspond to the orthogonal axes of continuity determined in the subtask, *Determine Axes of Continuity*. Assume the variogram modes that correspond to the major ellipsoid semiaxis is given by $\gamma_{max}(h)$, where h is separation distance. Similarly assume $\gamma_{min}(h)$ and $\gamma_{mid}(h)$ represent the model variograms that correspond to the minor and mid semiaxes of the ellipsoid, respectively. If one assumes
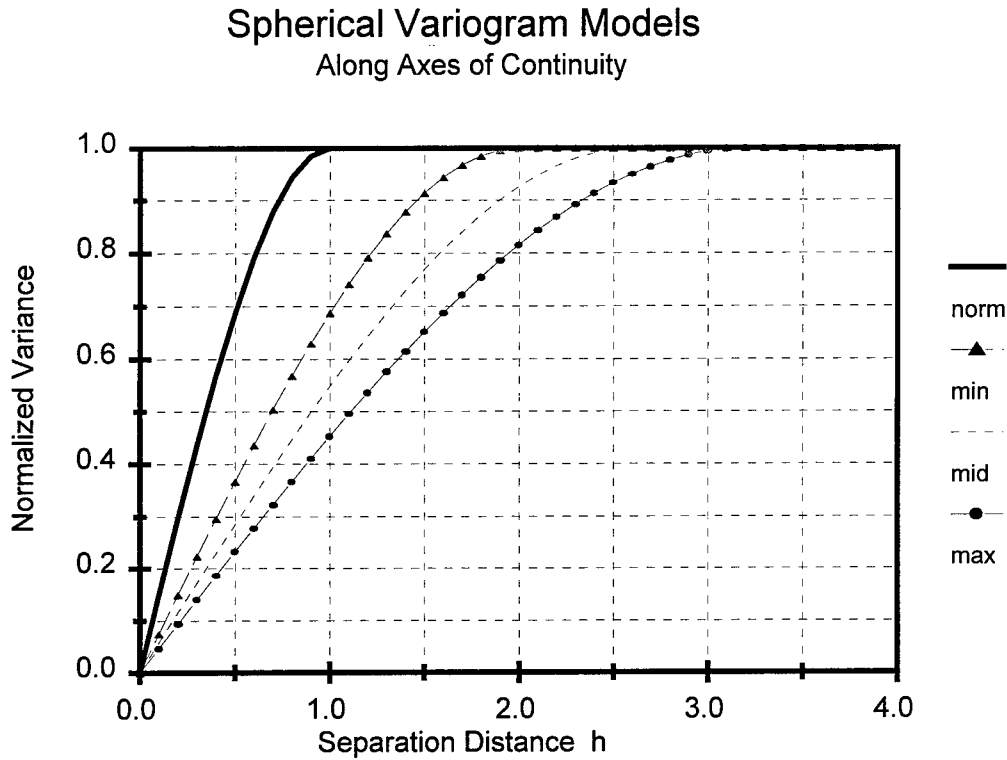
Figure 4-18. Range-Normalized Variogram

a_{max}, a_{mid} and a_{min} represent the ranges corresponding to the maximum, mid and minimum axes of continuity, respectively (as shown in Figure 4-18), then:

$$\gamma_{max}(h) = \gamma_{norm}\left(\frac{h}{a_{max}}\right) \tag{4-25}$$

$$\gamma_{mid}(h) = \gamma_{norm}\left(\frac{h}{a_{mid}}\right) \tag{4-26}$$

$$\gamma_{min}(h) = \gamma_{norm}\left(\frac{h}{a_{min}}\right) \tag{4-27}$$

where γ_{norm} represents the range-normalized variogram model. Given a vector distance $\bar{h}$ where h_{max} is the component in the direction of maximum continuity, h_{mid} is the component in the direction of mid continuity, and h_{min} is the component in the direction of minimum continuity, the variogram model $\gamma(\bar{h})$ can be written as,

$$\gamma(\bar{h}) = \gamma(h_{min}, h_{max}, h_{mid}) = \gamma_{norm}(h_{norm}) \tag{4-28}$$

where,

$$h_{norm} = \sqrt{\left(\frac{h_{min}}{a_{min}}\right)^2 + \left(\frac{h_{maj}}{a_{maj}}\right)^2 + \left(\frac{h_{mid}}{a_{mid}}\right)^2} \tag{4-29}$$

Because the range of a range-normalized variogram is 1, the range-normalized variogram models can be rewritten as:

$$\gamma_{gauss_{norm}}(h_{norm}) = C\left[1 - e^{-3h_{norm}^2}\right] \tag{4-30}$$

$$\gamma_{exp_{norm}}(h_{norm}) = C\left[1 - e^{-3h_{norm}}\right] \tag{4-31}$$

4-71

$$\gamma_{sph_{norm}}(h_{norm}) = \begin{cases} C\left[\dfrac{3h_{norm}}{2} - \dfrac{h_{norm}^{3}}{2}\right] , & h_{norm} \leq 1 \\[2em] C , & h_{norm} > 1 \\[1em] 0 , & h_{norm} = 0 \end{cases} \qquad (4\text{-}32)$$

In this manner, a three-dimensional anisotropic variogram model is constructed to describe spatial variation as a function of range-normalized distance, h_{norm}. The mathematical model is used to compute elements of each of the semivariance matrices of the ordinary kriging equations, from which kriging weights are obtained for each voxel that lies in the kriging neighborhood about a PTBE.

Kriging Voxels in the Neighborhood of Spatial Dependency to Obtain Modality Space Estimates

Given that the preceding three-dimensional structural analysis determines a spatially dependent local neighborhood of stationary residuals and a three-dimensional variogram model about a PTBE, an estimate may be obtained using kriging. Each estimate requires generating the system of ordinary kriging equations shown in equation (4-33),

$$\begin{bmatrix} C_{11} & \cdots & C_{1n} & 1 \\ \vdots & \ddots & \vdots & \vdots \\ C_{n1} & \cdots & C_{nn} & 1 \\ 1 & \cdots & 1 & 0 \end{bmatrix}_{(n+1)\times(n+1)} \begin{bmatrix} w_1 \\ \vdots \\ w_n \\ \mu \end{bmatrix}_{(n+1)} = \begin{bmatrix} C_{10} \\ \vdots \\ C_{n0} \\ 1 \end{bmatrix}_{(n+1)} \qquad (4\text{-}33)$$

where: C_{ij} is the semivariance between the ith and j^{th} subvolume values contained within the ellipsoid neighborhood; and w_i is the weight of the ith value of the subvolume

about the PTBE. The AFIT Kriging Algorithm task, *Krige Neighborhood Voxels*, generates and solves the ordinary kriging equations for each PTBE.

To obtain the values for the weights w_i, equation (4-33) is rewritten by multiplying both sides of the equation by the inverse of the *(n+1)* x *(n+1)* semivariance matrix on the left side of the equation to obtain:

$$\begin{bmatrix} w_1 \\ \vdots \\ w_n \\ \mu \end{bmatrix} = \begin{bmatrix} C_{11} & \cdots & C_{1n} & 1 \\ \vdots & \ddots & \vdots & \vdots \\ C_{n1} & \cdots & C_{nn} & 1 \\ 1 & \cdots & 1 & 0 \end{bmatrix}^{-1} \begin{bmatrix} C_{10} \\ \vdots \\ C_{n0} \\ 1 \end{bmatrix} \tag{4-34}$$

Sampled values s_i of the ellipsoid neighborhood about the PTBE are averaged in a linear weighted combination, using the weights w_i computed in equation (4-34) to generate a residual estimate $\hat{r}_0$ of the PTBE, as follows:

$$\hat{r}_0 = \sum_{i=1}^{n} w_i s_i \tag{4-35}$$

To obtain the estimate of the corresponding modality space value, the drift that had been modeled for the PTBE in the task *Characterize and Remove Drift* must be added to the residual estimate $\hat{r}_0$. If vol_med_0, col_med_0, row_med_0 and $slice\_med_0$ represent the median main effects for the subvolume, column, row and slice of the PTBE, then the modality space estimate $\hat{s}_0$ is given by equation (4-36).

$$\hat{s}_0 = \hat{r}_0 + vol\_med + col\_med_0 + row\_med_0 + slice\_med_0 \tag{4-36}$$

Each estimate is linear, unbiased, and optimal. It is linear in the sense that it is computed from a weighted linear combination of available known values. It is unbiased in the sense that the weights which determine the magnitude of contribution

from each known value sum to 1. Kriging is said to produce an optimal estimate in the sense that the *model* error variance is minimized. Though an objective of the AFIT Kriging Algorithm is to minimize the variance of estimation errors, in practice, actual errors are unknown since the value of the PTBE is unknown. Therefore, actual error variance cannot be guaranteed to be minimized. Ordinary kriging can only minimize the variance of estimation errors *based upon the spatial variation model employed.*

If the *(n+1)* x *(n+1)* and *(n+1)* semivariance and *(n+1)* weight matrices of equation (4-33) are redefined as **A**, **B** and **W**, respectively, equation (4-33) is rewritten as,

$$A \cdot W = B \qquad (4\text{-}37)$$

The ordinary kriging estimation error variance $\tilde{\sigma}^2_{OK}$ is then given by equation (4-38),

$$\tilde{\sigma}^2_{OK} = \tilde{\sigma}^2 - W \cdot B \qquad (4\text{-}38)$$

where $\tilde{\sigma}^2$ is the sill of the variogram model that describes the spatial variation about the PTBE. The computation of the estimation error variance associated with a given kriged estimate concludes an iteration of the top level task, *Structurally Analyze and Krige*. An iteration of the task is initiated for each modality space location that an estimate has been identified to be obtained.

Chapter V

INTERPOLATION RESULTS USING THE AFIT KRIGING ALGORITHM

The modality space volume from which the validation data and subsequent results of this research are generated is a data set consisting of 256 columns by 256 rows by 128 sagittal slices of a T1 weighted gradient echo MRI scan of a human head[1]. The column:row:slice voxel dimension aspect ratio is 1.0:1.0:1.25 ; that is, the interslice voxel spacing is 1.25 times greater than the intraslice voxel spacing. Aside from an input routine written in C to read the ANALYZE-formatted modality space data, the AFIT Kriging Algorithm described in Chapter IV is coded exclusively using the IDL programming language.[2]

The validation data set provides a set of known true values that correspond to each interpolated estimate, This is accomplished in the AFIT Kriging Algorithm task, *Generate Validation Data.* The validation volume is generated from every other column, row and slice of the original modality space volume. The volume is rendered in Figure 5-1. Figure 5-2 is a cutaway rendition of the validation volume. Figure 5-3 and Figure 5-4 show examples of a sagittal slice captured midway through the original modality space volume and the corresponding slice of the validation volume, respectively. The field of view remains constant between each slice, but the resolution of the original modality space data slice is twice that of the coincident validation data slice.

---

[1] Data is provided courtesy of Mallickrodt Institute of Radiology, Washington University School of Medicine.

[2] IDL is an analysis and visualization programming environment developed and distributed by Research Systems, Inc.
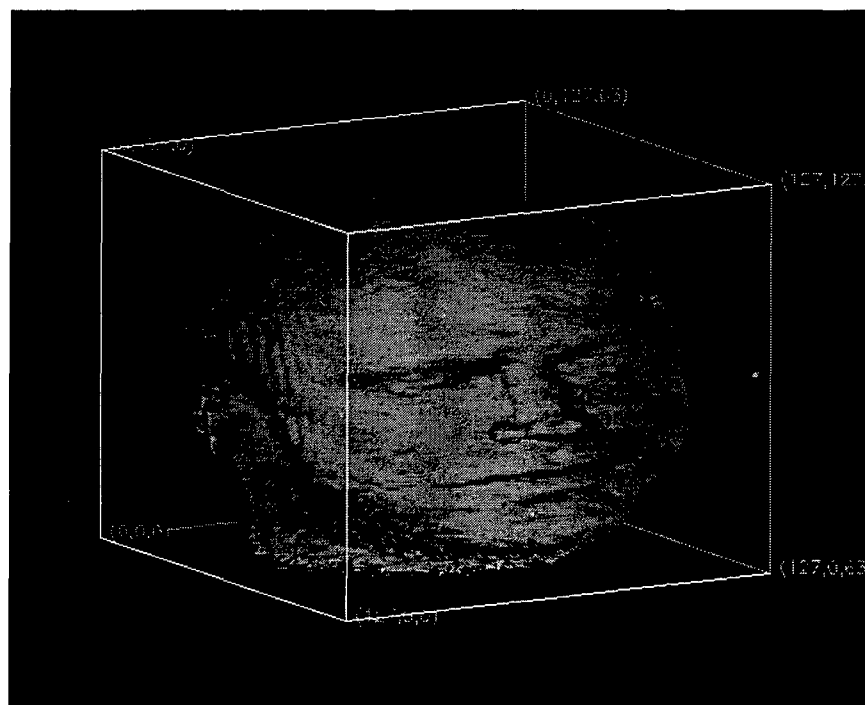
Figure 5-1. Validation Volume
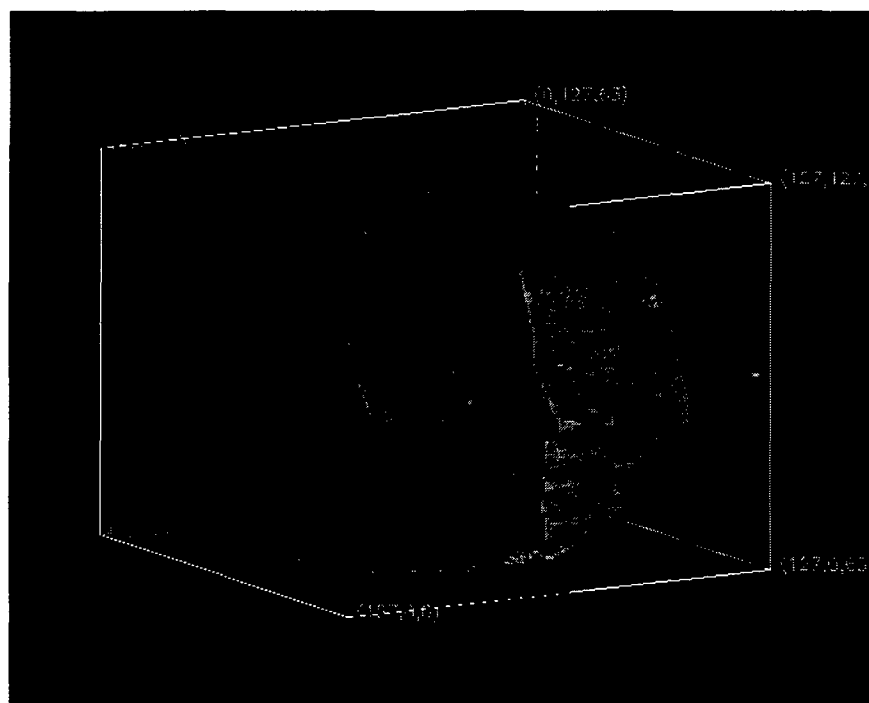
Figure 5-2. Validation Volume Cutaway

Figure 5-3. Original Modality Space Data Slice

Figure 5-4. Validation Data Slice

Given a validation volume, the AFIT Kriging Algorithm task, *Identify Border Regions*, identifies the border regions of the volume. Identification of border regions requires segmentation of the volume of interest from the background voxels, edge enhancement and thresholding of each modality space slice, and the generation of a resolution enhanced binary volume. Segmentation of the volume of interest from background voxels requires the user to specify a segmentation threshold value. The threshold value differentiates between background values and values that correspond to the volume of interest. Voxel values of the modality space validation data set range from 0 to 3001. Results published in this chapter are obtained using a segmentation threshold of 240 to segment the volume of interest from the background.

The kriging algorithm proceeds to identify voxels that lie in border regions of the interpolated volume. Estimates of these voxels are obtained using kriging. The task, *Edge Enhance and Threshold Slices* applies a 3x3 Sobel edge detection operator to each modality space validation slice to identify high gradient areas of each slice. Figure 5-5 depicts the intensity normalized grayscale image after applying the Sobel operator to the validation slice shown in the previous figure. The user enters a gradient threshold value to indirectly specify the degree of inhomogeneity that must exist about a voxel for the voxel to be classified as a border region voxel. Histograms are utilized to assist in the determination of this value. Results published in this chapter are obtained using a gradient threshold value that is 140 in a range of 256 intensity values. Using this gradient threshold, a binary volume is generated from the series of Sobel-enhanced slices. Each slice of the binary volume is a map whose binary voxels determine membership in the class of border region voxels. Figure 5-6 depicts the binary thresholding of the Sobel-enhanced slice shown in the previous figure.
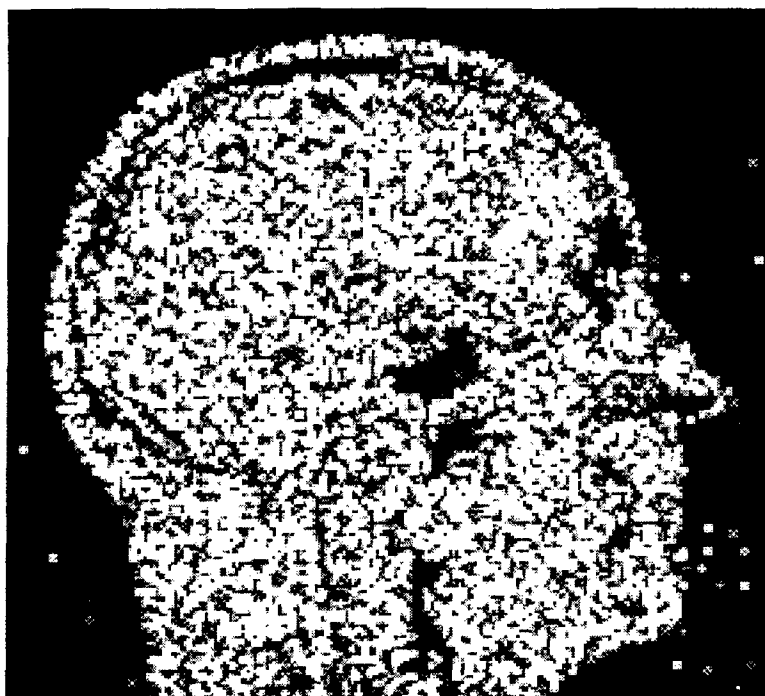
Figure 5-5. Sobel Enhanced Slice
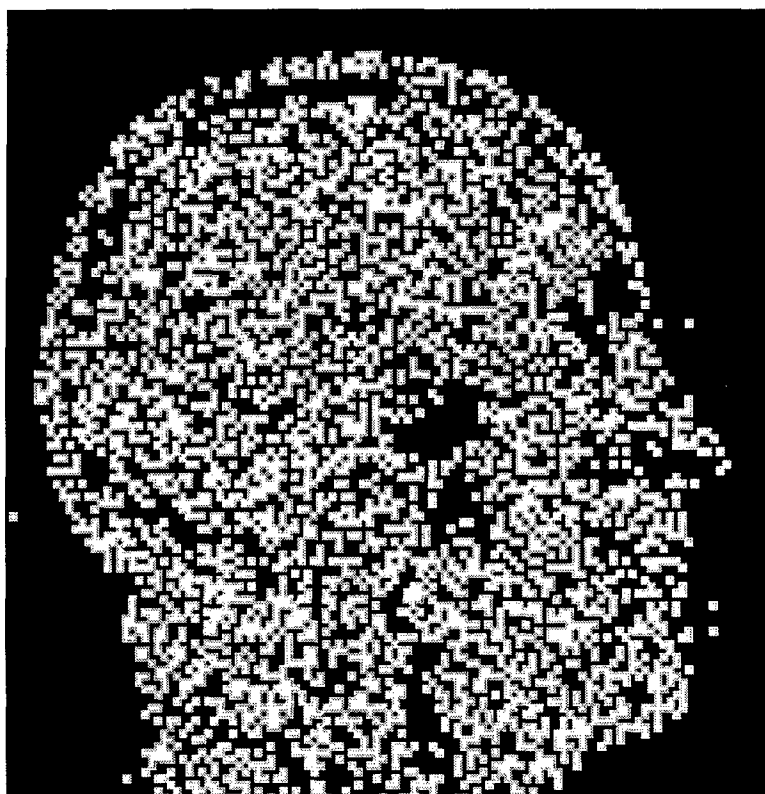
Figure 5-6.   Validation Data Slice Border Region Map

Dimensions of the binary volume of border region voxels are expanded in the subtask, *Expand Binary Volume,* to coincide with the desired dimensions of the interpolated volume. Figure 5-7 shows the result of the expansion of the border region mask depicted in the previous figure. Voxel density of the expanded binary border region volume is observed to be twice that of the border region volume that had been computed from the validation data set. (Compare Figure 5-7 and Figure 5-6). A morpholpogical binary dilation operator is applied to the expanded binary volume to close the "holes" created by the expansion process, thereby resulting in a three-dimensional border region mask that maps to the desired interpolated volume. This dilation is accomplished in the subtask, *Dilate Binary Data.*

During the task, *Structurally Analyze and Krige,* subvolumes are spatially analyzed about each PTBE. No perimeter voxel is interpolated by the AFIT Kriging
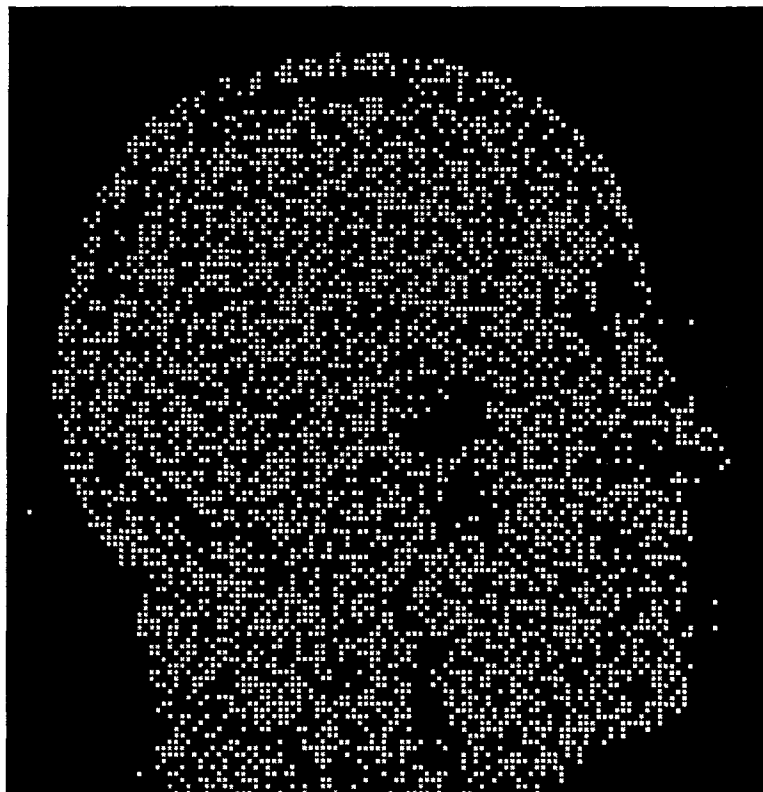
Figure 5-7.   Expanded Border Region Map

Algorithm if a sufficient extent of voxels does not exist about the voxel to be interpolated, thereby preventing a comprehensive structural analysis about that point. The subtask, *Crop Binary Volume Perimeter*, clears all voxel values along the perimeter of the binary volume to ensure a sufficiently large subvolume can be spatially analyzed about each PTBE. The resulting binary volume is a border region map of the desired interpolated volume. Only voxels of the interpolated volume that correspond to voxels whose values are set in the binary volume are interpolated using the AFIT Kriging Algorithm. Based upon data analyzed in this research, the results published in this chapter assume the extent of any subvolume about a PTBE does not exceed ±4 sampled voxels. Unsampled voxels of the interpolated volume that correspond to binary voxels of the border region interpolation map whose value are 1 are estimated using kriging. Figure 5-8 depicts the results after dilating and cropping the perimeter of the expanded border region map shown in the previous figure.

To expedite the data loading and processing of interim kriging trials, a subset of the original modality space volume is input to the AFIT Kriging Algorithm. The subset contains $^{1}/_{16}$ the number of voxels as the original modality space volume. A 64x64x64 volume of voxels is used to generate a 32x32x32 validation data set. The resultant validation volume is shown in Figure 5-9. A sagittal slice of the validation volume that is nearest to the center of the original modality space volume is shown in Figure 5-10. Using this validation volume, trials of the AFIT Kriging Algorithm were executed. Results of each trial are given in the following sections of this chapter.
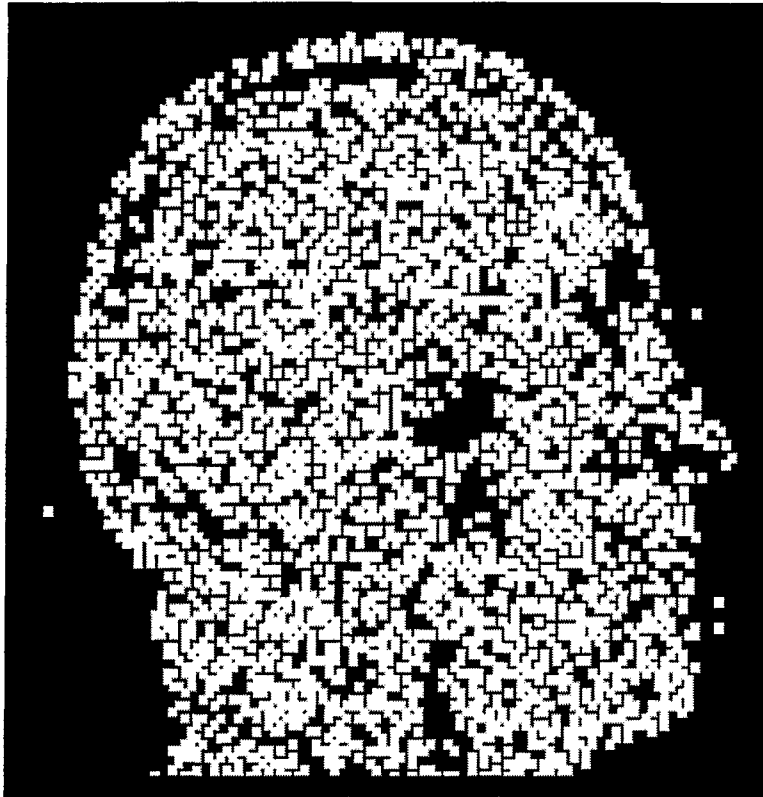
Figure 5-8.   Dilated and Cropped Border Region Map
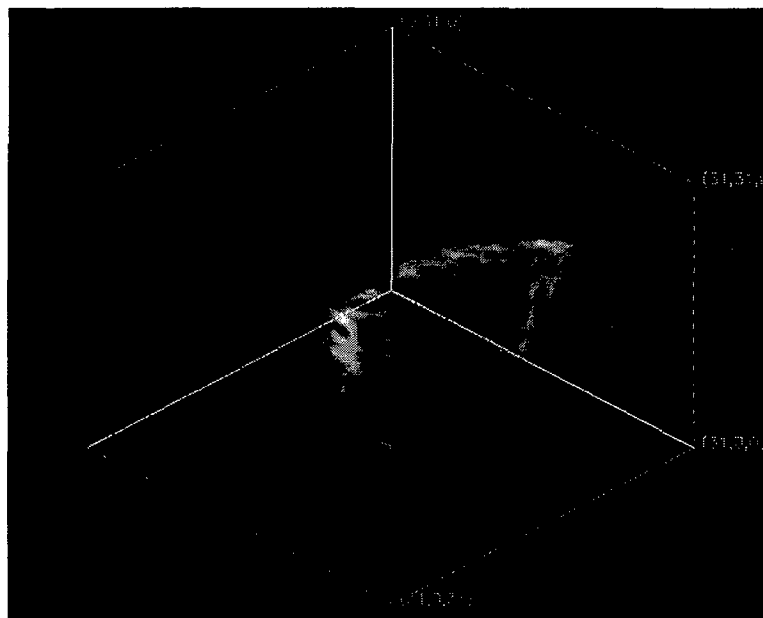
Figure 5-9.   Validation Volume for Kriging Trials
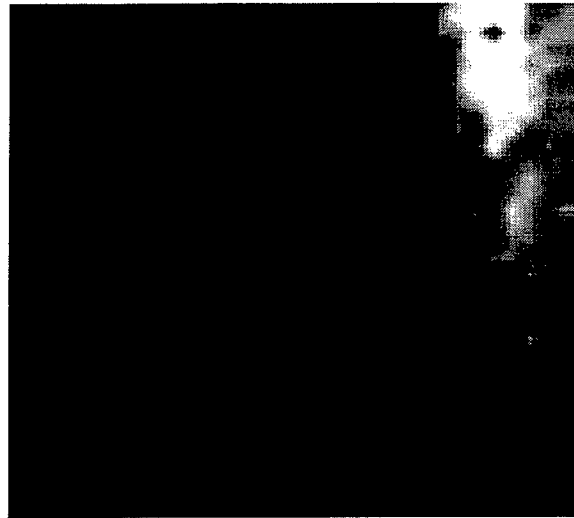
Figure 5-10.   Sagittal Slice of Validation
Volume

Kriging Results Using Discrete Directional Variograms to Interpolate the Validation Data

Given the significant processing demands of kriging, the initial trial of the AFIT

Kriging Algorithm was limited to estimating the values of the first 250 voxels of the

interpolated modality space volume.   Only this subset of modality space voxels was

interpolated to permit a preliminary performance assessment to be made before

proceeding.   This initial trial utilized discrete directional variograms to describe spatial

variation about each PTBE.   Voxels interpolated using kriging are identified in the

expanded border region map generated by the *Identify Border Regions* task.   Nine

significant parameters are computed and associated with each interpolated voxel.   They

are (in order): the number of voxels determined to lie in the local kriging neighborhood;

the ordinary kriging variance; the estimate obtained using kriging; the true modality

space value of the voxel; the trilinearly interpolated estimate using values of adjacent

surrounding voxels; the projection error of the kriged estimate; the projection error of

the trilinearly interpolated estimate; and model error statistics relating the three-

dimensional mathematical model of spatial variation to the actual spatial variation observed in a local subvolume centered about each PTBE.

Projection error is given as a percent value defined as the ratio of the absolute value of the difference between the true value and a corresponding interpolated estimate to the range of possible values assumed by the volume of interest. That is,

$$projection\ error\ (\%) = \frac{|estimate - actual\ value|}{range} \tag{5-1}$$

where the range of values assumed by the MRI modality space volume of interest used to obtain these results is 3001. Model error statistics include the mean and standard deviation of each set of estimates. These statistics consider for all directions analyzed the statistically weighted error between each computed experimental variogram value and the corresponding value predicted by the three-dimensional mathematical model.[3] Appendix C lists the values of all of the above parameters alongside their corresponding enhanced resolution modality space coordinate triple.

Comparing point by point projection errors obtained using kriging against those obtained using trilinear interpolation, kriging provides estimates that are more accurate than trilinear interpolation 29.2% of the time, as shown in Figure 5-11. For the voxels analyzed, kriging yields a mean projection error of 2.085% with a standard deviation of 1.459%. Trilinear interpolation yields a mean projection error of 1.693% with a standard deviation of 1.229%. Results of the two methods indicate projection errors that are within 0.4% of one another. Figure 5-12 depicts the distribution of these errors for

---

[3] The statistical weighting does not consider anisotropic effects.

Kriging Accuracy

vs. Trilinear Interpolation

Using Discrete Directional Variograms

>1.5% Worse (31)
1-1.5% Worse (36)
0-1% Worse (110)
0-1% Improvement (51)
1-1.5% Improvement (1
>1.5% Improvement (7)
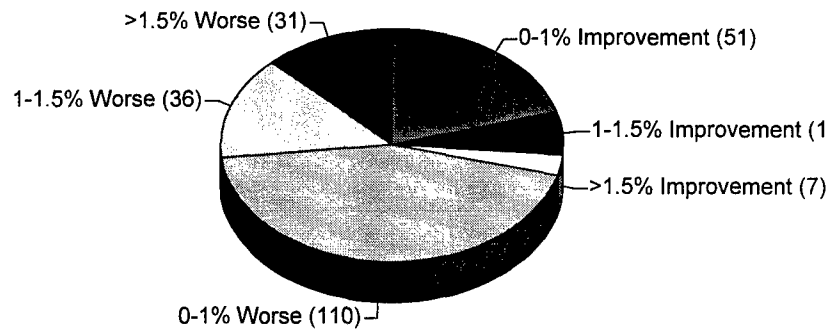
Figure 5-11. Kriging vs. Trilinear Accuracy Comparison
(Using Discrete Directional Variograms)

Kriging Accuracy

Projection Error Intervals (%)

Using Discrete Directional Variograms

[5.0,max] (4.00%)
[4.0,5.0) (7.60%)
[3.0,4.0) (14.80%)
[2.0,3.0) (23.60%)
[0.0,1.0) (30.40%)
[1.0,2.0) (19.60%)
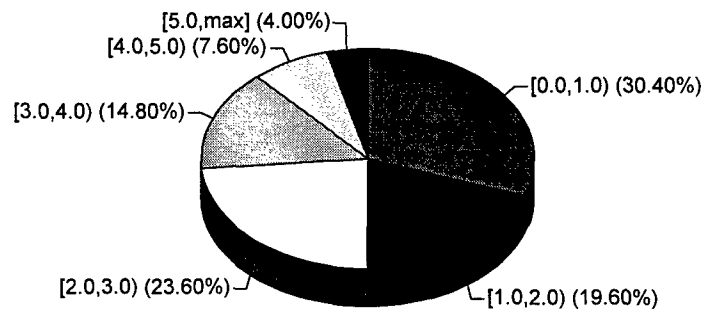
Figure 5-12. Kriging Accuracy Distribution
(Using Discrete Directional Variograms)

Table 5-1.   Projection Error Comparison
(Using Discrete Directional Variograms)

Projection Error (%)		
Method	Kriging	Trilinear
# estimates	250	250
Mean	2.085	1.688
Std Dev	1.459	1.229

the results obtained using kriging. Table 5-1 summarizes the results of the two interpolation techniques in terms of estimation accuracy.

From Figure 5-11 It is observed that in 68% of the cases, kriging estimation accuracy is less than the accuracy achieved using trilinear interpolation. Figure 5-12 Shows that in 50% of the cases observed, projection errors using kriging are less than 2.0%, and only in 4% of the cases do projection errors exceed 5.0%. Due to the unsatisfactory results obtained from this trial that used discrete directional variograms to describe spatial variability about each PTBE, additional trials that use discrete directional variograms were not run. Rather, an approach that utilizes composite directional variograms was developed, implemented and investigated. Results obtained using this approach follow.

Kriging Results Using Composite Directional Variograms to Interpolate the Validation Data

The use of discrete directional variograms limits the number of variogram data points from which the extent and orientation of the axes of spatial continuity can be determined. Hence, the accuracy of these parameters is limited. A single discrete

directional variogram is unable to sufficiently describe the complexity of intervoxel spatial dependence of modality space MRI data along a general direction in three-dimensional space. The concept of a composite directional variogram to describe spatial variation in a general, bounded direction was therefore developed and applied to the validation data set. Results are provided in the following sections of this chapter.

Using Composite Directional Variograms with ±50° Angular Tolerance

This trial estimates the values of the first 650 voxels (of voxels identified in the expanded border region map) of the interpolated modality space volume using composite directional variograms to describe spatial variation about each PTBE. The angular tolerance of each composite variogram is ±50°. Similar to Appendix C, several parameters are computed and associated with each interpolated voxel. They include: the number of voxels in the local kriging neighborhood; the ordinary kriging variance; kriging modality space estimates; the true value of each voxel; trilinear modality space estimates; the projection error of the kriged and trilinearly interpolated estimates; and error statistics of the three-dimensional mathematical model relative to local modality space voxel values. These parameters are provided in Appendix D alongside their corresponding enhanced resolution modality space coordinate triple. Statistics are computed for all 650 voxels, as well as for the first 250 voxels estimated so that direct comparisons may be made to results obtained using discrete directional variograms.

Comparing projection errors between kriging using composite variograms and trilinear interpolation for the first 250 estimates, kriging provides estimates that are more accurate than trilinear interpolation 35.2% of the time, as depicted in Figure 5-13. For the voxels interpolated, kriging yields a mean projection error of 1.951% with a standard deviation of 1.343%. Trilinear interpolation yields a mean projection error of

1.693% with a standard deviation of 1.229%. Figure 5-14 depicts the distribution of these errors for the results obtained using kriging.

The results obtained using composite directional variograms with ±50° angular tolerance are similar to those obtained (in Figure 5-11 and Figure 5-12) using discrete directional variograms. From Figure 5-13 it is observed that in 65% of the 250 cases, kriging estimation accuracy is less than the accuracy achieved using trilinear interpolation. Figure 5-14 Shows that in 54% of the 250 cases observed, the projection errors using kriging are less than 2.0%, and in only 2% of the cases do the projection errors exceed 5.0%.

Comparing projection errors point by point for all 650 estimates, kriging provides estimates that are more accurate than trilinear interpolation 36.2% of the time, as depicted in Figure 5-15. For all voxels interpolated, kriging yields a mean projection error of 1.891% with a standard deviation of 1.297%. Trilinear interpolation yields a mean projection error of 1.647% with a standard deviation of 1.231%. Figure 5-16 depicts the distribution of these errors for the results using kriging. Table 5-2 summarizes the results of each interpolation method in terms of estimation accuracy.

Error statistics obtained by computing 650 estimates using composite directional variograms with ±50° angular tolerance are very similar to those obtained when only

Table 5-2.   Projection Error Comparison
(Composite Variograms with 50° Angular Tolerance)

Projection Error (%)				
Method	Kriging		Trilinear	
# estimates	650	250	650	250
Mean	1.891	1.951	1.647	1.693
Std Dev	1.297	1.343	1.231	1.229

250 estimates were captured. From Figure 5-15 it is observed that in 64% of the 650 cases, kriging estimation accuracy is less than the accuracy achieved using trilinear interpolation. Figure 5-16 shows that in 56% of the 650 cases observed, the projection errors using kriging are less than 2.0%, and in just over 2% of the cases do the projection errors exceed 5.0%.

Kriging theory guarantees that estimates computed using kriging are optimal with respect to the employed model of spatial variation. However, results obtained using discrete directional variograms and composite directional variograms with $\pm 50^{\circ}$ angular tolerance to structurally analyze the data about each PTBE suggest the three-dimensional mathematical model of spatial variation may not sufficiently represent modality space. Therefore, when interpolating border region voxels using kriging, estimation optimality that is guaranteed with respect to the mathematical model of spatial variation does not necessarily extend to modality space. Model accuracy is critical to obtain accurate estimates.

Kriging Accuracy

vs. Trilinear Interpolation

Using Composite Directional Variograms
with 50 deg Angular Tolerance

>1.5% Worse (19)
1-1.5% Worse (29)
0-1% Improvement (73)
1-1.5% Improvement (11)
>1.5% Improvement (4)
0-1% Worse (114)
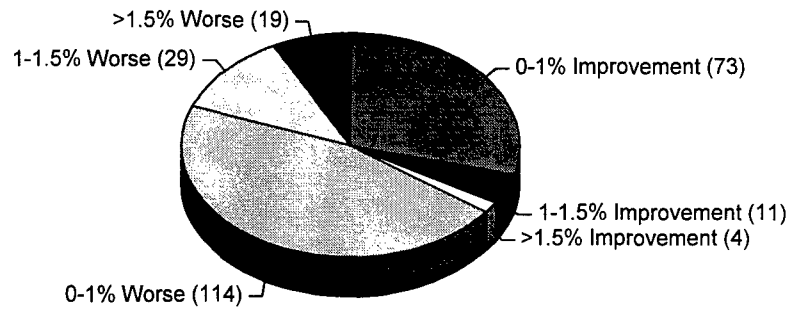
Figure 5-13. Kriging vs. Trilinear Accuracy Comparison
(Composite Variograms with 50° Angular
Tolerance, 250 voxels estimated)

Kriging Accuracy

Projection Error Intervals (%)

Using Composite Directional Variograms
with 50 deg Angular Tolerance

[5.0,max] (2.00%)
[4.0,5.0) (6.80%)
[3.0,4.0) (13.60%)
[0.0,1.0) (30.80%)
[2.0,3.0) (23.60%)
[1.0,2.0) (23.20%)
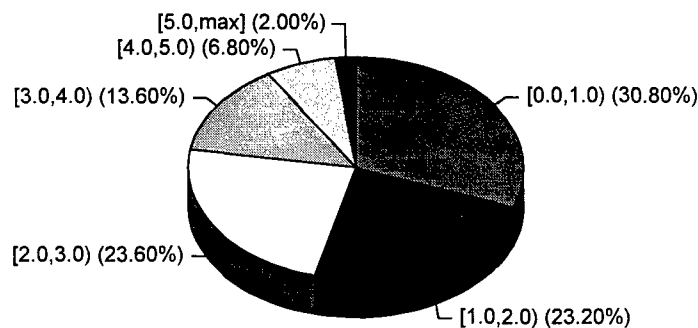
Figure 5-14. Kriging Accuracy Distribution
(Composite Variograms with 50° Angular
Tolerance, 250 voxels estimated)

Kriging Accuracy

vs. Trilinear Interpolation

Using Composite Directional Variograms
with 50 deg Angular Tolerance

>1.5% Worse (57)
1-1.5% Worse (73)
0-1% Improvement (181)
1-1.5% Improvement (30)
>1.5% Improvement (24)
0-1% Worse (285)
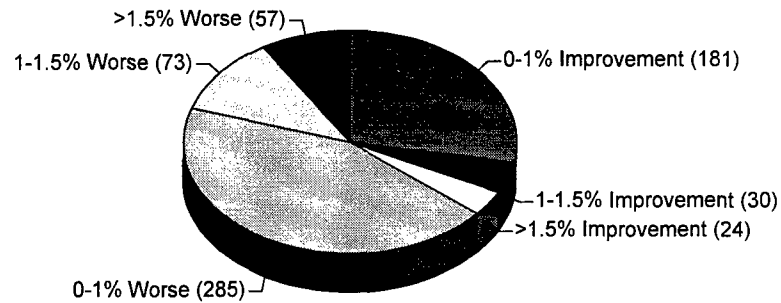
Figure 5-15. Kriging vs. Trilinear Accuracy Comparison
(Composite Variograms with 50° Angular
Tolerance, 650 voxels estimated)

Kriging Accuracy

Projection Error Intervals (%)

Using Composite Directional Variograms
with 50 deg Angular Tolerance

[5.0,max] (2.31%)
[4.0,5.0) (4.78%)
[3.0,4.0) (12.33%)
[0.0,1.0) (30.51%)
[2.0,3.0) (24.19%)
[1.0,2.0) (25.89%)
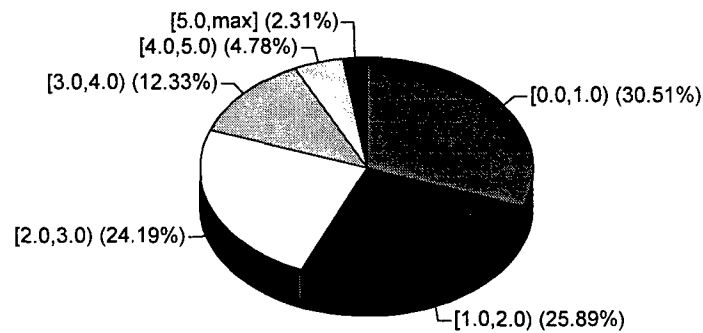
Figure 5-16. Kriging Accuracy Distribution
(Composite Variograms with 50° Angular
Tolerance, 650 voxels estimated)

Using Composite Directional Variograms with ±60° Angular Tolerance

Since the AFIT Kriging Algorithm derives a three-dimensional model of modality space spatial variation as a function of Cartesian coordinates, it was hypothesized that the three-dimensional model accuracy could be improved if the angular tolerance of the composite directional variograms is increased to ensure all variations within an irregularly spaced modality space Cartesian coordinate quadrant are considered in the model derivation. Therefore, this interpolation trial was conducted using an angular tolerance of ±60° when computing each composite variogram. As in the previous trial, this trial estimated the values of the first 650 voxels (of voxels identified in the expanded border region map) of the interpolated modality space volume. The same parameters provided in Appendices B and C are computed and provided in Appendix D alongside each enhanced resolution modality space coordinate triple. Statistics are computed for all 650 voxels, as well as for the first 250 voxels estimated so that direct comparisons may be made to results obtained using discrete directional variograms and composite directional variograms with ±50° angular tolerance.

Comparing projection errors between kriging using the described composite variograms and trilinear interpolation for the first 250 estimates, kriging provides estimates that are more accurate than trilinear interpolation 34.00% of the time, as depicted in Figure 5-17. For the voxels interpolated, kriging yields a mean projection error 1.932% with a standard deviation of 1.331%. Figure 5-18 depicts the distribution of these errors for the results obtained using kriging.

The results observed using composite directional variograms with ±60° angular tolerance are similar to the results obtained using composite directional variograms with ±50° angular tolerance (see Figure 5-13 through Figure 5-16), as well the results obtained using discrete directional variograms (see Figure 5-11 and Figure 5-12) . From

Kriging Accuracy

vs. Trilinear Interpolation

Using Composite Directional Variograms
with 60 deg Angular Tolerance

>1.5% Worse (15)
1-1.5% Worse (27)
0-1% Improvement (71)
1-1.5% Improvement (10)
>1.5% Improvement (4)
0-1% Worse (123)
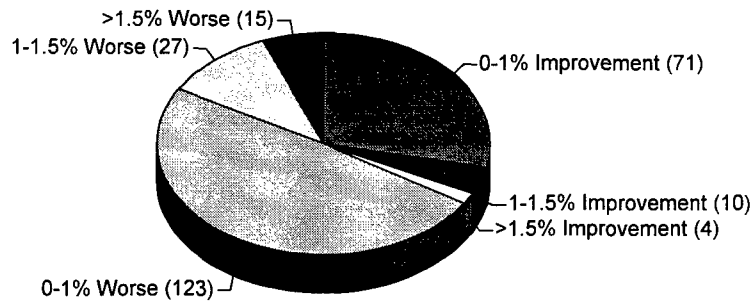
Figure 5-17. Kriging vs. Trilinear Accuracy Comparison (Composite Variograms with 60° Angular Tolerance, 250 voxels estimated)

Kriging Accuracy

Projection Error Intervals (%)

Using Composite Directional Variograms
with 60 deg Angular Tolerance

[5.0,max] (1.60%)
[4.0,5.0) (5.60%)
[3.0,4.0) (15.20%)
[0.0,1.0) (31.20%)
[2.0,3.0) (22.80%)
[1.0,2.0) (23.60%)
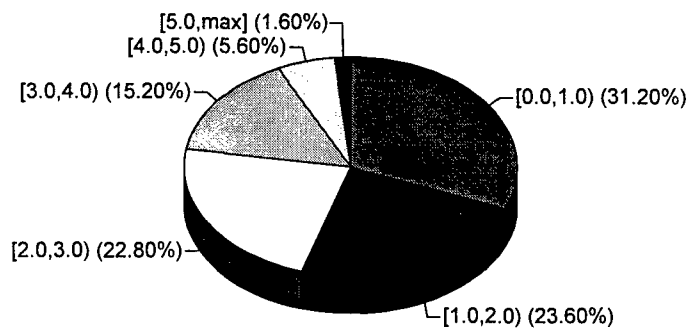
Figure 5-18. Kriging Accuracy Distribution (Composite Variograms with 60° Angular Tolerance, 250 voxels estimated)

Figure 5-17 and Figure 5-19 it is observed that in 66% and 64% of the 250 and 650 cases, respectively, kriging estimation accuracy is less than the accuracy achieved using trilinear interpolation. Figure 5-18 and Figure 5-20 shows that in 55% of the 250 and 650 cases respectively observed, the projection errors using kriging are less than 2.0%. In both the 250 and 650 cases observed, projection errors exceed 5.0% in less than 2% of the cases.

Comparing projection errors point by point for all 650 estimates, kriging provides estimates that are more accurate than trilinear interpolation 36.62% of the time, as depicted in Figure 5-19. For all voxels interpolated, kriging yields a mean projection error of 1.863% with a standard deviation of 1.295%. Figure 5-20 depicts the distribution of these errors for the results using kriging. Table 5-3 summarizes the results of each interpolation method in terms of estimation accuracy.

Table 5-3.   Projection Error Comparison
(Composite Variograms with 60° Angular Tolerance)

Projection Error (%)				
Method	Kriging		Trilinear	
# estimates	650	250	650	250
Mean	1.863	1.932	1.647	1.693
Std Dev	1.295	1.331	1.231	1.229

Although a slight improvement in estimation accuracy is observed when using composite directional variograms with $\pm 60^\circ$ angular tolerance versus $\pm 50^\circ$ angular tolerance, the improvement is not statistically significant. The results indicate that the estimation optimality that is kriging guarantees with respect to the mathematical model of spatial variation may not necessarily extend to modality space. Model accuracy is therefore critical.

Kriging Accuracy

vs. Trilinear Interpolation

Using Composite Directional Variograms
with 60 deg Angular Tolerance
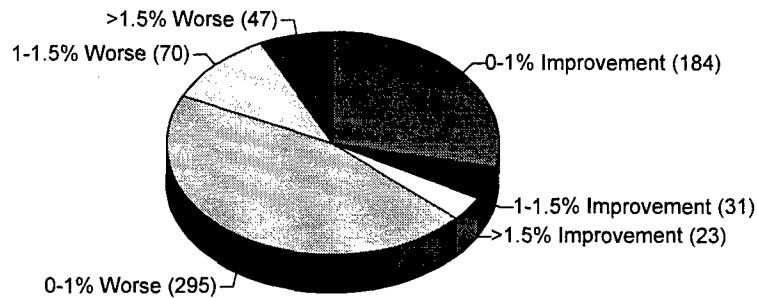
Figure 5-19. Kriging vs. Trilinear Accuracy Comparison
(Composite Variograms with 60° Angular
Tolerance, 650 voxels estimated)

Kriging Accuracy

Projection Error Intervals (%)

Using Composite Directional Variograms
with 60 deg Angular Tolerance
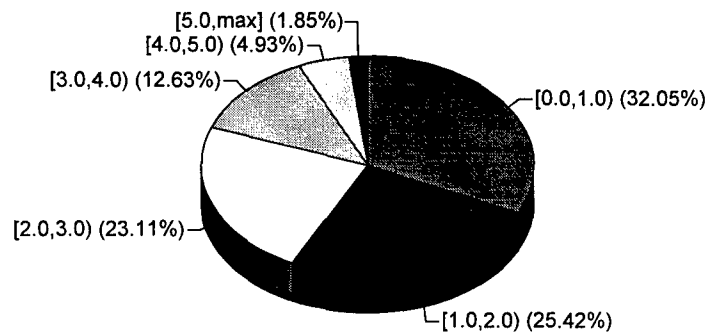
Figure 5-20. Kriging Accuracy Distribution
(Composite Variograms with 60° Angular
Tolerance, 650 voxels estimated)

Analysis of the Kriging Interpolation Results

In each previous trial, trilinear interpolation appears to provide better estimates than kriging. *Better* is defined in terms of minimizing the estimate errors. Table 5-5 and Table 5-4 summarize projection error statistics that lead to this conclusion for trials of 250 and 650 voxels, respectively.

Several observations relative to mean projection error are made from these results. First, when using kriging as an interpolator, as one progresses from utilizing discrete directional variograms to composite directional variograms with angular tolerances of $\pm 50^\circ$ and $\pm 60^\circ$, in turn, an improvement (lessening) in the mean and

Table 5-5.   Projection Error Statistics (250 voxels estimated)

Projection Error (%)				
Method	Kriging			Trilinear
	Discrete	Composite $\pm 50^\circ$	Composite $\pm 60^\circ$	
# estimates	250	250	250	250
Mean	2.085	1.951	1.932	1.693
Std Dev	1.459	1.343	1.331	1.229

Table 5-4.   Projection Error Statistics (650 voxels estimated)

Projection Error (%)			
Method	Kriging		Trilinear
	Composite $\pm 50^\circ$	Composite $\pm 60^\circ$	
# estimates	650	650	650
Mean	1.891	1.862	1.647
Std Dev	1.297	1.294	1.231

standard deviation of mean projection errors occurs. Second, in all cases studied the trilinear method of interpolation provides the smallest mean projection error and the least variance of that error. These two observations are tested for statistical significance in the two sections of this chapter that follow.

Testing the Significance of Using Composite Directional Variograms

A trend in Table 5-5 and Table 5-4 suggests that the use of composite directional variograms provides better estimates when kriging than estimates obtained using discrete directional variograms. To verify the significance of this trend a one-sided test of statistical significance is accomplished between the projection error statistics obtained when kriging using discrete directional variograms and those obtained using composite directional variograms. Results obtained using composite directional variograms with an angular tolerance of $\pm 60^{o}$ are considered in this test since they appear to provide the most optimal kriging trial results.

Assume the null hypothesis H_0 states there is no significant difference between the mean projection errors obtained when kriging using either type of directional variogram. Assume the alternative hypothesis H_1 states there is a significant difference between the mean projection errors obtained between the two methods. Stated mathematically,

$$H_0: \mu_{cdv} = \mu_{dv}$$
$$H_1: \mu_{cdv} \neq \mu_{dv}$$

(5-2)

where the subscript cdv references statistics obtained using composite directional variograms with an angular tolerance of $\pm 60^{o}$, and the subscript dv references statistics obtained using discrete directional variograms.

5-23

Assuming a normal distribution of mean projection errors, the mean and standard deviation of the mean projection errors (for the trial estimating 250 voxels) consistent with the null hypothesis are given by equation (5-3) and equation (5-4), respectively.

$$\mu_{cdv-dv} = 0 \tag{5-3}$$

$$\sigma_{cdv-dv} = \sqrt{\frac{\sigma_{cdv}^2 + \sigma_{dv}^2}{250}} \tag{5-4}$$
$$= 0.1249$$

The standardized variable z is then given by,

$$z = \frac{\mu_{cdv} - \mu_{dv}}{\sigma_{cdv-dv}} \tag{5-5}$$
$$= -1.225$$

Given a one-sided test and a level of significance of 0.05, results are significant when the standardized variable z satisfies the following equation:

$$|z| > 1.645 \tag{5-6}$$

Hence, the null hypothesis cannot be rejected; no significant difference exists between mean projection errors obtained using either of the two methods tested. In fact, it can be shown the two methods do not exhibit a statistically significant difference unless the level of significance is relaxed to just beyond 0.11 . That is, no statistically significant estimation accuracy difference is observed between kriging results obtained using

composite directional variograms (with $\pm 50^{\circ}$ or $\pm 60^{\circ}$ angular tolerance) and results obtained using discrete directional variograms.

Testing the Significance of the Better Estimator

In all trials the trilinear method of interpolation exhibits the smallest mean projection error and the least estimation error variance. As a result, one may assume trilinear interpolation is the better estimator. To verify this assumption, a one-sided test of statistical significance is accomplished between the mean projection errors that result when kriging with composite directional variograms of $\pm 60^{\circ}$ and those that result when using trilinear interpolation.

Assume the null hypothesis H_0 states there is no significant difference between the mean projection errors obtained when kriging using composite variograms and errors obtained using trilinear interpolation. Assume the alternative hypothesis H_1 states there is a significant difference between the mean projection errors obtained between the two methods. Stated mathematically,

$$H_0: \mu_{cdv} = \mu_{tri}$$
$$H_1: \mu_{cdv} \neq \mu_{tri}$$

(5-7)

where: the subscript cdv references statistics obtained using composite directional variograms with an angular tolerance of $\pm 60^{\circ}$; and the subscript tri references statistics obtained using trilinear interpolation.

Assuming a normal distribution of mean projection errors, the mean and standard deviation of the mean projection errors (for the trial estimating 650 voxels) consistent with the null hypothesis are given by equation (5-8) and equation (5-9), respectively.

$$\mu_{cdv-tri} = 0 \qquad \text{(5-8)}$$

$$\sigma_{cdv-tri} = \sqrt{\frac{\sigma_{cdv}^2 + \sigma_{tri}^2}{650}} \qquad \text{(5-9)}$$

$$= 0.0700$$

The standardized variable z is then given by,

$$z = \frac{\mu_{cdv} - \mu_{tri}}{\sigma_{cdv-tri}} \qquad \text{(5-10)}$$

$$= 3.071$$

Given a one-sided test and a level of significance of 0.01, results are significant when the standardized variable z satisfies the following equation:

$$|z| > 2.326 \qquad \text{(5-11)}$$

Hence, the null hypothesis is rejected; trilinear interpolation is significantly better than kriging using composite directional variograms with angular tolerances of $\pm 60^{\circ}$. In fact, the null hypothesis is rejected even at the 0.005 level of significance.

Validating Previous Research Using Kriging to Obtain Trilinear Estimates

Previous research has shown kriging could be made to behave like deterministic interpolation techniques, producing estimates that are generally as accurate as the modeled deterministic method [Parr91]. Parrott made several assumptions regarding

the modality space volume to simplify his implementation of kriging theory. A structural analysis of the modality space volume was not accomplished. The modality space data was assumed stationary. The extent of spatial dependency was assumed constant throughout the volume. Spatial variation was assumed to behave deterministically and isotropically. In spite of these assumptions, his research produced results similar to those obtained using deterministic techniques.

Consistent with geostatistical theory, Parrott predicted estimation accuracy would improve if kriging is used in conjunction with a structural analysis of the modality space data [Parr91]. This research is based upon the validity of this predication. However, results presented in previous sections indicate this prediction is not necessarily valid, but is dependent upon the derived model of spatial variation. Therefore his results are revalidated. However, revalidation of Parrott's results support Parrott's prediction. Since kriging estimation accuracy of medical data produces estimates that are statistically no different than trilinear interpolation, then utilizing additional information obtained through a structural analysis of modality space data about a PTBE should improve kriging estimation accuracy. Revalidation of Parrott's results is described in the following paragraphs.

The validation data is interpolated using the AFIT Kriging Algorithm as in previous trials to estimate the values of the first 250 voxels. The exception is this trial assumes the following: drift does not exist, data is stationary; spatial variation is isotropically linear in three dimensions; and the extent of spatial dependency is equivalent to the neighborhood of adjacent voxels, the same voxels that are used to obtain a trilinearly interpolated estimate of a PTBE. These assumptions cause kriging to behave like trilinear interpolation.

For each voxel that is interpolated, the following parameters are computed or provided: the kriged estimate; the true value of the voxel; the trilinear estimate; the projection error of the kriged estimate; the projection error of the trilinearly interpolated estimate; and error statistics of the three-dimensional mathematical model relative to local modality space voxel values. These parameters are provided in Appendix G alongside their corresponding enhanced resolution modality space coordinate triple.

Comparing projection errors between estimates obtained using kriging (made to behave like trilinear interpolation) and trilinear interpolation, kriging is observed to provide estimates that are more accurate than trilinear interpolation 48% of the time, as depicted in Figure 5-21. In all cases observed, kriging estimation accuracy is within 1% of the accuracy obtained using trilinear interpolation. For the voxels interpolated, kriging yields a mean projection error of 1.687% with a standard deviation of 1.235%. Trilinear interpolation yields a mean projection error of 1.693% with a standard deviation of 1.229%. Figure 5-22 depicts the distribution of these errors for the results obtained using kriging.

The results of this trial validate previous research; estimates obtained using kriging when made to behave like trilinear interpolation are indistinguishable from estimates obtained using trilinear interpolation. Rounding the mean projection error statistics to the second significant digit beyond the decimal, both techniques yield identical means and standard deviations.

Kriging Accuracy

vs. Trilinear Interpolation

Kriging Made To Behave Like
Trilinear Interpolation

0-1% Worse (130)

0-1% Improvement (120)
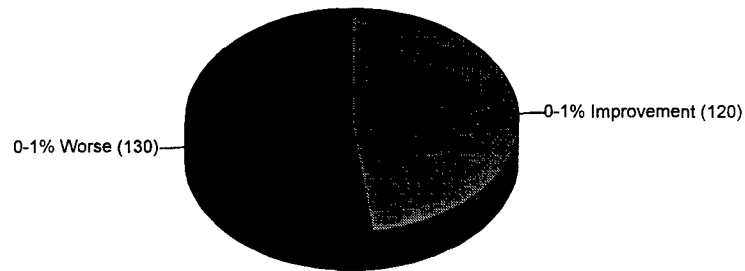
Figure 5-21. Kriging vs. Trilinear Accuracy Comparison
(Kriging Made to Behave Like Trilinear
Interpolation, 250 voxels estimated)

Kriging Accuracy

Projection Error Intervals (%)

Kriging Made To Behave Like
Trilinear Interpolation

[5.0,max] (1.20%)
[4.0,5.0) (5.60%)
[3.0,4.0) (6.40%)
[2.0,3.0) (20.00%)
[0.0,1.0) (34.80%)
[1.0,2.0) (32.00%)
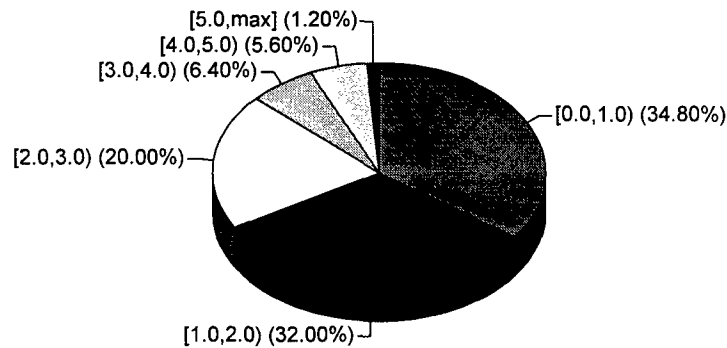
Figure 5-22. Kriging Accuracy Distribution
(Kriging Made to Behave Like Trilinear
Interpolation, 250 voxels estimated)

Attributing Kriging Inaccuracies to the 3D Mathematical Model

This research seeks to improve the accuracy of interpolated modality space estimates by using kriging in conjunction with a three-dimensional structural analysis of spatial variation of the modality space data about each PTBE. It has been shown that kriging can be made to behave like deterministic interpolation techniques. Without the benefit of any structural analysis about a PTBE kriging can provide estimates that are statistically no different than those obtained using deterministic interpolation techniques. The purpose of conducting a structural analysis is to derive a three-dimensional mathematical model of spatial variation that does not assume stationarity, nor isotropic variation, nor a symmetric neighborhood of spatial dependency. Yet (in the trials presented in this chapter), when a structural analysis of the local region about a PTBE is accomplished this research has shown kriging estimation accuracy not only fails to improve, but rather deteriorates. These results contradict both theory and intuition.

The reason for the observed kriging estimation inaccuracies must be attributed to the derived three-dimensional mathematical model of spatial variation. Though the goal of ordinary kriging is to compute unbiased, optimal estimates using sampled voxel values in the local neighborhood of each PTBE, in theory the goal is unattainable because the mean error and error variance of a set of kriged estimates is unknown. In practice, kriged estimates can only be unbiased and optimal with respect to a model that is considered representative of the spatial variation of a modality space volume. If the three-dimensional mathematical model fails to accurately represent the spatial variation for which it is derived, kriging estimates obtained using the model cannot, in general, be considered unbiased, optimal estimates of the modality space data.

Although the assumptions made in previous research by Parrott [Parr91] are removed, the AFIT Kriging Algorithm implemented in this research makes two assumptions (previously discussed) that simplify the derivation of a three-dimensional mathematical model of spatial variation. First, the extent of spatial dependency extends elliptically about any PTBE. Second, the orthogonal semiaxes of the ellipsoid neighborhood sufficiently characterizes the maximum, mid, and minimum directions of spatial continuity. Results of the trials presented in this chapter indicate that these assumptions may not, in general, be valid for the MRI medical data and may contribute to the derivation of a mathematical model of spatial variation that insufficiently represents the modality space data.

It is hypothesized that if a three-dimensional mathematical model can be constructed such that it accurately and sufficiently characterizes the spatial variation of modality space data, then the accuracy of kriging estimates obtained using the model will be significantly improved. The section that follows presents trials that are conducted to test this hypothesis.

Kriging and Analysis of a Phantom Volume of Known Spatial Variation

To test the hypothesis that kriging estimates improve if the three-dimensional mathematical model of spatial variation is improved so that it accurately represents the modality space data, a phantom volume of known spatial variation is required. Kriging is then accomplished using a function known to precisely describe the spatial variation of the phantom volume. Two approaches were immediately considered. In the first approach, a phantom volume would be generated such that its voxel values would follow a deterministic function. Guassian, exponential and spherical functions were analyzed.

Variograms of the volume would be computed and subsequently used to krige the phantom data. Unfortunately, variograms of these volumes cannot be represented by transition variogram models that reach a sill.

The other approach that was considered would compute a phantom volume from a specified mathematical model of spatial variation. Unfortunately, experimentation revealed that generating coherent volumes from three-dimensional variogram models is not a trivial process. Another approach was desired to test the hypothesis.

The answer utilizes the later approach coupled with interpolated results obtained from previous trials discussed in this chapter. This approach possesses the desirable characteristic that the phantom volume used to confirm the hypothesis is representative of real-world medical data. In fact, since the phantom volume is an interpolated volume of an actual MRI modality space volume, a significant subset of voxel values of the phantom volume *is* real-world data. Since the remaining voxel values are interpolated using known spatial models, the spatial variation of the phantom volume is precisely characterized. Through the use of a phantom volume that is generated in this manner, kriging estimation accuracy is shown to be superior to trilinear interpolation estimation accuracy *if* a sufficiently accurate modality space spatial model of spatial variation can be generated.

Using the validation data set whose voxel values are obtained from an actual MRI scan of a human patient, the dimensions of the validation data set are approximately doubled. Columns, rows and slices are added between every other column, row and slice of the validation data set, as depicted in Figure 5-23. Voxel values of the newly added columns, rows and slices are consistent with local three-dimensional mathematical models that are generated under the constraint of the AFIT Kriging Algorithm assumptions previously discussed; that is, the extent of spatial dependency
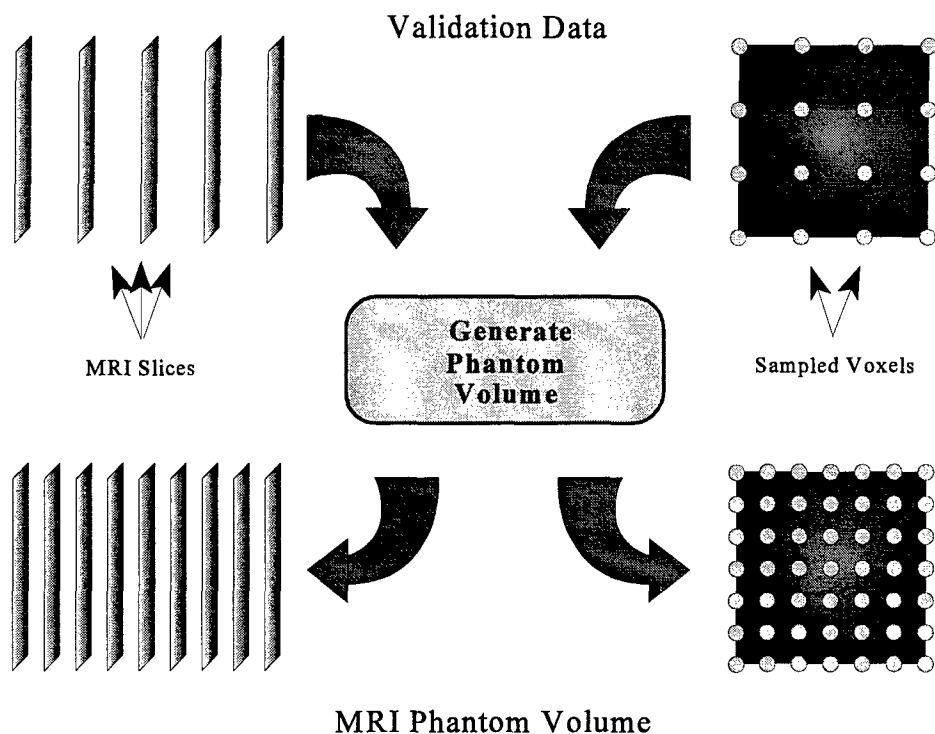
Figure 5-23. Generation of Phantom Volume

extends elliptically about any PTBE, and the orthogonal semiaxes of the ellipsoid neighborhood sufficiently characterizes the maximum, mid, and minimum directions of spatial continuity.

The local mathematical models of spatial variation that are employed in the derivation of each added voxel value use composite directional variograms with $\pm 50^{\circ}$ angular tolerance to determine spatial variation along each of three orthogonal directions of continuity. Each added voxel value is rounded to its nearest integer value, thereby simulating the discrete voxel intensity increments provided by digital imaging equipment. If theses values are compared to the interpolated values obtained from the kriging trial using composite variograms with $\pm 50^{\circ}$ angular tolerance, once rounded to nearest integers, the values are equivalent. Additionally, these newly added voxel values are consistent with real-world modality space data. That is, each value is generated from a linear combination of neighboring real-world MRI values.

As a result, the mean projection error between the phantom volume and the real-world MRI volume from which it is generated is less than 2%. The newly added voxel values are hereafter considered the true values of the phantom volume that is used to test the kriging accuracy hypothesis previously stated.

Using the phantom modality space volume described, the AFIT Kriging Algorithm estimates the first 650 voxels of the interpolated volume using composite directional variograms for each of two trials. The first trial uses composite variograms with $\pm 50^o$ angular tolerance to describe spatial variation about each PTBE. Since voxel values of the phantom volume are generated using mathematical models that are consistent with those implemented in the AFIT Kriging Algorithm and that are derived using composite variograms with $\pm 50^o$ angular tolerance, the kriging accuracy hypothesis predicts kriging estimates will be far more accurate than any previous results.

The second trial uses composite variograms with $\pm 60^o$ angular tolerance. Results of previous trials has shown kriging estimates obtained using composite variograms with angular tolerances of $\pm 50^o$ and $\pm 60^o$ to be similar. However, since the phantom modality space volume is generated using mathematical models of spatial variation derived from structural analyses that use composite variograms of $\pm 50^o$ angular tolerance, the kriging accuracy hypothesis predicts that the accuracy of estimates obtained using kriging with composite variograms of $\pm 60^o$ angular tolerance will lessen. In general, however, the accuracy of these estimates are predicted to exceed that observed using trilinear interpolation.

Appendix I lists the results of the two phantom trials, providing the kriged estimates associated with each trial alongside their true phantom values. Trilinear interpolated results are also provided for comparative purposes. Consistent with the

kriging accuracy hypothesis, kriging with composite variograms of $\pm 50^\circ$ angular tolerances provides estimates in the first phantom trial that are more accurate than trilinear interpolation in 96.15% of the cases, as depicted in Figure 5-24. For the voxels interpolated, kriging yields a mean projection error of only 0.009% with a standard deviation of 0.005%. Projection errors never exceed 0.017%. Interpolating estimates using the phantom modality space volume and trilinear interpolation yields estimates whose mean projection error is 0.795% with a standard deviation of 0.805%.

Estimates obtained in the second phantom trial using kriging with composite variograms of $\pm 60^\circ$ angular tolerance are more accurate than those obtained using trilinear interpolation 81.69% of the time, as depicted in Figure 5-25. For the voxels interpolated in this trial, kriging yields a mean projection error of 0.198% with a standard deviation of 0.314%. The projection error never exceeds 2.21%. These statistics of the two phantom trials are listed in Table 5-6 alongside those obtained using trilinear interpolation. These statistics support the kriging accuracy hypothesis that implies kriging estimation accuracy is a function of how well the three-dimensional mathematical model of spatial variation represents the physical data that is estimated.

Phantom Kriging Accuracy

vs. Trilinear Interpolation

Using Composite Directional Variograms
with 50 deg Angular Tolerance
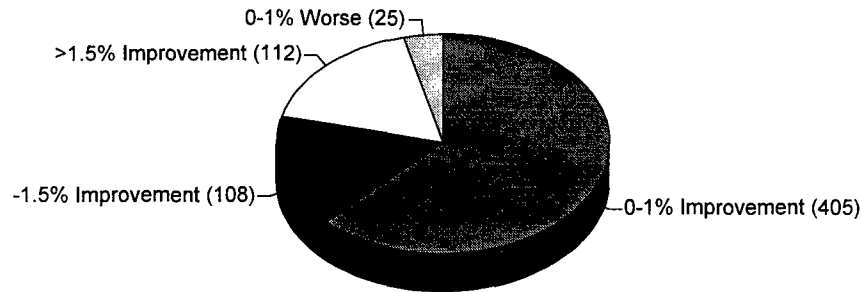
Figure 5-24. Phantom Kriging Accuracy
(Composite Variograms with 50° Angular
Tolerance, 650 voxels estimated)

Phantom Kriging Accuracy

vs. Trilinear Interpolation

Using Composite Directional Variograms
with 60 deg Angular Tolerance
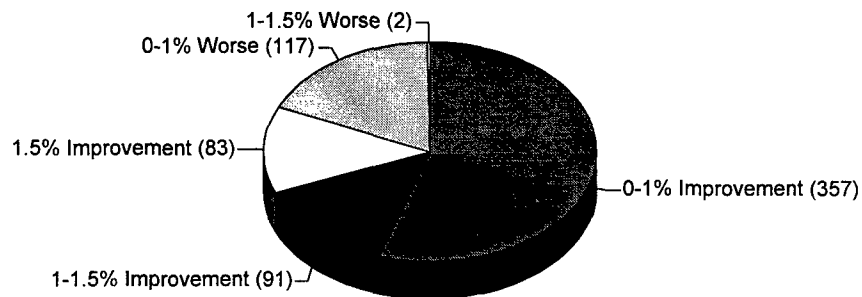
Figure 5-25. Phantom Kriging Accuracy
(Composite Variograms with 60° Angular
Tolerance, 650 voxels estimated)

Table 5-6.   Phantom Volume Projection Error Statistics (650 voxels estimated)

Method	Projection Error (%)		
	Kriging		Trilinear
	Composite ±50°	Composite ±60°	
# estimates	650	650	650
Mean	0.009	0.198	0.795
Std Dev	0.005	0.314	0.805

Chapter VI

CONCLUSIONS

The objective of my research has been to improve the estimation accuracy of interpolated three-dimensional medical data. Routine diagnostic cases in radiology require that volumetric data sets that are acquired using three-dimensional imaging modalities be interpolated prior to rendering. Inaccurate renditions of interpolated volumes can lead to patient misdiagnoses. Therefore, it is essential that interpolated medical imaging volumes accurately represent patient space. My research bridges the geosciences and medical imaging communities by recognizing the similarities that exist between each discipline and applying a geostatistical estimation technique to obtain optimal estimates of volumetric modality space MRI data.

Kriging is the estimation technique that has been explored in this research. The use of kriging to obtain estimates of natural phenomena is not new. Matheron introduced kriging and regionalized variables to estimate geological phenomena based upon spatial characteristics exhibited by their sampled values [Math63]. The use of kriging in the medical imaging community, however, is relatively new. Its introduction was made with several assumptions that simplified and tailored kriging to behave like conventional linear interpolation techniques. [Parr91, Parr92, Parr93, Styt93]. Under the constraints of these assumptions, kriging was shown to produce volumetric MRI estimates that on average were as good as conventional linear techniques. Given these results, medical imaging researchers concluded kriging to be a robust estimator.

My working hypothesis was that the assumptions made by previous medical imaging researchers could be relaxed and that this would improve estimation accuracy beyond that provided by conventional linear techniques. My research extended and

validated the findings of previous researchers by demonstrating that if kriging employs a spatial model that bases its estimates solely upon a function of the distance to and values of nearest neighbor voxels, then its estimates are statistically equivalent to those obtained using trilinear interpolation. These results were obtained independent of any structural analysis about each interpolated location.

Since its introduction, kriging has been considered a robust estimator by the geoscience community. It has also been concluded to be the same by previous medical imaging researchers. Results of my research indicate that kriging is not, in general, the robust estimator that its previous usage and research assumed. Using medical data I have shown that kriging estimation accuracies are critically dependent upon how closely the kriging model of spatial variation represents the patient space data.

This research demonstrated that kriging **can** provide significantly improved estimation accuracy over conventional techniques. This research has also demonstrated that spatial models that insufficiently characterize the associated physical space for which estimates are desired can produce kriging estimates that are less accurate than those obtained using conventional linear interpolation techniques.

This research is the first documented instance wherein kriging has been applied in conjunction with a comprehensive, automated structural analysis of modality space volume data to obtain interpolated estimates of medical data. My research has demonstrated that if a model of spatial variation can be derived from the modality space data such that it characterizes the behavior of the associated patient space data, then kriging can provide significantly more accurate estimates than can be obtained using conventional interpolation techniques.

My research required the development of two major software tools. The first tool modeled the distortive effects of an MRI scanner to enable the reconstruction and analysis of modality space MRI data relative to its patient space source. This modeling and analysis process was necessary to demonstrate that MRI modality space data can be represented using regionalized variables. The representation of data using regionalized variables is a kriging prerequisite. The requirements, implementation, use and results of this tool are described in Chapter III. Similarly scoped demonstrations have not been previously accomplished using medical data.

The second tool developed to accomplish the objectives of this research was the AFIT Kriging Algorithm. It performs the automated interpolation of volume data using kriging. Its design is described in detail in Chapter IV. Though the AFIT Kriging Algorithm was specifically developed to enable the use of kriging in conjunction with a comprehensive structural analysis of modality space medical data, its utility is not limited to medical data. It can be carried back across the geoscience-medical imaging bridge that has been established by this research and employed by the geoscience and other scientific communities to improve estimation accuracies of nonmedical phenomena beyond those currently achievable. The AFIT Kriging Algorithm's search mechanism for identifying local three-dimensional regions of spatial dependency about each point to be estimated can also be utilized by any interpolation technique that requires the specification of spatially dependent voxel neighborhoods prior to computing values of its estimates.

This chapter summarizes my research by addressing the specifics of each of these major contribution areas. It closes with recommendations for future research.

Kriging Performance and Robustness

This research demonstrated that kriging can be used to obtain modality space estimates of three-dimensional medical data that are significantly more accurate than estimates obtained using conventional linear techniques. This improvement has been demonstrated while restricting the domain of voxels estimated to be those within the least homogeneous regions of an MRI volume. These high contrast regions, called *border regions*, are worst case regions for estimators due to the high variability that exists between neighboring voxels. High intervoxel variability inevitably increases estimation variance. The advantage of using this research approach is that the results of this research have not been biased by considering the average estimation error of the ensemble of all voxels of a modality space volume. Only regions that are inherently the most difficult to accurately estimate voxel values are structurally analyzed and kriged. In other words, the results obtained by this research are worst case results.

The improvement in estimation accuracy that was reported must be qualified. The successful use of kriging as a geostatistical estimator led to its characterization as a robust estimator. Previous medical imaging research also supported this characterization. Models that are less comprehensive than those explored in this research have provided estimation accuracies in the geoscience domain that exceed those obtained in that same domain using conventional linear estimation techniques. My research demonstrated that kriging can provide medical imaging estimates that are as accurate as conventional techniques when kriging is made to behave like conventional interpolation techniques. Based upon these results and given that no structural analysis was accomplished to assist in the computation of these results, kriging was initially regarded as a robust estimator.

6-4

Further investigation forced me to reach the contrary conclusion- kriging is not, in general, a robust estimator. My research demonstrated that, in general, *simple* mathematical models cannot sufficiently characterize the relatively high resolution spatial variation of all naturally occurring, spatially regionalized physical phenomena. I have further demonstrated that the derivation of an accurate model of spatial variation is critical to improving kriging estimation accuracy. These conclusions were reached based upon results obtain by interpolating medical MRI data. Although the medical data exhibited spatial characteristics that allowed it to be represented using regionalized variables, the nonstationary anisotropic variation present in border regions of the data could not be accurately characterized using simple mathematical models. Estimation accuracy deteriorates under these conditions and are less accurate than those obtained using trilinear interpolation.

Simple mathematical models were defined to be functions of regionalized variables that assume geometric-only anisotropies with orthogonally oriented maximum, minimum and intermediate directions of continuity specifying an ellipsoid support; no nugget effect, and local drift that can be modeled and removed using a third-order polynomial function. The use of spatial models with this complexity seemed reasonable at the time of its formulation and was not inconsistent with practices that have been successfully employed by geostatisticians estimating geological data.

Results obtained using simple mathematical models to describe the local variation about each point estimated are reported in Chapter V. In general, kriging estimates were less accurate than those obtained using trilinear interpolation, even though a comprehensive structural analysis of the physical space volume was accomplished. I concluded that practices that are successfully employed by

geostatisticians estimating geological cannot be extended to all naturally occurring phenomena. In general, these practices are not valid. However, I desired additional proof to support this conclusion. An experiment was therefore conducted to confirm that observed estimation inaccuracies were a result of the inability of derived models to sufficiently characterize intervoxel spatial relationships present in the modality space data. Details of the experiment and its results are discussed in Chapter V and are briefly summarized here.

A phantom MRI modality space volume was generated from real MRI data. The phantom volume appears visually indistinguishable from the real source data from which it was generated. In fact, the phantom volume was generated such that voxel values of every other row, column and slice of the source volume from which it was generated and the phantom volume are equivalent. Remaining voxel values of the phantom volume were slightly increased or decreased (prior to interpolation by the AFIT Kriging Algorithm) in a manner such that the local variation about any point to be interpolated was guaranteed to be consistent with the constraints assumed by the domain of mathematical models that could be derived by the AFIT Kriging Algorithm. That is, voxel values of the phantom MRI volume were generated such that the following conditions were satisfied: (1) the extent of spatial dependency could be approximated by an ellipsoid about each point interpolated; (2) the maximum, minimum, and intermediate directions of anisotropy were orthogonal to one another about each point interpolated; (3) nonisotropic conditions were attributable to geometric-only anisotropies; (4) local drift about each point to be interpolated could be sufficiently modeled using a third-order polynomial; and (5) no significant nugget effect could be observed. Note that these constraints are consistent with the definition given for a

simple mathematical spatial model. Therefore, it was hypothesized that the AFIT Kriging Algorithm should be able to construct spatial models that are known to accurately describe the phantom MRI volume and hence, provide estimates that would be significantly more accurate than those obtained using conventional linear techniques. This, in fact, did occur. As hypothesized, when the resolution of the phantom volume was increased through interpolation using the AFIT Kriging Algorithm, the estimation accuracies of interpolated estimates were found to be significantly better than those obtained using trilinear interpolation. The kriging mean error was less and the kriging estimation variance was less than the same error statistics that were obtained from the same data using trilinear interpolation.

Traditionally, geoscientists that analyze geological structure beneath the earth's surface have had relatively few samples from which to draw their conclusions. Coordinating the necessary logistics to conduct a drilling campaign to obtain ore grade samples requires a costly investment of time, effort and finances. It is therefore not surprising that given relatively few number of samples geoscientists have been satisfied with each interpolated value being analyzed and computed on a case-by-case basis. Furthermore, geostatisticians suggests that rule-based model identification techniques cannot recognize patterns or characteristics as reliably as well-trained geostatisticians.

The use of kriging as a medical imaging interpolation technique raises an economic tradeoff that has not been a factor in the geosciences, but that must be addressed in medical imaging. This tradeoff concerns the number of samples and interpolation values of interest. Unlike typical geoscience data volumes, medical imaging volumes such as MRI may contain millions of sampled modality space voxels. If a radiologist were required to increase the effective resolution of such a volume by a

factor of only two, the number of interpolated estimates can easily extend into the billions. As resolutions of medical imaging devices increase, this number increases exponentially. Therefore, economics mandate that if kriging is to be accepted and integrated into commercial medical imaging systems as a viable method of interpolation, the structural analysis and interpolation processes of kriging must be automated. The AFIT Kriging Algorithm tool developed as part of this research effort provides this automated, unsupervised capability. It is coded in the IDL programming language.[1]

Automated Volumetric Structural Analysis Capabilities Provided by the AFIT Kriging Algorithm

The AFIT Kriging Algorithm differs from the kriging implementation of previous medical imaging researchers in three ways. First, modality space data is not assumed to be stationary. The AFIT Kriging Algorithm removes the local drift about each PTBE generating a volume of stationary residuals to interpolate. Second, spatial variability about each PTBE is not assumed. The AFIT Kriging Algorithm structurally analyzes the stationary residuals to determine which of several models shares characteristics with those observed in variograms of the sampled modality space data. Third, a fixed size neighborhood is not globally assumed about each PTBE. The AFIT Kriging Algorithm utilizes information obtained through a structural analysis of stationary residual values to determine the kriging neighborhood about each PTBE. The extent and orientation of the kriging neighborhood is computed for each point to be estimated based upon the ranges of spatial dependency observed along each analyzed direction. Once initial parameters are entered by the user, the structural analysis, variogram

---

[1] IDL is an analysis and visualization programming environment developed and distributed by Research Systems, Inc.

modeling and kriging interpolation proceed in an automated, unsupervised manner and are adapted in accordance with the variability about each point that is interpolated.

The automated, unsupervised, point-by-point three-dimensional structural analysis capabilities that the AFIT Kriging Algorithm tool provides are not available in their entirety in geostatistical software packages that are currently available.[2] These capabilities include variogram model and parameter determination, as well as arbitrarily-oriented, noncubic, nonsymmetrical neighborhood identification.

The domain of spatial models that had been considered for incorporation into the algorithm is strongly rooted in the geosciences. Spatial models that have proven successful when interpolating natural geological phenomena were incorporated into the automated variogram model fitting routines of the AFIT Kriging Algorithm. The AFIT Kriging Algorithm, however, extends capabilities that are currently available to geostatisticians by adaptively determining the spatial model type, model parameters and the extent and orientation of the spatially dependent neighborhood about each voxel whose value is to be interpolated. The AFIT Kriging Algorithm is adaptive in that the model type, parameters and neighborhood extent and orientation are not assumed to be constant for the entire volume of interest, but rather are computed point-by-point through an automated, local structural analysis about each point.

Composite variograms were incorporated into the AFIT Kriging Algorithm to analyze spatial variation along a *general* direction, as opposed to a discrete line-of-sight direction. Composite variograms, specified by a principle line-of-sight direction and an angular tolerance about the principle direction, were shown to reduce variogram variability when compared to their discrete counterparts.

---

[2] Ref: [Carr80, Davi77, Deut92, ISAT94, Parr91]

The neighborhood search mechanism of the AFIT Kriging Algorithm is itself another contribution to the general class of spatial estimators. This mechanism, though integrated into the AFIT Kriging Algorithm, functions independently of subsequent tasks that are included in the AFIT Kriging Algorithm.

MRI Scanner Distortion Model to Simulate the Distorted Representation of Patient Space

For kriging to be used, neighboring modality space voxels must be shown to exhibit a spatial dependency upon one another such that they can justifiably be represented using regionalized variables. This enables kriging to be considered a valid method of interpolation for the data. The need to show the presence of spatial continuity led me to limit the scope of analysis and interpolation to data obtained from a single modality - magnetic resonance imaging.

Experiments and algorithms that characterize MRI scanner distortion were investigated.[3] Though information contained in the associated publications was incorporated into the MRI Scanner Distortion Model where applicable, none independently satisfied the requirements of this research. Previously published experiments were designed to either correct modality space distortion, as opposed to reconstructing distorted modality space data; independently operate on two dimensional slices; or assume perfect gradient fields. This research required the generation of three-dimensional distorted modality space reconstructions based upon real, not ideal, MRI gradient fields. Therefore, the patient space acquisition and modality space

---

[3] [Chan90], [Chan92], [DeSo92], [Feig86], [Lai83], [Odon85], [Will87]

reconstruction processes of an MRI scanner were simulated in an MRI scanner distortion model described in Chapter III.

My model permits a comparative analysis between volumetric spatially dependent patient space data and its corresponding MRI modality space representation to be accomplished. It simulates MRI scanner distortion to generate three-dimensional modality space representations of phantom patient space volumes. Modality space is distorted based upon sampled voxel shifts that occur during reconstruction due to the following simulated nonideal fields: an inhomogeneous static magnetic field; three orthogonally oriented nonlinear gradient magnetic fields; and gaussian shaped rf pulses. Nonuniformity of these magnetic fields and the frequency rolloff characteristics of the rf excitation pulses determine the geometric and intensity distortion that appears in the reconstructed modality space data. Practical considerations drove the decision to simulate the MRI modality space reconstruction of a patient space scan. The MRI scanner distortion model provides virtually unlimited access to the reconstruction processes of an MRI scanner. The model also provides the researcher with total control over the characteristics of the nonuniform magnetic and rf fields, which in turn determine the extent of distortion present in the modality space reconstruction.

Results of the MRI patient space to modality space simulation using the MRI scanner distortion model analysis indicated that MRI modality space data exhibits spatial dependencies between neighboring voxels, even in relatively heterogeneous regions of high contrast. These results justify representing MRI modality space data using regionalized variables and, in turn, justifies its interpolation using kriging.

Results provided by the MRI scanner distortion simulator also indicate that the spatial variation of modality space MRI data exhibits spatial extent and dependency

characteristics that are similar to those of the patient space source data. Since this is not a necessary kriging condition it is beyond the scope of this research to quantify the similarity beyond the description provided in Chapter V. This is, nonetheless, significant because any linear interpolator that uses modality space voxels to compute its estimates inherently generates reconstructions that are distorted when compared to patient space. Even if the interpolator were ideal and introduced no error to the reconstructed volume, the modality space samples used by a linear interpolator would be distorted due to physical limitations of the scanning device. Comparisons between the patient space and modality space variograms can quantify the spatial deviation that is introduced by the scanning device.

A Method to Determine the Existence of Spatial Continuity in a Modality Space Volume is Demonstrated

To justify using kriging to interpolate medical MRI data, the MRI modality space data was shown to be representable using regionalized variables. Though the scope of this analysis had been limited to MRI data, data acquired through any other three-dimensional imaging modality can be similarly analyzed for spatial continuity. If spatial continuity is shown to exist such that it can be represented using a deterministic, continuous, positive-definite function, then the data can be interpolated using kriging. This research demonstrates how this process can be accomplished for a specific imaging modality.

The physical data collection and reconstruction processes that are responsible for distorting the modality space reconstruction of a patient space volume must be modeled. Patient space phantoms known to exhibit spatially homogeneous characteristics are transformed to their distorted modality space representations using

a simulation that distorts modality space in accordance with the modeled data collection and reconstruction processes. Spatial analysis of the simulated modality space data proceeds using geostatistical theory and practices developed for geological applications, but modified and automated in this research to account for medical data characteristics that differ from geological data. The significant difference between these two data sets is the modality space sampling density and the resultant number of estimates that are required to increase the effective resolution of a volumetric medical imaging data set. As in geostatistical estimation applications, the variogram is the tool used that describes and quantifies directional dependency between neighboring modality space voxels.

Recommendations for Future Research

My research demonstrated that kriging estimation accuracy can be significantly improved and made to exceed that of linear interpolation techniques if a sufficiently accurate mathematical model of patient space spatial variation can be derived. My research also demonstrated that the cause of the observed kriging estimation error is due to simplifying assumptions that have been employed successfully in the geosciences. As currently implemented, the AFIT Kriging Algorithm constructs a three-dimensional mathematical model that relies upon the simplifying assumptions used in the geosciences. To construct a more accurate model of spatial variation from the variograms computed as part of the modality space structural analysis, these simplifying assumptions and the algorithm must be modified to account for these departures. These assumptions and proposals for their removal are discussed in the following paragraphs.

For ease of aligning the major and minor axes of anisotropy with the modality space Cartesian coordinate axes, the major and minor (and intermediate) anisotropic characteristics of modality space data are assumed to lie along directions orthogonal to one another. In general, this condition is infrequently observed in real medical data. Assigning orthogonal directions to represent nonorthogonal directions of anisotropy clearly introduces error into the mathematical model. To reduce this error it is recommended that shearing equations be considered and incorporated into the mathematical model.

To simplify the complexity of the mathematical model, anisotropic conditions are assumed to be strictly geometric. That is, nested structures associated with zonal anisotropies are not present. This assumption can result in an averaging, or smoothing, effect if significant zonal anisotropies are present. Therefore, it is recommended that zonal anisotropy be analyzed and, if present, nested structure be incorporated into the mathematical model to account for their additive, directional effects. Again, it is recommended that shearing equations be considered for each nested structure that is isolated.

Given a simple orthogonal model of spatial variation that assumes geometric-only anisotropies, the surface of an ellipsoid is able to consistently represent the extent of spatial dependency about each PTBE. However, when general anisotropic conditions are permitted, the ellipsoid is unable to reflect the complex three-dimensional isosurfaces of the range of support about a PTBE. It is recommended that the extent of this neighborhood be interpolated using the ranges associated with the directional variograms. The PTBE would still be assumed to be centrally located within its spatially dependent neighborhood. This is characteristic of a model derived from

variograms whose complimentary directions produce equivalent results. However, complexity of the isosurface that represents the extent of the neighborhood of spatial dependency about a PTBE would not be forced to be approximated by three orthogonal axes.

The AFIT Kriging Algorithm also assumes no nugget effect is observed in the modality space data. This assumption is based upon the fact that a single density value is associated with each sampled voxel.[4] In reality, measurement errors are known to occur. The *uncertainty principle for measurement* asserts variability occurs in all measurements [Resn89]. Therefore it is recommended that the capability to determine and/or incorporate experimentally or theoretically obtained measurement error parameters, as a nugget effect, into the mathematical model of spatial variation.

Incorporating these recommendations into future enhancements of the AFIT Kriging Algorithm will provide more accurate mathematical models to describe the spatial variation of detrended modality space data. Since kriging provides linear, unbiased, optimal estimates consistent with an employed model of spatial variation, if one assumes modality space is an accurate representation of its patient space source data, then the incorporation of these recommendations should significantly improve kriging estimation accuracy.

Though the AFIT Kriging Algorithm tool had been developed specifically with the medical imaging community in mind, its benefits extend beyond the medical imaging domain. The ability of the AFIT Kriging Algorithm to adaptively determine the spatial model type and parameters, and spatial extent and orientation based upon the local neighborhood about each point to be estimated on a point-by-point basis can

---

[4] A single acquisition scan is assumed.

improve kriging estimation accuracies in the geosciences. Previously assumed global assumptions of spatial variation are no longer necessary. Models of spatial variation can be derived on a point-by-point basis and as a result can more accurately describe the variation about each point. This research demonstrates that estimation accuracies increase when model accuracies similarly increase.

The automated capabilities of the AFIT Kriging Algorithm tool also can be utilized within the geosciences in areas that have become increasingly more reliant upon the technical advances in remote digital sensing. In areas such as these that require an automated method to interpolate a relatively large number of spatially dependent estimates before kriging can be considered a viable method of interpolation, this research has resulted in a turnkey tool whose capabilities can once again be immediately utilized to provide increased estimation accuracies using kriging.

There is another area where the AFIT Kriging Algorithm can contribute to the state-of-the-art. It can be utilized in the dissemination of telemedicine, or other three-dimensional data, to reduce transmission and storage bandwidth requirements. This research has focused on increasing the resolution of rendered medical volumes beyond that acquired by the scanning device. To do so requires the prediction of the behavior of patient space based upon the local spatial variation of modality space voxels. Disseminating medical imagery from stationary medical facilities to airborne, naval or ground-based medical evacuation platforms has somewhat different requirements from imagery resolution enhancement.

Telemedicine dissemination requirements are directed towards the compression of imagery as opposed to its resolution expansion. Therefore, spatial models would not play a predictive role; rather, they would be constructed to characterize known voxel

values to a specified level of accuracy. The model parameters, integer coefficients, subsequently could be transmitted or stored along with a significantly reduced resolution subset of modality space. The storage and transmission of model parameters would effectively decrease transmission and storage bandwidth requirements when compared to the original modality space volume, while maintaining the capability to accurately reconstruct the original modality space imagery. The Battlefield Awareness and Dissemination Demonstration of the Information for the Warrior Program offers a specific opportunity where the technique could be demonstrated [Rome96].

Appendix A

GLOSSARY

alternative hypothesis - a hypothesis that is used in statistical decision theory and that differs from the null hypothesis.

anisotropy - having properties whose values vary as a function of direction.

averaging - an interpolation technique that averages the values of the nearest sampled voxels to determine the value of the estimated voxel.

bias - the measure of the consistent systematic difference between results and an accepted reference or true value [Beth91]. The expected value of the estimation error at any particular location [Isaa89].

border region - declared by the Kriging Algorithm to be the region of a volume whose voxel values are most dissimilar.

bound water -water molecules that are bound to the surface of proteins in biological tissue. Relaxation times for these molecules are less than those associated with free water.

common model - the variogram model that is identified by the Kriging Algorithm to represent all directional variograms computed about a given point.

composite directional variogram - a variogram computed for all sampled values of a VOI that are separated by a specified distance and that lie along any direction within a given angular tolerance of a specified direction.

computational cell - a logical cube formed by eight sampled voxels such that the four vertices of the cube are formed by four voxels in one data slice and the other four vertices by four voxels in an adjacent data slice.

computed tomography - a 3D imaging modality that uses a collimated X-ray radiation source opposite a linear array of detectors that is rotated around a patient to acquire each transaxial slice [Ney93].

continuity - describes the change in spatial variation as a function of separation distance and direction. Properties of continuous data change little as distance and direction are varied.

cross excitation - occurs in an MRI scanner when rf energy directed to excite nuclei in a defined region or slice also excites nuclei in an adjacent region or slice. Results in a distorted representation of the proton density present in the intended region.

CT - see *computed tomography*

dilation - a morphological operation that increases the geometrical region of an object by setting background voxels that are adjacent to the object to the same value as the object.

discrete directional variogram - a variogram computed for all sampled values of a VOI that are separated by a specified distance and that lie along a specified direction. Also see *variogram.*

drift - a statistical property that varies as a function of position.

estimation error - the difference between an interpolated value and its true value at the same location.

estimation error variance - the variance of the estimation errors over a set of estimates. Ordinary kriging minimizes the estimation error variance.

exactness - an estimation property that is satisfied when an estimator predicts sampled values with zero error.

excitation pulse - the rf pulse emitted by an MRI scanner to excite hydrogen nuclei in body tissue to a higher energy state. When the nuclei return to their equilibrium state, the potential energy gained during the excitation is emitted as electromagnetic energy that is received and spatially correlated by the MRI scanner.

expected value - the mean value of a random variable.

experimental variogram - a variogram whose values are computed from the values of sampled locations. The domain of this function consists of the set of vector distances that can be computed between all pairs of sampled locations. Also see *variogram.*

field of view - the extent of the physical world region for which data is collected, analyzed, processed, and rendered.

FOV - see *field of view*

free water - water molecules that are not bound to proteins. Unbounded, these water molecules are relatively small, orient themselves to external magnetic fields more rapidly than larger molecules and assume relatively high precessional frequencies. Consequently, their relaxation times are longer than those of larger molecules.

geometrical distortion - the expansion or compression of physical world object dimensions in its OS voxel representation.

geostatistics - a hybrid discipline of mining engineering, geology, mathematics and statistics [Cres91].

gyromagnetic ratio - a characteristic constant for each nuclear species given by the ratio of the nuclear magnetic moment to the angular momentum. For protons, its value is 2.675×10^8 radians $s^{-1} T^{-1}$ [Beal84].

image space - the three dimensional space that represents a transformed object space. Geometric viewing transformations and signal processing operations are typically applied to object space to produce the desired image space representation.

intensity distortion - the misrepresentation of values of a physical world property in its OS voxel representation.

inter - a prefix that means between two separate elements, such as between voxels or slices.

interpolation - the process of generating a volume with finer resolution than the volume from which it is generated. The number of voxels increases and voxel size decreases in the new volume. New voxel values are estimated using voxel values from the original volume; An informed estimate of the unknown [Wats92].

intra - a prefix that means within an element, such as within a voxel or slice.

in vitro - observed outside the body

in vivo - observed within the living body.

isosurface - a contour surface of constant value voxels.

isotopes - atoms that have the same number of electrons (atomic number), but have different atomic weights and, therefore, different nuclear spins.

isotropic - having properties whose values are stationary and independent of direction.

kriging - a geostatistical estimator that is linear, unbiased and optimal. Does not assume variability of the data.

kriging neighborhood - the set of spatially dependent samples about a PTBE whose values contribute to the value of the kriged estimate.

kriging weights - obtained from the kriging system of equations. Determines the magnitude of contribution from each sampled value of the kriging neighborhood.

Larmor frequency - the angular frequency of precessional motion of the orbital spin of an electron about its nucleus in the presence of an external magnetic field.

level of significance - the maximum probability for which one is willing to risk rejecting a statistical hypothesis that should be accepted, otherwise known as a Type I error.

linear estimator - an interpolation operator whose estimate is a linear combination of values from contributing samples.

logical slice - a two dimensional data slice whose voxel values are estimated.

longitudinal relaxation time - the exponential time constant that characterizes the growth or decay of the component of magnetization parallel to an external magnetic field as a result of the interaction of the nucleus with its entire surroundings. Also referred to as the spin-lattice or T1 time.

magnetic resonance imaging - a 3D imaging modality based upon the transfer of energy from a pulsed rf field to nuclear particles when the rf frequency equals the frequency of precession of the magnetic moment of the nuclear particles in a large external magnetic field.

magnetic susceptibility - a characteristic property of a substance that indicates the intensity of magnetization produced in the substance when exposed to an external magnetic field.

main effects - see *median main effects*

median main effects - components of global drift that are computed at intervals along each coordinate axis of a VOI.

median polish - a technique that decomposes and removes global drift from a data set leaving behind stationary residuals.

modality - a method of data collection. 3D medical imaging examples include CT and MRI.

modality space - the three dimensional object space of a specific imaging modality

MRI - see *magnetic resonance imaging*

MS - see *modality space*

nearest neighbor - an interpolation technique that uses the value of the nearest sampled voxel to determine the value of the interpolated voxel.

normalized variogram - computed by scaling the values of a variogram so that they range from 0 to 1.

nuclear magnetic moment - the magnetic moment associated with a nucleus as a consequence of its inherent charge and spin [Beal84].

nugget effect - the variance of a totally random component superimposed on a REV [Davi77]. Consists of measurement errors and microscale variations within the data [Cres88]. Causes a discontinuity at the origin of a variogram.

null hypothesis - a hypothesis that is used in statistical decision theory and that is generated with the intent of disproving.

OK variance - see *ordinary kriging variance*

OS - see *Object Space*

object space - the three dimensional sampled representation of (a subset of) patient space.

optimal estimator - an interpolation operator that minimizes the variance between predicted values and corresponding true values.

ordinary kriging - a geostatistical estimation technique that requires the mean of the data that is interpolated be stationary, though it does not require the mean be known.

ordinary kriging variance - the minimized error variance of an estimate obtained using ordinary kriging.

patient space - physical space in the context of medical imaging.

PET - see *positron emission tomography*

phase encoding - an MRI positional encoding technique that utilizes the phase of the magnetic resonant signal. Nuclear spins at locations of large magnetic fields precess faster than at locations of lesser magnetic fields.

physical space - the three dimensional, continuous real world.

positive definite - a property that ensures the existence of a unique solution to the kriging system of equations. Each of the following is a necessary and sufficient condition for a real symmetric matrix C to possess this property [Isaa89]:
(1) $\mathbf{w}^T \mathbf{C} \mathbf{w} > 0$ $\forall \mathbf{w} \neq 0$;
(2)   All eigenvalues of C are greater than 0;
(3)   All submatrices of C have positive determinants;
(4)   All pivots (without row exchanges) are greater than 0.

positron emission tomography - a 3D imaging modality that quantitatively portrays the 3D distribution of a radioisotope tracer within an organ of interest to measure fluid movement and metabolism [Styt89]. Unlike SPECT, the radioisotope is incorporated into the chemical structure of the carrier pharmaceutical.

precession - a rotation of the spin axis about which an object is spinning that results from a torque that is applied perpendicular to the spin axis and to the axis of the resulting rotational motion.

PS - see *patient space*

PTBE - point to be estimated

pulse width - in the frequency domain, the bandwidth of an rf pule. In the time domain, the duration of an rf pulse.

range - the separation distance beyond which samples are spatially independent. The sill of a variogram curve is reached at this separation distance.

range-normalized variogram - computed by scaling the abscissa of a variogram, (separation distance), so that the range of the variogram is 1.

regionalized variable - a random variable that varies continuously but cannot be described precisely using a deterministic function due to its complex variation.

relaxation - the process by which nuclei in an excited energy state return to a lower energy state such as their equilibrium ground state.

residual - the small scale variation that remains after large scale drift is removed [Cres91]. The result of a median polish drift removal process.

REV - see *regionalized variable*

rf - radio-frequency

rf pulse - a short burst of electromagnetic radiation, generally having a rectangular time domain amplitude envelope.

sampling error - error introduced to the OS representation of a physical volume due to the data acquisition process.

semivariogram - a geostatistical tool that describes spatial variation within a VOI as one-half the mean square of the difference between values that are separated by a specified vector distance. Often referred to as the *variogram*.

separation distance - the vector distance between a pair of voxels.

sill - the variogram value obtained when the variogram curve reaches a plateau at its range. Indicates the global variance of the data for which spatial variation is computed.

single photon emission computed tomography - a 3D imaging modality that uses radioisotope tags to track fluid movement and metabolic activity in the body.

spatial dependency - a spatial correlation between values of a characteristic property of a substance. Occurs within the zone of influence of a REV.

SPECT - see *single photon emission computed tomography*

spin density - the density of resonating nuclei in a defined region.

spin-lattice relaxation time - see *longitudinal relaxation time*

spin-spin relaxation time - see *transverse relaxation time*

standard deviation - the root mean square of the deviation of a set of values from their mean.

stationarity - a property that requires the mean of a regionalized variable is constant.

statistical hypothesis - statements about the probability distribution of a sample population. The statements may be true or false and therefore need to be proven or disproven.

structural analysis - the process of analyzing characteristic structure of a continuous phenomenon using only a sampled subset of values to represent the phenomenon.

T1 time - see *longitudinal relaxation time*

T2 time - see *traverse relaxation time*

theoretical variogram - see *variogram model*

transverse relaxation time - the exponential time constant that characterizes the decay of the component of magnetization transverse to an external magnetic field as a result of the mutual interaction of the nucleus with other neighboring nuclei. Also referred to as the spin-spin or T2 time.

trilinear interpolation - an interpolation technique that incorporates a distance-weighted averaging of the nearest sampled voxels to determine the value of the estimate.

unbiased estimator - an interpolation operator that produces an average estimation error of zero [Huij73]. Requires the weights of all contributing samples sum to unity.

universal kriging - a geostatistical estimation technique that allows the data that is interpolated to exhibit a nonstationary, unknown mean as long as the mean is of a known functional form.

validation data - a reduced resolution MS volume interpolated by the Kriging Algorithm to its original resolution. Enables the computation of estimation error statistics for each estimate obtained.

variance - the expected squared difference from the mean of a random variable U, given by $Var\{U\} = E\{ [U - E\{U\}]^2 \}$; the square of the standard deviation.

variogram - a geostatistical tool that describes spatial variation within a VOI as the mean square of the difference between values that are separated by a specified vector distance. The resulting curve is a function of distance and direction.

variogram model - a continuous function that represents an experimental variogram. Its values can be calculated for any separation distance.

VOI - volume of interest

voxel - a volume element that is shaped like a parallelpiped. A 3D set of voxels, all the same size, form a discrete representation of a continuous volume.

zone of influence - the region about a sample of interest beyond which all other samples exhibit independent characteristics. The range of a directional variogram characterizes the extent of this region along a specific direction.

Appendix B

Kriging Estimates Using Discrete Directional Variograms

File: dat1204; discrete directional variograms

Enh-Res Coord.	Neigh Voxels	OK Variance	Kriging Estimate	True Value	Trilinear Estimate	% Project Err Krige	% Project Err Trilin	Model Error Mean	Model Error STD
(7,45,45)	34	2779.3	164.34	38	137.63	4.210	3.320	0.245	0.284
(7,45,46)	36	3422.4	153.04	83	129.79	2.334	1.559	0.249	0.298
(7,45,47)	20	1645.6	132.63	132	123.63	0.021	0.279	0.375	0.311
(7,46,45)	36	2729.2	178.95	163	137.84	0.531	0.838	0.298	0.289
(7,46,46)	56	3970.2	153.32	265	126.71	3.721	4.608	0.242	0.294
(7,46,47)	44	3119.9	119.06	160	111.62	1.364	1.612	0.293	0.307
(7,47,45)	20	1741.8	173.94	197	138.38	0.768	1.954	0.542	0.357
(7,47,46)	42	3217.5	128.34	259	118.22	4.354	4.691	0.285	0.323
(7,47,47)	28	2624.5	49.29	71	99.88	0.723	0.962	0.259	0.346
(7,53,45)	12	742.6	149.78	92	141.63	1.925	1.654	0.301	0.289
(7,53,46)	30	2766.7	195.42	189	142.60	0.214	1.546	0.339	0.307
(7,53,47)	24	2110.0	168.41	74	148.13	3.146	2.470	0.344	0.293
(7,54,45)	16	1846.8	122.58	159	129.52	1.213	0.982	0.301	0.299
(7,54,46)	14	2363.2	181.08	37	133.15	4.801	3.204	0.278	0.300
(7,54,47)	22	2194.3	178.39	100	138.54	2.612	1.284	0.302	0.291
(7,55,45)	14	1771.3	135.16	59	118.25	2.538	1.974	0.309	0.321
(7,55,46)	18	2812.1	180.00	150	123.57	1.000	0.881	0.277	0.308
(7,55,47)	30	2695.7	145.39	85	132.13	2.012	1.570	0.315	0.300
(9,33,53)	26	2456.5	154.11	225	136.75	2.362	2.941	0.213	0.305
(9,33,54)	26	2750.5	127.64	128	126.69	0.012	0.044	0.241	0.314
(9,33,55)	26	2136.0	131.89	37	116.88	3.162	2.662	0.285	0.323
(9,34,53)	12	570.2	163.41	124	140.06	1.313	0.535	0.212	0.288
(9,34,54)	20	2622.9	158.26	192	130.03	1.124	2.065	0.205	0.296
(9,34,55)	16	1671.2	107.12	36	119.60	2.370	2.786	0.239	0.306
(9,35,53)	8	526.7	149.30	77	147.88	2.409	2.362	0.199	0.289
(9,35,54)	22	2808.4	146.59	105	136.64	1.386	1.054	0.216	0.307
(9,35,55)	16	1294.4	120.22	51	125.63	2.307	2.487	0.260	0.321
(10,33,53)	24	2431.5	167.36	92	139.39	2.511	1.579	0.222	0.286
(10,33,54)	24	2999.0	167.77	170	128.60	0.074	1.379	0.205	0.303
(10,33,55)	24	2175.6	154.27	26	115.49	4.274	2.982	0.205	0.289
(10,34,53)	22	2477.8	209.22	164	142.49	1.507	0.717	0.207	0.283
(10,34,55)	18	1954.6	168.98	58	121.70	3.698	2.123	0.192	0.277
(10,35,53)	26	2572.2	198.99	104	148.38	3.165	1.479	0.204	0.297
(10,35,54)	24	3195.8	177.56	21	142.92	5.217	4.063	0.235	0.308
(10,35,55)	14	2018.0	139.12	70	127.50	2.303	1.916	0.259	0.307
(11,33,53)	22	2098.0	150.44	60	145.25	3.014	2.841	0.227	0.271
(11,33,54)	24	2632.0	156.20	154	131.32	0.073	0.756	0.217	0.282
(11,33,55)	22	1950.6	140.47	66	118.13	2.481	1.737	0.242	0.293
(11,34,53)	18	2066.9	179.45	24	147.25	5.180	4.107	0.191	0.266
(11,34,54)	40	3254.2	176.63	64	137.22	3.753	2.440	0.204	0.277
(11,34,55)	20	1969.7	143.62	92	122.41	1.720	1.013	0.223	0.274
(11,35,53)	22	2271.5	164.00	15	154.00	4.965	4.632	0.236	0.294
(11,35,54)	26	2823.2	152.33	123	142.53	0.977	0.651	0.258	0.308
(11,35,55)	34	2542.3	136.43	116	130.25	0.681	0.475	0.316	0.315
(11,36,55)	36	2760.3	119.22	310	130.32	6.357	5.987	0.253	0.281
(11,37,55)	26	2374.0	176.54	121	127.88	1.851	0.229	0.291	0.290
(12,35,55)	32	2685.2	137.33	121	116.39	0.544	0.154	0.293	0.311
(12,36,55)	22	2204.9	127.31	244	121.00	3.888	4.099	0.231	0.281
(12,37,55)	24	2431.0	138.51	75	118.95	2.116	1.464	0.275	0.288

File: dat1204; discrete directional variograms

Enh-Res Coord.	Neigh Voxels	OK Variance	Kriging Estimate	True Value	Trilinear Estimate	% Project Err		Model Error	
						Krige	Trilin	Mean	STD
(13, 9,39)	40	1587.1	66.05	162	95.88	3.197	2.203	0.295	0.275
(13, 9,40)	20	507.0	99.07	61	86.66	1.269	0.855	0.220	0.267
(13, 9,41)	24	1381.6	72.39	58	79.63	0.480	0.721	0.244	0.266
(13,10,39)	34	1578.5	109.85	9	102.11	3.361	3.102	0.330	0.332
(13,10,40)	28	1748.2	137.81	37	95.18	3.359	1.939	0.314	0.279
(13,10,41)	26	1601.1	73.07	73	84.20	0.002	0.373	0.224	0.244
(13,11,39)	26	1524.7	164.77	77	107.25	2.925	1.008	0.316	0.318
(13,11,40)	34	1782.5	160.93	26	95.95	4.496	2.331	0.324	0.282
(13,11,41)	22	1384.4	83.27	147	89.75	2.124	1.908	0.252	0.245
(13,33,35)	20	1234.6	116.19	94	113.00	0.739	0.633	0.442	0.312
(13,33,36)	16	2147.9	144.11	30	114.41	3.802	2.813	0.259	0.281
(13,33,37)	28	2604.5	133.46	97	119.88	1.215	0.762	0.221	0.260
(13,34,35)	18	1530.1	122.86	94	118.11	0.962	0.803	0.275	0.258
(13,34,36)	36	2999.4	155.19	164	122.51	0.294	1.383	0.316	0.282
(13,34,37)	32	2911.7	112.06	145	126.19	1.098	0.627	0.279	0.264
(13,35,35)	14	1735.7	137.85	101	122.00	1.228	0.700	0.231	0.258
(13,35,36)	34	3144.5	171.03	122	124.74	1.634	0.091	0.316	0.286
(13,35,37)	40	2788.1	154.28	132	131.88	0.743	0.004	0.425	0.290
(13,35,55)	24	2244.9	105.69	21	103.88	2.822	2.762	0.299	0.306
(13,36,55)	28	2309.4	97.71	167	106.87	2.309	2.004	0.282	0.296
(13,37,55)	22	2254.3	92.48	104	110.13	0.384	0.204	0.265	0.280
(13,39,41)	12	1895.0	140.03	36	129.00	3.466	3.099	0.312	0.289
(13,39,42)	20	3037.8	157.33	162	119.77	0.156	1.407	0.353	0.300
(13,39,43)	14	2342.6	140.25	59	118.00	2.707	1.966	0.338	0.310
(13,40,41)	14	1895.7	123.62	54	146.62	2.320	3.086	0.337	0.280
(13,40,42)	14	2583.9	204.05	255	142.12	1.698	3.761	0.317	0.285
(13,40,43)	18	2308.3	116.16	106	137.38	0.339	1.046	0.310	0.283
(13,41,41)	8	185.4	155.89	25	164.13	4.362	4.636	0.296	0.288
(13,41,42)	12	2506.2	213.56	273	157.05	1.981	3.864	0.272	0.282
(13,41,43)	24	2586.5	166.22	66	156.50	3.340	3.016	0.311	0.284
(13,41,47)	40	3101.3	150.43	140	129.38	0.348	0.354	0.351	0.332
(13,41,48)	34	3345.3	140.09	148	125.71	0.264	0.743	0.313	0.314
(13,41,49)	14	1703.4	162.68	24	121.88	4.621	3.261	0.283	0.300
(13,42,47)	42	3424.4	193.97	199	139.89	0.168	1.970	0.258	0.273
(13,42,48)	32	3715.7	188.33	186	133.75	0.078	1.741	0.235	0.273
(13,42,49)	14	1912.4	147.28	103	121.34	1.476	0.611	0.205	0.264
(13,43,47)	38	3572.6	187.56	196	155.88	0.281	1.337	0.261	0.278
(13,43,48)	32	3461.3	175.71	173	139.50	0.090	1.116	0.259	0.291
(13,43,49)	20	2008.1	153.50	46	125.38	3.582	2.645	0.250	0.295
(14, 9,39)	32	1775.3	88.97	109	94.67	0.667	0.477	0.260	0.276
(14, 9,40)	24	2016.9	141.44	122	87.71	0.648	1.143	0.258	0.286
(14, 9,41)	22	1666.3	120.83	83	78.42	1.261	0.153	0.250	0.275
(14,10,39)	30	1683.6	137.32	37	100.28	3.343	2.108	0.305	0.303
(14,10,41)	22	1542.1	121.90	99	84.94	0.763	0.469	0.226	0.257
(14,11,39)	20	1507.9	162.95	151	102.41	0.398	1.619	0.267	0.282
(14,11,40)	20	2076.3	194.98	132	97.03	2.098	1.165	0.278	0.357
(14,11,41)	18	1719.8	93.46	60	89.58	1.115	0.986	0.190	0.245
(14,33,35)	20	1559.3	148.46	57	117.53	3.048	2.017	0.278	0.245
(14,33,36)	34	3040.9	174.26	35	123.97	4.640	2.965	0.276	0.280

File: dat1204; discrete directional variograms

Enh-Res Coord.	Neigh Voxels	OK Variance	Kriging Estimate	True Value	Trilinear Estimate	% Project Err		Model Error	
						Krige	Trilin	Mean	STD
(14,33,37)	26	2713.2	147.86	131	130.27	0.562	0.024	0.268	0.242
(14,34,35)	14	1540.0	155.70	100	118.26	1.856	0.608	0.246	0.242
(14,34,37)	34	3031.4	177.74	150	136.80	0.924	0.440	0.230	0.240
(14,35,35)	14	2104.2	186.92	198	121.29	0.369	2.556	0.230	0.245
(14,35,36)	42	3387.2	220.54	125	133.66	3.184	0.289	0.316	0.266
(14,35,37)	32	3131.5	192.95	138	144.64	1.831	0.221	0.314	0.251
(14,39,41)	20	2185.1	152.77	123	122.99	0.992	0.000	0.268	0.274
(14,39,42)	16	3124.2	226.21	309	129.30	2.759	5.988	0.274	0.289
(14,39,43)	14	2892.0	179.04	117	130.26	2.067	0.442	0.249	0.270
(14,40,41)	14	2070.4	179.79	100	135.60	2.659	1.186	0.276	0.266
(14,40,43)	16	2323.7	174.22	213	144.31	1.292	2.289	0.235	0.260
(14,41,41)	20	2627.3	193.13	65	148.05	4.270	2.767	0.259	0.277
(14,41,42)	30	3927.6	254.17	193	154.80	2.038	1.273	0.246	0.279
(14,41,43)	24	2982.4	197.20	237	153.44	1.326	2.784	0.253	0.269
(14,41,47)	44	3074.1	133.55	45	117.73	2.951	2.424	0.417	0.346
(14,41,48)	40	3727.2	147.00	79	120.00	2.266	1.366	0.318	0.316
(14,41,49)	14	1784.6	156.85	109	117.59	1.594	0.286	0.293	0.298
(14,42,47)	42	3365.2	183.11	94	132.96	2.969	1.298	0.275	0.284
(14,42,49)	12	1765.1	178.57	45	123.03	4.451	2.600	0.190	0.265
(14,43,47)	48	3674.8	175.01	178	146.22	0.100	1.059	0.281	0.289
(14,43,48)	24	3886.7	213.86	198	138.84	0.528	1.971	0.267	0.293
(14,43,49)	14	2092.8	128.95	99	127.31	0.998	0.943	0.214	0.278
(15, 9,39)	30	1615.4	84.45	95	97.50	0.352	0.083	0.335	0.281
(15, 9,40)	34	1862.9	141.33	102	86.38	1.310	0.520	0.338	0.286
(15, 9,41)	28	1606.1	133.61	97	79.50	1.220	0.583	0.341	0.295
(15,10,39)	26	1521.2	106.61	93	98.57	0.454	0.186	0.329	0.276
(15,10,40)	28	1897.9	161.47	40	93.56	4.048	1.785	0.306	0.275
(15,10,41)	26	1718.0	115.45	120	84.43	0.152	1.185	0.284	0.276
(15,11,39)	22	1487.1	122.02	133	102.38	0.366	1.020	0.244	0.257
(15,11,40)	22	1819.3	140.38	38	95.27	3.412	1.908	0.237	0.271
(15,11,41)	22	1585.6	87.67	45	92.75	1.422	1.591	0.233	0.258
(15,33,35)	20	1595.0	137.24	121	126.25	0.541	0.175	0.295	0.249
(15,33,36)	16	2201.0	159.00	118	132.19	1.366	0.473	0.295	0.252
(15,33,37)	20	1727.5	126.98	67	141.13	1.999	2.470	0.320	0.251
(15,33,38)	16	2475.9	134.55	115	134.72	0.651	0.657	0.251	0.260
(15,33,39)	24	2594.7	134.09	52	127.38	2.735	2.512	0.252	0.267
(15,34,35)	14	1569.9	152.38	149	125.43	0.113	0.785	0.262	0.244
(15,34,36)	16	2319.8	187.61	80	136.60	3.586	1.886	0.284	0.251
(15,34,37)	18	1838.4	159.22	119	146.99	1.340	0.933	0.275	0.240
(15,34,38)	12	2506.6	174.03	91	142.93	2.767	1.730	0.249	0.253
(15,34,39)	18	1962.7	178.07	81	137.02	3.235	1.867	0.259	0.251
(15,35,35)	14	1826.8	142.55	27	128.00	3.850	3.366	0.257	0.252
(15,35,36)	18	2850.8	173.14	85	141.86	2.937	1.895	0.249	0.255
(15,35,37)	34	3142.1	215.84	78	160.13	4.593	2.737	0.294	0.247
(15,35,38)	20	2873.5	164.71	137	155.95	0.923	0.631	0.257	0.256
(15,35,39)	20	2059.2	190.16	59	150.38	4.371	3.045	0.270	0.262
(15,39,41)	8	231.5	123.58	54	123.00	2.319	2.299	0.288	0.282
(15,39,42)	12	2792.3	170.00	126	132.72	1.466	0.224	0.258	0.273
(15,39,43)	16	2079.6	121.55	59	147.50	2.084	2.949	0.241	0.269

File: dat1204; discrete directional variograms

Enh-Res Coord.	Neigh Voxels	OK Variance	Kriging Estimate	True Value	Trilinear Estimate	% Project Err Krige	% Project Err Trilin	Model Error Mean	Model Error STD
(15,39,55)	22	2108.8	139.41	44	122.13	3.179	2.603	0.250	0.284
(15,40,41)	4	766.2	123.62	153	131.36	0.979	0.721	0.252	0.268
(15,40,42)	18	3262.9	183.66	152	141.08	1.055	0.364	0.246	0.266
(15,40,43)	4	598.3	140.86	54	151.33	2.894	3.243	0.217	0.254
(15,40,55)	18	1901.1	131.97	121	123.41	0.366	0.080	0.296	0.288
(15,41,41)	20	2367.2	139.86	69	138.50	2.361	2.316	0.315	0.287
(15,41,42)	24	3270.7	172.93	141	144.65	1.064	0.122	0.250	0.278
(15,41,43)	22	2614.1	170.98	71	153.50	3.332	2.749	0.274	0.268
(15,41,44)	18	3007.8	163.03	42	133.88	4.033	3.062	0.230	0.273
(15,41,45)	8	188.9	115.61	74	115.38	1.387	1.379	0.217	0.280
(15,41,47)	14	1573.9	74.69	263	108.50	6.275	5.148	0.554	0.376
(15,41,48)	18	2840.0	72.21	174	110.28	3.392	2.123	0.290	0.307
(15,41,49)	14	1734.0	112.86	102	114.50	0.362	0.417	0.263	0.288
(15,41,55)	22	1905.5	146.90	75	128.75	2.396	1.791	0.352	0.314
(15,42,43)	22	2824.1	189.23	103	154.34	2.873	1.711	0.243	0.248
(15,42,44)	14	2591.2	173.83	85	141.69	2.960	1.889	0.230	0.244
(15,42,45)	8	305.1	141.71	134	128.65	0.257	0.178	0.208	0.259
(15,42,47)	16	1653.5	107.58	258	122.64	5.012	4.510	0.497	0.325
(15,42,48)	14	2515.3	163.19	123	121.30	1.339	0.057	0.236	0.278
(15,42,49)	14	1848.1	192.94	124	121.62	2.297	0.079	0.183	0.263
(15,43,43)	28	3017.5	180.29	116	157.00	2.142	1.366	0.272	0.254
(15,43,44)	12	530.0	161.69	128	149.54	1.123	0.718	0.233	0.254
(15,43,45)	8	1198.0	138.08	16	144.25	4.068	4.274	0.249	0.267
(15,43,47)	40	2817.2	151.55	136	139.75	0.518	0.125	0.487	0.333
(15,43,48)	18	2691.4	215.35	190	135.05	0.845	1.831	0.320	0.297
(15,43,49)	14	1662.6	158.44	180	133.25	0.718	1.558	0.298	0.298
(16,33,37)	30	2779.3	165.43	168	131.95	0.086	1.201	0.309	0.253
(16,33,38)	20	3076.3	169.80	142	130.43	0.926	0.386	0.240	0.265
(16,33,39)	18	2620.7	179.17	72	124.31	3.571	1.743	0.257	0.277
(16,34,37)	34	3203.4	219.16	63	135.67	5.203	2.422	0.260	0.238
(16,34,39)	22	2823.9	170.49	77	130.59	3.115	1.786	0.213	0.249
(16,35,37)	34	3464.8	188.47	86	144.20	3.415	1.939	0.263	0.247
(16,35,38)	20	3862.9	190.40	101	145.89	2.979	1.496	0.236	0.269
(16,35,39)	20	2724.2	142.49	83	143.37	1.982	2.012	0.261	0.274
(16,39,55)	16	2084.5	110.38	119	126.77	0.287	0.259	0.220	0.278
(16,40,55)	26	2624.3	180.41	132	131.91	1.613	0.003	0.247	0.267
(16,41,43)	20	2848.8	139.42	124	129.51	0.514	0.184	0.274	0.280
(16,41,44)	4	2392.4	191.94	134	129.54	1.931	0.148	0.256	0.284
(16,41,45)	4	1180.5	132.96	106	121.59	0.898	0.519	0.279	0.299
(16,41,55)	14	2030.8	207.99	10	138.43	6.597	4.280	0.260	0.272
(16,42,43)	20	2907.9	157.94	265	131.88	3.568	4.436	0.266	0.256
(16,42,45)	6	1457.9	168.72	68	129.41	3.356	2.046	0.249	0.270
(16,43,43)	16	2000.4	137.72	166	135.33	0.942	1.022	0.271	0.268
(16,43,44)	4	2664.5	199.03	133	138.84	2.200	0.195	0.239	0.272
(16,43,45)	18	2151.8	182.51	121	140.78	2.050	0.659	0.293	0.286
(17,33,37)	22	2252.4	110.33	17	125.00	3.110	3.599	0.299	0.273
(17,33,38)	30	3149.0	141.93	47	123.67	3.163	2.555	0.275	0.283
(17,33,39)	26	2438.9	158.76	111	124.13	1.592	0.437	0.337	0.329
(17,34,37)	32	3021.9	169.65	51	123.40	3.954	2.412	0.258	0.250

File: dat1204; discrete directional variograms

Enh-Res Coord.	Neigh Voxels	OK Variance	Kriging Estimate	True Value	Trilinear Estimate	% Project Err		Model Error	
						Krige	Trilin	Mean	STD
(17,34,38)	28	3535.7	192.26	140	127.97	1.741	0.401	0.258	0.269
(17,34,39)	32	3154.8	137.94	90	129.79	1.597	1.326	0.296	0.303
(17,35,37)	40	3437.2	129.56	48	129.75	2.718	2.724	0.270	0.258
(17,35,38)	38	3996.5	171.13	186	131.78	0.496	1.807	0.250	0.268
(17,35,39)	38	3513.2	165.27	180	138.13	0.491	1.395	0.274	0.298
(17,39,55)	20	1626.0	102.71	102	131.25	0.024	0.975	0.433	0.302
(17,40,55)	36	2596.2	187.74	30	138.59	5.256	3.618	0.296	0.268
(17,41,43)	24	2942.3	101.54	44	105.63	1.917	2.053	0.282	0.282
(17,41,44)	26	3255.1	162.38	180	114.71	0.587	2.176	0.273	0.284
(17,41,45)	8	172.0	129.10	5	129.63	4.135	4.153	0.371	0.338
(17,41,55)	20	1781.5	195.25	32	151.00	5.440	3.965	0.368	0.287
(17,42,43)	20	2846.5	112.46	219	109.36	3.550	3.653	0.254	0.263
(17,42,44)	6	978.4	182.16	50	119.40	4.404	2.313	0.213	0.261
(17,42,45)	8	307.7	154.10	83	132.62	2.369	1.654	0.268	0.286
(17,43,43)	16	2427.5	119.37	54	116.00	2.178	2.066	0.251	0.271
(17,43,44)	12	2721.9	169.41	170	125.27	0.020	1.491	0.241	0.267
(17,43,45)	16	2148.1	152.93	75	140.13	2.597	2.170	0.343	0.300
(17,45,55)	14	1599.8	84.01	160	96.25	2.532	2.124	0.319	0.299
(17,46,55)	20	1824.9	123.63	46	100.40	2.587	1.813	0.278	0.290
(17,47,55)	18	1564.3	142.23	65	107.25	2.574	1.408	0.275	0.283
(17,53,29)	40	1835.3	142.51	123	128.13	0.650	0.171	0.393	0.302
(17,53,30)	20	1474.2	133.85	32	127.67	3.394	3.188	0.367	0.315
(17,53,31)	20	1367.5	149.24	99	126.75	1.674	0.925	0.399	0.334
(17,54,29)	18	1011.3	128.83	155	121.85	0.872	1.105	0.352	0.288
(17,54,30)	16	1380.8	140.87	66	122.80	2.495	1.893	0.352	0.311
(17,54,31)	18	1084.6	142.97	139	120.64	0.132	0.612	0.312	0.310
(17,55,29)	16	940.9	142.70	67	119.88	2.523	1.762	0.385	0.303
(17,55,30)	16	1258.7	129.56	69	118.14	2.018	1.637	0.407	0.337
(17,55,31)	20	979.9	138.36	70	117.75	2.278	1.591	0.399	0.337
(18,45,55)	14	1841.5	41.80	31	85.51	0.360	1.816	0.259	0.283
(18,46,55)	26	2009.9	111.49	40	97.47	2.382	1.915	0.238	0.269
(18,47,55)	20	1858.4	130.41	49	105.62	2.713	1.887	0.261	0.269
(18,53,29)	20	1207.2	137.52	95	123.03	1.417	0.934	0.320	0.282
(18,53,30)	20	1720.2	142.45	124	123.86	0.615	0.005	0.332	0.299
(18,53,31)	20	1092.1	139.70	151	121.81	0.377	0.973	0.359	0.287
(18,54,29)	18	1069.1	141.78	123	117.35	0.626	0.188	0.305	0.277
(18,54,31)	18	1172.9	150.70	102	116.97	1.623	0.499	0.260	0.287
(18,55,29)	14	1138.5	148.32	64	113.91	2.810	1.663	0.333	0.297
(18,55,30)	20	1625.0	175.52	159	117.10	0.551	1.396	0.343	0.339
(18,55,31)	20	1043.7	140.73	107	115.28	1.124	0.276	0.372	0.333
(19,19,53)	60	2029.9	100.24	130	112.25	0.992	0.591	0.476	0.382
(19,19,54)	62	2375.4	129.11	71	116.56	1.936	1.518	0.451	0.368
(19,19,55)	70	2263.2	122.79	134	124.75	0.374	0.308	0.459	0.393
(19,20,53)	42	1809.9	126.11	103	113.44	0.770	0.348	0.391	0.324
(19,20,54)	62	2407.5	148.07	87	116.73	2.035	0.991	0.399	0.322
(19,20,55)	56	2259.6	127.95	148	121.57	0.668	0.881	0.354	0.326
(19,21,53)	52	1851.4	134.61	175	117.25	1.346	1.924	0.419	0.352
(19,21,54)	40	2141.4	168.59	71	116.63	3.252	1.521	0.373	0.327
(19,21,55)	28	1797.2	127.76	31	118.38	3.224	2.912	0.259	0.299

File: dat1204; discrete directional variograms

Enh-Res Coord.	Neigh Voxels	OK Variance	Kriging Estimate	True Value	Trilinear Estimate	% Project Err		Model Error	
						Krige	Trilin	Mean	STD
(19,45,55)	12	1611.5	28.37	90	76.75	2.054	0.442	0.219	0.259
(19,46,55)	22	2233.2	43.22	228	90.44	6.157	4.584	0.253	0.262
(19,47,55)	22	1748.7	101.35	185	105.38	2.787	2.653	0.291	0.273
(19,53,29)	16	1002.6	107.75	47	119.38	2.024	2.412	0.363	0.293
(19,53,30)	18	1571.0	153.52	33	118.57	4.016	2.852	0.330	0.296
					Mean	2.085	1.693	0.285	0.286
					Std Dev	1.459	1.229	0.062	
					Max	6.597	5.988		

Appendix C

Kriging Estimates Using
Composite Directional Variograms,
Angular Tolerance ±50°

File: dat1207; composite directional variograms (50 deg)

Enh-Res Coord.	Neigh Voxels	OK Variance	Kriging Estimate	True Value	Trilinear Estimate	% Projection Er Krige	Trilin	Model Error Mean	STD
(7,45,45)	8	479.6	139.56	38	137.63	3.384	3.320	0.165	0.27
(7,45,46)	8	1283.3	141.04	83	129.79	1.934	1.559	0.173	0.292
(7,45,47)	8	463.5	122.76	132	123.63	0.308	0.279	0.175	0.283
(7,46,45)	12	850.7	140.53	163	137.84	0.749	0.838	0.178	0.269
(7,46,46)	8	2410.4	138.64	265	126.71	4.210	4.608	0.179	0.293
(7,46,47)	4	568.6	114.32	160	111.62	1.522	1.612	0.149	0.275
(7,47,45)	8	795.0	158.97	197	138.38	1.267	1.954	0.228	0.288
(7,47,46)	12	483.3	125.14	259	118.22	4.460	4.691	0.198	0.304
(7,47,47)	8	201.7	98.34	71	99.88	0.911	0.962	0.168	0.279
(7,53,45)	8	-325.9	143.54	92	141.63	1.717	1.654	0.171	0.259
(7,53,46)	8	1009.9	176.43	189	142.60	0.419	1.546	0.2	0.278
(7,53,47)	8	-362.7	147.86	74	148.13	2.461	2.470	0.187	0.264
(7,54,45)	12	1082.1	135.06	159	129.52	0.798	0.982	0.164	0.257
(7,54,46)	14	1411.7	170.65	37	133.15	4.453	3.204	0.193	0.279
(7,54,47)	4	919.8	160.57	100	138.54	2.018	1.284	0.172	0.261
(7,55,45)	8	699.8	118.22	59	118.25	1.973	1.974	0.181	0.268
(7,55,46)	8	953.7	146.25	150	123.57	0.125	0.881	0.201	0.285
(7,55,47)	8	-514.1	131.93	85	132.13	1.564	1.570	0.187	0.265
(9,33,53)	8	139.9	136.47	225	136.75	2.950	2.941	0.153	0.262
(9,33,54)	4	-88.3	128.77	128	126.69	0.026	0.044	0.163	0.289
(9,33,55)	10	251.6	114.65	37	116.88	2.587	2.662	0.176	0.293
(9,34,53)	12	431.0	159.65	124	140.06	1.188	0.535	0.154	0.261
(9,34,54)	10	900.8	153.34	192	130.03	1.288	2.065	0.151	0.283
(9,34,55)	4	94.3	145.10	36	119.60	3.635	2.786	0.164	0.273
(9,35,53)	8	207.9	148.70	77	147.88	2.389	2.362	0.16	0.265
(9,35,54)	8	746.0	137.48	105	136.64	1.082	1.054	0.162	0.291
(9,35,55)	8	-324.8	126.00	51	125.63	2.499	2.487	0.168	0.274
(10,33,53)	6	1474.1	169.63	92	139.39	2.587	1.579	0.156	0.264
(10,33,54)	6	2139.4	168.41	170	128.60	0.053	1.379	0.14	0.279
(10,33,55)	6	353.5	123.60	26	115.49	3.252	2.982	0.147	0.274
(10,34,53)	6	1985.3	205.91	164	142.49	1.397	0.717	0.141	0.259
(10,34,55)	4	518.4	167.66	58	121.70	3.654	2.123	0.14	0.26
(10,35,53)	4	1229.7	187.19	104	148.38	2.772	1.479	0.147	0.265
(10,35,54)	8	2802.6	193.18	21	142.92	5.738	4.063	0.157	0.285
(10,35,55)	4	794.8	133.76	70	127.50	2.125	1.916	0.163	0.268
(11,33,53)	8	432.5	145.53	60	145.25	2.850	2.841	0.166	0.264
(11,33,54)	12	758.7	135.54	154	131.32	0.615	0.756	0.153	0.274
(11,33,55)	8	-64.0	116.44	66	118.13	1.681	1.737	0.159	0.258
(11,34,53)	12	564.6	169.94	24	147.25	4.863	4.107	0.132	0.253
(11,34,54)	10	890.2	162.18	64	137.22	3.272	2.440	0.155	0.272
(11,34,55)	12	507.6	139.20	92	122.41	1.573	1.013	0.157	0.255
(11,35,53)	8	367.7	154.28	15	154.00	4.641	4.632	0.164	0.27
(11,35,54)	12	711.6	138.06	123	142.53	0.502	0.651	0.197	0.291
(11,35,55)	8	212.6	140.10	116	130.25	0.803	0.475	0.201	0.272
(11,36,55)	4	473.8	110.74	310	130.32	6.640	5.987	0.186	0.261
(11,37,55)	10	1178.8	172.72	121	127.88	1.724	0.229	0.19	0.262
(12,35,55)	12	1346.6	158.03	121	116.39	1.234	0.154	0.181	0.274
(12,36,55)	6	1636.8	130.02	244	121.00	3.798	4.099	0.168	0.259
(12,37,55)	4	1456.6	130.21	75	118.95	1.840	1.464	0.163	0.259

File: dat1207; composite directional variograms (50 deg)

Enh-Res Coord.	Neigh Voxels	OK Variance	Kriging Estimate	True Value	Trilinear Estimate	% Projection Er		Model Error	
						Krige	Trilin	Mean	STD
(13, 9,39)	10	296.0	97.11	162	95.88	2.162	2.203	0.185	0.265
(13, 9,40)	4	706.2	85.62	61	86.66	0.820	0.855	0.188	0.283
(13, 9,41)	8	-289.7	79.60	58	79.63	0.720	0.721	0.174	0.27
(13,10,39)	8	530.6	98.72	9	102.11	2.990	3.102	0.19	0.268
(13,10,40)	6	829.0	132.28	37	95.18	3.175	1.939	0.185	0.28
(13,10,41)	6	-22.8	89.93	73	84.20	0.564	0.373	0.157	0.26
(13,11,39)	10	384.6	95.21	77	107.25	0.607	1.008	0.213	0.268
(13,11,40)	4	740.9	149.64	26	95.95	4.120	2.331	0.201	0.279
(13,11,41)	8	223.0	96.45	147	89.75	1.685	1.908	0.171	0.256
(13,33,35)	8	-439.6	113.86	94	113.00	0.662	0.633	0.229	0.262
(13,33,36)	8	710.3	134.58	30	114.41	3.485	2.813	0.167	0.28
(13,33,37)	8	-498.5	121.03	97	119.88	0.801	0.762	0.164	0.267
(13,34,35)	4	-657.0	109.18	94	118.11	0.506	0.803	0.195	0.248
(13,34,36)	2	658.7	165.18	164	122.51	0.039	1.383	0.171	0.275
(13,34,37)	4	-782.7	121.50	145	126.19	0.783	0.627	0.175	0.264
(13,35,35)	8	-443.7	123.15	101	122.00	0.738	0.700	0.195	0.255
(13,35,36)	4	320.4	159.35	122	124.74	1.245	0.091	0.197	0.28
(13,35,37)	8	-511.1	132.37	132	131.88	0.012	0.004	0.215	0.274
(13,35,55)	8	317.0	106.57	21	103.88	2.851	2.762	0.212	0.277
(13,36,55)	8	225.1	106.13	167	106.87	2.028	2.004	0.172	0.261
(13,37,55)	8	58.6	110.69	104	110.13	0.223	0.204	0.168	0.26
(13,39,41)	8	882.6	129.05	36	129.00	3.101	3.099	0.176	0.261
(13,39,42)	4	964.1	175.03	162	119.77	0.434	1.407	0.19	0.272
(13,39,43)	8	64.9	119.24	59	118.00	2.007	1.966	0.18	0.254
(13,40,41)	12	1545.0	146.74	54	146.62	3.090	3.086	0.171	0.257
(13,40,42)	10	1563.2	197.63	255	142.12	1.912	3.761	0.217	0.276
(13,40,43)	4	634.3	137.26	106	137.38	1.042	1.046	0.182	0.257
(13,41,41)	8	575.0	165.20	25	164.13	4.672	4.636	0.191	0.267
(13,41,42)	12	564.5	188.86	273	157.05	2.804	3.864	0.189	0.272
(13,41,43)	8	236.5	159.32	66	156.50	3.110	3.016	0.197	0.266
(13,41,47)	8	227.5	129.31	140	129.38	0.356	0.354	0.207	0.273
(13,41,48)	12	559.4	125.47	148	125.71	0.751	0.743	0.21	0.281
(13,41,49)	8	212.1	121.15	24	121.88	3.237	3.261	0.168	0.258
(13,42,47)	4	587.7	181.05	199	139.89	0.598	1.970	0.168	0.257
(13,42,48)	10	1058.7	176.16	186	133.75	0.328	1.741	0.174	0.272
(13,42,49)	12	608.3	142.92	103	121.34	1.330	0.611	0.15	0.253
(13,43,47)	8	432.9	156.30	196	155.88	1.323	1.337	0.177	0.269
(13,43,48)	12	563.4	150.61	173	139.50	0.746	1.116	0.191	0.285
(13,43,49)	8	386.6	125.30	46	125.38	2.642	2.645	0.17	0.261
(14, 9,39)	4	531.6	126.35	109	94.67	0.578	0.477	0.165	0.263
(14, 9,40)	6	689.3	137.49	122	87.71	0.516	1.143	0.161	0.281
(14, 9,41)	4	334.7	94.05	83	78.42	0.368	0.153	0.152	0.267
(14,10,39)	2	-70.3	156.24	37	100.28	3.973	2.108	0.174	0.269
(14,10,41)	2	439.4	138.62	99	84.94	1.320	0.469	0.154	0.262
(14,11,39)	4	-364.3	138.43	151	102.41	0.419	1.619	0.188	0.268
(14,11,40)	4	859.7	178.69	132	97.03	1.556	1.165	0.175	0.281
(14,11,41)	4	-176.9	115.39	60	89.58	1.846	0.986	0.158	0.26
(14,33,35)	4	-225.5	149.31	57	117.53	3.076	2.017	0.196	0.258
(14,33,36)	2	756.2	183.14	35	123.97	4.936	2.965	0.167	0.274

File: dat1207; composite directional variograms (50 deg)

Enh-Res Coord.	Neigh Voxels	OK Variance	Kriging Estimate	True Value	Trilinear Estimate	% Projection Er		Model Error	
						Krige	Trilin	Mean	STD
(14,33,37)	12	442.4	134.86	131	130.27	0.129	0.024	0.176	0.264
(14,34,35)	6	-111.4	164.43	100	118.26	2.147	0.608	0.185	0.249
(14,34,37)	6	1565.7	172.60	150	136.80	0.753	0.440	0.159	0.251
(14,35,35)	4	-105.4	177.30	198	121.29	0.690	2.556	0.18	0.254
(14,35,36)	10	2295.9	217.05	125	133.66	3.067	0.289	0.19	0.268
(14,35,37)	4	1291.0	165.14	138	144.64	0.904	0.221	0.201	0.258
(14,39,41)	12	1620.3	164.54	123	122.99	1.384	0.000	0.165	0.253
(14,39,42)	10	2315.8	235.55	309	129.30	2.448	5.988	0.209	0.275
(14,39,43)	4	899.5	167.67	117	130.26	1.688	0.442	0.177	0.252
(14,40,41)	10	2444.6	174.39	100	135.60	2.479	1.186	0.197	0.259
(14,40,43)	10	2485.0	176.62	213	144.31	1.212	2.289	0.195	0.255
(14,41,41)	12	1453.2	194.21	65	148.05	4.306	2.767	0.168	0.255
(14,41,42)	10	2179.9	247.19	193	154.80	1.806	1.273	0.175	0.27
(14,41,43)	4	1499.8	178.00	237	153.44	1.966	2.784	0.162	0.258
(14,41,47)	4	1426.2	153.32	45	117.73	3.609	2.424	0.223	0.274
(14,41,48)	6	2016.7	155.38	79	120.00	2.545	1.366	0.213	0.287
(14,41,49)	4	1348.3	126.06	109	117.59	0.568	0.286	0.172	0.261
(14,42,47)	6	2256.2	197.67	94	132.96	3.454	1.298	0.182	0.26
(14,42,49)	6	2139.8	184.02	45	123.03	4.632	2.600	0.141	0.25
(14,43,47)	4	1486.6	169.50	178	146.22	0.283	1.059	0.2	0.277
(14,43,48)	6	2191.2	199.94	198	138.84	0.065	1.971	0.192	0.29
(14,43,49)	4	1612.6	156.33	99	127.31	1.910	0.943	0.166	0.26
(15, 9,39)	8	311.4	94.50	95	97.50	0.017	0.083	0.196	0.272
(15, 9,40)	4	126.2	120.39	102	86.38	0.613	0.520	0.196	0.285
(15, 9,41)	8	-51.2	82.30	97	79.50	0.490	0.583	0.206	0.282
(15,10,39)	4	122.4	119.39	93	98.57	0.879	0.186	0.182	0.271
(15,10,40)	4	1176.1	167.96	40	93.56	4.264	1.785	0.189	0.278
(15,10,41)	10	570.3	115.52	120	84.43	0.149	1.185	0.214	0.277
(15,11,39)	8	-290.1	102.55	133	102.38	1.015	1.020	0.188	0.267
(15,11,40)	4	218.7	129.49	38	95.27	3.049	1.908	0.18	0.28
(15,11,41)	8	-366.7	93.07	45	92.75	1.602	1.591	0.17	0.266
(15,33,35)	8	-448.9	127.22	121	126.25	0.207	0.175	0.208	0.261
(15,33,36)	4	487.8	155.52	118	132.19	1.250	0.473	0.186	0.277
(15,33,37)	8	-484.8	142.31	67	141.13	2.510	2.470	0.213	0.267
(15,33,38)	4	529.1	128.77	115	134.72	0.459	0.657	0.171	0.28
(15,33,39)	8	-529.6	129.03	52	127.38	2.567	2.512	0.173	0.263
(15,34,35)	12	-243.0	129.58	149	125.43	0.647	0.785	0.195	0.25
(15,34,36)	6	866.8	195.27	80	136.60	3.841	1.886	0.185	0.268
(15,34,37)	8	358.4	181.04	119	146.99	2.067	0.933	0.162	0.249
(15,34,38)	6	958.0	159.69	91	142.93	2.289	1.730	0.163	0.271
(15,34,39)	4	-108.0	164.83	81	137.02	2.794	1.867	0.15	0.247
(15,35,35)	8	-13.8	126.53	27	128.00	3.317	3.366	0.201	0.264
(15,35,36)	4	1015.1	175.41	85	141.86	3.013	1.895	0.195	0.271
(15,35,37)	8	684.5	160.23	78	160.13	2.740	2.737	0.196	0.26
(15,35,38)	12	900.3	148.57	137	155.95	0.386	0.631	0.181	0.274
(15,35,39)	8	375.1	151.55	59	150.38	3.084	3.045	0.177	0.255
(15,39,41)	8	548.6	123.44	54	123.00	2.314	2.299	0.168	0.255
(15,39,42)	12	638.7	157.32	126	132.72	1.044	0.224	0.18	0.272
(15,39,43)	8	263.5	149.13	59	147.50	3.003	2.949	0.177	0.257

C-4

File: dat1207; composite directional variograms (50 deg)

Enh-Res Coord.	Neigh Voxels	OK Variance	Kriging Estimate	True Value	Trilinear Estimate	% Projection Er Krige	Trilin	Model Error Mean	STD
(15,39,55)	8	6.6	127.99	44	122.13	2.799	2.603	0.163	0.257
(15,40,41)	12	1234.4	124.98	153	131.36	0.934	0.721	0.171	0.251
(15,40,42)	10	1091.4	159.90	152	141.08	0.263	0.364	0.188	0.271
(15,40,43)	4	627.2	140.86	54	151.33	2.894	3.243	0.173	0.25
(15,40,55)	4	131.3	154.55	121	123.41	1.118	0.080	0.184	0.267
(15,41,41)	8	234.7	139.83	69	138.50	2.360	2.316	0.179	0.257
(15,41,42)	12	585.0	157.34	141	144.65	0.544	0.122	0.169	0.273
(15,41,43)	8	242.8	154.73	71	153.50	2.790	2.749	0.182	0.258
(15,41,44)	12	563.5	140.30	42	133.88	3.276	3.062	0.177	0.269
(15,41,45)	8	216.6	117.49	74	115.38	1.449	1.379	0.186	0.269
(15,41,47)	8	210.6	110.05	263	108.50	5.097	5.148	0.241	0.279
(15,41,48)	12	537.8	123.37	174	110.28	1.687	2.123	0.208	0.287
(15,41,49)	8	236.0	113.03	102	114.50	0.367	0.417	0.171	0.262
(15,41,55)	8	178.5	123.83	75	128.75	1.627	1.791	0.228	0.276
(15,42,43)	4	618.8	169.43	103	154.34	2.214	1.711	0.168	0.248
(15,42,44)	10	1047.6	165.95	85	141.69	2.697	1.889	0.183	0.259
(15,42,45)	4	295.6	148.23	134	128.65	0.474	0.178	0.164	0.257
(15,42,47)	4	516.6	145.24	258	122.64	3.757	4.510	0.226	0.27
(15,42,48)	10	988.2	159.04	123	121.30	1.201	0.057	0.187	0.28
(15,42,49)	10	416.1	140.03	124	121.62	0.534	0.079	0.148	0.256
(15,43,43)	8	243.7	158.45	116	157.00	1.414	1.366	0.18	0.251
(15,43,44)	12	557.6	161.69	128	149.54	1.123	0.718	0.191	0.264
(15,43,45)	8	252.0	149.71	16	144.25	4.455	4.274	0.197	0.267
(15,43,47)	8	291.9	139.15	136	139.75	0.105	0.125	0.278	0.28
(15,43,48)	12	509.0	147.96	190	135.05	1.401	1.831	0.24	0.293
(15,43,49)	8	248.2	132.53	180	133.25	1.582	1.558	0.189	0.269
(16,33,37)	10	696.4	145.14	168	131.95	0.762	1.201	0.184	0.264
(16,33,38)	8	2988.0	166.90	142	130.43	0.830	0.386	0.172	0.273
(16,33,39)	4	633.2	148.58	72	124.31	2.552	1.743	0.172	0.26
(16,34,37)	2	-125.4	219.54	63	135.67	5.216	2.422	0.157	0.247
(16,34,39)	10	680.3	157.34	77	130.59	2.677	1.786	0.164	0.251
(16,35,37)	12	1308.5	153.51	86	144.20	2.250	1.939	0.176	0.253
(16,35,38)	10	2210.7	179.91	101	145.89	2.629	1.496	0.168	0.27
(16,35,39)	12	1125.1	154.84	83	143.37	2.394	2.012	0.169	0.257
(16,39,55)	10	732.6	118.62	119	126.77	0.013	0.259	0.153	0.264
(16,40,55)	14	1543.6	165.51	132	131.91	1.117	0.003	0.168	0.261
(16,41,43)	4	1539.0	130.60	124	129.51	0.220	0.184	0.176	0.258
(16,41,44)	6	2109.1	186.00	134	129.54	1.733	0.148	0.187	0.275
(16,41,45)	4	559.3	135.98	106	121.59	0.999	0.519	0.21	0.269
(16,41,55)	12	1491.1	125.69	10	138.43	3.855	4.280	0.2	0.27
(16,42,43)	6	2601.3	160.48	265	131.88	3.483	4.436	0.162	0.247
(16,42,45)	6	2269.2	170.67	68	129.41	3.421	2.046	0.172	0.258
(16,43,43)	4	1547.2	153.45	166	135.33	0.418	1.022	0.157	0.25
(16,43,44)	6	2164.9	196.42	133	138.84	2.113	0.195	0.167	0.268
(16,43,45)	4	1374.1	162.87	121	140.78	1.395	0.659	0.179	0.264
(17,33,37)	10	1040.6	120.77	17	125.00	3.458	3.599	0.188	0.276
(17,33,38)	4	688.5	138.83	47	123.67	3.060	2.555	0.186	0.284
(17,33,39)	8	383.9	124.47	111	124.13	0.449	0.437	0.199	0.274
(17,34,37)	4	372.3	182.42	51	123.40	4.379	2.412	0.181	0.26

C-5

File: dat1207; composite directional variograms (50 deg)

Enh-Res Coord.	Neigh Voxels	OK Variance	Kriging Estimate	True Value	Trilinear Estimate	% Projection Er		Model Error	
						Krige	Trilin	Mean	STD
(17,34,38)	6	2113.0	195.76	140	127.97	1.858	0.401	0.172	0.27
(17,34,39)	8	677.8	144.07	90	129.79	1.802	1.326	0.193	0.262
(17,35,37)	10	1253.0	125.84	48	129.75	2.594	2.724	0.199	0.266
(17,35,38)	8	2272.3	171.84	186	131.78	0.472	1.807	0.183	0.271
(17,35,39)	8	622.9	140.42	180	138.13	1.319	1.395	0.177	0.263
(17,39,55)	8	1008.6	142.12	102	131.25	1.337	0.975	0.201	0.276
(17,40,55)	16	1815.4	180.15	30	138.59	5.003	3.618	0.199	0.267
(17,41,43)	8	255.4	105.70	44	105.63	2.056	2.053	0.179	0.264
(17,41,44)	12	583.3	141.36	180	114.71	1.288	2.176	0.185	0.282
(17,41,45)	8	-132.8	131.02	5	129.63	4.199	4.153	0.256	0.283
(17,41,55)	14	1761.0	148.73	32	151.00	3.890	3.965	0.236	0.28
(17,42,43)	4	659.5	131.39	219	109.36	2.919	3.653	0.148	0.253
(17,42,44)	10	1085.6	175.09	50	119.40	4.168	2.313	0.172	0.275
(17,42,45)	4	577.2	167.25	83	132.62	2.808	1.654	0.181	0.268
(17,43,43)	8	258.7	116.61	54	116.00	2.086	2.066	0.167	0.254
(17,43,44)	12	604.2	151.30	170	125.27	0.623	1.491	0.173	0.271
(17,43,45)	8	230.7	141.16	75	140.13	2.205	2.170	0.211	0.273
(17,45,55)	8	-447.9	96.25	160	96.25	2.124	2.124	0.194	0.274
(17,46,55)	4	-657.5	120.79	46	100.40	2.492	1.813	0.186	0.266
(17,47,55)	8	-416.9	107.48	65	107.25	1.415	1.408	0.198	0.264
(17,53,29)	8	230.0	126.72	123	128.13	0.124	0.171	0.211	0.257
(17,53,30)	14	1426.6	142.10	32	127.67	3.669	3.188	0.231	0.278
(17,53,31)	8	-238.4	127.33	99	126.75	0.944	0.925	0.207	0.259
(17,54,29)	8	488.8	141.51	155	121.85	0.450	1.105	0.184	0.251
(17,54,30)	12	1508.8	163.19	66	122.80	3.238	1.893	0.208	0.272
(17,54,31)	4	-381.8	144.77	139	120.64	0.192	0.612	0.183	0.253
(17,55,29)	8	-224.0	122.03	67	119.88	1.834	1.762	0.196	0.261
(17,55,30)	4	772.2	129.25	69	118.14	2.008	1.637	0.213	0.28
(17,55,31)	8	-276.6	118.42	70	117.75	1.614	1.591	0.224	0.263
(18,45,55)	4	429.8	101.01	31	85.51	2.333	1.816	0.167	0.27
(18,46,55)	6	-126.6	113.19	40	97.47	2.439	1.915	0.169	0.263
(18,47,55)	4	-275.6	116.21	49	105.62	2.240	1.887	0.179	0.264
(18,53,29)	4	259.8	134.50	95	123.03	1.316	0.934	0.18	0.256
(18,53,30)	10	1744.6	142.89	124	123.86	0.629	0.005	0.197	0.274
(18,53,31)	8	427.1	132.50	151	121.81	0.616	0.973	0.182	0.257
(18,54,29)	10	735.6	160.04	123	117.35	1.234	0.188	0.159	0.248
(18,54,31)	2	-450.5	177.23	102	116.97	2.507	0.499	0.169	0.249
(18,55,29)	8	381.2	127.44	64	113.91	2.114	1.663	0.172	0.261
(18,55,30)	6	1073.0	168.98	159	117.10	0.333	1.396	0.201	0.285
(18,55,31)	4	-42.0	144.92	107	115.28	1.263	0.276	0.209	0.266
(19,19,53)	12	1259.6	105.24	130	112.25	0.825	0.591	0.225	0.297
(19,19,54)	8	1260.3	150.20	71	116.56	2.639	1.518	0.213	0.299
(19,19,55)	14	1337.7	111.69	134	124.75	0.744	0.308	0.24	0.293
(19,20,53)	18	1381.3	112.10	103	113.44	0.303	0.348	0.221	0.278
(19,20,54)	6	1332.6	151.97	87	116.73	2.165	0.991	0.212	0.292
(19,20,55)	16	1258.2	129.11	148	121.57	0.630	0.881	0.218	0.283
(19,21,53)	18	1191.9	133.36	175	117.25	1.388	1.924	0.242	0.283
(19,21,54)	10	1537.1	171.74	71	116.63	3.357	1.521	0.225	0.289
(19,21,55)	10	1022.9	156.87	31	118.38	4.194	2.912	0.21	0.276

File: dat1207; composite directional variograms (50 deg)

Enh-Res Coord.	Neigh Voxels	OK Variance	Kriging Estimate	True Value	Trilinear Estimate	% Projection Er		Model Error	
						Krige	Trilin	Mean	STD
(19,45,55)	8	204.6	76.74	90	76.75	0.442	0.442	0.165	0.268
(19,46,55)	12	145.0	93.50	228	90.44	4.482	4.584	0.173	0.263
(19,47,55)	8	-170.0	105.69	185	105.38	2.643	2.653	0.199	0.266
(19,53,29)	8	-233.0	121.20	47	119.38	2.473	2.412	0.209	0.268
(19,53,30)	10	1309.4	114.77	33	118.57	2.725	2.852	0.223	0.279
(19,53,31)	8	-328.0	119.77	96	118.50	0.792	0.750	0.208	0.267
(19,54,29)	8	454.2	147.58	141	112.43	0.219	0.952	0.19	0.263
(19,54,30)	8	1194.7	170.42	82	114.68	2.946	1.089	0.212	0.278
(19,54,31)	8	477.8	143.81	42	114.91	3.393	2.429	0.201	0.263
(19,55,29)	8	-198.1	111.70	115	110.38	0.110	0.154	0.179	0.273
(19,55,30)	4	704.7	132.13	39	112.31	3.103	2.443	0.203	0.286
(19,55,31)	8	-230.5	117.99	74	116.75	1.466	1.425	0.204	0.28
(20,19,53)	4	-191.9	120.80	102	100.87	0.627	0.038	0.191	0.282
(20,19,54)	6	1375.8	164.95	126	114.52	1.298	0.382	0.198	0.297
(20,19,55)	4	172.9	135.17	118	123.23	0.572	0.174	0.205	0.286
(20,20,53)	10	26.6	126.30	63	108.02	2.109	1.500	0.191	0.271
(20,20,55)	6	-109.6	137.44	80	125.74	1.914	1.524	0.19	0.277
(20,21,53)	12	355.6	123.14	37	111.38	2.870	2.479	0.187	0.266
(20,21,54)	6	1233.9	141.78	217	115.56	2.507	3.380	0.19	0.285
(20,21,55)	4	289.9	131.21	80	122.28	1.707	1.409	0.176	0.262
(21,19,53)	8	-154.6	101.77	156	92.13	1.807	2.128	0.197	0.277
(21,19,54)	8	1604.3	126.30	121	107.07	0.177	0.464	0.211	0.301
(21,19,55)	8	166.2	113.26	106	123.25	0.242	0.575	0.209	0.302
(21,20,53)	4	-352.9	123.80	47	98.35	2.559	1.711	0.172	0.266
(21,20,54)	6	1387.6	153.92	155	113.38	0.036	1.387	0.191	0.289
(21,20,55)	12	-115.9	127.68	100	123.98	0.922	0.799	0.187	0.276
(21,21,53)	8	4.4	112.91	37	107.88	2.529	2.362	0.176	0.264
(21,21,54)	10	1576.8	96.48	69	116.63	0.916	1.587	0.176	0.281
(21,21,55)	8	-37.1	124.92	56	127.25	2.296	2.374	0.163	0.26
(21,39,41)	8	1240.8	108.72	77	109.13	1.057	1.070	0.212	0.272
(21,39,42)	20	2800.6	150.20	122	109.57	0.940	0.414	0.197	0.28
(21,39,43)	8	1362.3	110.99	104	115.88	0.233	0.396	0.215	0.276
(21,40,41)	16	1998.3	138.12	21	115.81	3.903	3.159	0.207	0.266
(21,40,42)	12	3200.3	193.28	131	119.02	2.075	0.399	0.217	0.284
(21,40,43)	16	2121.5	138.10	85	122.75	1.769	1.258	0.208	0.267
(21,41,41)	8	1259.4	125.92	69	125.88	1.897	1.895	0.225	0.273
(21,41,42)	20	2733.3	176.82	234	125.71	1.905	3.609	0.231	0.291
(21,41,43)	8	1716.0	131.27	103	131.88	0.942	0.962	0.227	0.27
(21,49,41)	8	581.0	103.76	141	107.88	1.241	1.104	0.203	0.268
(21,49,42)	8	2127.8	165.50	145	121.71	0.683	0.776	0.216	0.279
(21,49,43)	8	662.0	133.53	89	140.88	1.484	1.729	0.208	0.267
(21,50,41)	12	532.4	121.95	104	116.65	0.598	0.421	0.182	0.262
(21,50,42)	12	2429.6	184.25	167	125.92	0.575	1.369	0.187	0.275
(21,50,43)	10	1346.0	135.90	97	133.59	1.296	1.219	0.172	0.257
(21,51,41)	8	527.5	126.02	174	127.38	1.599	1.554	0.188	0.271
(21,51,42)	4	212.2	153.32	98	125.69	1.844	0.923	0.182	0.28
(21,51,43)	8	557.2	130.47	57	127.63	2.448	2.353	0.172	0.256
(22,39,41)	12	1501.3	130.47	41	127.50	2.981	2.882	0.182	0.261
(22,39,42)	12	3162.9	177.38	317	133.56	4.653	6.113	0.199	0.276

C-7

File: dat1207; composite directional variograms (50 deg)

Enh-Res Coord.	Neigh Voxels	OK Variance	Kriging Estimate	True Value	Trilinear Estimate	% Projection Er		Model Error	
						Krige	Trilin	Mean	STD
(22,39,43)	16	2087.7	156.99	150	150.79	0.233	0.026	0.194	0.265
(22,40,41)	18	2243.0	165.39	81	127.67	2.812	1.555	0.193	0.26
(22,40,43)	18	2354.6	182.65	121	145.93	2.054	0.831	0.2	0.259
(22,41,41)	12	1434.6	159.25	149	129.79	0.342	0.640	0.209	0.267
(22,41,42)	10	2195.0	243.42	255	134.91	0.386	4.002	0.217	0.287
(22,41,43)	12	1775.8	161.51	78	142.48	2.783	2.149	0.214	0.266
(22,49,41)	4	1422.0	114.60	50	121.05	2.153	2.368	0.177	0.263
(22,49,42)	14	2946.2	199.22	32	128.88	5.572	3.228	0.191	0.277
(22,49,43)	4	1478.8	178.61	181	140.54	0.080	1.348	0.172	0.262
(22,50,41)	10	2510.2	125.44	242	123.01	3.884	3.965	0.194	0.271
(22,50,43)	8	1293.4	181.08	117	137.24	2.135	0.674	0.163	0.257
(22,51,41)	18	2060.4	143.15	98	129.66	1.504	1.055	0.217	0.285
(22,51,42)	12	3559.6	197.43	183	131.60	0.481	1.713	0.207	0.279
(22,51,43)	4	380.6	164.76	184	133.37	0.641	1.687	0.178	0.263
(23,37,41)	8	445.7	116.05	121	116.13	0.165	0.162	0.331	0.301
(23,37,42)	12	841.5	152.39	287	139.29	4.486	4.922	0.239	0.296
(23,37,43)	8	511.9	164.87	165	165.13	0.004	0.004	0.209	0.285
(23,38,41)	12	1219.1	130.34	63	130.96	2.244	2.265	0.214	0.26
(23,38,42)	10	1246.3	178.54	175	147.95	0.118	0.901	0.212	0.275
(23,38,43)	12	634.6	176.72	154	175.69	0.757	0.723	0.193	0.266
(23,39,41)	10	1059.2	152.10	97	146.38	1.836	1.645	0.201	0.264
(23,39,42)	12	1468.3	223.40	251	162.11	0.920	2.962	0.214	0.277
(23,39,43)	8	1165.5	187.43	254	186.50	2.218	2.249	0.215	0.261
(23,40,41)	12	1585.1	149.49	41	141.16	3.615	3.337	0.214	0.264
(23,40,42)	10	2520.1	262.77	302	152.39	1.307	4.985	0.228	0.283
(23,40,43)	12	1142.5	186.91	129	169.71	1.930	1.357	0.22	0.261
(23,41,41)	8	735.1	130.22	186	138.13	1.859	1.595	0.213	0.273
(23,41,42)	8	1033.7	218.15	194	140.97	0.805	1.767	0.226	0.291
(23,41,43)	8	866.7	156.99	122	156.38	1.166	1.145	0.22	0.27
(23,49,41)	8	570.7	134.95	231	133.25	3.200	3.257	0.195	0.276
(23,49,42)	12	1215.5	184.38	205	135.68	0.687	2.310	0.225	0.294
(23,49,43)	10	1149.3	163.22	147	145.25	0.541	0.058	0.197	0.277
(23,50,41)	12	1654.6	136.86	141	129.58	0.138	0.381	0.229	0.301
(23,50,42)	14	1749.7	224.22	209	134.30	0.507	2.489	0.59	0.364
(23,50,43)	12	1627.4	161.27	204	142.68	1.424	2.043	0.188	0.272
(23,51,41)	14	1823.5	125.51	183	129.75	1.916	1.774	0.276	0.327
(23,51,42)	12	2582.1	203.59	88	131.91	3.852	1.463	0.251	0.302
(23,51,43)	12	1529.3	149.07	205	143.13	1.864	2.062	0.212	0.286
(24,37,41)	12	1561.2	138.10	57	109.05	2.702	1.734	0.186	0.276
(24,37,42)	10	3054.6	187.10	249	129.67	2.063	3.976	0.178	0.28
(24,37,43)	8	2090.3	191.71	280	150.14	2.942	4.327	0.162	0.265
(24,38,41)	10	1878.1	172.62	66	123.56	3.553	1.918	0.181	0.259
(24,38,43)	10	2337.6	220.98	181	160.50	1.332	0.683	0.169	0.257
(24,39,41)	8	1602.3	165.48	84	133.57	2.715	1.652	0.171	0.264
(24,39,42)	10	3041.0	267.55	193	148.67	2.484	1.477	0.187	0.273
(24,39,43)	8	2057.3	229.22	185	165.21	1.473	0.660	0.184	0.255
(25,37,41)	8	545.6	108.77	168	105.25	1.974	2.091	0.212	0.289
(25,37,42)	20	1077.1	132.77	80	121.03	1.758	1.367	0.194	0.291
(25,37,43)	8	519.4	141.88	257	140.13	3.836	3.895	0.18	0.27

File: dat1207; composite directional variograms (50 deg)

Enh-Res Coord.	Neigh Voxels	OK Variance	Kriging Estimate	True Value	Trilinear Estimate	% Projection Er Krige	Trilin	Model Error Mean	STD
(25,38,41)	12	869.2	126.44	55	113.93	2.380	1.964	0.197	0.277
(25,38,42)	10	997.8	161.93	112	127.40	1.664	0.513	0.183	0.281
(25,38,43)	12	626.6	149.41	109	145.11	1.347	1.203	0.174	0.267
(25,39,41)	8	228.9	126.76	64	124.50	2.091	2.016	0.194	0.288
(25,39,42)	8	823.7	171.36	109	134.48	2.078	0.849	0.182	0.282
(25,39,43)	8	412.1	151.72	87	150.75	2.157	2.124	0.178	0.268
(25,41,51)	8	-116.2	138.64	131	136.75	0.254	0.192	0.198	0.258
(25,41,52)	4	465.4	161.98	90	126.94	2.399	1.231	0.199	0.265
(25,41,53)	8	-458.8	122.81	112	121.75	0.360	0.325	0.224	0.258
(25,42,51)	4	-333.6	152.27	109	126.11	1.442	0.570	0.163	0.26
(25,42,52)	2	674.1	189.65	142	123.83	1.588	0.606	0.162	0.268
(25,42,53)	4	-756.8	125.34	102	121.40	0.778	0.646	0.17	0.255
(25,43,51)	10	828.7	99.73	126	118.88	0.875	0.237	0.179	0.266
(25,43,52)	4	-102.8	149.51	217	118.10	2.249	3.296	0.166	0.275
(25,43,53)	8	-540.7	121.67	44	121.50	2.588	2.582	0.175	0.256
(25,53,41)	8	872.7	131.99	24	133.38	3.598	3.645	0.213	0.281
(25,53,42)	12	1503.7	150.37	93	141.22	1.912	1.607	0.204	0.293
(25,53,43)	8	384.4	151.40	64	150.38	2.912	2.878	0.189	0.278
(25,54,41)	4	824.7	154.86	192	140.44	1.238	1.718	0.163	0.264
(25,54,42)	10	1337.9	163.19	175	140.44	0.394	1.152	0.177	0.287
(25,54,43)	4	620.3	156.12	102	148.03	1.803	1.534	0.17	0.265
(25,55,41)	8	161.1	155.87	177	149.25	0.704	0.925	0.175	0.273
(25,55,42)	8	804.2	174.75	328	145.22	5.106	6.091	0.189	0.3
(25,55,43)	8	253.0	148.44	176	146.63	0.918	0.979	0.192	0.285
(26,41,51)	4	827.2	186.53	53	142.07	4.449	2.968	0.179	0.255
(26,41,52)	4	1294.8	212.22	210	134.61	0.074	2.512	0.201	0.261
(26,41,53)	4	-301.7	144.02	135	120.01	0.300	0.500	0.23	0.264
(26,42,51)	2	156.4	224.37	122	131.21	3.411	0.307	0.163	0.251
(26,42,53)	2	157.7	169.17	45	118.96	4.137	2.465	0.185	0.259
(26,43,51)	10	1016.3	135.84	146	115.29	0.339	1.023	0.162	0.259
(26,43,52)	2	690.7	202.09	119	117.93	2.769	0.036	0.165	0.273
(26,43,53)	4	-279.4	170.53	97	117.53	2.450	0.684	0.176	0.256
(26,53,41)	4	585.3	175.72	148	138.19	0.924	0.327	0.168	0.265
(26,53,42)	14	3160.8	189.74	240	147.29	1.675	3.089	0.175	0.277
(26,53,43)	4	1487.3	199.21	125	163.17	2.473	1.272	0.16	0.264
(26,54,41)	10	1509.8	201.93	276	140.74	2.468	4.507	0.143	0.257
(26,54,43)	10	2465.4	211.76	200	155.64	0.392	1.478	0.151	0.256
(26,55,41)	12	1565.2	185.00	227	139.76	1.399	2.907	0.155	0.265
(26,55,42)	10	2263.9	224.33	395	141.88	5.687	8.435	0.175	0.283
(26,55,43)	4	1488.8	182.84	186	147.67	0.105	1.277	0.177	0.274
(27,41,51)	8	194.0	154.49	100	153.25	1.816	1.774	0.185	0.256
(27,41,52)	4	1148.0	174.97	154	136.44	0.699	0.585	0.215	0.264
(27,41,53)	8	173.2	129.31	101	121.38	0.943	0.679	0.277	0.28
(27,42,51)	4	-96.4	153.68	155	133.66	0.044	0.711	0.174	0.256
(27,42,52)	6	895.6	145.58	57	127.03	2.952	2.333	0.181	0.266
(27,42,53)	8	368.0	154.34	41	120.48	3.777	2.648	0.207	0.269
(27,43,51)	8	217.8	116.03	23	116.63	3.100	3.120	0.171	0.266
(27,43,52)	4	685.2	108.05	149	118.35	1.365	1.021	0.174	0.271
(27,43,53)	8	197.4	125.27	27	120.63	3.275	3.120	0.196	0.266

File: dat1207; composite directional variograms (50 deg)

Enh-Res Coord.	Neigh Voxels	OK Variance	Kriging Estimate	True Value	Trilinear Estimate	% Projection Er		Model Error	
						Krige	Trilin	Mean	STD
(27,53,41)	8	836.7	148.92	195	147.88	1.536	1.570	0.202	0.271
(27,53,42)	12	2305.4	193.57	310	161.77	3.880	4.939	0.204	0.286
(27,53,43)	8	777.3	181.67	132	180.63	1.655	1.620	0.192	0.272
(27,54,41)	12	1476.8	166.86	101	140.42	2.195	1.314	0.18	0.268
(27,54,42)	10	2080.2	207.52	195	148.85	0.417	1.538	0.182	0.275
(27,54,43)	12	1378.3	191.14	66	165.10	4.170	3.302	0.194	0.266
(27,55,41)	8	612.4	135.72	166	136.50	1.009	0.983	0.193	0.277
(27,55,42)	8	1798.4	189.49	210	141.67	0.683	2.277	0.199	0.288
(27,55,43)	8	493.0	154.37	89	153.25	2.178	2.141	0.711	0.379
(29,47,47)	8	-561.5	118.24	124	118.63	0.192	0.179	0.165	0.259
(29,47,48)	8	867.6	115.41	124	111.23	0.286	0.426	0.175	0.271
(29,47,49)	8	-586.3	105.06	108	104.50	0.098	0.117	0.187	0.267
(29,48,47)	12	-436.1	128.14	164	128.25	1.195	1.191	0.161	0.252
(29,48,48)	10	1097.1	152.35	53	118.39	3.311	2.179	0.151	0.265
(29,48,49)	12	581.8	131.53	141	109.46	0.316	1.051	0.162	0.259
(29,49,47)	8	580.1	139.81	80	140.63	1.993	2.020	0.182	0.268
(29,49,48)	12	964.2	151.91	104	127.82	1.597	0.794	0.169	0.272
(29,49,49)	8	355.1	122.03	17	119.25	3.500	3.407	0.15	0.265
(30,47,47)	4	1767.0	121.92	122	115.22	0.003	0.226	0.163	0.257
(30,47,48)	6	2502.6	131.20	115	107.98	0.540	0.234	0.158	0.267
(30,47,49)	4	-325.7	113.36	53	99.20	2.011	1.540	0.179	0.258
(30,48,47)	6	2410.5	163.22	287	121.89	4.125	5.502	0.158	0.253
(30,48,49)	6	1598.4	177.76	125	111.13	1.758	0.462	0.186	0.262
(30,49,47)	4	1728.8	172.56	89	132.55	2.784	1.451	0.159	0.254
(30,49,48)	8	2950.0	212.52	53	127.49	5.316	2.482	0.156	0.266
(30,49,49)	12	855.8	143.19	147	120.33	0.127	0.889	0.156	0.257
(31,47,47)	8	412.3	106.21	75	114.88	1.040	1.329	0.166	0.26
(31,47,48)	4	617.7	100.04	88	105.69	0.401	0.590	0.157	0.273
(31,47,49)	8	-637.7	95.88	219	95.75	4.102	4.107	0.182	0.265
(31,48,47)	12	687.7	132.57	119	120.42	0.452	0.047	0.15	0.256
(31,48,48)	8	1085.5	144.68	148	116.19	0.111	1.060	0.14	0.268
(31,48,49)	6	588.6	109.28	193	108.35	2.790	2.821	0.161	0.26
(31,49,47)	8	-465.9	127.74	199	128.75	2.375	2.341	0.152	0.266
(31,49,48)	12	979.1	140.86	113	125.71	0.928	0.424	0.153	0.277
(31,49,49)	8	467.6	125.63	27	125.63	3.287	3.286	0.17	0.266
(33,33,55)	10	1364.2	121.28	92	104.25	0.976	0.408	0.202	0.275
(33,34,55)	14	1664.8	158.15	107	104.13	1.704	0.096	0.183	0.268
(33,35,55)	24	2195.5	110.99	65	110.75	1.533	1.524	0.187	0.277
(33,51,17)	10	366.6	88.28	10	94.63	2.608	2.820	0.222	0.267
(33,51,18)	4	107.6	129.84	35	98.35	3.160	2.111	0.225	0.281
(33,51,19)	8	186.0	111.31	72	105.00	1.310	1.100	0.235	0.284
(33,52,17)	4	257.8	126.47	69	94.27	1.915	0.842	0.185	0.265
(33,52,18)	4	629.3	155.78	47	99.36	3.625	1.745	0.189	0.281
(33,52,19)	12	522.2	113.15	87	103.05	0.871	0.535	0.19	0.266
(33,53,17)	10	231.6	119.25	53	98.50	2.207	1.516	0.19	0.267
(33,53,18)	4	108.7	126.30	96	99.30	1.010	0.110	0.173	0.278
(33,53,19)	8	-346.0	102.82	95	103.00	0.261	0.267	0.172	0.266
(33,55,41)	8	922.2	115.83	118	116.25	0.072	0.058	0.209	0.283
(33,55,42)	12	1805.5	187.77	91	136.13	3.224	1.504	0.19	0.282

C-10

File: dat1207; composite directional variograms (50 deg)

Enh-Res Coord.	Neigh Voxels	OK Variance	Kriging Estimate	True Value	Trilinear Estimate	% Projection Er Krige	% Projection Er Trilin	Model Error Mean	Model Error STD
(33,55,43)	8	1039.3	159.33	108	163.13	1.710	1.837	0.196	0.275
(34,33,55)	4	-233.7	115.92	57	93.89	1.963	1.229	0.172	0.261
(34,34,55)	6	-133.9	139.62	2	101.75	4.586	3.324	0.174	0.264
(34,35,55)	4	-248.9	142.14	135	108.69	0.238	0.877	0.16	0.262
(34,51,17)	4	90.6	99.65	164	94.12	2.144	2.328	0.151	0.254
(34,51,18)	14	1274.0	146.15	77	97.79	2.304	0.693	0.181	0.272
(34,51,19)	8	1061.2	112.76	33	100.07	2.658	2.235	0.241	0.274
(34,52,17)	8	499.3	140.91	89	98.90	1.730	0.330	0.157	0.249
(34,52,19)	14	997.0	141.27	83	100.23	1.942	0.574	0.209	0.261
(34,53,17)	4	191.4	133.54	85	98.37	1.617	0.445	0.161	0.262
(34,53,18)	6	772.6	168.52	152	101.41	0.550	1.686	0.156	0.273
(34,53,19)	4	44.9	129.67	47	96.89	2.755	1.662	0.172	0.262
(34,55,41)	12	1084.9	162.38	89	127.67	2.445	1.289	0.188	0.272
(34,55,42)	20	4011.0	293.47	224	144.79	2.315	2.639	0.197	0.277
(34,55,43)	12	1344.7	197.77	107	159.17	3.025	1.738	0.177	0.264
(35,33,55)	8	-187.5	85.61	120	86.63	1.146	1.112	0.228	0.282
(35,34,55)	12	-127.4	105.55	2	95.65	3.450	3.121	0.204	0.265
(35,35,55)	8	-205.5	110.29	46	111.13	2.142	2.170	0.203	0.271
(35,51,17)	10	641.4	158.56	118	94.38	1.351	0.787	0.169	0.265
(35,51,18)	8	475.1	121.35	117	93.01	0.145	0.799	0.184	0.277
(35,51,19)	12	871.8	127.50	41	96.50	2.882	1.849	0.261	0.277
(35,52,17)	4	-305.9	110.62	27	97.83	2.786	2.360	0.174	0.262
(35,52,18)	4	816.5	166.74	37	99.67	4.323	2.088	0.172	0.274
(35,52,19)	8	202.7	101.07	46	95.44	1.835	1.647	0.236	0.269
(35,53,17)	8	-241.8	104.14	95	102.88	0.304	0.262	0.191	0.266
(35,53,18)	4	200.5	113.00	96	97.70	0.567	0.057	0.185	0.277
(35,53,19)	8	-306.1	95.71	50	95.25	1.523	1.508	0.239	0.269
(35,55,41)	8	1528.2	131.16	147	145.50	0.528	0.050	0.216	0.272
(35,55,42)	22	3476.3	236.64	297	150.17	2.011	4.893	0.202	0.277
(35,55,43)	8	1861.0	166.10	132	162.13	1.136	1.004	0.176	0.257
(37, 9,53)	8	-376.3	102.88	19	102.75	2.795	2.791	0.177	0.26
(37, 9,54)	4	630.4	144.60	188	99.38	1.446	2.953	0.197	0.277
(37, 9,55)	8	-379.9	101.55	81	101.25	0.685	0.675	0.201	0.272
(37,10,53)	12	-274.8	105.10	99	105.46	0.203	0.215	0.16	0.252
(37,10,54)	10	1185.6	148.86	47	103.71	3.394	1.890	0.182	0.274
(37,10,55)	4	-7.4	111.37	173	107.03	2.054	2.198	0.186	0.262
(37,11,53)	8	-393.4	109.42	33	109.75	2.547	2.557	0.165	0.258
(37,11,54)	12	972.2	148.79	19	108.53	4.325	2.983	0.181	0.276
(37,11,55)	8	-57.8	110.44	62	113.38	1.614	1.712	0.189	0.266
(37,23,27)	14	1487.5	128.07	50	101.50	2.602	1.716	0.179	0.259
(37,23,28)	4	375.8	120.41	131	91.49	0.353	1.317	0.158	0.276
(37,23,29)	8	182.9	85.28	50	85.00	1.176	1.166	0.18	0.269
(37,24,27)	12	513.8	123.54	67	107.34	1.884	1.344	0.165	0.253
(37,24,28)	8	1316.4	151.46	60	95.99	3.048	1.199	0.147	0.269
(37,24,29)	12	187.2	101.07	119	84.56	0.597	1.148	0.161	0.259
(37,25,27)	8	685.3	104.74	66	117.25	1.291	1.708	0.185	0.253
(37,25,28)	10	1189.4	101.86	77	100.55	0.828	0.785	0.201	0.279
(37,25,29)	8	19.0	88.00	19	86.75	2.299	2.258	0.178	0.261
(37,41,45)	8	296.4	172.46	65	170.13	3.581	3.503	0.189	0.271

File: dat1207; composite directional variograms (50 deg)

Enh-Res Coord.	Neigh Voxels	OK Variance	Kriging Estimate	True Value	Trilinear Estimate	% Projection Er		Model Error	
						Krige	Trilin	Mean	STD
(37,41,46)	4	1275.8	210.19	100	149.29	3.672	1.642	0.189	0.281
(37,41,47)	8	670.3	138.80	106	136.25	1.093	1.008	0.196	0.274
(37,42,45)	8	572.9	185.63	193	153.66	0.246	1.311	0.176	0.265
(37,42,46)	6	1845.4	231.83	80	143.75	5.059	2.124	0.186	0.275
(37,42,47)	4	401.0	157.00	69	138.46	2.932	2.315	0.205	0.268
(37,43,45)	8	225.4	143.85	255	142.63	3.704	3.745	0.173	0.27
(37,43,46)	4	1130.7	190.23	95	139.51	3.173	1.483	0.173	0.279
(37,43,47)	8	187.8	144.00	28	143.13	3.865	3.836	0.194	0.274
(38, 9,53)	4	-186.3	120.52	114	98.64	0.217	0.512	0.154	0.253
(38, 9,54)	4	2070.6	192.39	127	99.12	2.179	0.929	0.172	0.274
(38, 9,55)	4	-196.1	112.34	21	94.97	3.044	2.465	0.172	0.265
(38,10,53)	6	1439.6	149.71	78	103.13	2.389	0.837	0.155	0.246
(38,10,55)	2	1517.0	145.88	48	102.27	3.262	1.808	0.151	0.255
(38,11,53)	8	1477.6	137.71	70	104.70	2.256	1.156	0.161	0.254
(38,11,54)	6	1796.7	192.74	64	107.17	4.290	1.439	0.168	0.277
(38,11,55)	12	333.1	123.20	17	106.43	3.539	2.980	0.169	0.258
(38,23,27)	4	581.7	147.29	83	103.62	2.142	0.687	0.145	0.264
(38,23,28)	8	1747.8	186.60	125	95.07	2.053	0.997	0.154	0.282
(38,23,29)	14	1003.8	115.91	42	84.44	2.463	1.414	0.163	0.272
(38,24,27)	6	835.6	185.86	56	107.32	4.327	1.710	0.154	0.255
(38,24,29)	10	1026.0	141.94	81	87.48	2.031	0.216	0.155	0.257
(38,25,27)	4	-62.0	158.29	120	105.92	1.276	0.469	0.169	0.259
(38,25,28)	8	1358.3	174.58	62	97.67	3.751	1.189	0.175	0.281
(38,25,29)	10	439.6	95.30	134	87.82	1.290	1.539	0.159	0.256
(38,41,45)	12	1199.8	184.16	151	171.34	1.105	0.678	0.185	0.266
(38,41,46)	10	2089.4	213.96	244	145.32	1.001	3.288	0.187	0.279
(38,41,47)	10	1421.0	124.61	159	120.38	1.146	1.287	0.188	0.266
(38,42,45)	10	1364.7	209.34	131	156.42	2.610	0.847	0.163	0.256
(38,42,47)	12	1358.0	155.50	130	121.39	0.850	0.287	0.202	0.267
(38,43,45)	4	601.1	167.71	164	143.12	0.124	0.696	0.157	0.262
(38,43,46)	6	2041.7	202.96	148	131.37	1.831	0.554	0.18	0.283
(38,43,47)	10	1113.2	150.95	172	122.28	0.701	1.657	0.189	0.265
(39, 9,53)	8	-353.5	97.05	119	97.50	0.732	0.716	0.178	0.249
(39, 9,54)	4	473.4	122.01	96	92.22	0.867	0.126	0.177	0.268
(39, 9,55)	8	-358.5	90.40	80	91.00	0.346	0.367	0.186	0.263
(39,10,53)	12	348.2	109.34	75	98.80	1.144	0.793	0.163	0.248
(39,10,54)	6	623.4	139.03	75	96.52	2.134	0.717	0.189	0.274
(39,10,55)	6	301.2	124.42	61	96.58	2.113	1.186	0.182	0.261
(39,11,53)	8	357.7	100.92	67	103.00	1.130	1.200	0.179	0.254
(39,11,54)	4	499.8	130.99	59	101.03	2.399	1.401	0.204	0.277
(39,11,55)	8	105.4	101.05	124	103.25	0.765	0.691	0.205	0.266
(39,23,27)	8	12.4	112.64	92	111.25	0.688	0.641	0.152	0.263
(39,23,28)	12	1521.9	146.90	38	97.85	3.629	1.994	0.173	0.283
(39,23,29)	14	1348.3	129.41	90	88.75	1.313	0.042	0.187	0.28
(39,24,27)	4	-314.5	122.34	43	105.27	2.644	2.075	0.147	0.259
(39,24,28)	12	1742.6	151.39	87	97.87	2.146	0.362	0.165	0.277
(39,24,29)	12	599.4	94.23	61	91.14	1.107	1.004	0.161	0.266
(39,25,27)	8	-314.7	101.57	97	101.63	0.152	0.154	0.177	0.261
(39,25,28)	6	1257.8	155.00	19	96.13	4.532	2.570	0.172	0.279

File: dat1207; composite directional variograms (50 deg)

Enh-Res Coord.	Neigh Voxels	OK Variance	Kriging Estimate	True Value	Trilinear Estimate	% Projection Er Krige	Trilin	Model Error Mean	STD
(39,25,29)	12	1054.5	120.31	85	94.38	1.177	0.312	0.171	0.256
(39,25,35)	8	343.0	109.15	124	108.88	0.495	0.504	0.183	0.265
(39,25,36)	12	914.6	138.09	58	112.58	2.669	1.819	0.178	0.28
(39,25,37)	8	-210.5	121.16	68	120.00	1.771	1.733	0.212	0.27
(39,26,35)	12	-212.0	103.63	31	102.19	2.420	2.372	0.169	0.263
(39,26,36)	10	1047.9	144.92	123	106.67	0.731	0.544	0.172	0.274
(39,26,37)	4	493.8	122.63	94	111.26	0.954	0.575	0.175	0.263
(39,27,35)	8	66.3	91.49	50	98.50	1.383	1.616	0.183	0.273
(39,27,36)	8	975.8	128.60	91	99.94	1.253	0.298	0.189	0.282
(39,27,37)	10	1124.5	169.96	129	104.00	1.365	0.833	0.203	0.271
(39,41,45)	8	471.3	181.60	13	174.25	5.618	5.373	0.19	0.267
(39,41,46)	4	1608.3	176.49	180	137.33	0.117	1.422	0.192	0.288
(39,41,47)	10	857.5	108.40	107	105.63	0.047	0.046	0.188	0.268
(39,42,45)	4	479.2	194.27	44	158.14	5.007	3.804	0.175	0.256
(39,42,46)	6	2050.6	197.74	132	129.49	2.191	0.084	0.173	0.277
(39,42,47)	10	1071.8	109.57	33	103.36	2.552	2.345	0.176	0.259
(39,43,45)	8	190.1	151.70	78	146.88	2.456	2.295	0.187	0.27
(39,43,46)	4	1279.5	158.38	48	123.05	3.678	2.501	0.198	0.293
(39,43,47)	8	-46.2	101.40	164	104.00	2.086	1.999	0.203	0.275
(39,47,35)	8	-428.0	91.26	19	91.88	2.408	2.428	0.198	0.271
(39,47,36)	6	1692.1	121.58	130	106.34	0.281	0.789	0.163	0.273
(39,47,37)	8	-279.2	120.50	169	124.00	1.616	1.500	0.157	0.259
(39,48,35)	12	-100.0	97.60	67	90.05	1.020	0.768	0.191	0.269
(39,48,36)	6	1809.4	160.18	66	103.00	3.138	1.233	0.17	0.277
(39,48,37)	8	435.4	145.64	221	116.97	2.511	3.466	0.151	0.259
(39,49,35)	8	273.9	92.59	24	92.88	2.286	2.295	0.216	0.272
(39,49,36)	4	1472.6	119.35	98	103.27	0.712	0.176	0.196	0.278
(39,49,37)	20	2129.6	142.87	159	115.88	0.537	1.437	0.223	0.267
(39,49,39)	18	2236.3	148.10	161	124.00	0.430	1.233	0.221	0.277
(39,49,40)	16	2932.4	127.44	103	117.58	0.814	0.486	0.189	0.287
(39,49,41)	8	1814.5	114.16	166	113.63	1.727	1.745	0.193	0.278
(39,50,39)	16	2217.6	153.43	146	136.51	0.248	0.316	0.2	0.27
(39,50,40)	12	2712.0	155.45	119	134.88	1.214	0.529	0.204	0.287
(39,50,41)	16	2027.4	117.60	73	130.00	1.486	1.899	0.192	0.277
(39,51,39)	10	2098.7	144.21	50	146.38	3.139	3.211	0.226	0.281
(39,51,40)	14	2450.1	184.84	95	142.19	2.994	1.572	0.216	0.289
(39,51,41)	12	2314.1	174.87	29	142.63	4.861	3.786	0.214	0.283
(40,25,35)	4	8.6	143.68	60	105.37	2.788	1.512	0.167	0.268
(40,25,36)	8	2083.2	207.17	90	114.96	3.904	0.832	0.166	0.276
(40,25,37)	4	-172.4	144.23	92	117.39	1.740	0.846	0.179	0.264
(40,26,35)	6	1573.5	172.91	4	104.31	5.628	3.343	0.147	0.257
(40,26,37)	10	1131.0	172.39	145	116.40	0.913	0.953	0.168	0.263
(40,27,35)	14	1293.5	138.19	207	101.93	2.293	3.501	0.165	0.265
(40,27,36)	6	1286.9	177.34	58	109.47	3.977	1.715	0.166	0.282
(40,27,37)	14	1185.1	134.43	66	111.02	2.280	1.500	0.187	0.263
(40,47,35)	8	449.8	119.07	83	102.52	1.202	0.651	0.169	0.271
(40,47,36)	10	2743.4	197.26	82	115.74	3.841	1.124	0.159	0.276
(40,47,37)	6	641.3	165.74	230	129.41	2.141	3.352	0.148	0.255
(40,48,35)	12	1408.9	137.82	89	98.06	1.627	0.302	0.157	0.26

File: dat1207; composite directional variograms (50 deg)

Enh-Res Coord.	Neigh Voxels	OK Variance	Kriging Estimate	True Value	Trilinear Estimate	% Projection Er		Model Error	
						Krige	Trilin	Mean	STD
(40,48,37)	2	160.8	245.52	84	127.68	5.382	1.456	0.16	0.258
(40,49,35)	14	1470.3	90.50	32	96.54	1.949	2.151	0.161	0.261
(40,49,36)	6	1827.2	141.49	109	109.79	1.083	0.026	0.174	0.28
(40,49,37)	4	281.9	149.70	103	122.69	1.556	0.656	0.173	0.269
(40,49,39)	4	-633.2	149.53	176	131.87	0.882	1.470	0.191	0.278
(40,49,40)	16	3522.3	144.27	218	117.71	2.457	3.342	0.18	0.281
(40,49,41)	12	1684.3	113.36	83	107.51	1.011	0.817	0.171	0.276
(40,50,39)	12	1085.8	166.94	61	135.20	3.530	2.473	0.177	0.267
(40,50,41)	12	1233.8	133.38	137	118.77	0.121	0.607	0.161	0.273
(40,51,39)	10	1072.8	150.77	154	139.66	0.108	0.478	0.2	0.273
(40,51,40)	12	3424.1	210.14	266	132.55	1.861	4.447	0.181	0.283
(40,51,41)	8	644.0	153.84	225	124.68	2.371	3.343	0.178	0.277
(41,19,55)	8	-98.7	121.02	131	120.38	0.333	0.354	0.24	0.269
(41,20,55)	4	338.8	133.09	56	108.47	2.569	1.748	0.186	0.258
(41,21,55)	8	402.4	82.77	115	99.88	1.074	0.504	0.188	0.257
(41,25,35)	8	385.6	106.29	101	107.00	0.176	0.200	0.184	0.273
(41,25,36)	4	567.3	131.04	110	111.36	0.701	0.045	0.185	0.287
(41,25,37)	8	-360.1	118.11	146	118.38	0.929	0.921	0.193	0.269
(41,26,35)	12	-255.4	107.49	54	106.72	1.782	1.757	0.171	0.266
(41,26,36)	10	975.8	148.68	92	110.14	1.889	0.604	0.167	0.278
(41,26,37)	12	707.4	144.13	89	117.56	1.837	0.952	0.167	0.26
(41,27,35)	8	-294.1	110.88	121	110.13	0.337	0.362	0.185	0.279
(41,27,36)	10	1417.8	159.52	150	114.18	0.317	1.194	0.187	0.293
(41,27,37)	10	857.9	79.83	88	121.25	0.272	1.108	0.172	0.268
(41,47,35)	8	-285.2	115.45	88	116.25	0.915	0.941	0.193	0.278
(41,47,36)	4	1408.3	161.84	216	127.52	1.805	2.948	0.168	0.275
(41,47,37)	10	198.9	142.09	75	142.38	2.236	2.245	0.157	0.26
(41,47,49)	8	-119.9	132.64	185	131.50	1.745	1.783	0.199	0.265
(41,47,50)	10	2026.6	155.65	126	116.28	0.988	0.324	0.208	0.282
(41,47,51)	10	773.4	93.96	117	100.63	0.768	0.546	0.213	0.273
(41,48,35)	12	-109.9	115.91	11	105.80	3.496	3.159	0.164	0.268
(41,48,36)	6	1571.8	172.08	215	121.80	1.430	3.106	0.162	0.274
(41,48,37)	6	539.1	138.19	73	135.13	2.172	2.070	0.153	0.257
(41,48,49)	10	1178.7	129.28	154	141.66	0.824	0.411	0.195	0.266
(41,48,50)	6	817.8	136.54	19	123.86	3.917	3.494	0.203	0.283
(41,48,51)	4	240.6	110.14	95	103.23	0.504	0.274	0.197	0.27
(41,49,35)	14	1458.3	108.07	42	101.88	2.201	1.995	0.183	0.264
(41,49,36)	4	321.9	115.15	38	117.27	2.571	2.641	0.184	0.289
(41,49,37)	10	1197.8	120.58	43	133.13	2.585	3.003	0.197	0.283
(41,49,39)	10	1244.2	150.92	115	141.88	1.197	0.896	0.198	0.283
(41,49,40)	8	1845.2	179.65	256	120.83	2.544	4.504	0.188	0.289
(41,49,41)	10	1104.4	98.56	252	102.13	5.113	4.994	0.192	0.284
(41,49,49)	8	-231.9	154.02	41	153.38	3.766	3.745	0.18	0.265
(41,49,50)	8	1399.0	155.07	91	129.54	2.135	1.284	0.176	0.28
(41,49,51)	8	-424.7	107.40	156	106.88	1.620	1.637	0.191	0.27
(41,50,39)	8	1009.9	142.73	128	138.74	0.491	0.358	0.166	0.269
(41,50,40)	6	1546.5	172.39	224	124.36	1.720	3.320	0.171	0.281
(41,50,41)	6	507.0	133.86	148	106.71	0.471	1.376	0.159	0.272
(41,51,39)	8	-518.6	138.67	220	137.88	2.710	2.737	0.212	0.271

C-14

File: dat1207; composite directional variograms (50 deg)

Enh-Res Coord.	Neigh Voxels	OK Variance	Kriging Estimate	True Value	Trilinear Estimate	% Projection Er		Model Error	
						Krige	Trilin	Mean	STD
(41,51,40)	4	1328.1	138.96	165	123.28	0.868	1.390	0.179	0.275
(41,51,41)	8	-49.1	114.41	58	111.00	1.880	1.766	0.169	0.266
(42,19,55)	4	414.4	163.78	72	114.30	3.058	1.409	0.189	0.256
(42,20,55)	10	1640.6	200.63	251	111.10	1.679	4.662	0.173	0.26
(42,21,55)	4	448.7	136.31	117	101.84	0.643	0.505	0.164	0.258
(42,47,49)	4	875.6	176.92	139	129.18	1.264	0.327	0.163	0.259
(42,47,50)	6	994.1	140.51	114	111.63	0.883	0.079	0.16	0.275
(42,47,51)	4	470.8	108.10	100	95.54	0.270	0.149	0.187	0.27
(42,48,49)	10	1291.7	184.09	136	138.58	1.602	0.086	0.169	0.26
(42,48,51)	8	918.8	124.00	124	98.05	0.000	0.865	0.192	0.274
(42,49,49)	6	1583.6	183.09	122	146.44	2.035	0.814	0.174	0.267
(42,49,50)	8	2693.6	185.80	149	124.70	1.226	0.810	0.173	0.282

	Krige	Trilin	Mean	STD
Mean	1.891	1.647	0.186	0.270
Std. Dev.	1.297	1.231	0.035	
Max	6.640	8.435		

Based on 1st 250 Estimates			
Mean	1.951	1.693	0.184	0.268
Std. Dev.	1.343	1.229	0.023	
Max	6.640	5.988		

Appendix D

KRIGING ESTIMATES USING
COMPOSITE DIRECTIONAL VARIOGRAMS,
ANGULAR TOLERANCE $\pm 60^{O}$

File: dat1208; composite directional variograms (60 deg)

Enh-Res Coord.	Neigh Voxels	OK Variance	Kriging Estimate	True Value	Trilinear Estimate	% Projection Er		Model Error	
						Krige	Trilin	Mean	STD
(7,45,45)	8	316.9	138.21	38	137.63	3.339	3.320	0.158	0.277
(7,45,46)	12	1151.7	139.77	83	129.79	1.892	1.559	0.155	0.276
(7,45,47)	8	698.3	122.76	132	123.63	0.308	0.279	0.152	0.276
(7,46,45)	4	410.2	141.09	163	137.84	0.730	0.838	0.159	0.270
(7,46,46)	10	1667.0	149.52	265	126.71	3.848	4.608	0.158	0.276
(7,46,47)	4	418.3	113.09	160	111.62	1.563	1.612	0.137	0.276
(7,47,45)	8	199.0	138.45	197	138.38	1.951	1.954	0.190	0.275
(7,47,46)	12	493.9	125.14	259	118.22	4.460	4.691	0.176	0.277
(7,47,47)	8	205.6	98.34	71	99.88	0.911	0.962	0.157	0.278
(7,53,45)	8	-364.3	143.46	92	141.63	1.715	1.654	0.165	0.269
(7,53,46)	8	863.3	174.16	189	142.60	0.494	1.546	0.165	0.266
(7,53,47)	8	-486.2	148.06	74	148.13	2.468	2.470	0.170	0.264
(7,54,45)	12	-374.7	130.94	159	129.52	0.935	0.982	0.152	0.268
(7,54,46)	6	963.1	171.63	37	133.15	4.486	3.204	0.158	0.265
(7,54,47)	12	-303.6	140.03	100	138.54	1.334	1.284	0.154	0.263
(7,55,45)	8	-532.5	119.23	59	118.25	2.007	1.974	0.161	0.271
(7,55,46)	8	962.9	146.22	150	123.57	0.126	0.881	0.158	0.268
(7,55,47)	8	-522.1	131.93	85	132.13	1.564	1.570	0.166	0.271
(9,33,53)	8	46.6	136.75	225	136.75	2.941	2.941	0.146	0.264
(9,33,54)	4	187.9	128.75	128	126.69	0.025	0.044	0.130	0.267
(9,33,55)	8	-154.9	117.43	37	116.88	2.680	2.662	0.153	0.267
(9,34,53)	12	567.8	162.63	124	140.06	1.287	0.535	0.139	0.263
(9,34,54)	6	881.3	147.77	192	130.03	1.474	2.065	0.128	0.266
(9,34,55)	4	-85.1	144.21	36	119.60	3.606	2.786	0.150	0.270
(9,35,53)	8	214.4	148.70	77	147.88	2.389	2.362	0.140	0.262
(9,35,54)	12	720.3	138.50	105	136.64	1.116	1.054	0.136	0.267
(9,35,55)	8	193.0	125.60	51	125.63	2.486	2.487	0.147	0.272
(10,33,53)	4	1307.0	168.66	92	139.39	2.555	1.579	0.139	0.262
(10,33,54)	8	2430.8	171.45	170	128.60	0.048	1.379	0.120	0.264
(10,33,55)	4	481.0	145.67	26	115.49	3.988	2.982	0.130	0.265
(10,34,53)	6	2017.7	208.58	164	142.49	1.486	0.717	0.124	0.257
(10,34,55)	6	1112.3	165.21	58	121.70	3.572	2.123	0.126	0.262
(10,35,53)	4	1254.5	187.19	104	148.38	2.772	1.479	0.133	0.262
(10,35,54)	8	2868.5	193.18	21	142.92	5.738	4.063	0.131	0.268
(10,35,55)	4	1163.2	133.58	70	127.50	2.119	1.916	0.144	0.270
(11,33,53)	8	445.4	145.53	60	145.25	2.850	2.841	0.143	0.261
(11,33,54)	12	765.0	135.54	154	131.32	0.615	0.756	0.134	0.267
(11,33,55)	8	173.5	117.96	66	118.13	1.731	1.737	0.151	0.262
(11,34,53)	12	568.0	169.94	24	147.25	4.863	4.107	0.131	0.262
(11,34,54)	10	904.5	162.18	64	137.22	3.272	2.440	0.133	0.267
(11,34,55)	12	511.4	139.10	92	122.41	1.569	1.013	0.148	0.267
(11,35,53)	8	379.2	154.28	15	154.00	4.641	4.632	0.137	0.268
(11,35,54)	12	838.6	137.95	123	142.53	0.498	0.651	0.148	0.273
(11,35,55)	8	193.4	129.13	116	130.25	0.437	0.475	0.168	0.271
(11,36,55)	4	497.9	110.74	310	130.32	6.640	5.987	0.156	0.269
(11,37,55)	8	466.2	129.03	121	127.88	0.267	0.229	0.177	0.280
(12,35,55)	4	1177.1	126.29	121	116.39	0.176	0.154	0.149	0.269
(12,36,55)	6	1984.5	133.35	244	121.00	3.687	4.099	0.145	0.264
(12,37,55)	8	1832.0	123.19	75	118.95	1.606	1.464	0.159	0.273

File: dat1208; composite directional variograms (60 deg)

Enh-Res Coord.	Neigh Voxels	OK Variance	Kriging Estimate	True Value	Trilinear Estimate	% Projection Er		Model Error	
						Krige	Trilin	Mean	STD
(13, 9,39)	8	-172.7	95.16	162	95.88	2.227	2.203	0.182	0.276
(13, 9,40)	4	460.5	102.64	61	86.66	1.388	0.855	0.157	0.267
(13, 9,41)	8	-292.6	79.60	58	79.63	0.720	0.721	0.161	0.273
(13,10,39)	12	296.7	97.63	9	102.11	2.953	3.102	0.176	0.269
(13,10,40)	6	937.5	136.92	37	95.18	3.329	1.939	0.157	0.269
(13,10,41)	12	0.2	87.23	73	84.20	0.474	0.373	0.150	0.274
(13,11,39)	8	13.8	106.66	77	107.25	0.988	1.008	0.183	0.265
(13,11,40)	4	825.1	133.95	26	95.95	3.597	2.331	0.175	0.271
(13,11,41)	8	-235.9	90.41	147	89.75	1.886	1.908	0.172	0.269
(13,33,35)	8	-455.4	113.86	94	113.00	0.662	0.633	0.205	0.258
(13,33,36)	4	752.6	145.13	30	114.41	3.837	2.813	0.138	0.262
(13,33,37)	8	-508.6	121.03	97	119.88	0.801	0.762	0.145	0.266
(13,34,35)	4	-657.8	109.18	94	118.11	0.506	0.803	0.195	0.257
(13,34,36)	6	870.8	158.86	164	122.51	0.171	1.383	0.148	0.265
(13,34,37)	4	-805.1	121.50	145	126.19	0.783	0.627	0.151	0.263
(13,35,35)	8	-509.0	123.07	101	122.00	0.735	0.700	0.197	0.266
(13,35,36)	4	438.4	158.56	122	124.74	1.218	0.091	0.165	0.264
(13,35,37)	8	-36.2	132.90	132	131.88	0.030	0.004	0.177	0.266
(13,35,55)	8	355.9	104.29	21	103.88	2.775	2.762	0.166	0.271
(13,36,55)	4	-729.1	108.81	167	106.87	1.939	2.004	0.149	0.262
(13,37,55)	8	-500.3	110.84	104	110.13	0.228	0.204	0.158	0.266
(13,39,41)	8	895.9	129.05	36	129.00	3.101	3.099	0.160	0.269
(13,39,42)	4	552.9	175.05	162	119.77	0.435	1.407	0.160	0.264
(13,39,43)	8	276.0	119.24	59	118.00	2.007	1.966	0.174	0.264
(13,40,41)	12	1562.6	146.74	54	146.62	3.090	3.086	0.161	0.267
(13,40,42)	10	1140.8	189.86	255	142.12	2.171	3.761	0.162	0.264
(13,40,43)	4	643.0	137.26	106	137.38	1.042	1.046	0.175	0.263
(13,41,41)	8	572.8	165.20	25	164.13	4.672	4.636	0.192	0.270
(13,41,42)	12	563.7	188.86	273	157.05	2.804	3.864	0.182	0.264
(13,41,43)	8	237.8	159.32	66	156.50	3.110	3.016	0.186	0.263
(13,41,47)	8	237.3	129.31	140	129.38	0.356	0.354	0.168	0.268
(13,41,48)	12	573.5	125.47	148	125.71	0.751	0.743	0.176	0.266
(13,41,49)	8	212.2	121.15	24	121.88	3.237	3.261	0.157	0.268
(13,42,47)	4	600.5	181.05	199	139.89	0.598	1.970	0.152	0.266
(13,42,48)	10	1077.4	176.16	186	133.75	0.328	1.741	0.150	0.265
(13,42,49)	12	610.1	142.79	103	121.34	1.326	0.611	0.143	0.269
(13,43,47)	8	473.3	156.34	196	155.88	1.321	1.337	0.166	0.277
(13,43,48)	12	569.7	150.61	173	139.50	0.746	1.116	0.164	0.272
(13,43,49)	8	385.4	125.30	46	125.38	2.642	2.645	0.161	0.272
(14, 9,39)	4	-157.1	124.55	109	94.67	0.518	0.477	0.156	0.262
(14, 9,40)	4	1792.9	159.72	122	87.71	1.257	1.143	0.139	0.267
(14, 9,41)	4	-174.3	95.67	83	78.42	0.422	0.153	0.149	0.269
(14,10,39)	6	574.7	142.55	37	100.28	3.517	2.108	0.157	0.256
(14,10,41)	6	325.0	116.60	99	84.94	0.586	0.469	0.146	0.265
(14,11,39)	4	252.0	138.20	151	102.41	0.426	1.619	0.174	0.258
(14,11,40)	8	1847.9	191.49	132	97.03	1.982	1.165	0.155	0.265
(14,11,41)	4	-179.2	115.39	60	89.58	1.846	0.986	0.148	0.263
(14,33,35)	4	-230.3	149.31	57	117.53	3.076	2.017	0.181	0.261
(14,33,36)	4	2904.3	182.26	35	123.97	4.907	2.965	0.150	0.267

File: dat1208; composite directional variograms (60 deg)

Enh-Res Coord.	Neigh Voxels	OK Variance	Kriging Estimate	True Value	Trilinear Estimate	% Projection Er Krige	Trilin	Model Error Mean	STD
(14,33,37)	4	-237.9	135.03	131	130.27	0.134	0.024	0.157	0.269
(14,34,35)	6	-112.3	164.43	100	118.26	2.147	0.608	0.181	0.256
(14,34,37)	6	-154.0	154.53	150	136.80	0.151	0.440	0.142	0.259
(14,35,35)	4	-290.9	177.30	198	121.29	0.690	2.556	0.176	0.266
(14,35,36)	12	2778.1	227.34	125	133.66	3.410	0.289	0.163	0.264
(14,35,37)	6	1814.9	172.75	138	144.64	1.158	0.221	0.173	0.263
(14,39,41)	12	1631.0	164.54	123	122.99	1.384	0.000	0.157	0.265
(14,39,42)	10	2448.6	234.55	309	129.30	2.481	5.988	0.157	0.264
(14,39,43)	4	1656.1	167.67	117	130.26	1.688	0.442	0.165	0.263
(14,40,41)	10	2606.8	174.39	100	135.60	2.479	1.186	0.152	0.259
(14,40,43)	10	2609.9	176.90	213	144.31	1.203	2.289	0.164	0.259
(14,41,41)	12	1446.1	194.21	65	148.05	4.306	2.767	0.169	0.265
(14,41,42)	10	2205.1	247.19	193	154.80	1.806	1.273	0.157	0.263
(14,41,43)	4	1500.0	178.00	237	153.44	1.966	2.784	0.158	0.263
(14,41,47)	4	1495.8	153.32	45	117.73	3.609	2.424	0.175	0.272
(14,41,48)	6	2098.5	155.38	79	120.00	2.545	1.366	0.169	0.271
(14,41,49)	4	1621.6	126.06	109	117.59	0.568	0.286	0.161	0.268
(14,42,47)	6	2329.7	197.67	94	132.96	3.454	1.298	0.156	0.264
(14,42,49)	10	2156.3	182.99	45	123.03	4.598	2.600	0.138	0.265
(14,43,47)	4	1637.7	169.50	178	146.22	0.283	1.059	0.172	0.277
(14,43,48)	6	2056.8	198.73	198	138.84	0.024	1.971	0.168	0.273
(14,43,49)	4	1610.0	156.33	99	127.31	1.910	0.943	0.160	0.270
(15, 9,39)	8	565.8	97.83	95	97.50	0.094	0.083	0.176	0.266
(15, 9,40)	12	542.8	110.55	102	86.38	0.285	0.520	0.177	0.272
(15, 9,41)	8	411.0	79.98	97	79.50	0.567	0.583	0.180	0.279
(15,10,39)	12	465.0	113.89	93	98.57	0.696	0.186	0.165	0.263
(15,10,40)	10	998.2	157.12	40	93.56	3.903	1.785	0.170	0.270
(15,10,41)	12	844.5	108.62	120	84.43	0.379	1.185	0.176	0.278
(15,11,39)	8	-149.5	102.60	133	102.38	1.013	1.020	0.168	0.257
(15,11,40)	4	417.5	129.34	38	95.27	3.043	1.908	0.164	0.266
(15,11,41)	8	-170.4	93.68	45	92.75	1.622	1.591	0.159	0.267
(15,33,35)	8	-457.1	127.22	121	126.25	0.207	0.175	0.191	0.264
(15,33,36)	8	843.4	154.66	118	132.19	1.221	0.473	0.168	0.270
(15,33,37)	8	-502.9	142.31	67	141.13	2.510	2.470	0.180	0.274
(15,33,38)	4	817.7	129.16	115	134.72	0.472	0.657	0.150	0.270
(15,33,39)	8	57.9	130.06	52	127.38	2.601	2.512	0.151	0.282
(15,34,35)	12	-206.1	130.54	149	125.43	0.615	0.785	0.197	0.261
(15,34,36)	6	905.0	191.53	80	136.60	3.716	1.886	0.160	0.264
(15,34,37)	12	-383.7	149.18	119	146.99	1.006	0.933	0.163	0.265
(15,34,38)	10	1039.2	169.02	91	142.93	2.600	1.730	0.136	0.264
(15,34,39)	4	124.6	165.48	81	137.02	2.815	1.867	0.140	0.267
(15,35,35)	8	-351.4	131.96	27	128.00	3.497	3.366	0.195	0.273
(15,35,36)	4	1064.3	175.11	85	141.86	3.003	1.895	0.180	0.268
(15,35,37)	8	-439.5	159.50	78	160.13	2.716	2.737	0.187	0.269
(15,35,38)	12	917.7	148.57	137	155.95	0.386	0.631	0.154	0.265
(15,35,39)	8	570.0	158.72	59	150.38	3.323	3.045	0.154	0.261
(15,39,41)	8	670.7	123.42	54	123.00	2.313	2.299	0.163	0.266
(15,39,42)	12	650.9	157.32	126	132.72	1.044	0.224	0.155	0.262
(15,39,43)	8	266.3	149.13	59	147.50	3.003	2.949	0.168	0.267

File: dat1208; composite directional variograms (60 deg)

Enh-Res Coord.	Neigh Voxels	OK Variance	Kriging Estimate	True Value	Trilinear Estimate	% Projection Er Krige	Trilin	Model Error Mean	STD
(15,39,55)	8	-93.8	123.00	44	122.13	2.633	2.603	0.161	0.259
(15,40,41)	12	1531.6	124.21	153	131.36	0.959	0.721	0.164	0.264
(15,40,42)	10	1399.0	161.56	152	141.08	0.319	0.364	0.157	0.262
(15,40,43)	4	634.2	140.86	54	151.33	2.894	3.243	0.168	0.262
(15,40,55)	4	399.6	154.67	121	123.41	1.122	0.080	0.148	0.263
(15,41,41)	8	483.1	139.78	69	138.50	2.359	2.316	0.175	0.268
(15,41,42)	12	581.8	157.34	141	144.65	0.544	0.122	0.154	0.267
(15,41,43)	8	244.9	154.73	71	153.50	2.790	2.749	0.173	0.267
(15,41,44)	12	560.5	140.30	42	133.88	3.276	3.062	0.168	0.265
(15,41,45)	8	222.9	117.49	74	115.38	1.449	1.379	0.172	0.264
(15,41,47)	8	221.8	110.05	263	108.50	5.097	5.148	0.191	0.272
(15,41,48)	12	553.0	123.37	174	110.28	1.687	2.123	0.168	0.270
(15,41,49)	8	235.7	114.90	102	114.50	0.430	0.417	0.157	0.271
(15,41,55)	8	-173.6	130.42	75	128.75	1.847	1.791	0.159	0.265
(15,42,43)	4	632.2	169.43	103	154.34	2.214	1.711	0.163	0.264
(15,42,44)	10	1071.1	165.95	85	141.69	2.697	1.889	0.165	0.262
(15,42,45)	4	561.4	148.23	134	128.65	0.474	0.178	0.160	0.269
(15,42,47)	4	542.3	145.24	258	122.64	3.757	4.510	0.183	0.269
(15,42,48)	10	1013.7	159.04	123	121.30	1.201	0.057	0.157	0.266
(15,42,49)	12	587.5	143.36	124	121.62	0.645	0.079	0.143	0.272
(15,43,43)	8	246.5	158.45	116	157.00	1.414	1.366	0.168	0.266
(15,43,44)	12	564.5	161.69	128	149.54	1.123	0.718	0.174	0.265
(15,43,45)	8	222.0	146.55	16	144.25	4.350	4.274	0.178	0.273
(15,43,47)	8	215.1	139.38	136	139.75	0.113	0.125	0.215	0.275
(15,43,48)	12	526.6	147.96	190	135.05	1.401	1.831	0.195	0.274
(15,43,49)	8	292.5	132.46	180	133.25	1.584	1.558	0.180	0.277
(16,33,37)	16	994.1	147.09	168	131.95	0.697	1.201	0.172	0.277
(16,33,38)	8	1279.0	155.32	142	130.43	0.444	0.386	0.153	0.271
(16,33,39)	4	877.3	149.02	72	124.31	2.566	1.743	0.162	0.281
(16,34,37)	10	1061.7	183.31	63	135.67	4.009	2.422	0.158	0.264
(16,34,39)	10	1095.5	158.71	77	130.59	2.723	1.786	0.152	0.263
(16,35,37)	12	965.9	152.00	86	144.20	2.199	1.939	0.174	0.267
(16,35,38)	10	2225.6	179.91	101	145.89	2.629	1.496	0.149	0.265
(16,35,39)	12	1148.2	154.84	83	143.37	2.394	2.012	0.154	0.266
(16,39,55)	4	87.8	125.90	119	126.77	0.230	0.259	0.139	0.265
(16,40,55)	6	455.8	160.76	132	131.91	0.958	0.003	0.139	0.262
(16,41,43)	4	1527.4	130.60	124	129.51	0.220	0.184	0.174	0.267
(16,41,44)	6	2133.2	186.00	134	129.54	1.733	0.148	0.166	0.267
(16,41,45)	4	1357.5	136.50	106	121.59	1.016	0.519	0.185	0.267
(16,41,55)	4	623.4	167.12	10	138.43	5.236	4.280	0.152	0.268
(16,42,43)	6	2570.5	160.48	265	131.88	3.483	4.436	0.165	0.265
(16,42,45)	6	2322.6	170.67	68	129.41	3.421	2.046	0.155	0.267
(16,43,43)	4	1543.6	153.45	166	135.33	0.418	1.022	0.156	0.267
(16,43,44)	6	2189.9	196.42	133	138.84	2.113	0.195	0.149	0.267
(16,43,45)	4	1410.5	162.87	121	140.78	1.395	0.659	0.156	0.273
(17,33,37)	16	1351.5	131.02	17	125.00	3.799	3.599	0.186	0.286
(17,33,38)	8	1969.1	140.90	47	123.67	3.129	2.555	0.177	0.283
(17,33,39)	8	427.5	125.21	111	124.13	0.474	0.437	0.192	0.289
(17,34,37)	12	566.8	156.17	51	123.40	3.505	2.412	0.171	0.271

File: dat1208; composite directional variograms (60 deg)

Enh-Res Coord.	Neigh Voxels	OK Variance	Kriging Estimate	True Value	Trilinear Estimate	% Projection Er Krige	Trilin	Model Error Mean	STD
(17,34,38)	6	2133.8	197.06	140	127.97	1.901	0.401	0.158	0.271
(17,34,39)	8	601.0	143.86	90	129.79	1.795	1.326	0.183	0.280
(17,35,37)	8	858.4	129.73	48	129.75	2.723	2.724	0.182	0.272
(17,35,38)	12	1436.5	162.03	186	131.78	0.799	1.807	0.167	0.270
(17,35,39)	8	628.9	138.80	180	138.13	1.373	1.395	0.169	0.274
(17,39,55)	8	305.6	134.23	102	131.25	1.074	0.975	0.276	0.281
(17,40,55)	12	571.3	165.02	30	138.59	4.499	3.618	0.159	0.271
(17,41,43)	8	258.9	105.70	44	105.63	2.056	2.053	0.167	0.270
(17,41,44)	12	586.5	141.36	180	114.71	1.288	2.176	0.167	0.270
(17,41,45)	8	52.7	130.96	5	129.63	4.197	4.153	0.212	0.276
(17,41,55)	8	498.7	148.60	32	151.00	3.885	3.965	0.175	0.274
(17,42,43)	4	657.8	131.39	219	109.36	2.919	3.653	0.146	0.272
(17,42,44)	10	1109.9	175.09	50	119.40	4.168	2.313	0.149	0.269
(17,42,45)	4	593.2	167.25	83	132.62	2.808	1.654	0.161	0.274
(17,43,43)	8	260.9	116.61	54	116.00	2.086	2.066	0.157	0.272
(17,43,44)	12	603.4	151.30	170	125.27	0.623	1.491	0.157	0.269
(17,43,45)	8	239.7	141.16	75	140.13	2.205	2.170	0.177	0.277
(17,45,55)	8	-482.4	96.25	160	96.25	2.124	2.124	0.166	0.269
(17,46,55)	4	-683.1	120.79	46	100.40	2.492	1.813	0.161	0.268
(17,47,55)	8	-426.0	107.48	65	107.25	1.415	1.408	0.184	0.269
(17,53,29)	8	-107.9	133.70	123	128.13	0.357	0.171	0.161	0.263
(17,53,30)	4	701.2	125.11	32	127.67	3.103	3.188	0.164	0.264
(17,53,31)	8	-88.3	123.59	99	126.75	0.819	0.925	0.170	0.262
(17,54,29)	4	-66.3	166.31	155	121.85	0.377	1.105	0.151	0.259
(17,54,30)	6	899.5	154.80	66	122.80	2.959	1.893	0.153	0.261
(17,54,31)	4	-68.0	135.96	139	120.64	0.101	0.612	0.171	0.258
(17,55,29)	8	-236.0	122.03	67	119.88	1.834	1.762	0.155	0.259
(17,55,30)	4	487.3	129.25	69	118.14	2.008	1.637	0.161	0.265
(17,55,31)	8	-244.6	118.28	70	117.75	1.609	1.591	0.176	0.259
(18,45,55)	4	-104.7	112.03	31	85.51	2.700	1.816	0.151	0.266
(18,46,55)	2	-102.3	145.67	40	97.47	3.521	1.915	0.151	0.266
(18,47,55)	4	-263.6	116.21	49	105.62	2.240	1.887	0.171	0.268
(18,53,29)	4	-14.7	134.50	95	123.03	1.316	0.934	0.143	0.262
(18,53,30)	6	1289.3	142.82	124	123.86	0.627	0.005	0.143	0.264
(18,53,31)	4	-67.9	134.09	151	121.81	0.564	0.973	0.145	0.261
(18,54,29)	8	224.3	151.58	123	117.35	0.952	0.188	0.139	0.257
(18,54,31)	8	235.4	150.93	102	116.97	1.630	0.499	0.150	0.253
(18,55,29)	4	-42.5	132.91	64	113.91	2.296	1.663	0.138	0.261
(18,55,30)	6	1125.5	169.42	159	117.10	0.347	1.396	0.144	0.265
(18,55,31)	4	-156.8	144.92	107	115.28	1.263	0.276	0.156	0.260
(19,19,53)	8	294.2	113.08	130	112.25	0.564	0.591	0.192	0.289
(19,19,54)	8	1307.0	150.21	71	116.56	2.640	1.518	0.172	0.274
(19,19,55)	8	313.9	126.18	134	124.75	0.261	0.308	0.194	0.279
(19,20,53)	12	339.6	125.91	103	113.44	0.763	0.348	0.183	0.278
(19,20,54)	12	1944.2	154.96	87	116.73	2.265	0.991	0.169	0.272
(19,20,55)	12	366.3	122.62	148	121.57	0.846	0.881	0.182	0.274
(19,21,53)	8	757.1	122.03	175	117.25	1.765	1.924	0.206	0.291
(19,21,54)	4	841.5	137.57	71	116.63	2.218	1.521	0.185	0.278
(19,21,55)	8	137.4	122.19	31	118.38	3.039	2.912	0.184	0.278

File: dat1208; composite directional variograms (60 deg)

Enh-Res Coord.	Neigh Voxels	OK Variance	Kriging Estimate	True Value	Trilinear Estimate	% Projection Er		Model Error	
						Krige	Trilin	Mean	STD
(19,45,55)	8	171.9	75.64	90	76.75	0.478	0.442	0.159	0.272
(19,46,55)	4	90.1	99.65	228	90.44	4.277	4.584	0.168	0.273
(19,47,55)	8	-378.1	105.92	185	105.38	2.635	2.653	0.193	0.272
(19,53,29)	8	-110.4	120.94	47	119.38	2.464	2.412	0.160	0.268
(19,53,30)	4	539.4	124.88	33	118.57	3.062	2.852	0.164	0.269
(19,53,31)	8	-103.6	120.96	96	118.50	0.832	0.750	0.163	0.272
(19,54,29)	4	-203.9	149.21	141	112.43	0.273	0.952	0.149	0.260
(19,54,30)	6	854.6	163.49	82	114.68	2.716	1.089	0.153	0.263
(19,54,31)	4	-299.2	156.00	42	114.91	3.799	2.429	0.154	0.262
(19,55,29)	8	-268.8	111.87	115	110.38	0.104	0.154	0.145	0.262
(19,55,30)	4	476.9	132.13	39	112.31	3.103	2.443	0.153	0.262
(19,55,31)	8	-331.9	117.76	74	116.75	1.458	1.425	0.161	0.264
(20,19,53)	12	630.4	115.54	102	100.87	0.451	0.038	0.165	0.271
(20,19,54)	8	2283.4	174.74	126	114.52	1.624	0.382	0.159	0.271
(20,19,55)	12	688.3	132.17	118	123.23	0.472	0.174	0.174	0.275
(20,20,53)	10	277.9	132.82	63	108.02	2.326	1.500	0.155	0.263
(20,20,55)	10	733.5	146.46	80	125.74	2.215	1.524	0.159	0.264
(20,21,53)	4	158.1	129.32	37	111.38	3.076	2.479	0.171	0.268
(20,21,54)	6	1449.4	142.33	217	115.56	2.488	3.380	0.158	0.264
(20,21,55)	4	361.1	131.21	80	122.28	1.707	1.409	0.162	0.262
(21,19,53)	8	548.4	109.07	156	92.13	1.564	2.128	0.174	0.271
(21,19,54)	4	1208.9	118.00	121	107.07	0.100	0.464	0.171	0.282
(21,19,55)	8	335.4	125.46	106	123.25	0.648	0.575	0.186	0.290
(21,20,53)	12	405.8	114.35	47	98.35	2.244	1.711	0.158	0.266
(21,20,54)	6	1406.2	156.68	155	113.38	0.056	1.387	0.154	0.269
(21,20,55)	12	379.2	136.29	100	123.98	1.209	0.799	0.166	0.271
(21,21,53)	8	-105.5	110.39	37	107.88	2.446	2.362	0.162	0.267
(21,21,54)	4	687.3	131.13	69	116.63	2.070	1.587	0.149	0.265
(21,21,55)	8	3.6	129.64	56	127.25	2.454	2.374	0.156	0.266
(21,39,41)	8	1420.0	107.25	77	109.13	1.008	1.070	0.187	0.271
(21,39,42)	16	2414.0	150.68	122	109.57	0.956	0.414	0.186	0.279
(21,39,43)	8	1244.6	116.42	104	115.88	0.414	0.396	0.203	0.279
(21,40,41)	12	1573.2	148.72	21	115.81	4.256	3.159	0.190	0.275
(21,40,42)	14	3118.1	178.25	131	119.02	1.574	0.399	0.197	0.286
(21,40,43)	16	2510.9	140.59	85	122.75	1.852	1.258	0.204	0.277
(21,41,41)	8	1238.5	125.20	69	125.88	1.873	1.895	0.213	0.276
(21,41,42)	16	1905.4	171.55	234	125.71	2.081	3.609	0.208	0.284
(21,41,43)	8	1421.3	131.27	103	131.88	0.942	0.962	0.221	0.278
(21,49,41)	8	330.8	108.22	141	107.88	1.092	1.104	0.177	0.272
(21,49,42)	12	626.2	147.68	145	121.71	0.089	0.776	0.184	0.275
(21,49,43)	8	220.7	140.91	89	140.88	1.730	1.729	0.185	0.273
(21,50,41)	12	1092.3	129.70	104	116.65	0.856	0.421	0.176	0.283
(21,50,42)	6	1433.3	178.42	167	125.92	0.380	1.369	0.167	0.274
(21,50,43)	4	-820.4	144.23	97	133.59	1.574	1.219	0.173	0.281
(21,51,41)	8	1000.1	127.81	174	127.38	1.539	1.554	0.187	0.290
(21,51,42)	4	1299.9	152.98	98	125.69	1.832	0.923	0.174	0.280
(21,51,43)	8	554.6	130.06	57	127.63	2.434	2.353	0.171	0.281
(22,39,41)	12	1598.1	124.28	41	127.50	2.775	2.882	0.174	0.266
(22,39,42)	20	3213.2	177.18	317	133.56	4.659	6.113	0.180	0.276

File: dat1208; composite directional variograms (60 deg)

Enh-Res Coord.	Neigh Voxels	OK Variance	Kriging Estimate	True Value	Trilinear Estimate	% Projection Er		Model Error	
						Krige	Trilin	Mean	STD
(22,39,43)	12	2194.9	157.43	150	150.79	0.247	0.026	0.187	0.273
(22,40,41)	10	2373.1	165.16	81	127.67	2.804	1.555	0.183	0.269
(22,40,43)	10	2818.4	184.32	121	145.93	2.110	0.831	0.192	0.268
(22,41,41)	12	1438.1	159.31	149	129.79	0.343	0.640	0.197	0.272
(22,41,42)	18	2358.5	240.85	255	134.91	0.472	4.002	0.194	0.283
(22,41,43)	12	1858.8	165.86	78	142.48	2.928	2.149	0.208	0.275
(22,49,41)	12	1434.2	115.07	50	121.05	2.168	2.368	0.174	0.269
(22,49,42)	10	2110.6	190.25	32	128.88	5.273	3.228	0.180	0.273
(22,49,43)	4	1494.9	178.61	181	140.54	0.080	1.348	0.167	0.270
(22,50,41)	10	2401.8	128.94	242	123.01	3.768	3.965	0.197	0.285
(22,50,43)	10	2468.4	191.72	117	137.24	2.490	0.674	0.164	0.274
(22,51,41)	12	1488.8	115.60	98	129.66	0.587	1.055	0.208	0.295
(22,51,42)	10	2971.4	201.57	183	131.60	0.619	1.713	0.197	0.280
(22,51,43)	4	1795.7	164.81	184	133.37	0.639	1.687	0.174	0.278
(23,37,41)	8	515.8	116.05	121	116.13	0.165	0.162	0.204	0.279
(23,37,42)	12	888.5	152.39	287	139.29	4.486	4.922	0.191	0.279
(23,37,43)	8	526.3	164.87	165	165.13	0.004	0.004	0.189	0.282
(23,38,41)	12	1389.9	134.74	63	130.96	2.391	2.265	0.204	0.272
(23,38,42)	18	2076.5	183.72	175	147.95	0.291	0.901	0.203	0.278
(23,38,43)	12	1400.1	178.04	154	175.69	0.801	0.723	0.188	0.275
(23,39,41)	8	948.2	146.49	97	146.38	1.649	1.645	0.203	0.274
(23,39,42)	16	2011.6	226.53	251	162.11	0.815	2.962	0.206	0.284
(23,39,43)	8	1621.7	187.50	254	186.50	2.216	2.249	0.213	0.277
(23,40,41)	16	2119.5	164.82	41	141.16	4.126	3.337	0.204	0.276
(23,40,42)	20	3109.7	269.38	302	152.39	1.087	4.985	0.212	0.291
(23,40,43)	16	2443.8	211.19	129	169.71	2.739	1.357	0.215	0.278
(23,41,41)	8	741.6	138.47	186	138.13	1.584	1.595	0.199	0.275
(23,41,42)	12	1603.3	232.66	194	140.97	1.288	1.767	0.201	0.288
(23,41,43)	8	1475.0	156.61	122	156.38	1.153	1.145	0.212	0.280
(23,49,41)	8	757.6	135.03	231	133.25	3.198	3.257	0.185	0.274
(23,49,42)	12	1350.1	185.90	205	135.68	0.636	2.310	0.203	0.274
(23,49,43)	8	781.4	145.93	147	145.25	0.036	0.058	0.186	0.271
(23,50,41)	16	2266.2	161.14	141	129.58	0.671	0.381	0.210	0.295
(23,50,42)	12	3231.8	232.56	209	134.30	0.785	2.489	0.212	0.282
(23,50,43)	12	1577.1	165.26	204	142.68	1.291	2.043	0.182	0.276
(23,51,41)	8	734.4	134.81	183	129.75	1.606	1.774	0.239	0.313
(23,51,42)	16	2262.3	206.23	88	131.91	3.940	1.463	0.223	0.288
(23,51,43)	8	911.9	145.11	205	143.13	1.996	2.062	0.195	0.283
(24,37,41)	12	1373.9	132.73	57	109.05	2.524	1.734	0.174	0.272
(24,37,42)	12	3151.4	187.21	249	129.67	2.059	3.976	0.171	0.274
(24,37,43)	8	2180.9	191.22	280	150.14	2.958	4.327	0.160	0.270
(24,38,41)	10	2126.9	170.04	66	123.56	3.467	1.918	0.179	0.268
(24,38,43)	10	2480.6	221.79	181	160.50	1.359	0.683	0.166	0.263
(24,39,41)	12	1737.8	163.37	84	133.57	2.645	1.652	0.164	0.267
(24,39,42)	12	3162.7	263.44	193	148.67	2.347	1.477	0.176	0.276
(24,39,43)	16	2432.5	231.34	185	165.21	1.544	0.660	0.184	0.268
(25,37,41)	8	707.9	105.24	168	105.25	2.091	2.091	0.197	0.282
(25,37,42)	12	870.2	140.35	80	121.03	2.011	1.367	0.185	0.291
(25,37,43)	8	529.4	142.20	257	140.13	3.825	3.895	0.167	0.269

File: dat1208; composite directional variograms (60 deg)

Enh-Res Coord.	Neigh Voxels	OK Variance	Kriging Estimate	True Value	Trilinear Estimate	% Projection Er		Model Error	
						Krige	Trilin	Mean	STD
(25,38,41)	12	1257.6	127.28	55	113.93	2.409	1.964	0.179	0.272
(25,38,42)	10	1654.5	166.60	112	127.40	1.819	0.513	0.177	0.283
(25,38,43)	12	817.1	148.97	109	145.11	1.332	1.203	0.160	0.266
(25,39,41)	8	203.6	124.68	64	124.50	2.022	2.016	0.173	0.273
(25,39,42)	12	867.4	169.25	109	134.48	2.008	0.849	0.173	0.280
(25,39,43)	8	517.7	151.28	87	150.75	2.142	2.124	0.173	0.268
(25,41,51)	8	-50.6	137.76	131	136.75	0.225	0.192	0.180	0.261
(25,41,52)	4	594.7	162.47	90	126.94	2.415	1.231	0.178	0.261
(25,41,53)	8	-470.7	122.81	112	121.75	0.360	0.325	0.194	0.262
(25,42,51)	4	-759.4	152.43	109	126.11	1.447	0.570	0.148	0.260
(25,42,52)	6	900.1	171.31	142	123.83	0.977	0.606	0.147	0.264
(25,42,53)	4	-769.9	125.34	102	121.40	0.778	0.646	0.155	0.263
(25,43,51)	8	-194.2	119.80	126	118.88	0.207	0.237	0.151	0.261
(25,43,52)	4	745.3	149.50	217	118.10	2.249	3.296	0.145	0.268
(25,43,53)	8	-548.3	121.67	44	121.50	2.588	2.582	0.162	0.263
(25,53,41)	8	799.4	134.42	24	133.38	3.679	3.645	0.206	0.281
(25,53,42)	12	1718.2	151.25	93	141.22	1.941	1.607	0.179	0.278
(25,53,43)	8	629.5	151.52	64	150.38	2.916	2.878	0.178	0.282
(25,54,41)	4	691.2	154.86	192	140.44	1.238	1.718	0.162	0.267
(25,54,42)	10	1615.8	163.24	175	140.44	0.392	1.152	0.150	0.273
(25,54,43)	4	624.8	156.12	102	148.03	1.803	1.534	0.161	0.277
(25,55,41)	8	259.8	151.27	177	149.25	0.857	0.925	0.165	0.269
(25,55,42)	12	621.1	171.51	328	145.22	5.214	6.091	0.153	0.273
(25,55,43)	8	260.0	148.44	176	146.63	0.918	0.979	0.167	0.274
(26,41,51)	4	1108.6	186.53	53	142.07	4.449	2.968	0.169	0.266
(26,41,52)	4	2575.8	234.25	210	134.61	0.808	2.512	0.188	0.265
(26,41,53)	4	-245.2	144.21	135	120.01	0.307	0.500	0.204	0.273
(26,42,51)	6	-134.3	178.35	122	131.21	1.878	0.307	0.152	0.256
(26,42,53)	6	-146.9	159.07	45	118.96	3.801	2.465	0.172	0.267
(26,43,51)	4	1384.4	146.56	146	115.29	0.019	1.023	0.145	0.260
(26,43,52)	2	2483.1	202.09	119	117.93	2.769	0.036	0.143	0.266
(26,43,53)	4	-284.7	170.53	97	117.53	2.450	0.684	0.161	0.265
(26,53,41)	4	775.4	175.72	148	138.19	0.924	0.327	0.168	0.271
(26,53,42)	6	2398.8	193.29	240	147.29	1.557	3.089	0.161	0.272
(26,53,43)	12	1477.8	196.88	125	163.17	2.395	1.272	0.163	0.276
(26,54,41)	10	1502.0	201.93	276	140.74	2.468	4.507	0.146	0.264
(26,54,43)	10	2456.4	211.93	200	155.64	0.398	1.478	0.146	0.269
(26,55,41)	12	1573.2	185.00	227	139.76	1.399	2.907	0.152	0.268
(26,55,42)	10	2291.5	224.33	395	141.88	5.687	8.435	0.156	0.270
(26,55,43)	4	1520.5	182.84	186	147.67	0.105	1.277	0.158	0.269
(27,41,51)	8	194.4	154.49	100	153.25	1.816	1.774	0.181	0.270
(27,41,52)	12	1124.3	149.73	154	136.44	0.142	0.585	0.201	0.269
(27,41,53)	8	166.3	123.36	101	121.38	0.745	0.679	0.231	0.283
(27,42,51)	12	487.7	144.88	155	133.66	0.337	0.711	0.158	0.263
(27,42,52)	6	1378.5	146.43	57	127.03	2.980	2.333	0.170	0.269
(27,42,53)	12	-26.4	124.75	41	120.48	2.791	2.648	0.194	0.280
(27,43,51)	8	223.9	116.03	23	116.63	3.100	3.120	0.152	0.266
(27,43,52)	4	593.7	121.49	149	118.35	0.917	1.021	0.155	0.269
(27,43,53)	8	-542.8	121.47	27	120.63	3.148	3.120	0.187	0.279

File: dat1208; composite directional variograms (60 deg)

Enh-Res Coord.	Neigh Voxels	OK Variance	Kriging Estimate	True Value	Trilinear Estimate	% Projection Er		Model Error	
						Krige	Trilin	Mean	STD
(27,53,41)	8	897.9	148.56	195	147.88	1.547	1.570	0.197	0.277
(27,53,42)	8	2252.2	218.08	310	161.77	3.063	4.939	0.186	0.284
(27,53,43)	8	922.8	181.67	132	180.63	1.655	1.620	0.191	0.282
(27,54,41)	12	807.4	160.11	101	140.42	1.970	1.314	0.180	0.270
(27,54,42)	10	2385.1	209.17	195	148.85	0.472	1.538	0.180	0.274
(27,54,43)	12	1507.5	192.01	66	165.10	4.199	3.302	0.186	0.273
(27,55,41)	8	1232.6	138.50	166	136.50	0.916	0.983	0.186	0.273
(27,55,42)	16	1909.5	182.99	210	141.67	0.900	2.277	0.190	0.280
(27,55,43)	8	775.2	154.37	89	153.25	2.178	2.141	0.186	0.275
(29,47,47)	8	-570.4	118.24	124	118.63	0.192	0.179	0.155	0.270
(29,47,48)	4	908.4	116.69	124	111.23	0.244	0.426	0.147	0.265
(29,47,49)	8	-509.5	105.07	108	104.50	0.098	0.117	0.157	0.266
(29,48,47)	12	-452.0	127.74	164	128.25	1.208	1.191	0.156	0.268
(29,48,48)	10	1105.0	152.35	53	118.39	3.311	2.179	0.136	0.263
(29,48,49)	4	-775.3	145.79	141	109.46	0.159	1.051	0.138	0.263
(29,49,47)	8	-567.3	140.47	80	140.63	2.015	2.020	0.168	0.272
(29,49,48)	8	973.1	157.44	104	127.82	1.781	0.794	0.153	0.267
(29,49,49)	8	-501.0	119.73	17	119.25	3.423	3.407	0.140	0.267
(30,47,47)	4	-275.1	137.58	122	115.22	0.519	0.226	0.154	0.271
(30,47,48)	4	3188.4	132.81	115	107.98	0.593	0.234	0.140	0.266
(30,47,49)	4	-336.5	113.36	53	99.20	2.011	1.540	0.147	0.266
(30,48,47)	6	-169.0	152.00	287	121.89	4.499	5.502	0.144	0.261
(30,48,49)	6	-140.5	142.97	125	111.13	0.599	0.462	0.138	0.262
(30,49,47)	8	572.8	157.26	89	132.55	2.274	1.451	0.156	0.268
(30,49,48)	4	3422.9	218.06	53	127.49	5.500	2.482	0.147	0.265
(30,49,49)	12	863.4	143.19	147	120.33	0.127	0.889	0.144	0.263
(31,47,47)	8	-584.8	113.80	75	114.88	1.293	1.329	0.153	0.272
(31,47,48)	4	803.0	99.26	88	105.69	0.375	0.590	0.136	0.266
(31,47,49)	8	-563.0	95.88	219	95.75	4.102	4.107	0.142	0.270
(31,48,47)	12	-427.7	119.61	119	120.42	0.020	0.047	0.141	0.267
(31,48,48)	6	1044.2	145.84	148	116.19	0.072	1.060	0.126	0.263
(31,48,49)	4	-789.6	143.30	193	108.35	1.656	2.821	0.134	0.266
(31,49,47)	8	-458.4	127.74	199	128.75	2.375	2.341	0.143	0.270
(31,49,48)	4	930.2	147.54	113	125.71	1.151	0.424	0.134	0.266
(31,49,49)	8	473.7	125.63	27	125.63	3.287	3.286	0.151	0.269
(33,33,55)	8	-220.6	103.33	92	104.25	0.377	0.408	0.183	0.279
(33,34,55)	12	-146.8	113.34	107	104.13	0.211	0.096	0.172	0.266
(33,35,55)	8	-245.1	110.24	65	110.75	1.508	1.524	0.166	0.272
(33,51,17)	8	-306.0	95.11	10	94.63	2.836	2.820	0.187	0.273
(33,51,18)	4	314.8	120.76	35	98.35	2.858	2.111	0.185	0.278
(33,51,19)	8	-86.6	97.28	72	105.00	0.843	1.100	0.196	0.288
(33,52,17)	8	418.2	145.95	69	94.27	2.564	0.842	0.172	0.278
(33,52,18)	6	1051.9	148.82	47	99.36	3.393	1.745	0.164	0.277
(33,52,19)	4	148.2	116.34	87	103.05	0.978	0.535	0.166	0.276
(33,53,17)	8	-114.6	99.98	53	98.50	1.566	1.516	0.176	0.275
(33,53,18)	4	110.4	126.29	96	99.30	1.009	0.110	0.159	0.277
(33,53,19)	8	-159.9	103.60	95	103.00	0.287	0.267	0.164	0.274
(33,55,41)	8	934.9	115.83	118	116.25	0.072	0.058	0.191	0.274
(33,55,42)	12	2090.4	194.61	91	136.13	3.452	1.504	0.186	0.276

File: dat1208; composite directional variograms (60 deg)

Enh-Res Coord.	Neigh Voxels	OK Variance	Kriging Estimate	True Value	Trilinear Estimate	% Projection Er		Model Error	
						Krige	Trilin	Mean	STD
(33,55,43)	8	974.0	163.01	108	163.13	1.833	1.837	0.183	0.271
(34,33,55)	4	-235.1	115.92	57	93.89	1.963	1.229	0.165	0.268
(34,34,55)	6	-136.6	139.62	2	101.75	4.586	3.324	0.162	0.261
(34,35,55)	4	-251.9	142.14	135	108.69	0.238	0.877	0.147	0.263
(34,51,17)	4	248.0	99.63	164	94.12	2.145	2.328	0.147	0.268
(34,51,18)	6	1212.6	147.26	77	97.79	2.341	0.693	0.160	0.274
(34,51,19)	4	790.0	140.89	33	100.07	3.595	2.235	0.197	0.286
(34,52,17)	10	519.6	139.80	89	98.90	1.693	0.330	0.157	0.264
(34,52,19)	10	525.5	129.22	83	100.23	1.540	0.574	0.174	0.272
(34,53,17)	4	-249.1	133.54	85	98.37	1.617	0.445	0.156	0.271
(34,53,18)	6	1154.2	178.77	152	101.41	0.892	1.686	0.145	0.269
(34,53,19)	4	-254.8	130.03	47	96.89	2.767	1.662	0.161	0.268
(34,55,41)	12	1299.1	165.72	89	127.67	2.556	1.289	0.175	0.265
(34,55,42)	12	3666.0	278.14	224	144.79	1.804	2.639	0.176	0.270
(34,55,43)	12	1913.3	201.58	107	159.17	3.152	1.738	0.166	0.265
(35,33,55)	8	-109.7	85.23	120	86.63	1.159	1.112	0.207	0.292
(35,34,55)	12	-128.5	105.55	2	95.65	3.450	3.121	0.187	0.275
(35,35,55)	8	-208.6	110.29	46	111.13	2.142	2.170	0.181	0.276
(35,51,17)	8	163.7	94.78	118	94.38	0.774	0.787	0.156	0.275
(35,51,18)	4	907.7	129.44	117	93.01	0.414	0.799	0.160	0.276
(35,51,19)	8	365.1	96.21	41	96.50	1.840	1.849	0.206	0.286
(35,52,17)	8	655.6	108.86	27	97.83	2.728	2.360	0.166	0.272
(35,52,18)	6	1104.7	158.86	37	99.67	4.061	2.088	0.154	0.270
(35,52,19)	4	148.0	102.82	46	95.44	1.893	1.647	0.186	0.279
(35,53,17)	8	-312.2	103.64	95	102.88	0.288	0.262	0.182	0.270
(35,53,18)	4	657.4	118.50	96	97.70	0.750	0.057	0.167	0.268
(35,53,19)	8	-319.4	95.71	50	95.25	1.523	1.508	0.202	0.273
(35,55,41)	8	211.0	147.48	147	145.50	0.016	0.050	0.193	0.268
(35,55,42)	12	3041.1	225.86	297	150.17	2.371	4.893	0.175	0.271
(35,55,43)	8	1109.1	163.82	132	162.13	1.060	1.004	0.177	0.267
(37, 9,53)	8	-380.4	102.88	19	102.75	2.795	2.791	0.168	0.264
(37, 9,54)	4	614.9	138.83	188	99.38	1.639	2.953	0.173	0.263
(37, 9,55)	8	-419.4	103.20	81	101.25	0.740	0.675	0.185	0.274
(37,10,53)	12	-286.0	105.05	99	105.46	0.202	0.215	0.153	0.261
(37,10,54)	6	1219.2	154.13	47	103.71	3.570	1.890	0.153	0.259
(37,10,55)	12	-234.5	107.49	173	107.03	2.183	2.198	0.169	0.266
(37,11,53)	8	-396.1	109.42	33	109.75	2.547	2.557	0.157	0.267
(37,11,54)	12	978.8	149.36	19	108.53	4.344	2.983	0.161	0.263
(37,11,55)	8	-405.3	113.35	62	113.38	1.711	1.712	0.175	0.269
(37,23,27)	8	-18.9	101.66	50	101.50	1.721	1.716	0.158	0.274
(37,23,28)	4	695.5	117.74	131	91.49	0.442	1.317	0.143	0.272
(37,23,29)	8	216.9	85.44	50	85.00	1.181	1.166	0.170	0.285
(37,24,27)	4	338.0	156.99	67	107.34	2.999	1.344	0.153	0.276
(37,24,28)	8	900.9	144.72	60	95.99	2.823	1.199	0.137	0.273
(37,24,29)	12	398.7	98.90	119	84.56	0.670	1.148	0.155	0.280
(37,25,27)	8	-173.7	120.95	66	117.25	1.831	1.708	0.170	0.281
(37,25,28)	8	1027.8	125.24	77	100.55	1.608	0.785	0.167	0.280
(37,25,29)	8	192.4	87.19	19	86.75	2.272	2.258	0.163	0.276
(37,41,45)	8	378.0	171.38	65	170.13	3.545	3.503	0.183	0.269

File: dat1208; composite directional variograms (60 deg)

Enh-Res Coord.	Neigh Voxels	OK Variance	Kriging Estimate	True Value	Trilinear Estimate	% Projection Er		Model Error	
						Krige	Trilin	Mean	STD
(37,41,46)	4	1280.3	208.23	100	149.29	3.606	1.642	0.173	0.274
(37,41,47)	8	138.2	136.99	106	136.25	1.033	1.008	0.176	0.280
(37,42,45)	6	526.1	189.21	193	153.66	0.126	1.311	0.167	0.266
(37,42,46)	6	1888.7	231.67	80	143.75	5.054	2.124	0.165	0.269
(37,42,47)	4	416.1	157.00	69	138.46	2.932	2.315	0.173	0.271
(37,43,45)	8	153.6	143.86	255	142.63	3.704	3.745	0.155	0.270
(37,43,46)	4	1138.3	190.23	95	139.51	3.173	1.483	0.156	0.274
(37,43,47)	8	147.0	144.00	28	143.13	3.865	3.836	0.165	0.276
(38, 9,53)	4	-180.3	120.52	114	98.64	0.217	0.512	0.148	0.264
(38, 9,54)	8	2133.3	185.74	127	99.12	1.957	0.929	0.149	0.264
(38, 9,55)	4	-25.8	112.34	21	94.97	3.044	2.465	0.169	0.273
(38,10,53)	6	58.6	129.63	78	103.13	1.720	0.837	0.152	0.259
(38,10,55)	6	210.7	129.00	48	102.27	2.699	1.808	0.149	0.262
(38,11,53)	4	-187.0	128.85	70	104.70	1.961	1.156	0.153	0.265
(38,11,54)	8	2203.9	203.23	64	107.17	4.639	1.439	0.147	0.264
(38,11,55)	4	-208.5	134.27	17	106.43	3.908	2.980	0.158	0.266
(38,23,27)	4	390.1	144.83	83	103.62	2.060	0.687	0.137	0.275
(38,23,28)	2	1354.1	187.01	125	95.07	2.066	0.997	0.133	0.278
(38,23,29)	12	1059.3	122.22	42	84.44	2.673	1.414	0.148	0.291
(38,24,27)	6	572.3	182.47	56	107.32	4.214	1.710	0.149	0.272
(38,24,29)	10	580.9	130.74	81	87.48	1.657	0.216	0.150	0.280
(38,25,27)	4	-262.3	158.84	120	105.92	1.294	0.469	0.162	0.277
(38,25,28)	6	1384.8	178.57	62	97.67	3.884	1.189	0.146	0.273
(38,25,29)	4	266.6	129.37	134	87.82	0.154	1.539	0.145	0.268
(38,41,45)	4	469.6	184.93	151	171.34	1.131	0.678	0.162	0.269
(38,41,46)	6	2158.5	219.88	244	145.32	0.804	3.288	0.153	0.269
(38,41,47)	4	-259.7	129.32	159	120.38	0.989	1.287	0.153	0.275
(38,42,45)	10	642.5	197.14	131	156.42	2.204	0.847	0.152	0.261
(38,42,47)	10	419.2	143.17	130	121.39	0.439	0.287	0.154	0.271
(38,43,45)	4	475.9	168.06	164	143.12	0.135	0.696	0.151	0.267
(38,43,46)	6	2021.7	202.32	148	131.37	1.810	0.554	0.146	0.271
(38,43,47)	4	450.8	141.31	172	122.28	1.023	1.657	0.160	0.273
(39, 9,53)	8	-359.1	97.05	119	97.50	0.732	0.716	0.169	0.262
(39, 9,54)	4	507.6	122.01	96	92.22	0.867	0.126	0.159	0.262
(39, 9,55)	8	-359.1	90.40	80	91.00	0.346	0.367	0.177	0.272
(39,10,53)	12	-260.0	97.70	75	98.80	0.756	0.793	0.158	0.263
(39,10,54)	6	653.2	137.21	75	96.52	2.073	0.717	0.157	0.264
(39,10,55)	12	-135.2	97.21	61	96.58	1.207	1.186	0.171	0.272
(39,11,53)	8	-371.0	101.61	67	103.00	1.153	1.200	0.170	0.267
(39,11,54)	4	511.0	130.83	59	101.03	2.393	1.401	0.172	0.268
(39,11,55)	8	-363.6	102.70	124	103.25	0.710	0.691	0.183	0.276
(39,23,27)	8	-20.4	109.92	92	111.25	0.597	0.641	0.141	0.279
(39,23,28)	4	942.2	129.23	38	97.85	3.040	1.994	0.148	0.283
(39,23,29)	8	726.9	88.27	90	88.75	0.058	0.042	0.166	0.302
(39,24,27)	4	-505.0	122.20	43	105.27	2.639	2.075	0.144	0.273
(39,24,28)	6	1447.5	148.34	87	97.87	2.044	0.362	0.141	0.276
(39,24,29)	6	148.4	102.83	61	91.14	1.394	1.004	0.151	0.289
(39,25,27)	8	-369.7	101.59	97	101.63	0.153	0.154	0.165	0.271
(39,25,28)	4	447.2	124.08	19	96.13	3.501	2.570	0.145	0.271

File: dat1208; composite directional variograms (60 deg)

Enh-Res Coord.	Neigh Voxels	OK Variance	Kriging Estimate	True Value	Trilinear Estimate	% Projection Er		Model Error	
						Krige	Trilin	Mean	STD
(39,25,29)	8	-65.8	95.00	85	94.38	0.333	0.312	0.149	0.269
(39,25,35)	8	-337.9	109.07	124	108.88	0.498	0.504	0.163	0.262
(39,25,36)	4	811.3	140.40	58	112.58	2.746	1.819	0.155	0.265
(39,25,37)	8	-258.8	121.03	68	120.00	1.767	1.733	0.178	0.270
(39,26,35)	12	-243.7	102.66	31	102.19	2.388	2.372	0.148	0.262
(39,26,36)	6	924.4	146.01	123	106.67	0.767	0.544	0.145	0.264
(39,26,37)	12	-203.1	112.17	94	111.26	0.605	0.575	0.157	0.267
(39,27,35)	8	324.9	99.18	50	98.50	1.639	1.616	0.161	0.271
(39,27,36)	16	1143.5	116.86	91	99.94	0.862	0.298	0.161	0.273
(39,27,37)	8	-163.6	103.76	129	104.00	0.841	0.833	0.178	0.278
(39,41,45)	8	265.5	175.00	13	174.25	5.398	5.373	0.161	0.270
(39,41,46)	4	1429.8	176.49	180	137.33	0.117	1.422	0.160	0.275
(39,41,47)	8	-55.3	105.97	107	105.63	0.034	0.046	0.157	0.280
(39,42,45)	4	245.3	197.70	44	158.14	5.122	3.804	0.160	0.268
(39,42,46)	6	2163.6	198.81	132	129.49	2.226	0.084	0.150	0.270
(39,42,47)	4	-473.0	125.24	33	103.36	3.074	2.345	0.155	0.276
(39,43,45)	8	-55.1	152.07	78	146.88	2.468	2.295	0.173	0.272
(39,43,46)	4	810.5	158.38	48	123.05	3.678	2.501	0.168	0.276
(39,43,47)	8	-406.6	104.02	164	104.00	1.999	1.999	0.173	0.281
(39,47,35)	8	-449.4	91.26	19	91.88	2.408	2.428	0.163	0.261
(39,47,36)	4	1081.4	129.24	130	106.34	0.025	0.789	0.137	0.268
(39,47,37)	8	-186.1	122.22	169	124.00	1.559	1.500	0.138	0.267
(39,48,35)	12	-330.2	89.84	67	90.05	0.761	0.768	0.151	0.262
(39,48,36)	6	1869.1	159.06	66	103.00	3.101	1.233	0.145	0.265
(39,48,37)	8	560.3	149.09	221	116.97	2.396	3.466	0.138	0.266
(39,49,35)	8	-146.6	92.37	24	92.88	2.278	2.295	0.174	0.272
(39,49,36)	4	1471.9	119.35	98	103.27	0.712	0.176	0.176	0.273
(39,49,37)	8	997.7	126.47	159	115.88	1.084	1.437	0.181	0.277
(39,49,39)	8	1282.1	131.44	161	124.00	0.985	1.233	0.186	0.274
(39,49,40)	12	2493.7	135.11	103	117.58	1.070	0.486	0.171	0.282
(39,49,41)	8	1467.7	116.75	166	113.63	1.641	1.745	0.181	0.283
(39,50,39)	12	1623.6	108.07	146	136.51	1.264	0.316	0.173	0.277
(39,50,40)	12	3371.1	166.18	119	134.88	1.572	0.529	0.172	0.277
(39,50,41)	12	1657.9	122.30	73	130.00	1.643	1.899	0.177	0.280
(39,51,39)	10	1023.4	141.37	50	146.38	3.044	3.211	0.183	0.274
(39,51,40)	8	2350.1	179.27	95	142.19	2.808	1.572	0.181	0.272
(39,51,41)	12	1868.5	164.29	29	142.63	4.508	3.786	0.193	0.275
(40,25,35)	4	-192.8	143.55	60	105.37	2.784	1.512	0.143	0.262
(40,25,36)	4	2003.6	215.27	90	114.96	4.174	0.832	0.145	0.266
(40,25,37)	8	217.2	135.90	92	117.39	1.463	0.846	0.175	0.270
(40,26,35)	6	1515.5	172.40	4	104.31	5.611	3.343	0.132	0.255
(40,26,37)	6	-105.6	142.61	145	116.40	0.080	0.953	0.153	0.262
(40,27,35)	8	1323.3	140.55	207	101.93	2.214	3.501	0.144	0.262
(40,27,36)	8	2029.5	182.81	58	109.47	4.159	1.715	0.150	0.270
(40,27,37)	12	1009.4	129.93	66	111.02	2.130	1.500	0.167	0.274
(40,47,35)	8	285.4	116.79	83	102.52	1.126	0.651	0.144	0.266
(40,47,36)	6	2457.4	186.89	82	115.74	3.495	1.124	0.139	0.271
(40,47,37)	4	437.4	185.33	230	129.41	1.489	3.352	0.135	0.269
(40,48,35)	10	545.8	133.25	89	98.06	1.474	0.302	0.144	0.258

File: dat1208; composite directional variograms (60 deg)

Enh-Res Coord.	Neigh Voxels	OK Variance	Kriging Estimate	True Value	Trilinear Estimate	% Projection Er		Model Error	
						Krige	Trilin	Mean	STD
(40,48,37)	10	1030.7	203.28	84	127.68	3.975	1.456	0.133	0.263
(40,49,35)	16	806.4	106.15	32	96.54	2.471	2.151	0.155	0.267
(40,49,36)	6	1905.6	141.38	109	109.79	1.079	0.026	0.158	0.271
(40,49,37)	6	448.2	145.40	103	122.69	1.413	0.656	0.157	0.269
(40,49,39)	4	35.9	149.90	176	131.87	0.870	1.470	0.151	0.269
(40,49,40)	10	2734.3	141.09	218	117.71	2.563	3.342	0.154	0.275
(40,49,41)	12	1707.6	113.36	83	107.51	1.012	0.817	0.157	0.276
(40,50,39)	6	1738.4	167.02	61	135.20	3.533	2.473	0.152	0.265
(40,50,41)	10	2552.3	131.96	137	118.77	0.168	0.607	0.144	0.267
(40,51,39)	4	-308.0	176.67	154	139.66	0.756	0.478	0.157	0.265
(40,51,40)	8	3292.6	206.43	266	132.55	1.985	4.447	0.150	0.265
(40,51,41)	4	488.9	157.35	225	124.68	2.254	3.343	0.153	0.262
(41,19,55)	8	160.2	120.01	131	120.38	0.366	0.354	0.227	0.280
(41,20,55)	12	819.4	129.33	56	108.47	2.444	1.748	0.185	0.272
(41,21,55)	8	563.7	99.36	115	99.88	0.521	0.504	0.188	0.273
(41,25,35)	8	-361.2	107.42	101	107.00	0.214	0.200	0.157	0.267
(41,25,36)	4	572.8	131.04	110	111.36	0.701	0.045	0.158	0.274
(41,25,37)	8	-270.8	117.81	146	118.38	0.939	0.921	0.180	0.277
(41,26,35)	12	419.6	124.24	54	106.72	2.341	1.757	0.148	0.263
(41,26,36)	10	976.6	148.23	92	110.14	1.874	0.604	0.156	0.269
(41,26,37)	12	-91.9	123.65	89	117.56	1.155	0.952	0.166	0.272
(41,27,35)	8	-349.3	110.80	121	110.13	0.340	0.362	0.151	0.269
(41,27,36)	16	1157.4	138.47	150	114.18	0.384	1.194	0.161	0.273
(41,27,37)	8	190.4	119.54	88	121.25	1.051	1.108	0.162	0.274
(41,47,35)	8	-418.0	115.63	88	116.25	0.921	0.941	0.150	0.270
(41,47,36)	4	673.2	153.74	216	127.52	2.075	2.948	0.147	0.272
(41,47,37)	8	-193.3	142.36	75	142.38	2.245	2.245	0.145	0.269
(41,47,49)	8	-110.9	132.04	185	131.50	1.765	1.783	0.169	0.279
(41,47,50)	4	613.4	112.99	126	116.28	0.434	0.324	0.158	0.280
(41,47,51)	8	-492.8	101.86	117	100.63	0.505	0.546	0.162	0.278
(41,48,35)	12	-216.5	112.72	11	105.80	3.390	3.159	0.142	0.267
(41,48,36)	6	1311.4	178.16	215	121.80	1.228	3.106	0.140	0.269
(41,48,37)	4	-602.5	174.96	73	135.13	3.398	2.070	0.137	0.265
(41,48,49)	4	-754.3	154.50	154	141.66	0.017	0.411	0.158	0.273
(41,48,50)	6	883.3	135.37	19	123.86	3.878	3.494	0.146	0.272
(41,48,51)	4	-702.6	111.31	95	103.23	0.543	0.274	0.146	0.272
(41,49,35)	8	73.0	100.78	42	101.88	1.959	1.995	0.164	0.266
(41,49,36)	4	399.1	120.13	38	117.27	2.737	2.641	0.163	0.266
(41,49,37)	8	-43.0	133.94	43	133.13	3.030	3.003	0.170	0.268
(41,49,39)	8	-85.8	143.52	115	141.88	0.950	0.896	0.163	0.270
(41,49,40)	12	790.6	134.63	256	120.83	4.044	4.504	0.159	0.276
(41,49,41)	8	471.7	102.79	252	102.13	4.972	4.994	0.164	0.277
(41,49,49)	8	394.4	155.73	41	153.38	3.823	3.745	0.158	0.274
(41,49,50)	4	754.4	138.04	91	129.54	1.567	1.284	0.145	0.270
(41,49,51)	8	-437.3	107.40	156	106.88	1.620	1.637	0.143	0.269
(41,50,39)	4	7.5	155.68	128	138.74	0.922	0.358	0.145	0.269
(41,50,40)	10	1047.3	149.40	224	124.36	2.486	3.320	0.144	0.272
(41,50,41)	12	681.9	106.66	148	106.71	1.377	1.376	0.142	0.270
(41,51,39)	8	-534.3	138.67	220	137.88	2.710	2.737	0.183	0.269

File: dat1208; composite directional variograms (60 deg)

Enh-Res Coord.	Neigh Voxels	OK Variance	Kriging Estimate	True Value	Trilinear Estimate	% Projection Er		Model Error	
						Krige	Trilin	Mean	STD
(41,51,40)	4	839.4	140.73	165	123.28	0.809	1.390	0.166	0.269
(41,51,41)	8	-558.3	112.08	58	111.00	1.802	1.766	0.156	0.265
(42,19,55)	4	140.5	160.17	72	114.30	2.938	1.409	0.186	0.268
(42,20,55)	10	1646.2	200.23	251	111.10	1.692	4.662	0.168	0.266
(42,21,55)	4	473.4	139.29	117	101.84	0.743	0.505	0.165	0.268
(42,47,49)	4	1635.2	166.38	139	129.18	0.912	0.327	0.150	0.272
(42,47,50)	4	2827.8	141.74	114	111.63	0.924	0.079	0.138	0.266
(42,47,51)	4	-375.1	111.67	100	95.54	0.389	0.149	0.155	0.273
(42,48,49)	6	-154.4	175.10	136	138.58	1.303	0.086	0.139	0.266
(42,48,51)	6	-137.7	117.24	124	98.05	0.225	0.865	0.154	0.265
(42,49,49)	8	1846.0	179.68	122	146.44	1.922	0.814	0.152	0.275
(42,49,50)	8	2690.3	185.32	149	124.70	1.210	0.810	0.146	0.271

	Krige	Trilin	Mean	STD
Mean	1.863	1.647	0.165	0.270
Std. Dev.	1.295	1.231	0.019	
Max	6.640	8.435		

Based on 1st 250 Estimates				
Mean	1.932	1.693	0.163	0.268
Std. Dev.	1.331	1.229	0.018	
Max	6.640	5.988		

Appendix E

Kriging Estimates Using
Composite Directional Variograms,
Trilinear Model, Fixed Neighborhood, No Drift

File: dat1219; composite variograms, trilinear model, fixed neighborhood, no drift

Enh-Res Coord.	Kriging Estimate	True Value	Trilinear Estimate	% Projection Er Krige	% Projection Er Trilin	Model Error Mean	Model Error STD
(7,45,45)	138.21	38	137.63	3.339	3.320	0.697	0.120
(7,45,46)	127.78	83	129.79	1.492	1.559	0.694	0.105
(7,45,47)	122.76	132	123.63	0.308	0.279	0.673	0.107
(7,46,45)	137.37	163	137.84	0.854	0.838	0.678	0.120
(7,46,46)	124.01	265	126.71	4.698	4.608	0.685	0.124
(7,46,47)	109.68	160	111.62	1.677	1.612	0.695	0.105
(7,47,45)	139.05	197	138.38	1.931	1.954	0.646	0.176
(7,47,46)	116.42	259	118.22	4.751	4.691	0.669	0.145
(7,47,47)	99.12	71	99.88	0.937	0.962	0.681	0.131
(7,53,45)	143.32	92	141.63	1.710	1.654	0.703	0.123
(7,53,46)	135.75	189	142.60	1.775	1.546	0.670	0.135
(7,53,47)	148.06	74	148.13	2.468	2.470	0.684	0.139
(7,54,45)	129.24	159	129.52	0.992	0.982	0.704	0.117
(7,54,46)	124.62	37	133.15	2.920	3.204	0.673	0.126
(7,54,47)	132.59	100	138.54	1.086	1.284	0.683	0.120
(7,55,45)	119.23	59	118.25	2.007	1.974	0.699	0.141
(7,55,46)	119.39	150	123.57	1.020	0.881	0.682	0.134
(7,55,47)	131.93	85	132.13	1.564	1.570	0.692	0.141
(9,33,53)	137.04	225	136.75	2.931	2.941	0.703	0.105
(9,33,54)	126.74	128	126.69	0.042	0.044	0.691	0.090
(9,33,55)	117.64	37	116.88	2.687	2.662	0.682	0.109
(9,34,53)	133.01	124	140.06	0.300	0.535	0.694	0.098
(9,34,54)	123.19	192	130.03	2.293	2.065	0.696	0.082
(9,34,55)	114.43	36	119.60	2.613	2.786	0.677	0.103
(9,35,53)	148.59	77	147.88	2.386	2.362	0.694	0.115
(9,35,54)	136.61	105	136.64	1.053	1.054	0.700	0.109
(9,35,55)	125.11	51	125.63	2.470	2.487	0.693	0.118
(10,33,53)	132.76	92	139.39	1.358	1.579	0.682	0.098
(10,33,54)	120.15	170	128.60	1.661	1.379	0.704	0.082
(10,33,55)	107.87	26	115.49	2.728	2.982	0.696	0.080
(10,34,53)	126.47	164	142.49	1.251	0.717	0.687	0.080
(10,34,55)	110.16	58	121.70	1.738	2.123	0.696	0.082
(10,35,53)	139.16	104	148.38	1.172	1.479	0.697	0.103
(10,35,54)	136.29	21	142.92	3.842	4.063	0.693	0.099
(10,35,55)	125.04	70	127.50	1.834	1.916	0.692	0.110
(11,33,53)	144.76	60	145.25	2.824	2.841	0.681	0.107
(11,33,54)	128.89	154	131.32	0.837	0.756	0.704	0.094
(11,33,55)	117.88	66	118.13	1.729	1.737	0.711	0.111
(11,34,53)	139.11	24	147.25	3.836	4.107	0.711	0.078
(11,34,54)	128.79	64	137.22	2.159	2.440	0.693	0.081
(11,34,55)	115.61	92	122.41	0.787	1.013	0.698	0.099
(11,35,53)	154.38	15	154.00	4.645	4.632	0.681	0.111
(11,35,54)	143.11	123	142.53	0.670	0.651	0.658	0.119
(11,35,55)	129.62	116	130.25	0.454	0.475	0.663	0.147
(11,36,55)	135.76	310	130.32	5.806	5.987	0.659	0.121
(11,37,55)	127.60	121	127.88	0.220	0.229	0.681	0.140
(12,35,55)	113.69	121	116.39	0.244	0.154	0.668	0.123
(12,36,55)	122.20	244	121.00	4.059	4.099	0.669	0.103
(12,37,55)	119.22	75	118.95	1.473	1.464	0.695	0.116

File: dat1219; composite variograms, trilinear model, fixed neighborhood, no drift

Enh-Res Coord.	Kriging Estimate	True Value	Trilinear Estimate	% Projection Er Krige	% Projection Er Trilin	Model Error Mean	Model Error STD
(13, 9,39)	95.48	162	95.88	2.217	2.203	0.673	0.137
(13, 9,40)	82.51	61	86.66	0.717	0.855	0.670	0.119
(13, 9,41)	79.60	58	79.63	0.720	0.721	0.681	0.112
(13,10,39)	103.83	9	102.11	3.160	3.102	0.655	0.144
(13,10,40)	87.98	37	95.18	1.699	1.939	0.659	0.123
(13,10,41)	82.79	73	84.20	0.326	0.373	0.673	0.090
(13,11,39)	107.02	77	107.25	1.000	1.008	0.653	0.158
(13,11,40)	87.37	26	95.95	2.045	2.331	0.656	0.134
(13,11,41)	90.14	147	89.75	1.895	1.908	0.689	0.117
(13,33,35)	113.86	94	113.00	0.662	0.633	0.673	0.169
(13,33,36)	107.47	30	114.41	2.582	2.813	0.700	0.096
(13,33,37)	121.03	97	119.88	0.801	0.762	0.687	0.096
(13,34,35)	121.66	94	118.11	0.922	0.803	0.712	0.143
(13,34,36)	117.40	164	122.51	1.553	1.383	0.696	0.114
(13,34,37)	128.80	145	126.19	0.540	0.627	0.675	0.106
(13,35,35)	123.07	101	122.00	0.735	0.700	0.710	0.148
(13,35,36)	117.06	122	124.74	0.165	0.091	0.675	0.124
(13,35,37)	132.28	132	131.88	0.009	0.004	0.653	0.146
(13,35,55)	104.15	21	103.88	2.771	2.762	0.648	0.147
(13,36,55)	107.90	167	106.87	1.969	2.004	0.670	0.102
(13,37,55)	110.84	104	110.13	0.228	0.204	0.688	0.105
(13,39,41)	129.05	36	129.00	3.101	3.099	0.679	0.111
(13,39,42)	107.90	162	119.77	1.803	1.407	0.685	0.123
(13,39,43)	119.19	59	118.00	2.006	1.966	0.705	0.138
(13,40,41)	147.81	54	146.62	3.126	3.086	0.689	0.112
(13,40,42)	132.29	255	142.12	4.089	3.761	0.647	0.140
(13,40,43)	140.04	106	137.38	1.134	1.046	0.695	0.142
(13,41,41)	165.20	25	164.13	4.672	4.636	0.682	0.131
(13,41,42)	148.32	273	157.05	4.155	3.864	0.698	0.126
(13,41,43)	158.87	66	156.50	3.095	3.016	0.699	0.152
(13,41,47)	129.69	140	129.38	0.344	0.354	0.656	0.154
(13,41,48)	126.50	148	125.71	0.716	0.743	0.674	0.140
(13,41,49)	121.81	24	121.88	3.259	3.261	0.713	0.120
(13,42,47)	129.76	199	139.89	2.307	1.970	0.680	0.108
(13,42,48)	121.85	186	133.75	2.138	1.741	0.691	0.103
(13,42,49)	112.16	103	121.34	0.305	0.611	0.707	0.096
(13,43,47)	155.86	196	155.88	1.337	1.337	0.674	0.126
(13,43,48)	135.11	173	139.50	1.262	1.116	0.676	0.117
(13,43,49)	124.96	46	125.38	2.631	2.645	0.702	0.115
(14, 9,39)	87.49	109	94.67	0.717	0.477	0.691	0.108
(14, 9,40)	77.12	122	87.71	1.495	1.143	0.689	0.091
(14, 9,41)	74.65	83	78.42	0.278	0.153	0.695	0.095
(14,10,39)	90.63	37	100.28	1.787	2.108	0.673	0.131
(14,10,41)	76.81	99	84.94	0.739	0.469	0.676	0.090
(14,11,39)	93.42	151	102.41	1.919	1.619	0.672	0.130
(14,11,40)	82.16	132	97.03	1.661	1.165	0.675	0.115
(14,11,41)	84.43	60	89.58	0.814	0.986	0.690	0.092
(14,33,35)	110.83	57	117.53	1.794	2.017	0.692	0.141
(14,33,36)	113.91	35	123.97	2.629	2.965	0.698	0.107

E-3

File: dat1219; composite variograms, trilinear model, fixed neighborhood, no drift

Enh-Res Coord.	Kriging Estimate	True Value	Trilinear Estimate	% Projection Er		Model Error	
				Krige	Trilin	Mean	STD
(14,33,37)	130.84	131	130.27	0.005	0.024	0.666	0.104
(14,34,35)	107.77	100	118.26	0.259	0.608	0.694	0.128
(14,34,37)	129.65	150	136.80	0.678	0.440	0.688	0.102
(14,35,35)	108.63	198	121.29	2.978	2.556	0.705	0.130
(14,35,36)	116.45	125	133.66	0.285	0.289	0.681	0.123
(14,35,37)	139.48	138	144.64	0.049	0.221	0.664	0.139
(14,39,41)	112.85	123	122.99	0.338	0.000	0.695	0.109
(14,39,42)	110.67	309	129.30	6.609	5.988	0.651	0.132
(14,39,43)	123.98	117	130.26	0.232	0.442	0.693	0.134
(14,40,41)	127.65	100	135.60	0.921	1.186	0.647	0.126
(14,40,43)	141.68	213	144.31	2.376	2.289	0.662	0.142
(14,41,41)	138.03	65	148.05	2.433	2.767	0.705	0.117
(14,41,42)	139.76	193	154.80	1.774	1.273	0.696	0.111
(14,41,43)	151.17	237	153.44	2.860	2.784	0.707	0.118
(14,41,47)	115.31	45	117.73	2.343	2.424	0.633	0.161
(14,41,48)	116.67	79	120.00	1.255	1.366	0.653	0.136
(14,41,49)	116.99	109	117.59	0.266	0.286	0.694	0.121
(14,42,47)	120.95	94	132.96	0.898	1.298	0.659	0.120
(14,42,49)	109.98	45	123.03	2.165	2.600	0.709	0.085
(14,43,47)	141.48	178	146.22	1.217	1.059	0.643	0.143
(14,43,48)	128.09	198	138.84	2.329	1.971	0.666	0.122
(14,43,49)	120.29	99	127.31	0.709	0.943	0.698	0.108
(15, 9,39)	97.51	95	97.50	0.084	0.083	0.680	0.140
(15, 9,40)	79.85	102	86.38	0.738	0.520	0.678	0.136
(15, 9,41)	79.69	97	79.50	0.577	0.583	0.649	0.149
(15,10,39)	93.35	93	98.57	0.012	0.186	0.657	0.115
(15,10,40)	80.42	40	93.56	1.347	1.785	0.662	0.116
(15,10,41)	78.80	120	84.43	1.373	1.185	0.625	0.140
(15,11,39)	102.60	133	102.38	1.013	1.020	0.676	0.121
(15,11,40)	88.36	38	95.27	1.678	1.908	0.679	0.118
(15,11,41)	93.50	45	92.75	1.616	1.591	0.676	0.110
(15,33,35)	127.22	121	126.25	0.207	0.175	0.689	0.158
(15,33,36)	127.65	118	132.19	0.321	0.473	0.683	0.118
(15,33,37)	142.31	67	141.13	2.510	2.470	0.642	0.136
(15,33,38)	138.15	115	134.72	0.771	0.657	0.688	0.101
(15,33,39)	129.03	52	127.38	2.567	2.512	0.665	0.111
(15,34,35)	120.54	149	125.43	0.948	0.785	0.713	0.148
(15,34,36)	121.22	80	136.60	1.374	1.886	0.690	0.124
(15,34,37)	135.23	119	146.99	0.541	0.933	0.709	0.114
(15,34,38)	136.61	91	142.93	1.520	1.730	0.696	0.097
(15,34,39)	132.34	81	137.02	1.711	1.867	0.694	0.091
(15,35,35)	128.71	27	128.00	3.389	3.366	0.700	0.167
(15,35,36)	133.80	85	141.86	1.626	1.895	0.700	0.144
(15,35,37)	159.77	78	160.13	2.725	2.737	0.698	0.158
(15,35,38)	158.79	137	155.95	0.726	0.631	0.684	0.108
(15,35,39)	151.58	59	150.38	3.085	3.045	0.672	0.107
(15,39,41)	123.38	54	123.00	2.312	2.299	0.708	0.123
(15,39,42)	125.33	126	132.72	0.022	0.224	0.695	0.122
(15,39,43)	148.73	59	147.50	2.990	2.949	0.694	0.138

File: dat1219; composite variograms, trilinear model, fixed neighborhood, no drift

Enh-Res Coord.	Kriging Estimate	True Value	Trilinear Estimate	% Projection Er Krige	% Projection Er Trilin	Model Error Mean	Model Error STD
(15,39,55)	123.28	44	122.13	2.642	2.603	0.715	0.109
(15,40,41)	134.64	153	131.36	0.612	0.721	0.702	0.123
(15,40,42)	138.47	152	141.08	0.451	0.364	0.679	0.125
(15,40,43)	156.21	54	151.33	3.406	3.243	0.704	0.133
(15,40,55)	117.38	121	123.41	0.120	0.080	0.662	0.113
(15,41,41)	139.80	69	138.50	2.359	2.316	0.705	0.136
(15,41,42)	140.94	141	144.65	0.002	0.122	0.710	0.116
(15,41,43)	155.07	71	153.50	2.801	2.749	0.691	0.134
(15,41,44)	134.67	42	133.88	3.088	3.062	0.704	0.120
(15,41,45)	117.64	74	115.38	1.454	1.379	0.673	0.133
(15,41,47)	109.41	263	108.50	5.118	5.148	0.620	0.173
(15,41,48)	106.10	174	110.28	2.263	2.123	0.664	0.132
(15,41,49)	114.60	102	114.50	0.420	0.417	0.699	0.120
(15,41,55)	130.21	75	128.75	1.840	1.791	0.624	0.132
(15,42,43)	151.91	103	154.34	1.630	1.711	0.690	0.118
(15,42,44)	136.68	85	141.69	1.722	1.889	0.688	0.116
(15,42,45)	125.95	134	128.65	0.268	0.178	0.685	0.108
(15,42,47)	117.74	258	122.64	4.674	4.510	0.623	0.144
(15,42,48)	110.34	123	121.30	0.422	0.057	0.673	0.108
(15,42,49)	112.81	124	121.62	0.373	0.079	0.704	0.090
(15,43,43)	158.43	116	157.00	1.414	1.366	0.695	0.131
(15,43,44)	148.82	128	149.54	0.694	0.718	0.689	0.127
(15,43,45)	146.36	16	144.25	4.344	4.274	0.668	0.143
(15,43,47)	139.97	136	139.75	0.132	0.125	0.590	0.182
(15,43,48)	129.90	190	135.05	2.003	1.831	0.634	0.145
(15,43,49)	132.93	180	133.25	1.569	1.558	0.682	0.134
(16,33,37)	129.26	168	131.95	1.291	1.201	0.666	0.133
(16,33,38)	126.48	142	130.43	0.517	0.386	0.695	0.115
(16,33,39)	120.51	72	124.31	1.616	1.743	0.671	0.133
(16,34,37)	120.02	63	135.67	1.900	2.422	0.696	0.111
(16,34,39)	122.91	77	130.59	1.530	1.786	0.677	0.120
(16,35,37)	141.20	86	144.20	1.839	1.939	0.689	0.124
(16,35,38)	139.61	101	145.89	1.286	1.496	0.694	0.110
(16,35,39)	140.45	83	143.37	1.914	2.012	0.677	0.120
(16,39,55)	127.00	119	126.77	0.267	0.259	0.689	0.086
(16,40,55)	121.91	132	131.91	0.336	0.003	0.678	0.094
(16,41,43)	130.58	124	129.51	0.219	0.184	0.708	0.130
(16,41,44)	123.22	134	129.54	0.359	0.148	0.691	0.121
(16,41,45)	120.85	106	121.59	0.495	0.519	0.661	0.148
(16,41,55)	134.33	10	138.43	4.143	4.280	0.655	0.119
(16,42,43)	125.55	265	131.88	4.647	4.436	0.710	0.116
(16,42,45)	120.50	68	129.41	1.750	2.046	0.668	0.106
(16,43,43)	131.83	166	135.33	1.139	1.022	0.706	0.105
(16,43,44)	130.22	133	138.84	0.093	0.195	0.696	0.098
(16,43,45)	137.92	121	140.78	0.564	0.659	0.665	0.108
(17,33,37)	126.25	17	125.00	3.640	3.599	0.685	0.171
(17,33,38)	120.90	47	123.67	2.463	2.555	0.691	0.157
(17,33,39)	125.21	111	124.13	0.474	0.437	0.668	0.182
(17,34,37)	109.88	51	123.40	1.962	2.412	0.666	0.136

File: dat1219; composite variograms, trilinear model, fixed neighborhood, no drift

Enh-Res Coord.	Kriging Estimate	True Value	Trilinear Estimate	% Projection Er		Model Error	
				Krige	Trilin	Mean	STD
(17,34,38)	113.56	140	127.97	0.881	0.401	0.689	0.126
(17,34,39)	126.42	90	129.79	1.214	1.326	0.667	0.165
(17,35,37)	129.72	48	129.75	2.723	2.724	0.659	0.147
(17,35,38)	123.38	186	131.78	2.087	1.807	0.690	0.127
(17,35,39)	138.80	180	138.13	1.373	1.395	0.687	0.146
(17,39,55)	131.65	102	131.25	0.988	0.975	0.654	0.130
(17,40,55)	129.97	30	138.59	3.331	3.618	0.676	0.131
(17,41,43)	105.55	44	105.63	2.051	2.053	0.699	0.125
(17,41,44)	105.34	180	114.71	2.488	2.176	0.693	0.114
(17,41,45)	130.92	5	129.63	4.196	4.153	0.616	0.176
(17,41,55)	152.31	32	151.00	4.009	3.965	0.642	0.159
(17,42,43)	103.42	219	109.36	3.851	3.653	0.712	0.104
(17,42,44)	103.35	50	119.40	1.778	2.313	0.683	0.101
(17,42,45)	124.06	83	132.62	1.368	1.654	0.657	0.112
(17,43,43)	116.56	54	116.00	2.085	2.066	0.698	0.119
(17,43,44)	117.60	170	125.27	1.746	1.491	0.705	0.108
(17,43,45)	140.93	75	140.13	2.197	2.170	0.639	0.138
(17,45,55)	96.25	160	96.25	2.124	2.124	0.673	0.124
(17,46,55)	95.37	46	100.40	1.645	1.813	0.670	0.114
(17,47,55)	107.48	65	107.25	1.415	1.408	0.688	0.143
(17,53,29)	129.49	123	128.13	0.216	0.171	0.647	0.134
(17,53,30)	129.37	32	127.67	3.245	3.188	0.638	0.130
(17,53,31)	127.52	99	126.75	0.950	0.925	0.653	0.137
(17,54,29)	116.46	155	121.85	1.284	1.105	0.663	0.111
(17,54,30)	116.23	66	122.80	1.674	1.893	0.651	0.116
(17,54,31)	116.14	139	120.64	0.762	0.612	0.684	0.134
(17,55,29)	121.60	67	119.88	1.819	1.762	0.652	0.116
(17,55,30)	116.41	69	118.14	1.580	1.637	0.648	0.130
(17,55,31)	118.55	70	117.75	1.618	1.591	0.649	0.152
(18,45,55)	82.39	31	85.51	1.713	1.816	0.688	0.103
(18,46,55)	91.13	40	97.47	1.704	1.915	0.678	0.104
(18,47,55)	103.59	49	105.62	1.819	1.887	0.700	0.130
(18,53,29)	122.14	95	123.03	0.904	0.934	0.662	0.105
(18,53,30)	121.93	124	123.86	0.069	0.005	0.657	0.104
(18,53,31)	120.12	151	121.81	1.029	0.973	0.658	0.108
(18,54,29)	107.65	123	117.35	0.512	0.188	0.679	0.090
(18,54,31)	106.15	102	116.97	0.138	0.499	0.676	0.111
(18,55,29)	111.30	64	113.91	1.576	1.663	0.669	0.095
(18,55,30)	108.97	159	117.10	1.667	1.396	0.652	0.120
(18,55,31)	109.49	107	115.28	0.083	0.276	0.638	0.129
(19,19,53)	113.08	130	112.25	0.564	0.591	0.629	0.161
(19,19,54)	110.48	71	116.56	1.316	1.518	0.640	0.145
(19,19,55)	126.18	134	124.75	0.261	0.308	0.622	0.172
(19,20,53)	109.67	103	113.44	0.222	0.348	0.626	0.146
(19,20,54)	109.96	87	116.73	0.765	0.991	0.631	0.139
(19,20,55)	123.19	148	121.57	0.827	0.881	0.635	0.162
(19,21,53)	118.37	175	117.25	1.887	1.924	0.613	0.177
(19,21,54)	113.80	71	116.63	1.426	1.521	0.629	0.147
(19,21,55)	120.28	31	118.38	2.975	2.912	0.644	0.150

File: dat1219; composite variograms, trilinear model, fixed neighborhood, no drift

Enh-Res Coord.	Kriging Estimate	True Value	Trilinear Estimate	% Projection Er		Model Error	
				Krige	Trilin	Mean	STD
(19,45,55)	76.74	90	76.75	0.442	0.442	0.701	0.105
(19,46,55)	88.36	228	90.44	4.653	4.584	0.692	0.115
(19,47,55)	105.87	185	105.38	2.637	2.653	0.693	0.149
(19,53,29)	120.76	47	119.38	2.458	2.412	0.630	0.126
(19,53,30)	118.18	33	118.57	2.838	2.852	0.636	0.126
			Mean	1.687	1.693	0.678	0.123
			Std. Dev	1.235	1.229	0.023	
			Max	6.609	5.988		

Appendix F

KRIGING ESTIMATES USING

COMPOSITE DIRECTIONAL VARIOGRAMS

TO INTERPOLATE MRI PHANTOM VALIDATION DATA

File: dat0102; composite variograms, mri phantom validation data

Enh-Res Coord.	Phant. Value	Trilinear		Kriging, cdv=50		Kriging, cdv=60	
		Estimat	Proj Err	Estimate	Proj Err	Estimate	Proj Err
(7,45,45)	140	137.63	0.079	139.56	0.015	138.21	0.060
(7,45,46)	141	129.79	0.374	141.04	0.001	139.77	0.041
(7,45,47)	123	123.63	0.021	122.76	0.008	122.76	0.008
(7,46,45)	141	137.84	0.105	140.53	0.016	141.09	0.003
(7,46,46)	139	126.71	0.410	138.64	0.012	149.52	0.351
(7,46,47)	114	111.62	0.079	114.32	0.011	113.09	0.030
(7,47,45)	159	138.38	0.687	158.97	0.001	138.45	0.685
(7,47,46)	125	118.22	0.226	125.14	0.005	125.14	0.005
(7,47,47)	98	99.88	0.062	98.34	0.011	98.34	0.011
(7,53,45)	144	141.63	0.079	143.54	0.015	143.46	0.018
(7,53,46)	176	142.60	1.113	176.43	0.014	174.16	0.061
(7,53,47)	148	148.13	0.004	147.86	0.005	148.06	0.002
(7,54,45)	135	129.52	0.183	135.06	0.002	130.94	0.135
(7,54,46)	171	133.15	1.261	170.65	0.012	171.63	0.021
(7,54,47)	161	138.54	0.749	160.57	0.014	140.03	0.699
(7,55,45)	118	118.25	0.008	118.22	0.007	119.23	0.041
(7,55,46)	146	123.57	0.747	146.25	0.008	146.22	0.007
(7,55,47)	132	132.13	0.004	131.93	0.002	131.93	0.002
(9,33,53)	136	136.75	0.025	136.47	0.016	136.75	0.025
(9,33,54)	129	126.69	0.077	128.77	0.008	128.75	0.008
(9,33,55)	115	116.88	0.062	114.65	0.012	117.43	0.081
(9,34,53)	160	140.06	0.665	159.65	0.012	162.63	0.088
(9,34,54)	153	130.03	0.765	153.34	0.011	147.77	0.174
(9,34,55)	145	119.60	0.846	145.10	0.003	144.21	0.026
(9,35,53)	149	147.88	0.037	148.70	0.010	148.70	0.010
(9,35,54)	137	136.64	0.012	137.48	0.016	138.50	0.050
(9,35,55)	126	125.63	0.012	126.00	0.000	125.60	0.013
(10,33,53)	170	139.39	1.020	169.63	0.012	168.66	0.045
(10,33,54)	168	128.60	1.313	168.41	0.014	171.45	0.115
(10,33,55)	124	115.49	0.284	123.60	0.013	145.67	0.722
(10,34,53)	206	142.49	2.116	205.91	0.003	208.58	0.086
(10,34,55)	168	121.70	1.543	167.66	0.011	165.21	0.093
(10,35,53)	187	148.38	1.287	187.19	0.006	187.19	0.006
(10,35,54)	193	142.92	1.669	193.18	0.006	193.18	0.006
(10,35,55)	134	127.50	0.217	133.76	0.008	133.58	0.014
(11,33,53)	146	145.25	0.025	145.53	0.016	145.53	0.016
(11,33,54)	136	131.32	0.156	135.54	0.015	135.54	0.015
(11,33,55)	116	118.13	0.071	116.44	0.015	117.96	0.065
(11,34,53)	170	147.25	0.758	169.94	0.002	169.94	0.002
(11,34,54)	162	137.22	0.826	162.18	0.006	162.18	0.006
(11,34,55)	139	122.41	0.553	139.20	0.007	139.10	0.003
(11,35,53)	154	154.00	0.000	154.28	0.009	154.28	0.009
(11,35,54)	138	142.53	0.151	138.06	0.002	137.95	0.002
(11,35,55)	140	130.25	0.325	140.10	0.003	129.13	0.362
(11,36,55)	111	130.32	0.644	110.74	0.009	110.74	0.009
(11,37,55)	173	127.88	1.504	172.72	0.009	129.03	1.465
(12,35,55)	158	116.39	1.387	158.03	0.001	126.29	1.057
(12,36,55)	130	121.00	0.300	130.02	0.001	133.35	0.111
(12,37,55)	130	118.95	0.368	130.21	0.007	123.19	0.227

File: dat0102; composite variograms, mri phantom validation data

Enh-Res Coord.	Phant. Value	Trilinear		Kriging, cdv=50		Kriging, cdv=60	
		Estimat	Proj Err	Estimate	Proj Err	Estimate	Proj Err
(13, 9,39)	97	95.88	0.037	97.11	0.004	95.16	0.061
(13, 9,40)	86	86.66	0.022	85.62	0.013	102.64	0.555
(13, 9,41)	80	79.63	0.012	79.60	0.013	79.60	0.013
(13,10,39)	99	102.11	0.103	98.72	0.009	97.63	0.046
(13,10,40)	132	95.18	1.227	132.28	0.009	136.92	0.164
(13,10,41)	90	84.20	0.193	89.93	0.002	87.23	0.092
(13,11,39)	95	107.25	0.408	95.21	0.007	106.66	0.389
(13,11,40)	150	95.95	1.801	149.64	0.012	133.95	0.535
(13,11,41)	96	89.75	0.208	96.45	0.015	90.41	0.186
(13,33,35)	114	113.00	0.033	113.86	0.005	113.86	0.005
(13,33,36)	135	114.41	0.686	134.58	0.014	145.13	0.338
(13,33,37)	121	119.88	0.037	121.03	0.001	121.03	0.001
(13,34,35)	109	118.11	0.304	109.18	0.006	109.18	0.006
(13,34,36)	165	122.51	1.416	165.18	0.006	158.86	0.204
(13,34,37)	121	126.19	0.173	121.50	0.017	121.50	0.017
(13,35,35)	123	122.00	0.033	123.15	0.005	123.07	0.002
(13,35,36)	159	124.74	1.142	159.35	0.012	158.56	0.015
(13,35,37)	132	131.88	0.004	132.37	0.012	132.90	0.030
(13,35,55)	107	103.88	0.104	106.57	0.014	104.29	0.090
(13,36,55)	106	106.87	0.029	106.13	0.004	108.81	0.094
(13,37,55)	111	110.13	0.029	110.69	0.010	110.84	0.005
(13,39,41)	129	129.00	0.000	129.05	0.002	129.05	0.002
(13,39,42)	175	119.77	1.840	175.03	0.001	175.05	0.002
(13,39,43)	119	118.00	0.033	119.24	0.008	119.24	0.008
(13,40,41)	147	146.62	0.013	146.74	0.009	146.74	0.009
(13,40,42)	198	142.12	1.862	197.63	0.012	189.86	0.271
(13,40,43)	137	137.38	0.013	137.26	0.009	137.26	0.009
(13,41,41)	165	164.13	0.029	165.20	0.007	165.20	0.007
(13,41,42)	189	157.05	1.065	188.86	0.005	188.86	0.005
(13,41,43)	159	156.50	0.083	159.32	0.011	159.32	0.011
(13,41,47)	129	129.38	0.012	129.31	0.010	129.31	0.010
(13,41,48)	125	125.71	0.024	125.47	0.016	125.47	0.016
(13,41,49)	121	121.88	0.029	121.15	0.005	121.15	0.005
(13,42,47)	181	139.89	1.370	181.05	0.002	181.05	0.002
(13,42,48)	176	133.75	1.408	176.16	0.005	176.16	0.005
(13,42,49)	143	121.34	0.722	142.92	0.003	142.79	0.007
(13,43,47)	156	155.88	0.004	156.30	0.010	156.34	0.011
(13,43,48)	151	139.50	0.383	150.61	0.013	150.61	0.013
(13,43,49)	125	125.38	0.012	125.30	0.010	125.30	0.010
(14, 9,39)	126	94.67	1.044	126.35	0.012	124.55	0.048
(14, 9,40)	137	87.71	1.643	137.49	0.016	159.72	0.757
(14, 9,41)	94	78.42	0.519	94.05	0.001	95.67	0.056
(14,10,39)	156	100.28	1.857	156.24	0.008	142.55	0.448
(14,10,41)	139	84.94	1.801	138.62	0.013	116.60	0.747
(14,11,39)	138	102.41	1.186	138.43	0.014	138.20	0.007
(14,11,40)	179	97.03	2.731	178.69	0.010	191.49	0.416
(14,11,41)	115	89.58	0.847	115.39	0.013	115.39	0.013
(14,33,35)	149	117.53	1.049	149.31	0.010	149.31	0.010
(14,33,36)	183	123.97	1.967	183.14	0.005	182.26	0.025

File: dat0102; composite variograms, mri phantom validation data

Enh-Res Coord.	Phant. Value	Trilinear		Kriging, cdv=50		Kriging, cdv=60	
		Estimat	Proj Err	Estimate	Proj Err	Estimate	Proj Err
(14,33,37)	135	130.27	0.158	134.86	0.005	135.03	0.001
(14,34,35)	164	118.26	1.524	164.43	0.014	164.43	0.014
(14,34,37)	173	136.80	1.206	172.60	0.013	154.53	0.615
(14,35,35)	177	121.29	1.857	177.30	0.010	177.30	0.010
(14,35,36)	217	133.66	2.777	217.05	0.002	227.34	0.345
(14,35,37)	165	144.64	0.679	165.14	0.005	172.75	0.258
(14,39,41)	165	122.99	1.400	164.54	0.015	164.54	0.015
(14,39,42)	236	129.30	3.556	235.55	0.015	234.55	0.048
(14,39,43)	168	130.26	1.258	167.67	0.011	167.67	0.011
(14,40,41)	174	135.60	1.280	174.39	0.013	174.39	0.013
(14,40,43)	177	144.31	1.089	176.62	0.013	176.90	0.003
(14,41,41)	194	148.05	1.531	194.21	0.007	194.21	0.007
(14,41,42)	247	154.80	3.072	247.19	0.006	247.19	0.006
(14,41,43)	178	153.44	0.818	178.00	0.000	178.00	0.000
(14,41,47)	153	117.73	1.175	153.32	0.011	153.32	0.011
(14,41,48)	155	120.00	1.166	155.38	0.013	155.38	0.013
(14,41,49)	126	117.59	0.280	126.06	0.002	126.06	0.002
(14,42,47)	198	132.96	2.167	197.67	0.011	197.67	0.011
(14,42,49)	184	123.03	2.032	184.02	0.001	182.99	0.034
(14,43,47)	169	146.22	0.759	169.50	0.017	169.50	0.017
(14,43,48)	200	138.84	2.038	199.94	0.002	198.73	0.042
(14,43,49)	156	127.31	0.956	156.33	0.011	156.33	0.011
(15, 9,39)	94	97.50	0.117	94.50	0.017	97.83	0.128
(15, 9,40)	120	86.38	1.120	120.39	0.013	110.55	0.315
(15, 9,41)	82	79.50	0.083	82.30	0.010	79.98	0.067
(15,10,39)	119	98.57	0.681	119.39	0.013	113.89	0.170
(15,10,40)	168	93.56	2.480	167.96	0.001	157.12	0.363
(15,10,41)	116	84.43	1.052	115.52	0.016	108.62	0.246
(15,11,39)	103	102.38	0.021	102.55	0.015	102.60	0.013
(15,11,40)	129	95.27	1.124	129.49	0.016	129.34	0.011
(15,11,41)	93	92.75	0.008	93.07	0.002	93.68	0.023
(15,33,35)	127	126.25	0.025	127.22	0.007	127.22	0.007
(15,33,36)	156	132.19	0.793	155.52	0.016	154.66	0.045
(15,33,37)	142	141.13	0.029	142.31	0.010	142.31	0.010
(15,33,38)	129	134.72	0.191	128.77	0.008	129.16	0.005
(15,33,39)	129	127.38	0.054	129.03	0.001	130.06	0.035
(15,34,35)	130	125.43	0.152	129.58	0.014	130.54	0.018
(15,34,36)	195	136.60	1.946	195.27	0.009	191.53	0.116
(15,34,37)	181	146.99	1.133	181.04	0.001	149.18	1.060
(15,34,38)	160	142.93	0.569	159.69	0.010	169.02	0.300
(15,34,39)	165	137.02	0.932	164.83	0.006	165.48	0.016
(15,35,35)	127	128.00	0.033	126.53	0.016	131.96	0.165
(15,35,36)	175	141.86	1.104	175.41	0.014	175.11	0.004
(15,35,37)	160	160.13	0.004	160.23	0.007	159.50	0.017
(15,35,38)	149	155.95	0.232	148.57	0.014	148.57	0.014
(15,35,39)	152	150.38	0.054	151.55	0.015	158.72	0.224
(15,39,41)	123	123.00	0.000	123.44	0.015	123.42	0.014
(15,39,42)	157	132.72	0.809	157.32	0.011	157.32	0.011
(15,39,43)	149	147.50	0.050	149.13	0.004	149.13	0.004

File: dat0102; composite variograms, mri phantom validation data

Enh-Res Coord.	Phant. Value	Trilinear		Kriging, cdv=50		Kriging, cdv=60	
		Estimat	Proj Err	Estimate	Proj Err	Estimate	Proj Err
(15,39,55)	128	122.13	0.196	127.99	0.000	123.00	0.167
(15,40,41)	125	131.36	0.212	124.98	0.001	124.21	0.026
(15,40,42)	160	141.08	0.630	159.90	0.003	161.56	0.052
(15,40,43)	141	151.33	0.344	140.86	0.005	140.86	0.005
(15,40,55)	155	123.41	1.053	154.55	0.015	154.67	0.011
(15,41,41)	140	138.50	0.050	139.83	0.006	139.78	0.007
(15,41,42)	157	144.65	0.411	157.34	0.011	157.34	0.011
(15,41,43)	155	153.50	0.050	154.73	0.009	154.73	0.009
(15,41,44)	140	133.88	0.204	140.30	0.010	140.30	0.010
(15,41,45)	117	115.38	0.054	117.49	0.016	117.49	0.016
(15,41,47)	110	108.50	0.050	110.05	0.002	110.05	0.002
(15,41,48)	123	110.28	0.424	123.37	0.012	123.37	0.012
(15,41,49)	113	114.50	0.050	113.03	0.001	114.90	0.063
(15,41,55)	124	128.75	0.158	123.83	0.006	130.42	0.214
(15,42,43)	169	154.34	0.489	169.43	0.014	169.43	0.014
(15,42,44)	166	141.69	0.810	165.95	0.002	165.95	0.002
(15,42,45)	148	128.65	0.645	148.23	0.008	148.23	0.008
(15,42,47)	145	122.64	0.745	145.24	0.008	145.24	0.008
(15,42,48)	159	121.30	1.256	159.04	0.001	159.04	0.001
(15,42,49)	140	121.62	0.612	140.03	0.001	143.36	0.112
(15,43,43)	158	157.00	0.033	158.45	0.015	158.45	0.015
(15,43,44)	162	149.54	0.415	161.69	0.010	161.69	0.010
(15,43,45)	150	144.25	0.192	149.71	0.010	146.55	0.115
(15,43,47)	139	139.75	0.025	139.15	0.005	139.38	0.013
(15,43,48)	148	135.05	0.432	147.96	0.001	147.96	0.001
(15,43,49)	133	133.25	0.008	132.53	0.016	132.46	0.018
(16,33,37)	145	131.95	0.435	145.14	0.005	147.09	0.070
(16,33,38)	167	130.43	1.219	166.90	0.003	155.32	0.389
(16,33,39)	149	124.31	0.823	148.58	0.014	149.02	0.001
(16,34,37)	220	135.67	2.810	219.54	0.015	183.31	1.223
(16,34,39)	157	130.59	0.880	157.34	0.011	158.71	0.057
(16,35,37)	154	144.20	0.327	153.51	0.016	152.00	0.067
(16,35,38)	180	145.89	1.136	179.91	0.003	179.91	0.003
(16,35,39)	155	143.37	0.388	154.84	0.005	154.84	0.005
(16,39,55)	119	126.77	0.259	118.62	0.013	125.90	0.230
(16,40,55)	166	131.91	1.136	165.51	0.016	160.76	0.174
(16,41,43)	131	129.51	0.050	130.60	0.013	130.60	0.013
(16,41,44)	186	129.54	1.881	186.00	0.000	186.00	0.000
(16,41,45)	136	121.59	0.480	135.98	0.001	136.50	0.017
(16,41,55)	126	138.43	0.414	125.69	0.010	167.12	1.370
(16,42,43)	160	131.88	0.937	160.48	0.016	160.48	0.016
(16,42,45)	171	129.41	1.386	170.67	0.011	170.67	0.011
(16,43,43)	153	135.33	0.589	153.45	0.015	153.45	0.015
(16,43,44)	196	138.84	1.905	196.42	0.014	196.42	0.014
(16,43,45)	163	140.78	0.740	162.87	0.004	162.87	0.004
(17,33,37)	121	125.00	0.133	120.77	0.008	131.02	0.334
(17,33,38)	139	123.67	0.511	138.83	0.006	140.90	0.063
(17,33,39)	124	124.13	0.004	124.47	0.016	125.21	0.040
(17,34,37)	182	123.40	1.953	182.42	0.014	156.17	0.861

File: dat0102; composite variograms, mri phantom validation data

Enh-Res Coord.	Phant. Value	Trilinear		Kriging, cdv=50		Kriging, cdv=60	
		Estimat	Proj Err	Estimate	Proj Err	Estimate	Proj Err
(17,34,38)	196	127.97	2.267	195.76	0.008	197.06	0.035
(17,34,39)	144	129.79	0.474	144.07	0.002	143.86	0.005
(17,35,37)	126	129.75	0.125	125.84	0.005	129.73	0.124
(17,35,38)	172	131.78	1.340	171.84	0.005	162.03	0.332
(17,35,39)	140	138.13	0.062	140.42	0.014	138.80	0.040
(17,39,55)	142	131.25	0.358	142.12	0.004	134.23	0.259
(17,40,55)	180	138.59	1.380	180.15	0.005	165.02	0.499
(17,41,43)	106	105.63	0.012	105.70	0.010	105.70	0.010
(17,41,44)	141	114.71	0.876	141.36	0.012	141.36	0.012
(17,41,45)	131	129.63	0.046	131.02	0.001	130.96	0.001
(17,41,55)	149	151.00	0.067	148.73	0.009	148.60	0.013
(17,42,43)	131	109.36	0.721	131.39	0.013	131.39	0.013
(17,42,44)	175	119.40	1.853	175.09	0.003	175.09	0.003
(17,42,45)	167	132.62	1.146	167.25	0.008	167.25	0.008
(17,43,43)	117	116.00	0.033	116.61	0.013	116.61	0.013
(17,43,44)	151	125.27	0.857	151.30	0.010	151.30	0.010
(17,43,45)	141	140.13	0.029	141.16	0.005	141.16	0.005
(17,45,55)	96	96.25	0.008	96.25	0.008	96.25	0.008
(17,46,55)	121	100.40	0.686	120.79	0.007	120.79	0.007
(17,47,55)	107	107.25	0.008	107.48	0.016	107.48	0.016
(17,53,29)	127	128.13	0.037	126.72	0.009	133.70	0.223
(17,53,30)	142	127.67	0.478	142.10	0.003	125.11	0.563
(17,53,31)	127	126.75	0.008	127.33	0.011	123.59	0.114
(17,54,29)	142	121.85	0.672	141.51	0.016	166.31	0.810
(17,54,30)	163	122.80	1.340	163.19	0.006	154.80	0.273
(17,54,31)	145	120.64	0.812	144.77	0.008	135.96	0.301
(17,55,29)	122	119.88	0.071	122.03	0.001	122.03	0.001
(17,55,30)	129	118.14	0.362	129.25	0.008	129.25	0.008
(17,55,31)	118	117.75	0.008	118.42	0.014	118.28	0.009
(18,45,55)	101	85.51	0.516	101.01	0.000	112.03	0.368
(18,46,55)	113	97.47	0.517	113.19	0.006	145.67	1.089
(18,47,55)	116	105.62	0.346	116.21	0.007	116.21	0.007
(18,53,29)	135	123.03	0.399	134.50	0.017	134.50	0.017
(18,53,30)	143	123.86	0.638	142.89	0.004	142.82	0.006
(18,53,31)	132	121.81	0.340	132.50	0.017	134.09	0.069
(18,54,29)	160	117.35	1.421	160.04	0.001	151.58	0.281
(18,54,31)	177	116.97	2.000	177.23	0.008	150.93	0.869
(18,55,29)	127	113.91	0.436	127.44	0.015	132.91	0.197
(18,55,30)	169	117.10	1.730	168.98	0.001	169.42	0.014
(18,55,31)	145	115.28	0.990	144.92	0.003	144.92	0.003
(19,19,53)	105	112.25	0.242	105.24	0.008	113.08	0.269
(19,19,54)	150	116.56	1.114	150.20	0.007	150.21	0.007
(19,19,55)	112	124.75	0.425	111.69	0.010	126.18	0.472
(19,20,53)	112	113.44	0.048	112.10	0.003	125.91	0.463
(19,20,54)	152	116.73	1.175	151.97	0.001	154.96	0.099
(19,20,55)	129	121.57	0.248	129.11	0.004	122.62	0.213
(19,21,53)	133	117.25	0.525	133.36	0.012	122.03	0.365
(19,21,54)	172	116.63	1.845	171.74	0.009	137.57	1.147
(19,21,55)	157	118.38	1.287	156.87	0.004	122.19	1.160

File: dat0102; composite variograms, mri phantom validation data

Enh-Res Coord.	Phant. Value	Trilinear		Kriging, cdv=50		Kriging, cdv=60	
		Estimat	Proj Err	Estimate	Proj Err	Estimate	Proj Err
(19,45,55)	77	76.75	0.008	76.74	0.009	75.64	0.045
(19,46,55)	94	90.44	0.119	93.50	0.017	99.65	0.188
(19,47,55)	106	105.38	0.021	105.69	0.010	105.92	0.003
(19,53,29)	121	119.38	0.054	121.20	0.007	120.94	0.002
(19,53,30)	115	118.57	0.119	114.77	0.008	124.88	0.329
(19,53,31)	120	118.50	0.050	119.77	0.008	120.96	0.032
(19,54,29)	148	112.43	1.185	147.58	0.014	149.21	0.040
(19,54,30)	170	114.68	1.844	170.42	0.014	163.49	0.217
(19,54,31)	144	114.91	0.969	143.81	0.006	156.00	0.400
(19,55,29)	112	110.38	0.054	111.70	0.010	111.87	0.004
(19,55,30)	132	112.31	0.656	132.13	0.004	132.13	0.004
(19,55,31)	118	116.75	0.042	117.99	0.000	117.76	0.008
(20,19,53)	121	100.87	0.671	120.80	0.007	115.54	0.182
(20,19,54)	165	114.52	1.682	164.95	0.002	174.74	0.325
(20,19,55)	135	123.23	0.392	135.17	0.005	132.17	0.094
(20,20,53)	126	108.02	0.599	126.30	0.010	132.82	0.227
(20,20,55)	137	125.74	0.375	137.44	0.015	146.46	0.315
(20,21,53)	123	111.38	0.387	123.14	0.005	129.32	0.210
(20,21,54)	142	115.56	0.881	141.78	0.007	142.33	0.011
(20,21,55)	131	122.28	0.291	131.21	0.007	131.21	0.007
(21,19,53)	102	92.13	0.329	101.77	0.008	109.07	0.236
(21,19,54)	126	107.07	0.631	126.30	0.010	118.00	0.267
(21,19,55)	113	123.25	0.342	113.26	0.009	125.46	0.415
(21,20,53)	124	98.35	0.855	123.80	0.007	114.35	0.322
(21,20,54)	154	113.38	1.354	153.92	0.003	156.68	0.089
(21,20,55)	128	123.98	0.134	127.68	0.011	136.29	0.276
(21,21,53)	113	107.88	0.171	112.91	0.003	110.39	0.087
(21,21,54)	96	116.63	0.688	96.48	0.016	131.13	1.170
(21,21,55)	125	127.25	0.075	124.92	0.003	129.64	0.155
(21,39,41)	109	109.13	0.004	108.72	0.009	107.25	0.058
(21,39,42)	150	109.57	1.347	150.20	0.007	150.68	0.023
(21,39,43)	111	115.88	0.162	110.99	0.000	116.42	0.181
(21,40,41)	138	115.81	0.739	138.12	0.004	148.72	0.357
(21,40,42)	193	119.02	2.465	193.28	0.009	178.25	0.492
(21,40,43)	138	122.75	0.508	138.10	0.003	140.59	0.086
(21,41,41)	126	125.88	0.004	125.92	0.003	125.20	0.027
(21,41,42)	177	125.71	1.709	176.82	0.006	171.55	0.182
(21,41,43)	131	131.88	0.029	131.27	0.009	131.27	0.009
(21,49,41)	104	107.88	0.129	103.76	0.008	108.22	0.141
(21,49,42)	166	121.71	1.476	165.50	0.017	147.68	0.610
(21,49,43)	134	140.88	0.229	133.53	0.016	140.91	0.230
(21,50,41)	122	116.65	0.178	121.95	0.002	129.70	0.257
(21,50,42)	184	125.92	1.935	184.25	0.008	178.42	0.186
(21,50,43)	136	133.59	0.080	135.90	0.003	144.23	0.274
(21,51,41)	126	127.38	0.046	126.02	0.001	127.81	0.060
(21,51,42)	153	125.69	0.910	153.32	0.011	152.98	0.001
(21,51,43)	130	127.63	0.079	130.47	0.016	130.06	0.002
(22,39,41)	130	127.50	0.083	130.47	0.016	124.28	0.190
(22,39,42)	177	133.56	1.448	177.38	0.013	177.18	0.006

File: dat0102; composite variograms, mri phantom validation data

Enh-Res Coord.	Phant. Value	Trilinear		Kriging, cdv=50		Kriging, cdv=60	
		Estimat	Proj Err	Estimate	Proj Err	Estimate	Proj Err
(22,39,43)	157	150.79	0.207	156.99	0.000	157.43	0.014
(22,40,41)	165	127.67	1.244	165.39	0.013	165.16	0.005
(22,40,43)	183	145.93	1.235	182.65	0.012	184.32	0.044
(22,41,41)	159	129.79	0.973	159.25	0.008	159.31	0.010
(22,41,42)	243	134.91	3.602	243.42	0.014	240.85	0.072
(22,41,43)	162	142.48	0.650	161.51	0.016	165.86	0.129
(22,49,41)	115	121.05	0.202	114.60	0.013	115.07	0.002
(22,49,42)	199	128.88	2.337	199.22	0.007	190.25	0.292
(22,49,43)	179	140.54	1.282	178.61	0.013	178.61	0.013
(22,50,41)	125	123.01	0.066	125.44	0.015	128.94	0.131
(22,50,43)	181	137.24	1.458	181.08	0.003	191.72	0.357
(22,51,41)	143	129.66	0.444	143.15	0.005	115.60	0.913
(22,51,42)	197	131.60	2.179	197.43	0.014	201.57	0.152
(22,51,43)	165	133.37	1.054	164.76	0.008	164.81	0.006
(23,37,41)	116	116.13	0.004	116.05	0.002	116.05	0.002
(23,37,42)	152	139.29	0.424	152.39	0.013	152.39	0.013
(23,37,43)	165	165.13	0.004	164.87	0.004	164.87	0.004
(23,38,41)	130	130.96	0.032	130.34	0.011	134.74	0.158
(23,38,42)	179	147.95	1.035	178.54	0.015	183.72	0.157
(23,38,43)	177	175.69	0.044	176.72	0.009	178.04	0.035
(23,39,41)	152	146.38	0.187	152.10	0.003	146.49	0.184
(23,39,42)	223	162.11	2.029	223.40	0.013	226.53	0.118
(23,39,43)	187	186.50	0.017	187.43	0.014	187.50	0.017
(23,40,41)	149	141.16	0.261	149.49	0.016	164.82	0.527
(23,40,42)	263	152.39	3.686	262.77	0.008	269.38	0.213
(23,40,43)	187	169.71	0.576	186.91	0.003	211.19	0.806
(23,41,41)	130	138.13	0.271	130.22	0.007	138.47	0.282
(23,41,42)	218	140.97	2.567	218.15	0.005	232.66	0.488
(23,41,43)	157	156.38	0.021	156.99	0.000	156.61	0.013
(23,49,41)	135	133.25	0.058	134.95	0.002	135.03	0.001
(23,49,42)	184	135.68	1.610	184.38	0.013	185.90	0.063
(23,49,43)	163	145.25	0.591	163.22	0.007	145.93	0.569
(23,50,41)	137	129.58	0.247	136.86	0.005	161.14	0.804
(23,50,42)	224	134.30	2.989	224.22	0.007	232.56	0.285
(23,50,43)	161	142.68	0.611	161.27	0.009	165.26	0.142
(23,51,41)	126	129.75	0.125	125.51	0.016	134.81	0.294
(23,51,42)	204	131.91	2.402	203.59	0.014	206.23	0.074
(23,51,43)	149	143.13	0.196	149.07	0.002	145.11	0.130
(24,37,41)	138	109.05	0.965	138.10	0.003	132.73	0.176
(24,37,42)	187	129.67	1.910	187.10	0.003	187.21	0.007
(24,37,43)	192	150.14	1.395	191.71	0.010	191.22	0.026
(24,38,41)	173	123.56	1.648	172.62	0.013	170.04	0.099
(24,38,43)	221	160.50	2.016	220.98	0.001	221.79	0.026
(24,39,41)	165	133.57	1.047	165.48	0.016	163.37	0.054
(24,39,42)	268	148.67	3.976	267.55	0.015	263.44	0.152
(24,39,43)	229	165.21	2.126	229.22	0.007	231.34	0.078
(25,37,41)	109	105.25	0.125	108.77	0.008	105.24	0.125
(25,37,42)	133	121.03	0.399	132.77	0.008	140.35	0.245
(25,37,43)	142	140.13	0.062	141.88	0.004	142.20	0.007

File: dat0102; composite variograms, mri phantom validation data

Enh-Res Coord.	Phant. Value	Trilinear		Kriging, cdv=50		Kriging, cdv=60	
		Estimat	Proj Err	Estimate	Proj Err	Estimate	Proj Err
(25,38,41)	126	113.93	0.402	126.44	0.015	127.28	0.043
(25,38,42)	162	127.40	1.153	161.93	0.002	166.60	0.153
(25,38,43)	149	145.11	0.130	149.41	0.014	148.97	0.001
(25,39,41)	127	124.50	0.083	126.76	0.008	124.68	0.077
(25,39,42)	171	134.48	1.217	171.36	0.012	169.25	0.058
(25,39,43)	152	150.75	0.042	151.72	0.009	151.28	0.024
(25,41,51)	139	136.75	0.075	138.64	0.012	137.76	0.041
(25,41,52)	162	126.94	1.168	161.98	0.001	162.47	0.016
(25,41,53)	123	121.75	0.042	122.81	0.006	122.81	0.006
(25,42,51)	152	126.11	0.863	152.27	0.009	152.43	0.014
(25,42,52)	190	123.83	2.205	189.65	0.012	171.31	0.623
(25,42,53)	125	121.40	0.120	125.34	0.011	125.34	0.011
(25,43,51)	100	118.88	0.629	99.73	0.009	119.80	0.660
(25,43,52)	150	118.10	1.063	149.51	0.016	149.50	0.017
(25,43,53)	122	121.50	0.017	121.67	0.011	121.67	0.011
(25,53,41)	132	133.38	0.046	131.99	0.000	134.42	0.081
(25,53,42)	150	141.22	0.293	150.37	0.012	151.25	0.041
(25,53,43)	151	150.38	0.021	151.40	0.013	151.52	0.017
(25,54,41)	155	140.44	0.485	154.86	0.005	154.86	0.005
(25,54,42)	163	140.44	0.752	163.19	0.006	163.24	0.008
(25,54,43)	156	148.03	0.265	156.12	0.004	156.12	0.004
(25,55,41)	156	149.25	0.225	155.87	0.004	151.27	0.158
(25,55,42)	175	145.22	0.992	174.75	0.008	171.51	0.116
(25,55,43)	148	146.63	0.046	148.44	0.015	148.44	0.015
(26,41,51)	187	142.07	1.497	186.53	0.016	186.53	0.016
(26,41,52)	212	134.61	2.579	212.22	0.007	234.25	0.741
(26,41,53)	144	120.01	0.800	144.02	0.001	144.21	0.007
(26,42,51)	224	131.21	3.092	224.37	0.012	178.35	1.521
(26,42,53)	169	118.96	1.667	169.17	0.005	159.07	0.331
(26,43,51)	136	115.29	0.690	135.84	0.005	146.56	0.352
(26,43,52)	202	117.93	2.802	202.09	0.003	202.09	0.003
(26,43,53)	171	117.53	1.782	170.53	0.016	170.53	0.016
(26,53,41)	176	138.19	1.260	175.72	0.009	175.72	0.009
(26,53,42)	190	147.29	1.423	189.74	0.009	193.29	0.110
(26,53,43)	199	163.17	1.194	199.21	0.007	196.88	0.071
(26,54,41)	202	140.74	2.041	201.93	0.002	201.93	0.002
(26,54,43)	212	155.64	1.878	211.76	0.008	211.93	0.002
(26,55,41)	185	139.76	1.507	185.00	0.000	185.00	0.000
(26,55,42)	224	141.88	2.736	224.33	0.011	224.33	0.011
(26,55,43)	183	147.67	1.177	182.84	0.005	182.84	0.005
(27,41,51)	154	153.25	0.025	154.49	0.016	154.49	0.016
(27,41,52)	175	136.44	1.285	174.97	0.001	149.73	0.842
(27,41,53)	129	121.38	0.254	129.31	0.010	123.36	0.188
(27,42,51)	154	133.66	0.678	153.68	0.011	144.88	0.304
(27,42,52)	146	127.03	0.632	145.58	0.014	146.43	0.014
(27,42,53)	154	120.48	1.117	154.34	0.011	124.75	0.975
(27,43,51)	116	116.63	0.021	116.03	0.001	116.03	0.001
(27,43,52)	108	118.35	0.345	108.05	0.002	121.49	0.450
(27,43,53)	125	120.63	0.146	125.27	0.009	121.47	0.118

File: dat0102; composite variograms, mri phantom validation data

Enh-Res Coord.	Phant. Value	Trilinear		Kriging, cdv=50		Kriging, cdv=60	
		Estimat	Proj Err	Estimate	Proj Err	Estimate	Proj Err
(27,53,41)	149	147.88	0.037	148.92	0.003	148.56	0.015
(27,53,42)	194	161.77	1.074	193.57	0.014	218.08	0.802
(27,53,43)	182	180.63	0.046	181.67	0.011	181.67	0.011
(27,54,41)	167	140.42	0.886	166.86	0.005	160.11	0.230
(27,54,42)	208	148.85	1.971	207.52	0.016	209.17	0.039
(27,54,43)	191	165.10	0.863	191.14	0.005	192.01	0.034
(27,55,41)	136	136.50	0.017	135.72	0.009	138.50	0.083
(27,55,42)	189	141.67	1.577	189.49	0.016	182.99	0.200
(27,55,43)	154	153.25	0.025	154.37	0.012	154.37	0.012
(29,47,47)	118	118.63	0.021	118.24	0.008	118.24	0.008
(29,47,48)	115	111.23	0.126	115.41	0.014	116.69	0.056
(29,47,49)	105	104.50	0.017	105.06	0.002	105.07	0.002
(29,48,47)	128	128.25	0.008	128.14	0.005	127.74	0.009
(29,48,48)	152	118.39	1.120	152.35	0.012	152.35	0.012
(29,48,49)	132	109.46	0.751	131.53	0.016	145.79	0.459
(29,49,47)	140	140.63	0.021	139.81	0.006	140.47	0.016
(29,49,48)	152	127.82	0.806	151.91	0.003	157.44	0.181
(29,49,49)	122	119.25	0.092	122.03	0.001	119.73	0.076
(30,47,47)	122	115.22	0.226	121.92	0.003	137.58	0.519
(30,47,48)	131	107.98	0.767	131.20	0.006	132.81	0.060
(30,47,49)	113	99.20	0.460	113.36	0.012	113.36	0.012
(30,48,47)	163	121.89	1.370	163.22	0.007	152.00	0.367
(30,48,49)	178	111.13	2.228	177.76	0.008	142.97	1.167
(30,49,47)	173	132.55	1.348	172.56	0.015	157.26	0.525
(30,49,48)	213	127.49	2.849	212.52	0.016	218.06	0.169
(30,49,49)	143	120.33	0.755	143.19	0.006	143.19	0.006
(31,47,47)	106	114.88	0.296	106.21	0.007	113.80	0.260
(31,47,48)	100	105.69	0.190	100.04	0.001	99.26	0.025
(31,47,49)	96	95.75	0.008	95.88	0.004	95.88	0.004
(31,48,47)	133	120.42	0.419	132.57	0.014	119.61	0.446
(31,48,48)	145	116.19	0.960	144.68	0.011	145.84	0.028
(31,48,49)	109	108.35	0.022	109.28	0.009	143.30	1.143
(31,49,47)	128	128.75	0.025	127.74	0.009	127.74	0.009
(31,49,48)	141	125.71	0.509	140.86	0.005	147.54	0.218
(31,49,49)	126	125.63	0.012	125.63	0.012	125.63	0.012
(33,33,55)	121	104.25	0.558	121.28	0.009	103.33	0.589
(33,34,55)	158	104.13	1.795	158.15	0.005	113.34	1.488
(33,35,55)	111	110.75	0.008	110.99	0.000	110.24	0.025
(33,51,17)	88	94.63	0.221	88.28	0.009	95.11	0.237
(33,51,18)	130	98.35	1.055	129.84	0.005	120.76	0.308
(33,51,19)	111	105.00	0.200	111.31	0.010	97.28	0.457
(33,52,17)	126	94.27	1.057	126.47	0.016	145.95	0.665
(33,52,18)	156	99.36	1.888	155.78	0.007	148.82	0.239
(33,52,19)	113	103.05	0.332	113.15	0.005	116.34	0.111
(33,53,17)	119	98.50	0.683	119.25	0.008	99.98	0.634
(33,53,18)	126	99.30	0.890	126.30	0.010	126.29	0.010
(33,53,19)	103	103.00	0.000	102.82	0.006	103.60	0.020
(33,55,41)	116	116.25	0.008	115.83	0.006	115.83	0.006
(33,55,42)	188	136.13	1.728	187.77	0.008	194.61	0.220

File: dat0102; composite variograms, mri phantom validation data

Enh-Res Coord.	Phant. Value	Trilinear		Kriging, cdv=50		Kriging, cdv=60	
		Estimat	Proj Err	Estimate	Proj Err	Estimate	Proj Err
(33,55,43)	159	163.13	0.137	159.33	0.011	163.01	0.134
(34,33,55)	116	93.89	0.737	115.92	0.003	115.92	0.003
(34,34,55)	140	101.75	1.275	139.62	0.013	139.62	0.013
(34,35,55)	142	108.69	1.110	142.14	0.005	142.14	0.005
(34,51,17)	100	94.12	0.196	99.65	0.012	99.63	0.012
(34,51,18)	146	97.79	1.606	146.15	0.005	147.26	0.042
(34,51,19)	113	100.07	0.431	112.76	0.008	140.89	0.929
(34,52,17)	141	98.90	1.403	140.91	0.003	139.80	0.040
(34,52,19)	141	100.23	1.359	141.27	0.009	129.22	0.393
(34,53,17)	134	98.37	1.187	133.54	0.015	133.54	0.015
(34,53,18)	169	101.41	2.252	168.52	0.016	178.77	0.325
(34,53,19)	130	96.89	1.103	129.67	0.011	130.03	0.001
(34,55,41)	162	127.67	1.144	162.38	0.012	165.72	0.124
(34,55,42)	293	144.79	4.939	293.47	0.016	278.14	0.495
(34,55,43)	198	159.17	1.294	197.77	0.008	201.58	0.119
(35,33,55)	86	86.63	0.021	85.61	0.013	85.23	0.026
(35,34,55)	106	95.65	0.345	105.55	0.015	105.55	0.015
(35,35,55)	110	111.13	0.037	110.29	0.010	110.29	0.010
(35,51,17)	159	94.38	2.153	158.56	0.015	94.78	2.140
(35,51,18)	121	93.01	0.933	121.35	0.012	129.44	0.281
(35,51,19)	128	96.50	1.050	127.50	0.017	96.21	1.059
(35,52,17)	111	97.83	0.439	110.62	0.013	108.86	0.071
(35,52,18)	167	99.67	2.244	166.74	0.009	158.86	0.271
(35,52,19)	101	95.44	0.185	101.07	0.002	102.82	0.061
(35,53,17)	104	102.88	0.037	104.14	0.005	103.64	0.012
(35,53,18)	113	97.70	0.510	113.00	0.000	118.50	0.183
(35,53,19)	96	95.25	0.025	95.71	0.010	95.71	0.010
(35,55,41)	131	145.50	0.483	131.16	0.005	147.48	0.549
(35,55,42)	237	150.17	2.893	236.64	0.012	225.86	0.371
(35,55,43)	166	162.13	0.129	166.10	0.003	163.82	0.073
(37, 9,53)	103	102.75	0.008	102.88	0.004	102.88	0.004
(37, 9,54)	145	99.38	1.520	144.60	0.013	138.83	0.206
(37, 9,55)	102	101.25	0.025	101.55	0.015	103.20	0.040
(37,10,53)	105	105.46	0.015	105.10	0.003	105.05	0.002
(37,10,54)	149	103.71	1.509	148.86	0.005	154.13	0.171
(37,10,55)	111	107.03	0.132	111.37	0.012	107.49	0.117
(37,11,53)	109	109.75	0.025	109.42	0.014	109.42	0.014
(37,11,54)	149	108.53	1.348	148.79	0.007	149.36	0.012
(37,11,55)	110	113.38	0.112	110.44	0.015	113.35	0.112
(37,23,27)	128	101.50	0.883	128.07	0.002	101.66	0.878
(37,23,28)	120	91.49	0.950	120.41	0.014	117.74	0.075
(37,23,29)	85	85.00	0.000	85.28	0.009	85.44	0.014
(37,24,27)	124	107.34	0.555	123.54	0.015	156.99	1.099
(37,24,28)	151	95.99	1.833	151.46	0.015	144.72	0.209
(37,24,29)	101	84.56	0.548	101.07	0.002	98.90	0.070
(37,25,27)	105	117.25	0.408	104.74	0.009	120.95	0.532
(37,25,28)	102	100.55	0.048	101.86	0.005	125.24	0.775
(37,25,29)	88	86.75	0.042	88.00	0.000	87.19	0.027
(37,41,45)	172	170.13	0.062	172.46	0.015	171.38	0.021

File: dat0102; composite variograms, mri phantom validation data

Enh-Res Coord.	Phant. Value	Trilinear		Kriging, cdv=50		Kriging, cdv=60	
		Estimat	Proj Err	Estimate	Proj Err	Estimate	Proj Err
(37,41,46)	210	149.29	2.023	210.19	0.006	208.23	0.059
(37,41,47)	139	136.25	0.092	138.80	0.007	136.99	0.067
(37,42,45)	186	153.66	1.078	185.63	0.012	189.21	0.107
(37,42,46)	232	143.75	2.941	231.83	0.006	231.67	0.011
(37,42,47)	157	138.46	0.618	157.00	0.000	157.00	0.000
(37,43,45)	144	142.63	0.046	143.85	0.005	143.86	0.005
(37,43,46)	190	139.51	1.682	190.23	0.008	190.23	0.008
(37,43,47)	144	143.13	0.029	144.00	0.000	144.00	0.000
(38, 9,53)	121	98.64	0.745	120.52	0.016	120.52	0.016
(38, 9,54)	192	99.12	3.095	192.39	0.013	185.74	0.209
(38, 9,55)	112	94.97	0.568	112.34	0.011	112.34	0.011
(38,10,53)	150	103.13	1.562	149.71	0.010	129.63	0.679
(38,10,55)	146	102.27	1.457	145.88	0.004	129.00	0.566
(38,11,53)	138	104.70	1.110	137.71	0.010	128.85	0.305
(38,11,54)	193	107.17	2.860	192.74	0.009	203.23	0.341
(38,11,55)	123	106.43	0.552	123.20	0.007	134.27	0.376
(38,23,27)	147	103.62	1.446	147.29	0.010	144.83	0.072
(38,23,28)	187	95.07	3.063	186.60	0.013	187.01	0.000
(38,23,29)	116	84.44	1.052	115.91	0.003	122.22	0.207
(38,24,27)	186	107.32	2.622	185.86	0.005	182.47	0.118
(38,24,29)	142	87.48	1.817	141.94	0.002	130.74	0.375
(38,25,27)	158	105.92	1.736	158.29	0.010	158.84	0.028
(38,25,28)	175	97.67	2.577	174.58	0.014	178.57	0.119
(38,25,29)	95	87.82	0.239	95.30	0.010	129.37	1.145
(38,41,45)	184	171.34	0.422	184.16	0.005	184.93	0.031
(38,41,46)	214	145.32	2.289	213.96	0.001	219.88	0.196
(38,41,47)	125	120.38	0.154	124.61	0.013	129.32	0.144
(38,42,45)	209	156.42	1.752	209.34	0.011	197.14	0.395
(38,42,47)	156	121.39	1.153	155.50	0.017	143.17	0.428
(38,43,45)	168	143.12	0.829	167.71	0.010	168.06	0.002
(38,43,46)	203	131.37	2.387	202.96	0.001	202.32	0.023
(38,43,47)	151	122.28	0.957	150.95	0.002	141.31	0.323
(39, 9,53)	97	97.50	0.017	97.05	0.001	97.05	0.001
(39, 9,54)	122	92.22	0.992	122.01	0.000	122.01	0.000
(39, 9,55)	90	91.00	0.033	90.40	0.013	90.40	0.013
(39,10,53)	109	98.80	0.340	109.34	0.011	97.70	0.377
(39,10,54)	139	96.52	1.416	139.03	0.001	137.21	0.060
(39,10,55)	124	96.58	0.914	124.42	0.014	97.21	0.893
(39,11,53)	101	103.00	0.067	100.92	0.003	101.61	0.020
(39,11,54)	131	101.03	0.999	130.99	0.000	130.83	0.006
(39,11,55)	101	103.25	0.075	101.05	0.001	102.70	0.057
(39,23,27)	113	111.25	0.058	112.64	0.012	109.92	0.103
(39,23,28)	147	97.85	1.638	146.90	0.003	129.23	0.592
(39,23,29)	129	88.75	1.341	129.41	0.014	88.27	1.357
(39,24,27)	122	105.27	0.558	122.34	0.011	122.20	0.007
(39,24,28)	151	97.87	1.771	151.39	0.013	148.34	0.089
(39,24,29)	94	91.14	0.095	94.23	0.008	102.83	0.294
(39,25,27)	102	101.63	0.012	101.57	0.014	101.59	0.014
(39,25,28)	155	96.13	1.962	155.00	0.000	124.08	1.030

File: dat0102; composite variograms, mri phantom validation data

Enh-Res Coord.	Phant. Value	Trilinear		Kriging, cdv=50		Kriging, cdv=60	
		Estimat	Proj Err	Estimate	Proj Err	Estimate	Proj Err
(39,25,29)	120	94.38	0.854	120.31	0.010	95.00	0.833
(39,25,35)	109	108.88	0.004	109.15	0.005	109.07	0.002
(39,25,36)	138	112.58	0.847	138.09	0.003	140.40	0.080
(39,25,37)	121	120.00	0.033	121.16	0.005	121.03	0.001
(39,26,35)	104	102.19	0.060	103.63	0.012	102.66	0.045
(39,26,36)	145	106.67	1.277	144.92	0.003	146.01	0.034
(39,26,37)	123	111.26	0.391	122.63	0.012	112.17	0.361
(39,27,35)	91	98.50	0.250	91.49	0.016	99.18	0.273
(39,27,36)	129	99.94	0.968	128.60	0.013	116.86	0.405
(39,27,37)	170	104.00	2.199	169.96	0.001	103.76	2.207
(39,41,45)	182	174.25	0.258	181.60	0.013	175.00	0.233
(39,41,46)	176	137.33	1.289	176.49	0.016	176.49	0.016
(39,41,47)	108	105.63	0.079	108.40	0.013	105.97	0.068
(39,42,45)	194	158.14	1.195	194.27	0.009	197.70	0.123
(39,42,46)	198	129.49	2.283	197.74	0.009	198.81	0.027
(39,42,47)	110	103.36	0.221	109.57	0.014	125.24	0.508
(39,43,45)	152	146.88	0.171	151.70	0.010	152.07	0.002
(39,43,46)	158	123.05	1.165	158.38	0.013	158.38	0.013
(39,43,47)	101	104.00	0.100	101.40	0.013	104.02	0.101
(39,47,35)	91	91.88	0.029	91.26	0.009	91.26	0.009
(39,47,36)	122	106.34	0.522	121.58	0.014	129.24	0.241
(39,47,37)	120	124.00	0.133	120.50	0.017	122.22	0.074
(39,48,35)	98	90.05	0.265	97.60	0.013	89.84	0.272
(39,48,36)	160	103.00	1.900	160.18	0.006	159.06	0.031
(39,48,37)	146	116.97	0.967	145.64	0.012	149.09	0.103
(39,49,35)	93	92.88	0.004	92.59	0.014	92.37	0.021
(39,49,36)	119	103.27	0.524	119.35	0.012	119.35	0.012
(39,49,37)	143	115.88	0.904	142.87	0.004	126.47	0.551
(39,49,39)	148	124.00	0.800	148.10	0.003	131.44	0.552
(39,49,40)	127	117.58	0.314	127.44	0.015	135.11	0.270
(39,49,41)	114	113.63	0.012	114.16	0.005	116.75	0.092
(39,50,39)	153	136.51	0.549	153.43	0.014	108.07	1.497
(39,50,40)	155	134.88	0.670	155.45	0.015	166.18	0.373
(39,50,41)	118	130.00	0.400	117.60	0.013	122.30	0.143
(39,51,39)	144	146.38	0.079	144.21	0.007	141.37	0.088
(39,51,40)	185	142.19	1.427	184.84	0.005	179.27	0.191
(39,51,41)	175	142.63	1.079	174.87	0.004	164.29	0.357
(40,25,35)	144	105.37	1.287	143.68	0.011	143.55	0.015
(40,25,36)	207	114.96	3.067	207.17	0.006	215.27	0.276
(40,25,37)	144	117.39	0.887	144.23	0.008	135.90	0.270
(40,26,35)	173	104.31	2.289	172.91	0.003	172.40	0.020
(40,26,37)	172	116.40	1.853	172.39	0.013	142.61	0.979
(40,27,35)	138	101.93	1.202	138.19	0.006	140.55	0.085
(40,27,36)	177	109.47	2.250	177.34	0.011	182.81	0.194
(40,27,37)	134	111.02	0.766	134.43	0.014	129.93	0.136
(40,47,35)	119	102.52	0.549	119.07	0.002	116.79	0.074
(40,47,36)	197	115.74	2.708	197.26	0.009	186.89	0.337
(40,47,37)	166	129.41	1.219	165.74	0.009	185.33	0.644
(40,48,35)	138	98.06	1.331	137.82	0.006	133.25	0.158

F-13

File: dat0102; composite variograms, mri phantom validation data

Enh-Res Coord.	Phant. Value	Trilinear		Kriging, cdv=50		Kriging, cdv=60	
		Estimat	Proj Err	Estimate	Proj Err	Estimate	Proj Err
(40,48,37)	246	127.68	3.943	245.52	0.016	203.28	1.424
(40,49,35)	90	96.54	0.218	90.50	0.017	106.15	0.538
(40,49,36)	141	109.79	1.040	141.49	0.016	141.38	0.012
(40,49,37)	150	122.69	0.910	149.70	0.010	145.40	0.153
(40,49,39)	150	131.87	0.604	149.53	0.016	149.90	0.003
(40,49,40)	144	117.71	0.876	144.27	0.009	141.09	0.097
(40,49,41)	113	107.51	0.183	113.36	0.012	113.36	0.012
(40,50,39)	167	135.20	1.060	166.94	0.002	167.02	0.001
(40,50,41)	133	118.77	0.474	133.38	0.013	131.96	0.035
(40,51,39)	151	139.66	0.378	150.77	0.008	176.67	0.856
(40,51,40)	210	132.55	2.581	210.14	0.005	206.43	0.119
(40,51,41)	154	124.68	0.977	153.84	0.005	157.35	0.112
(41,19,55)	121	120.38	0.021	121.02	0.001	120.01	0.033
(41,20,55)	133	108.47	0.818	133.09	0.003	129.33	0.122
(41,21,55)	83	99.88	0.562	82.77	0.008	99.36	0.545
(41,25,35)	106	107.00	0.033	106.29	0.010	107.42	0.047
(41,25,36)	131	111.36	0.655	131.04	0.001	131.04	0.001
(41,25,37)	118	118.38	0.012	118.11	0.004	117.81	0.006
(41,26,35)	107	106.72	0.009	107.49	0.016	124.24	0.575
(41,26,36)	149	110.14	1.295	148.68	0.011	148.23	0.026
(41,26,37)	144	117.56	0.881	144.13	0.004	123.65	0.678
(41,27,35)	111	110.13	0.029	110.88	0.004	110.80	0.007
(41,27,36)	160	114.18	1.527	159.52	0.016	138.47	0.717
(41,27,37)	80	121.25	1.375	79.83	0.006	119.54	1.318
(41,47,35)	115	116.25	0.042	115.45	0.015	115.63	0.021
(41,47,36)	162	127.52	1.149	161.84	0.005	153.74	0.275
(41,47,37)	142	142.38	0.012	142.09	0.003	142.36	0.012
(41,47,49)	133	131.50	0.050	132.64	0.012	132.04	0.032
(41,47,50)	156	116.28	1.323	155.65	0.012	112.99	1.433
(41,47,51)	94	100.63	0.221	93.96	0.001	101.86	0.262
(41,48,35)	116	105.80	0.340	115.91	0.003	112.72	0.109
(41,48,36)	172	121.80	1.673	172.08	0.002	178.16	0.205
(41,48,37)	138	135.13	0.096	138.19	0.006	174.96	1.232
(41,48,49)	129	141.66	0.422	129.28	0.009	154.50	0.850
(41,48,50)	137	123.86	0.438	136.54	0.015	135.37	0.054
(41,48,51)	110	103.23	0.226	110.14	0.005	111.31	0.044
(41,49,35)	108	101.88	0.204	108.07	0.002	100.78	0.241
(41,49,36)	115	117.27	0.076	115.15	0.005	120.13	0.171
(41,49,37)	121	133.13	0.404	120.58	0.014	133.94	0.431
(41,49,39)	151	141.88	0.304	150.92	0.003	143.52	0.249
(41,49,40)	180	120.83	1.972	179.65	0.012	134.63	1.512
(41,49,41)	99	102.13	0.104	98.56	0.015	102.79	0.126
(41,49,49)	154	153.38	0.021	154.02	0.001	155.73	0.058
(41,49,50)	155	129.54	0.848	155.07	0.002	138.04	0.565
(41,49,51)	107	106.88	0.004	107.40	0.013	107.40	0.013
(41,50,39)	143	138.74	0.142	142.73	0.009	155.68	0.422
(41,50,40)	172	124.36	1.588	172.39	0.013	149.40	0.753
(41,50,41)	134	106.71	0.909	133.86	0.005	106.66	0.911
(41,51,39)	139	137.88	0.037	138.67	0.011	138.67	0.011

File: dat0102; composite variograms, mri phantom validation data

Enh-Res Coord.	Phant. Value	Trilinear		Kriging, cdv=50		Kriging, cdv=60	
		Estimat	Proj Err	Estimate	Proj Err	Estimate	Proj Err
(41,51,40)	139	123.28	0.524	138.96	0.001	140.73	0.058
(41,51,41)	114	111.00	0.100	114.41	0.014	112.08	0.064
(42,19,55)	164	114.30	1.656	163.78	0.007	160.17	0.128
(42,20,55)	201	111.10	2.996	200.63	0.012	200.23	0.026
(42,21,55)	136	101.84	1.138	136.31	0.010	139.29	0.110
(42,47,49)	177	129.18	1.594	176.92	0.003	166.38	0.354
(42,47,50)	141	111.63	0.979	140.51	0.016	141.74	0.025
(42,47,51)	108	95.54	0.415	108.10	0.003	111.67	0.122
(42,48,49)	184	138.58	1.513	184.09	0.003	175.10	0.297
(42,48,51)	124	98.05	0.865	124.00	0.000	117.24	0.225
(42,49,49)	183	146.44	1.218	183.09	0.003	179.68	0.111
(42,49,50)	186	124.70	2.043	185.80	0.007	185.32	0.023
Mean			0.795		0.009		0.198
Std. Dev.			0.805		0.005		0.314
Max			4.939		0.017		2.207

Appendix G

BIBLIOGRAPHY

Appendix G

BIBLIOGRAPHY

[Beal84]   Beall, Paula T.; Sharad R. Amtey and Sitapati R. Kusturi, *NMR Data Handbook for Biomedical Applications*, Pergamon Press: New York, 1984.

[Bo90]   Bo, Wolfman, Krueger and Meschan, *Basic Atlas of Sectional Anatomy*, Philadelphia: W.B. Saunders Company, 1990.

[Brod91]   Brodkin, Christopher, "The Application of Kriging for Controlled Minimization of Large Data Sets," Masters Thesis, College of Engineering, Air Force Institute of Technology, December 1991.

[Bush94]   Bushberg, Jerrold T.; J. Anthony Seibert; Edwin M. Leidholdt, Jr. and John M. Boone; *The Essential Physics of Medical Imaging*, Williams & Wilkins: Baltimore, 1994.

[Carr80]   Carr, James R., *uvkrig*, public domain software, University of Nevado - Reno: Reno, Nevada, 1980.

[Chan90]   Chang, Hsuan, *Geometrical Image Transformation to Compensate for Distortions in Magnetic Resonance Imaging*, PhD Dissertation, Graduate School of Vanderbilt University, August 1990.

[Chan92]   Chang, H. and J. M. Fitzpatrick, "A Technique for Accurate MRI in the Presence of Field Inhomogeneities," *IEEE Transactions on Medical Imaging*, 11(3), September 1992, pp. 319-329.

[Clar79]   Clark, Isobel, *Practicle Geostatistics*, Elsevier Applied Science Publishers: New York, 1979.

[Clar87]   Clark, Isobel, *Practical Geostatistics*, Elsevier Applied Science: London, 1987.

[Clin88]   Cline, H.E.; W.E. Lorensen; S. Ludke; C.R. Crawford and B.C. Teeter; "Two Algorithms for the Three-Dimensional Reconstruction of Tomograms, *Medical Physics*, Vol. 15 No. 3, May/June 1988, pp. 320-327.

[Clin90]   Cline, Harvey E.; William E. Lorensen; Ron Kikinis and Ferenc Jolesz; "Three-Dimensional Segmentation of MR Images of the Head Using Probability and Connectivity," *Journal of Computer Assisted Tomography*, Vol. 14 No. 6, November/December 1990, pp. 1037-1045.

[Cook85]   Cook, N.R., "Three-way Analyses," *Exploring Data Tables, Trends, and Shapes* (edited by D.C. Hoaglin, F. Mostellar and J.W. Tukey), Wiley: New York, 1985, pp. 125-188.

[Cres88]   Cressie, Noel, "Spatial Prediction and Ordinary Kriging," *Mathematical Geology*, Vol. 20 No. 4, 1988, pp. 405-421.

[Cres89]   Cressie, Noel, "Geostatistics," *The American Statistician*, Vol. 43 No. 4, November 1989, pp. 197-202.

[Cres91]   Cressie, Noel A. C., *Statistics for Spatial Data*, John Wiley and Sons: New York, 1991.

[Davi77]   David, Michael, *Geostatistical Ore Reserve Estimation*, Elsevier Scientific Publishing Company: New York, 1977.

[Davi86]   Davis, John C., *Statistics and Data Analysis in Geology* (Second Edition), John Wiley and Sons: New York, 1986.

[DeGr89]   DeGroat, Morris, H., *Probability and Statistics* (2nd edition), Addison-Wesley Publishing Company: Reading, Massachusetts, 1989.

[Delf73]   Delfiner, P. and J.P. Delhomme, "Optimum Interpolation by Kriging," *Display and Analysis of Spatial Data*, (edited by John C. Davis and Michael J. McCullagh), John Wiley and Sons: New York, 1973, pp. 97-114.

[DeSo92]   DeSoto, L.A., D.R. Haynor and Y. Kim, "Three-dimensional Model for Magnetic Resonance Images", *Image Capture, Formatting and Display*, SPIE Vol. 1653, 1992.

[Deut92]   Deut92, Clayton V. and Andre G. Journel, *GSLIB Geostatistical Software Library and Users Guide*, Oxford University Press: Oxford, 1992.

[Duck91]   Duckett, Donald P., Jr., "The Application of Statistical Estimation Techniques to Terrain Modeling," Masters Thesis, College of Engineering, Air Force Institute of Technology, December 1991.

[Feig86]   Feig, Ephraim, Fred Greenleaf and Mark Perlin, "Magnetic resonance imaging with non-uniform fields," *Phys. Med. Biol.*, 31(10), 1986, pp. 1091-1099.

[Fole90]   Foley, James D.; Andries van Dam; Steven K. Feiner and John F. Hughes, *Computer Graphics* (2nd edition), Addison-Wesley Publishing Company: New York, 1990.

[Frie85]   Frieder, Gideon; Dan Gordan and R. Anthony Reynolds; "Back-to-Front Display of Voxel-Based Objects," *IEEE Computer Graphics & Applications*, Vol. 5 No. 1, January 1985, pp. 52-60.

[Gran90]   Grant, Michael, "The Application of Kriging in the Statistical Analysis of Anthropometric Data," Masters Thesis, College of Engineering, Air Force Institute of Technology, March 1990.

[Haac88]   Haacke, E. Mark and Errol M. Bellon, "Artifacts," in *Magnetic Resonance Imaging* (edited by David D. Stark and William G. Bradley), The C.V. Mosby Company: St. Louis, 1988, pp. 138-160.

[Hayt81]   Hayt, William H, Jr., *Engineering Electromagnetics*, McGraw-Hill: New York, 1981.

[Hear86]   Hearn, Donald and M. Pauline Baker, *Computer Graphics*, Prentice-Hall Inc.: Englewood Cliffs, New Jersey, 1986.

[Herm79]   Herman, G.T. and H.K. Liu, "Three-Dimensional Display of Human Organs from Computed Tomograms," *Computer Graphics and Image Processing*, Vol. 9 No. 1, January 1979, pp. 1-21.

[Hill85]   Hill, Barbara C. and Waldo S. Hinshaw, "Fundamentals of NMR Imaging," in *Three-Dimensional Biomedical Imaging, Vol. II* (edited by Richard A. Robb), CRC Press: Boca Raton, 1985, pp. 79-124.

[Hohn89]   Hohne, K.H.; M. Bomans; A. Pommert; M. Riemer; C. Schiers; U. Tiede and G. Wiebecke; "3D-Visualization of Tomographic Volume Data Using the Generalized Voxel-Model," *Chapel Hill Workshop on Volume Visualization (Conference Proceedings)*, May 1989, pp. 51-57.

[Huij73]   Huijbregts, C., "Regionalized Variables and Quantitative Analysis of Spatial Data," *Display and Analysis of Spatial Data* (edited by John C. Davis and Michael J. McCullagh), John Wiley and Sons: New York, 1973.

[Isaa89]   Isaaks, Edward H. and R. Mohan Srivastava, *Applied Geostatistics*, Oxford University Press: New York, 1989.

[ISAT94]   *ISATIS, The Geoststistical Key*, Geovariances: Avon, France, 1994.

[Jour78]   Journel, A.G. and C.J. Huijbregts, *Mining Geostatistics*, Academic Press: New York, 1978.

[Jour89]   Journel, Andre G., *Fundamentals of Geostatistics in Five Lessons*, American Geophysical Union: Washington D.C., 1989.

[Kean86]   Kean,D.M. and M.A. Smith, *Magnetic Resonance Imaging: Principles and Applications*, Williams & Wilkens: Baltimore, 1986.

[Kerb66]   Kerbs, Lynda, "GeoStatistics: The Variogram," *COGS Computer Contributions*, Vol. 12 No. 2, August 1966, pp. 54-49.

[Lai83]   Lai, Ching-Ming, "Reconstructing NMR images from projections under inhomogeneous magnetic field and nonlinear field gradients," *Phys. Med. Biol.*, 28(8), 1983, pp. 925-938.

[Leah91]   Leahy, Richard; Tom Hebert and Rae Lee; "Applications of Markov Random Fields in Medical Imaging," in *Information Processing in Medical Imaging* (edited by Douglas A. Ortendahl and Jorge Llacer), Wiley-Liss: New York, 1991, pp. 1-14.

[Levo88]   Levoy, Marc, "Display of Surfaces from Volume Data," *IEEE Computer Graphics & Applications*, Vol. 8 No. 5, May 1988, pp. 29-37.

[Levo89]   Levoy, Marc, "Display of Surfaces from Volume Data," PhD Dissertation, Department of Computer Science, University of North Carolina at Chapel Hill, May 1989.

[Lore87]   Lorensen, W.E. and H.E. Cline, "Marching Cubes: A High Resolution 3D Surface Construction Algorithm," *Computer Graphics (SIGGRAPH'87 Proceedings)*, Vol. 21 No. 3, July 1987, pp. 163-169.

[Mack84]   Mackay, R. Stuart, *Medical Images and Displays*, John Wiley & Sons: New York, 1984.

[Math63]   Matheron, G., "Principles of Geostatistics," *Economic Geology*, Vol. 58, 1963, pp. 1246-1266.

[Math89]   Matheron, Georges, *Estimating and Choosing*, Springer-Verlag: New York, 1989.

[McGe91]   McGee, Donald W., Jr., "The Application of Statistical Kriging To Improve Satellite Imagery Resolution," Masters Thesis, College of Engineering, Air Force Institute of Technology, December 1991.

[McVe85]   McVeigh, E.R.; R.M. Henkelman and M.J. Bronskill, "Noise and Filtration in Magnetic Resonance Imaging," *Medical Physics*, Vol. 12 No. 5, September/October 1985, pp. 586-590.

[Mill56]   Miller, Geroge A., "The Magical Number Seven, Plus or Minus Two: Some Limits on Our Capacity for Processing Information," *The Psychological Review*, 63(2), 1956, pp. 81-96.

[Odon85]   O'Donnell, M. and W.A. Edelstein, "NMR Imaging in the presence of magnetic field inhomogeneities and gradients field nonlinearities," *Med. Phys.*, 12(1), Jan/Feb 1985, pp. 20-26.

[Park90]   Parker, Anthony J., *Image Reconstruction in Radiology*, CRC Press: Boston, 1990.

[Parr91]   Parrott, Rob W., "Evaluation of Scalar Value Estimation Techniques for 3D Medical Imaging," Masters Thesis, College of Engineering, Air Force Institute of Technology, December 1991.

[Parr92]   Parrott, R.W.; M.R. Stytz, P. Amburn; D. Robinson; "Statistically Optimal Interslice Value Interpolation in 3D Medical Imaging: Theory and Implementation," *Proceedings of the Fifth IEEE Symposium on Computer-Based Medical Systems*, Duke, North Carolina, June 1992, pp. 276-283.

[Parr93]   Parrott, Rob W.; Martin R. Stytz; Phillip Amburn; David Robinson; "Towards Statistically Optimal Interpolation for 3-D Medical Imaging," *IEEE Engineering in Medicine and Biology*, Vol. 12 No. 3, September 1993, pp. 49-59.

[Resn89]   Resnikoff, Howard L., *The Illusion of Reality*, Springer-Verlag: New York, 1989.

[Rinc93]   Rinck, Peter A., *Magnetic Resonance in Medicine*, Blackwell Scientific Publications: Oxford, 1993.

[Rome96]   Rome Laboratory, Directorate of Command, Control and Communications, *Information for the Warrior Program Review*, Rome Laboratory, New York, August, 27 1996.

[Russ94]   Russ, John C., *The Image Processing Handbook* (2nd edition), CRC Press: Boca Raton, 1994.

[Soch88]   Sochurek, Howard, *Medicine's New Vision*, Mack Publishing Company: Easton, Pennsylvania, 1988.

[Soly79]   Solymar, L. and D. Walsh, *Lectures on the Electrical Properties of Materials*, Oxford University Press: Oxford, 1979.

[Star88]   Stark, David D. and William G. Bradley, Jr., *Magnetic Resonance Imaging*, The C.V. Mosby Company: St. Louis, 1988.

[Styt89]   Stytz, Martin R., "Three-Dimensional Image Analysis Using Local Dynamic Algorithm Selection on a Multiple-Instruction, Multiple-Data Architecture," PhD Dissertation, University of Michigan, 1989.

[Styt90]   Stytz, M.R. and O. Frieder, "Three-Dimensional Medical Imaging Modalities: An Overview," *CRC Critical Review of Biomedical Engineering*, Vol. 18 No. 1, July 1990, pp. 1-26.

[Styt91]   Stytz, M.; G. Frieder and O. Frieder, "Three-Dimensional Medical Imaging: Algorithms and Computer Systems," *ACM Computer Surveys*, Vol. 23 No. 4, December 1991.

[Styt92b]   Stytz, Martin R. and Ophir Frieder, "Volume-Primitive Based Three-Dimensional Medical Image Rendering: Customized Architectural Approaches, *Comput. & Graphics*, 16(1), 1992, pp. 85-100.

[Styt93]   Stytz, Martin R. and Rob W. Parrott, "Using Kriging for 3D Medical Imaging," *Computerized Medical Imaging and Graphics*, Vol. 17 No. 6, November-December 1993, pp. 421-442.

[Tied90]   Tiede, Ulf; Karl Heinz Hoehne; Michael Bomans; Andreas Pommert; Martin Riemer and Gunnar Wiebecke; "Investigation of Medical 3D-Rendering Algorithms," *IEEE Computer Graphics and Applications*, March 1990, pp. 41-53.

[Udup91]   Udupa, Jayaram K., "Computer Aspects of 3D Imaging in Medicine: A Tutorial," in *3D Imaging in Medicine* (edited by J.K. Udupa and G.T. Herman), CRC Press: Boston, 1991, pp. 1-69.

[Udup92]   Udupa, Jayaram K. and Odhner, Dewey, "Shell Rendering: Fast Volume Rendering and Analysis of Fuzzy Surfaces," *Technical Report No. MIPG 184*, Medical Image Processing Group, University of Pennsylvania, January 1992.

[Upso88]   Upson, C. and M. Keeler, "V-BUFFER: Visible Volume Rendering," *Computer Graphics*, Vol. 22 No. 4, August 1988, pp. 59-64.

[Whee93]   Wheeler, Donald J., *Understanding Variation*, SPC Press: Knoxville, Tennessee, 1993.

[Wilh90]   Wilhelms, James and Allen VanGelder, *Topological Considerations in Isosurface Generation*, Technical Report, University of California, Santa Cruz, CA, April 1990.

[Will87]   Willcott, M.R., G.L. Mee and J.P. Chesick, "Magnetic Field Mapping in NMR Imaging," *Magnetic Resonance Imaging*, Vol. 5, 1987, pp. 301-306.

[Youn84]   Young, Stuart W., *Nuclear Magnetic Resonance Imaging: Basic Principles*, Raven Press: New York, 1984.

Appendix H

VITA

VITA

Maj Stephen M. Matechik ▓▓▓▓▓▓▓▓▓▓▓▓▓▓▓▓▓▓▓▓▓▓▓. He graduated from Bishop Hafey High School, Hazleton, Pennsylvania in 1979. His scholastic achievements earned him a four-year Air Force Reserve Officer Training Corps Scholarship with which he entered undergraduate engineering studies at the Pennsylvania State University, University Park, Pennsylvania. He graduated with a Bachelor of Science degree in Electrical Engineering and was commissioned a 2nd Lieutenant in August 1983. His first assignment was to the Aeronautical Systems Division at Wright-Patterson AFB, Ohio where he served as lead engineer for all F-16 fighter aircraft communications, navigation and identification avionics systems. He entered the Air Force Institute of Technology (AFIT) as a 1st Lieutenant in June 1987 to pursue graduate studies in electrical engineering. In December 1988 he graduated from AFIT with a Master of Science degree in Electrical Engineering and was reassigned to the Electronic Systems Division at Hanscom AFB, Massachusetts. His leadership and technical abilities earned him the recognition as one of the divisions top company grade officers. He rose through the engineering ranks of the Airborne Warning and Control System (AWACS) Program Office to become, as a Captain, the most junior officer to have assumed the responsibilities of Chief Engineer of the AWACS Radar System Improvement Program. In June 1992 he entered the doctoral program at AFIT, School of Engineering at Wright-Patterson AFB, Ohio to conduct research in volumetric medical imaging and interpolation. Upon completion of his research, he was reassigned to Rome Laboratory at the former Griffiss AFB in Rome, New York to assume the

position of Chief, Technology Development Branch, Intelligence Data Handling Division,

Intelligence and Reconnaissance Directorate.

Maj Matechik's military decorations include the Air Force Meritorious Service

Medal, the Air Force Commendation Medal and the Air Force Achievement Medal with

one oak leaf cluster.

1. AGENCY USE ONLY (Leave blank)	2. REPORT DATE	3. REPORT TYPE AND DATES COVERED
	Dec96	Doctoral Dissertation

4. TITLE AND SUBTITLE

Using Kriging To Interpolate Spatially Distributed
Volumetric Medical Data

5. FUNDING NUMBERS

6. AUTHOR(S)

Stephen M. Matechik, Major, USAF

7. PERFORMING ORGANIZATION NAME(S) AND ADDRESS(ES)

Air Force Institute of Technology
2750 P Street
WPAFB OH 45433-6583

8. PERFORMING ORGANIZATION REPORT NUMBER

AFIT/DS/ENG/96-15

9. SPONSORING/MONITORING AGENCY NAME(S) AND ADDRESS(ES)

LtCol Frederick Berg
RL/IRD
Rome Laboratory
Rome NY 13441-4114

10. SPONSORING/MONITORING AGENCY REPORT NUMBER

11. SUPPLEMENTARY NOTES

12a. DISTRIBUTION/AVAILABILITY STATEMENT

Distribution Unlimited

12b. DISTRIBUTION CODE

13. ABSTRACT (Maximum 200 words)

Routine cases in diagnostic radiology require the interpolation of volumetric medical imaging data sets. Inaccurate renditions of interpolated volumes can lead to the misdiagnosis of a patient's condition. It is therefore essential that interpolated modality space estimates accurately portray patient space. Kriging is investigated in this research to interpolate medical imaging volumes. Kriging requires data to be spatially distributed. Therefore, magnetic resonance imaging (MRI) data is shown to exhibit spatially regionalized characteristics such that it can be modeled using regionalized variables and subsequently be interpolated using kriging. A comprehensive, automated, three-dimensional structural analysis of the MRI data is accomplished to derive a mathematical model of spatial variation about each interpolated point. Kriging uses these models to compute estimates of minimal estimation variance. Estimation accuracy of the kriged, interpolated MRI volume is demonstrated to exceed that achieved using trilinear interpolation if the derived model of spatial variation sufficiently represents the regionalized neighborhoods about each interpolated voxel. Models of spatial variation that assume an ellipsoid extent with orthogonal axes of continuity are demonstrated to insufficiently characterize modality space MRI data. Model accuracy is concluded to be critical to achieve estimation accuracies that exceed those of trilinear interpolation.

14. SUBJECT TERMS
Medical Imaging, Magnetic Resonance Imaging, Kriging, Interpolation, Estimates, Optimization, Accuracy, Statistics, Three Dimensional, Models

15. NUMBER OF PAGES
348

16. PRICE CODE

17. SECURITY CLASSIFICATION OF REPORT	18. SECURITY CLASSIFICATION OF THIS PAGE	19. SECURITY CLASSIFICATION OF ABSTRACT	20. LIMITATION OF ABSTRACT
UNCLASSIFIED	UNCLASSIFIED	UNCLASSIFIED	UL